NATIONAL TECHNICAL UNIVERSITY OF ATHENS

SCHOOL OF MINING AND METALLURGICAL ENGINEERING

DEPARTMENT OF METALLURGY AND MATERIALS TECHNOLOGY

MINERALOGY AND DISTRIBUTION OF THE SECONDARY AND TRACE BAUXITE ELEMENTS THROUGH THE BAYER PROCESS AND ITS BY-PRODUCTS

ΟΡΥΚΤΟΛΟΓΙΚΗ ΔΙΕΡΕΥΝΗΣΗ ΚΑΙ ΠΡΟΣΔΙΟΡΙΣΜΟΣ ΤΗΣ ΚΑΤΑΝΟΜΗΣ ΤΩΝ ΔΕΥΤΕΡΕΥΟΝΤΩΝ ΣΤΟΙΧΕΙΩΝ ΚΑΙ ΙΧΝΟΣΤΟΙΧΕΙΩΝ ΚΑΤΑ ΤΗΝ ΕΠΕΞΕΡΓΑΣΙΑ ΒΩΞΙΤΗ ΜΕ ΤΙ ΜΕΘΟΔΟ BAYER

DOCTORAL THESIS OF

JOHANNES VIND

Graduate of Geology, University of Tartu, MSc

Athens 2019

NATIONAL TECHNICAL UNIVERSITY OF ATHENS

SCHOOL OF MINING AND METALLURGICAL ENGINEERING

DEPARTMENT OF METALLURGY AND MATERIALS TECHNOLOGY

MINERALOGY AND DISTRIBUTION OF THE SECONDARY AND TRACE BAUXITE ELEMENTS THROUGH THE BAYER PROCESS AND ITS BY-PRODUCTS

DOCTORAL THESIS

JOHANNES VIND
Graduate of Geology, University of Tartu, MSc

Advisory Committee:

Ioannis Paspaliaris, Professor, NTUA (Supervisor)

Dimitrios Panias, Professor, NTUA

Maria Taxiarhou, Assistant Professor, NTUA

Examination Committee:

Ioannis Paspaliaris, Professor, NTUA

Dimitrios Panias, Professor, NTUA

Maria Taxiarhou, Assist. Professor, NTUA

Elias Chatzitheodoridis, Assoc. Professor, NTUA

Maria Perraki, Assoc. Professor, NTUA

Athanassios Godelitsas, Assoc. Professor, UoA

Yiannis Pontikes, Assoc. Professor, KU Leuven

Athens 2019

ΕΘΝΙΚΌ ΜΕΤΣΌΒΙΟ ΠΟΛΥΤΕΧΝΕΊΟ

ΣΧΟΛΗ ΜΗΧΑΝΙΚΩΝ ΜΕΤΑΛΛΕΙΩΝ–ΜΕΤΑΛΛΟΥΡΓΩΝ
ΤΟΜΕΑΣ ΜΕΤΑΛΛΟΥΡΓΙΑΣ ΚΑΙ ΤΕΧΝΟΛΟΓΙΑΣ ΥΛΙΚΩΝ
ΕΡΓΑΣΤΗΡΙΟ ΜΕΤΑΛΛΟΥΡΓΙΑΣ

ΟΡΥΚΤΟΛΟΓΙΚΗ ΔΙΕΡΕΥΝΗΣΗ ΚΑΙ ΠΡΟΣΔΙΟΡΙΣΜΟΣ ΤΗΣ ΚΑΤΑΝΟΜΗΣ ΤΩΝ ΔΕΥΤΕΡΕΥΟΝΤΩΝ ΣΤΟΙΧΕΙΩΝ ΚΑΙ ΙΧΝΟΣΤΟΙΧΕΙΩΝ ΚΑΤΑ ΤΗΝ ΕΠΕΞΕΡΓΑΣΙΑ ΒΩΞΙΤΗ ΜΕ ΤΙ ΜΕΘΟΔΟ BAYER

ΔΙΔΑΚΤΟΡΙΚΗ ΔΙΑΤΡΙΒΗ

ΓΙΟΧΑΝΕΣ ΒΙΝΤ
Πτυχιούχος Γεωλογίας, Πανεπιστήμιο του Tartu, MSc

Συμβουλευτική Επιτροπή:
Ιωάννης Πασπαλιάρης, Καθηγητής ΕΜΠ (Επιβλέπων)
Δημήτριος Πάνιας, Καθηγητής ΕΜΠ
Μαρία Ταξιάρχου, Επικ. Καθηγήτρια ΕΜΠ

Επταμελής Εξεταστική Επιτροπή:
Ιωάννης Πασπαλιάρης, Καθηγητής ΕΜΠ
Δημήτριος Πάνιας, Καθηγητής ΕΜΠ
Μαρία Ταξιάρχου, Επικ. Καθηγήτρια ΕΜΠ
Ηλίας Χατζηθεοδωρίδης, Αν. Καθηγητής ΕΜΠ
Μαρία Περράκη, Αν. Καθηγήτρια ΕΜΠ
Αθανασιος Γκοντελίτσας, Αν. Κακθγθτισ ΕΚΠΑ
Γιάννης Ποντίκης, Αν. Κακθγθτισ KU Leuven

Αθήνα 2019

Approved by the seven-member examination committee:

Ioannis Paspaliaris
Professor, NTUA

Dimitrios Panias
Professor, NTUA

Maria Taxiarhou
Assist. Professor, NTUA

Elias Chatzitheodoridis
Assoc. Professor, NTUA

Maria Perraki
Assoc. Professor, NTUA

Athanassios Godelitsas
Assoc. Professor, UoA

Yiannis Pontikes
Assoc. Professor, KU Leuven

Dedicated to my dear family: Kristiina, Kirsi and Lennart.

Acknowledgements

First, I’m very grateful for the excellent academic supervision by professor Dimitrios Panias (NTUA) as well as for the supervision by doctor Vicky Vassiliadou (Aluminium of Greece, Mytilineos S.A.) from the industrial side of the project.

I received invaluable help from Aluminium of Greece by Sokratis Tekidis, Athina Filippou, Dritsa Athina, Soupsana Paraskevi and many more.

Petros Tsakiridis, Elias Chatzitheodoridis, Apostolos Kourtis, Ioanna Giannopoulou, Panagiotis Davris, Alexandra Alexandri and all other great researchers from NTUA whom I was honoured to meet and cooperate with are thanked for their professional help with many technical and academic questions.

I’m grateful for the cooperation with many researchers outside of NTUA who made possible the publication of several joint papers: Annelies Malfliet, Bart Blanpain from KU Leuven; Päärn Paiste, Kalle Kirsimäe, Marian Külaviir, Alan Tkaczyk, Andrei Goronovski from University of Tartu and István Sajó from University of Pécs.

The complete team of MSCA-ETN REDMUD consisting of PhD candidates, supervisors and supporting staff is thanked for providing so much new experiences and knowledge. Special thanks go to Rabab Nasser, Gyorgy Banvolgyi and Ken Evans.

The help of Konstantinos Kollias who translated the abstract of this thesis to Greek is greatly appreciated.

Last but not the least I would like to thank my closest colleagues Pritii Tam, Chiara Bonomi and Chiara Cardenia for creating a highly productive and creative atmosphere for working in NTUA.

The research leading to these results has received funding from the European Community’s Horizon 2020 Programme (H2020/2014–2019) under Grant Agreement no. 636876 (MSCA-ETN REDMUD). This publication reflects only the authors’ views, exempting the Community from any liability. Project website: http://www.etn.redmud.org.

Abstract

General Framework of the Research

This study was designed to elucidate the mineralogy and distribution of minor and trace elements (especially the rare earth elements — REEs, scandium — Sc, gallium — Ga and vanadium — V) during the production of alumina from bauxite ore in the Bayer process. The investigation was set up as a case study in the Aluminium of Greece refinery (Mytilineos S.A.). Bauxites can contain up to 50 chemical elements in concentrations above 1 mg/kg, most of which can be considered as trace elements. Of those trace elements, at least five metals or groups of metals (light REEs, heavy REEs, Sc, Ga and V) occur in elevated concentrations in Greek karstic bauxites and at the same time have been listed as critical raw materials by the European Commission. Bayer process accumulates those trace elements either to process liquor or to the main by-product known as the bauxite residue. Given the enhanced concentrations of certain trace elements, there exists an interest to extract some of those metals as valuable by-products of the Bayer process. However, the mineralogy of those critical metals in Bayer process materials as well as their distribution patterns during alumina production are so far poorly constrained. Therefore, the aim of this dissertation is to (1) explain the distribution characteristics of trace elements (especially those of the REEs, Sc, Ga, V, Th, As and U), and (2) elucidate the mineralogical characteristics of trace elements (especially the REEs and Sc) in the Bayer process materials including bauxite and the residues derived from it.

Methodology

Representative solid and liquid samples were collected from the complete flowsheet of the Bayer process, including bauxites from six different sources as well as derived residues. Additionally, minor by-products such as scales from plant piping and solids from different filters were collected and examined. The trace element composition of the samples was mainly determined by inductively coupled plasma mass spectrometry (ICP-MS) and optical emission spectrometry (ICP-OES) as well as with instrumental neutron activation analysis (INAA). Trace element concentrations were used in combination with the plant mass flow data to compile mass balance models of the trace elements to explain the distribution patterns of the trace elements in the Bayer process.

Mineralogical characteristics of the trace elements were studied with a combination of microanalytical techniques. General microscale characteristics were described by using scanning electron microscopy (SEM), nanoscale investigation was performed by high resolution transmission electron microscopy (HRTEM). Specific microscale analyses and in situ trace element quantification were performed by electron microprobe coupled with wavelength dispersive spectrometers (EPMA-WDS). In situ trace element analyses were also carried out by laser ablation (LA) ICP-MS and in situ phase identification by Raman microscopy.

Main Results

The assessment of trace element distribution revealed that the elements are mainly divided into two categories: (1) those that dissolve and accumulate into the Bayer process liquor and achieve different saturation levels (Ga, V, Cr, As, U), and (2) those that pass through the Bayer circuit in the composition of solid mineral matrix and do not occur in dissolved forms (Sc, REEs, Th). From the elements in the first category, only Ga and U have the property to enter to the composition of the aluminium hydroxide produced in the Bayer process. Namely, about 70% of the initial quantity of Ga and about 10% of U can be found in the aluminium hydroxide product, while the rest of their mass is separated with bauxite residue. Almost the complete mass (mostly >98%) of the other investigated trace elements (REEs, Sc, Th, V, Cr, As) ends up in the bauxite residue.

It was found that even though the REEs pass through the Bayer process in the forms of solid phases, their mineralogical properties and chemical composition of minerals are changed during the bauxite digestion. The precursor REE phases in bauxites are mainly REE fluorocarbonates of the bastnäsite group and cerium oxide in the form of cerianite (CeO_2). During the bauxite processing, they interact with the caustic process liquor as well as with the dissolved Ca, Ti and Fe ions and the resulting phases found in bauxite residue are REE ferrotitanates. They eventually form a solid solution series between the ideal end-members $(Ca,Na)(Ti,Fe)O_3$ and $(REE,Ca,Na)(Ti,Fe)O_3$, depending on the extent of transformation that has taken place. It is characteristic to the REE phases in bauxite residue that they are surrounded by calcium titanate shells, that might inhibit the leaching efficiency of the REEs from bauxite residue.

The modes of occurrences of Sc, however, remain practically the same in the bauxite and in the derived residue. Most of the Sc is associated with hematite, followed by goethite. Smaller amount of Sc is found in the composition of aluminium oxyhydroxide phases (boehmite and diaspore) and zircon. In bauxite residue, hematite, goethite and zircon host respectively 55±20 %, 25±20 % and 10±5 % of the total Sc. Since most of boehmite/diaspore is digested in the Bayer process, the proportion of Sc associated with those phases is assumed to be released during the digestion and thereafter probably precipitated on the mineral surfaces of bauxite residue's particulates.

Main Contribution of the Dissertation

The results obtained in this work provide an insight of the fate of selected trace elements in the Bayer process in terms of their distribution and mineralogy. The obtained knowledge can be utilised to improve and plan the extraction of trace elements that are also considered as critical raw materials. The compiled distribution models can also be used as one of the sources in global or local critical metals resource estimations. In addition, the elucidated mineralogical characteristics of especially the REEs and Sc provide explanations of why very high recovery rates of those elements are difficult to be achieved when leaching experiments of bauxite residue are performed.

Περίληψη/Abstract in Greek

Ευρύτερο πλαίσιο της έρευνας

Η παρούσα έρευνα σχεδιάστηκε με σκοπό την αποσαφήνιση της ορυκτολογίας και της κατανομής δευτερευόντων- και ιχνο- στοιχείων, κατά τη διάρκεια της παραγωγής αλουμίνας από βωξίτη με τη μέθοδο Bayer. Η έρευνα ως μελέτη περίπτωσης τοποθετείται στην εταιρεία «Αλουμίνιον της Ελλάδος» («Εταιρεία Μυτιληναίος Α.Ε.»). Οι βωξίτες δύναται να περιέχουν έως και 50 χημικά στοιχεία σε συγκεντρώσεις πάνω από 1 mg/kg και επομένως μπορούν να χαρακτηριστούν ιχνοστοιχεία. Από αυτά τα ιχνοστοιχεία, τουλάχιστον 5 μέταλλα ή ομάδες μετάλλων (π.χ. στοιχεία σπάνιων γαιών — REEs) εμφανίζονται σε αυξημένες συγκεντρώσεις στους ελληνικούς καρστικούς βωξίτες και την ίδια στιγμή αναφέρονται ως κρίσιμες πρώτες ύλες από την Ευρωπαϊκή Ένωση. Η μέθοδος Bayer συσσωρεύει αυτά τα ιχνοστοιχεία, είτε στην υδατική φάση είτε στα κύρια παραπροϊόντα γνωστά ως κατάλοιπα βωξίτη. Δεδομένων των αυξημένων συγκεντρώσεων ορισμένων ιχνοστοιχείων, υπάρχει ενδιαφέρον για την εξαγωγή ορισμένων εκ των μετάλλων αυτών ως πολύτιμα παραπροϊόντα της μεθόδου Bayer. Ωστόσο, η ορυκτολογία αυτών των κρίσιμων μετάλλων σε συνδυασμό με την κατανομή τους κατά την παραγωγή της αλουμίνας δεν είναι επαρκώς τεκμηριωμένα και κατανοητά. Επομένως, σκοπός της παρούσας διατριβής είναι (1) να εξηγηθούν τα χαρακτηριστικά κατανομής των ιχνοστοιχείων (ιδιαίτερα των REEs, σκάνδιο — Sc, γάλλιο — Ga και βανάδιο — V) και (2) να διασαφηνιστούν τα ορυκτολογικά χαρακτηριστικά των ιχνοστοιχείων (ιδιαίτερα των REEs και Sc) στις διάφορες φάσεις της μεθόδου Bayer, συμπεριλαμβανομένου του βωξίτη και των παραγόμενων υπολειμμάτων.

Μεθοδολογία

Αντιπροσωπευτικά στερεά και υδατικά δείγματα συλλέχθηκαν στο πλαίσιο του διαγράμματος ροής της μεθόδου Bayer, συμπεριλαμβανομένου βωξίτη από έξι διαφορετικές πηγές καθώς επίσης και παραγόμενα κατάλοιπα. Επιπρόσθετα, μικροποσότητες παραπροϊόντων από τις σωληνώσεις των εγκαταστάσεων και στερεά από διάφορα φίλτρα συλλέχθηκαν και εξετάστηκαν. Η σύσταση των δειγμάτων ως προς τα ιχνοστοιχεία προσδιορίστηκε με φασματομετρία επαγωγικά

συζευγμένου πλάσματος με φασματογράφο μάζας (ICP-MS) και οπτικής εκπομπής (ICP-OES), καθώς επίσης με ενόργανη νετρονική ενεργοποίηση (NAA). Οι συγκεντρώσεις των ιχνοστοιχείων χρησιμοποιήθηκαν σε συνδυασμό με τα δεδομένα ροής για να προκύψουν ισοζύγια μάζας των στοιχείων αυτών και να διευκρινιστούν τα μοντέλα κατανομής των ιχνοστοιχείων στη μέθοδο Bayer.

Τα ορυκτολογικά χαρακτηριστικά των ιχνοστοιχείων μελετήθηκαν με ένα συνδυασμό τεχνικών μικροανάλυσης. Τα γενικά χαρακτηριστικά σε μικρο- κλίμακα περιγράφονται με χρήση ηλεκτρονικού μικροσκοπίου σάρωσης, ενώ διερεύνηση σε νανο- κλίμακα πραγματοποιήθηκε με υψηλής ευκρίνειας μικροσκόπιο διερχόμενης δέσμης ηλεκτρονίων. Εξειδικευμένες αναλύσεις σε μικρο- κλίμακα των ιχνοστοιχείων πραγματοποιήθηκαν με ηλεκτρονικό μικροαναλυτή συνδυασμένο με σύστημα διασποράς μήκους κύματος. Επίσης, in situ αναλύσεις ιχνοστοιχείων και ταυτοποίηση ορυκτολογικών φάσεων πραγματοποιήθηκαν με φωτοαποδόμηση υλικών με λέιζερ σε φασματογράφο μάζας (laser ablation ICP-MS) και μικροσκοπία Raman, αντίστοιχα.

Κύρια αποτελέσματα

Η εκτίμηση της κατανομής των ιχνοστοιχείων έδειξε ότι τα στοιχεία αυτά διαχωρίζονται κυρίως σε δύο κατηγορίες: (1) στα στοιχεία που διαλυτοποιούνται και συσσωρεύονται στην υδατική φάση της μεθόδου Bayer με διαφορετικά επίπεδα κορεσμού (Ga, V, Cr, As, U), και (2) στα στοιχεία που διέρχονται από το κύκλωμα Bayer και δεν διαλυτοποιούνται (Sc, REEs, Th). Όσον αφορά τα στοιχεία της 1^{ης} κατηγορίας, μόνο το Ga και το U εισέρχονται στη σύνθεση υδροξειδίου του αργιλίου κατά τη μέθοδο Bayer. Συγκεκριμένα, το 70% της αρχικής ποσότητας Ga και το 10% του U βρίσκονται στο υδροξειδίου του αργιλίου, ενώ η υπόλοιπη ποσότητα εντοπίζεται στο κατάλοιπο βωξίτη.

Διαπιστώθηκε ότι παρά το γεγονός ότι τα REE διέρχονται μέσω της μεθόδου Bayer προς τη στερεά φάση, οι ορυκτολογικές ιδιότητές τους και η χημική σύσταση μεταβάλλονται κατά τη διάρκεια της εκχύλισης του βωξίτη. Οι πρόδρομες φάσεις REE στους βωξίτες είναι κυρίως REE-φθοροανθρακικά άλατα της ομάδας του μπαστναζίτη και οξείδιο του δημητρίου (CeO_2). Κατά τη διεργασία, οι προαναφερθείσες φάσεις αντιδρούν με το εκχυλιστικό μέσο και με διαλελυμένα ιόντα Ca, Ti και Fe με αποτέλεσμα να προκύπτουν REE-σιδηροτιτανιούχες φάσεις στο κατάλοιπο βωξίτη. Τελικά σχηματίζονται στερεά διαλύματα μεταξύ των ακραίων μελών $(Ca,Na)(Ti,Fe)O_3$ και $(REE,Ca,Na)(Ti,Fe)O_3$, ανάλογα με το βαθμό μετασχηματισμού που λαμβάνει χώρα. Είναι χαρακτηριστικό ότι οι φάσεις REE στο κατάλοιπο βωξίτη περιβάλλονται από φάσεις τιτανικού ασβεστίου ($CaTiO_3$).

Οι ορυκτολογικές φάσεις του Sc παραμένουν πρακτικά ίδιες στο βωξίτη και στο παραγόμενο κατάλοιπο. Η πλειονότητα του Sc σχετίζεται με τον αιματίτη και τον γκαιτίτη. Μικρότερη ποσότητα απαντάται σε οξυυδροξείδια του αργιλίου (βαιμίτης και διάσπορο) και στο ζιρκονίτη (zircon). Στο κατάλοιπο βωξίτη, ο αιματίτης, ο γκαιτίτης και ο ζιρκονίτης φιλοξενούν 55±20%, 25±20 % and 10±5% της αρχικής ποσότητας Sc, αντίστοιχα. Καθώς η μεγαλύτερη ποσότητα βαιμίτη/διασπόρου εκχυλίζεται κατά τη μέθοδο Bayer, το μέρος του Sc που σχετίζεται με αυτές τις φάσεις θεωρείται ότι απελευθερώνεται κατά τη διάρκεια της εκχύλισης και στη συνέχεια πιθανώς καταβυθίζεται στις επιφάνειες των ορυκτών που απαρτίζουν το κατάλοιπο βωξίτη.

Κύρια συνεισφορά της διατριβής

Τα αποτελέσματα που προέκυψαν από την παρούσα διατριβή συμβάλλουν στην κατανόηση της διαδρομής επιλεγμένων ιχνοστοιχείων στη μέθοδο Bayer ως προς την κατανομή και την ορυκτολογία τους. Η αποκτηθείσα γνώση μπορεί να χρησιμοποιηθεί για τη βελτίωση και το σχεδιασμό της εξαγωγής των ιχνοστοιχείων, τα οποία μπορούν να χαρακτηριστούν τόσο ως κρίσιμες πρώτες ύλες, όσο και παραπροϊόντα της μεθόδου Bayer. Εξειδικευμένα μοντέλα κατανομής μπορούν επίσης να χρησιμοποιηθούν σε εκτιμήσεις πηγών κρίσιμων μετάλλων σε παγκόσμια ή τοπική κλίμακα. Επιπρόσθετα, τα ορυκτολογικά χαρακτηριστικά, κυρίως, των REE και Sc παρέχουν σαφείς εξηγήσεις, σχετικά με τη αδυναμία επίτευξης υψηλών ποσοστών ανάκτησης, όταν πραγματοποιούνται δοκιμές εκχύλισης των καταλοίπων βωξίτη.

Abbreviations

AAS	Atomic Absorption Spectrometry
ICP-MS	Inductively Coupled Plasma-Mass Spectrometry
ICP-OES	Inductively Coupled Optical Emission Spectrometry
XRF	X-Ray Fluorescence
XRD	Powder X-Ray Diffraction
SEM-EDS	Scanning Electron Microscopy with Energy Dispersive Spectroscopy
EPMA	Electron Probe Microanalyzer
WDS	Wavelength Dispersive Spectroscopy
INAA	Instrumental Neutron Activation Analysis
DSP	Desilication Product
HMS	Heavy Media Separation
BSE	Backscattered Electron (image)
LOI	Loss on Ignition

List of Publications

This thesis is based on the following papers, published as open access articles distributed under the terms and conditions of the Creative Commons Attribution (CC BY 4.0) license (http://creativecommons.org/licenses/by/4.0/).

Peer-reviewed journal articles

1. Vind, J., Malfliet, A., Blanpain, B., Tsakiridis, P.E., Tkaczyk, A.H., Vassiliadou, V., Panias, D., 2018. Rare Earth Element Phases in Bauxite Residue. Minerals 8, 77. https://doi.org/10.3390/min8020077
2. Vind, J., Malfliet, A., Bonomi, C., Paiste, P., Sajó, I.E., Blanpain, B., Tkaczyk, A.H., Vassiliadou, V., Panias, D., 2018. Modes of occurrences of scandium in Greek bauxite and bauxite residue. Minerals Engineering 123, 35–48. https://doi.org/10.1016/j.mineng.2018.04.025
3. Vind, J., Alexandri, A., Vassiliadou, V., Panias, D., 2018. Distribution of selected trace elements in the Bayer process. Metals 8 (5), 327. https://doi.org/10.3390/met8050327

Peer-reviewed conference articles

1. Vind, J., Paiste, P., Tkaczyk, A.H., Vassiliadou, V., Panias, D., 2017. The behaviour of scandium in the Bayer process, in: Book of Abstracts. Presented at the 2nd Conference on European Rare Earth Resources, Heliotopos Conferences Ltd., Santorini, Greece, 28–31 May 2017, pp. 190–191.
2. Vind, J., Vassiliadou, V., Panias, D., 2017. Distribution of trace elements through the Bayer process and its by-products, in: Travaux 46. Presented at the 35th International ICSOBA Conference, Hamburg, Germany, 2–5 October 2017, pp. 255–267.
3. Vind, J., Vassiliadou, V., Panias, D., 2018. Rare earths and scandium mineralogy in bauxite residue, in: Proceedings. Presented at the 2nd International Bauxite Residue Valorisation and Best Practices Conference, Athens, Greece, 7–10 May 2018, pp. 387–392.

Contents

Abstract i

Περίληψη/Abstract in Greek ... iii

Abbreviations ... vii

List of Publications ... ix

Peer-reviewed journal articles ... ix

Peer-reviewed conference articles ... ix

Contents xi

List of Figures ... xv

List of Tables ... xxi

Introduction ... 1

1. Background ... 7

1.1 Bauxite ... 7

1.1.1 REEs and Sc Geochemistry and Phase Composition in Bauxites ... 9

1.1.2 Ga and V Geochemistry in Bauxite Context ... 11

1.2 Bayer Process Description ... 12

1.3 Trace Elements Behaviour Relating to the Bayer Circuit ... 14

1.4 REEs and Sc Abundance and Mineralogy in Bauxite Residue ... 16

1.4.1 REEs ... 16

1.4.2 Sc ... 17

2. Materials and Methods ... 19

2.1 Sampling and Technological Data 19
2.2 Compiling of the Mass Balance 21
2.3 Analytical Methods for Bulk Material Characterisation 21
2.4 Microanalytical Methods 22
2.4.1 Challenges in the Microanalysis of Bauxite Residue 24
3. General Characteristics of the Materials 27
3.1 Chemical and Mineralogical Composition of Solid Materials 27
3.2 Basic Microscale Characteristics 35
3.2.1 Bauxites..................35
3.2.2 Bauxite Residue 36
3.2.3 Aluminium Hydroxide and Alumina..................37
3.3 Chemical Composition of the Bayer Liquors 38
4. Distribution of Trace Elements in the Bayer Process 41
4.1 Metals (and Metalloids) that Accumulate to Processing Liquor 41
4.2 Metals that do not Accumulate to Liquor..................48
4.3 Fractionation Indexes and Systemic Predictions..................52
4.4 Trace Elements Distribution in Minor By-Products (Scales, Filtered Solids)..................54
4.5 Summary of the Trace Elements Distribution 63
5. Minor and Nano-Scaled Phases in Bauxite Residue 65
6. REEs Mineralogy in Bauxite and Bauxite Residue 73
6.1 Precursor REE phases in bauxite feed 73
6.2 Preheating Stage 77
6.3 REE Phases in Bauxite Residue 79
6.3.1 REE Carbonate and Phosphate Species 79
6.3.2 LREE Ferrotitanate Species, (REE,Ca,Na)(Ti,Fe)O_3 80
6.3.3 Manganese-Associated Ce Oxide or Oxyhydroxide..................92
6.3.4 Heavy REE Phosphates..................95
6.3.5 Mixed REE Occurrences 95
6.4 Summary of the REE Phases Physical Parameters..................97
6.5 Considerations for the Recovery of REEs from Bauxite Residue..................98
7. Modes of Occurrences of Sc in Bauxite and Bauxite Residue 101
7.1 Sc Hosted in Hematite and Goethite 101

7.1.1 Bauxite Samples 101
7.1.2 Bauxite Residue Sample 105
7.2 Aluminium Oxyhydroxides as Minor Sc Hosts 109
7.3 Minor and Secondary Phases 111
7.3.1 Sc-Hosting 111
7.3.2 Sc-Depleted 113
7.4 Distribution of Scandium Between its Host Minerals 115
7.5 The Route of Scandium Enrichment into Bauxite Residue 116
7.6 Linkages Between the Sc Occurrences and its Leaching Behaviour 117
8. Conclusions 119
8.1 Distribution of Trace Elements 119
8.2 REE Phases 120
8.3 Sc Occurrences 121
Appendix A 123
Appendix B 137
Appendix C 139
References 147

List of Figures

Figure 1. Stratigraphic column of Parnassos-Ghiona bauxite deposit showing the positions of first (B1), second (B2) and third (B3) bauxite horizons between the Mesozoic limestones. Modified after (Laskou and Economou-Eliopoulos, 2007). 8

Figure 2. Typical profile of Porto Trombetas bauxite, showing the transition from basal sediment to upper kaolinitic layer. Adapted after (Boulangé and Carvalho, 1997)...9

Figure 3. Simplified flowsheet of the Bayer process in AoG. Numbers indicate the sampled materials, while underlined numbers show samples in liquor form. Description of sampled materials can be found in Materials and Methods section 2.1, **Table 2**. 13

Figure 4. Macroscale photographs of bauxite samples: (a) first Greek Parnassos-Ghiona B3 horizon bauxite, DD-BX; (b) second Greek Parnassos-Ghiona B3 horizon bauxite, ST-BX; (c) Greek Parnassos-Ghiona B2 horizon bauxite, HS-BX; (d) Turkish bauxite from Milas area, TU-BX; (e) Brazilian bauxite from Porto Trombetas deposit, TR-BX; and (f) Ghanaian bauxite from Awaso deposit, GH-BX. 27

Figure 5. Appearance of bauxite residue shown on (a) macroscale photograph of a sample prepared in the manner of XRF pressed pellet impregnated with resin and polished, and (b) BSE composite image of a polished section of residue sample in resin. The images do not correspond to each other. On image (b), brighter particles are generally Fe oxides and greyish areas are generally composed of Al-Ca-Si-Ti matrix while black colour represents resin. 28

Figure 6. Chondrite-normalised plot of bauxites and bauxite residue. In the positions with gaps, the REE concentrations are below detection limit. Chondrite data is adapted from Anders and Grevesse, (1989). Gaps mark the analyses where the analyte concentration is below the available detection limit. 31

Figure 7. Examples of diffractograms and simulated patterns of (a) Greek Parnassos-Ghiona B3 horizon bauxite, DD-BX; and (b) bauxite residue. Intensity scale is linear....................................31

Figure 8. Comparison of AoG's bauxite residue phase composition deposited in different years. Abbreviations: hematite (Hema), hydrogarnet (Hgr), diaspore (Dias), Chamosite (ChmA), goethite

(Goet), cancrinite (Canc), perovskite (Pero), boehmite (Boeh), rutile (Ruti), calcite (Calc), gibbsite (GibS), quartz (Quar), anatase (Anat). 34

Figure 9. Average AoG's bauxite residue mineralogical phase composition based on 6 residue samples. 34

Figure 10. Microstructure of bauxite samples shown on BSE images: (a) first Greek Parnassos-Ghiona B3 horizon bauxite, DD-BX; (b) second Greek Parnassos-Ghiona B3 horizon bauxite, ST-BX; (c) Greek Parnassos-Ghiona B2 horizon bauxite, HS-BX; (d) Turkish bauxite from Milas area, TU-BX; (e) Brazilian bauxite from Porto Trombetas deposit, TR-BX; and (f) Ghanaian bauxite from Awaso deposit, GH-BX. Ti — titanium dioxide particle, Zr — zircon particle. Generally, the darker greyish areas are Al-dominant and brighter areas are Fe-dominant. 35

Figure 11. Microscale BSE images of bauxite residue's main mineral phases: (a) particles of Fe oxides (Fe) and undigested boehmite/diaspore (Al) particles as well as calcium aluminate particle in fine homogeneous Fe-Al-Ca-Si-Ti matrix of the residue, (b) fragment of an Fe oxide particle, (c) two Fe phases attached to each other, corresponding to hematite and goethite as identified by µ-Raman spectroscopy, (d) undigested boehmite/diaspore, (e) undigested boehmite/diaspore which edge areas are affected by the caustic leaching, (f) Ca phase corresponding to calcite, (g) titanium dioxide corresponding to anatase or rutile, (h) titanium dioxide, likely anatase, and a newly formed calcium titanate phase on the account of reacted anatase, and (i) calcium aluminium ferro-silicate phase probably corresponding to iron substituted hydrogarnet. 37

Figure 12. Microstructure of alumina (a–c) and aluminium hydroxide (d–f) with impurities. Cor — corundum (or other forms of Al_2O_3), Gb — gibbsite. 38

Figure 13. Mass distribution of Ga (mg/kg) normalised to mass of aluminium hydroxide produced, based on ICP-MS (solids) and ICP-OES (liquors) data. 42

Figure 14. Mass distribution of V (mg/kg) normalised to mass of aluminium hydroxide produced, based on XRF-st and ICP-OES data 43

Figure 15. Mass distribution of As (mg/kg) normalised to mass of aluminium hydroxide produced, based on ICP-MS (solids) and INAA (liquors) data. 45

Figure 16. Mass distribution of Cr (mg/kg) normalised to mass of aluminium hydroxide produced, based on ICP-MS (solids and liquors) data. 45

Figure 17. Mass distribution of U (mg/kg) normalised to mass of aluminium hydroxide produced, based on ICP-MS (solids and liquors) data. 46

Figure 18. Mass distribution of Ce (mg/kg) normalised to mass of aluminium hydroxide produced, based on INAA (solids) and ICP-MS (liquors) data. 48

Figure 19. Mass distribution of Y (mg/kg) normalised to mass of aluminium hydroxide produced, based on ICP-MS (solids and liquors) 49

Figure 20. Mass distribution of Sc (mg/kg) normalised to mass of aluminium hydroxide produced, based on INAA (solids and liquors). 50

Figure 21. Mass distribution of Th (mg/kg) normalised to mass of aluminium hydroxide produced, based on ICP-MS data (solids and liquors). 51

Figure 22. Mass distribution of Lu (mg/kg) normalised to mass of aluminium hydroxide produced, based on INAA (solids and liquors). 52

Figure 23. Fractionation indexes of trace elements calculated as trace element concentration in bauxite residue divided by trace element concentration in bauxite. Fractionation indexes are compared to the one of Fe_2O_3 during sampling period (horizontal dashed line)...........................53

Figure 24. Macroscopic photographs of minor by-products: (a) evaporator scale shown from the side that has been in contact with process liquor, (b) evaporator scale shown from the side that has been in contact with the plant tubing, (c) fragment of the red fraction of evaporator scale, (d) cross section view of the white fraction of evaporator scale, (e) digester autoclave scale, and (f) solids from security filtration embedded in resin (prepared for microscale analysis). 55

Figure 25. Microstructure of Bayer process minor by-products shown in BSE images: (a) white evaporator scale, (b) red evaporator scale, (c) digester scale, (d) security filtration solid material with Fe-Cr-Mn particle in the middle, (e) calciner electrofilter dust overview image, and (f) elongated particles of calciner dust that are irregular compared to aluminium hydroxide or calcined alumina. Abbreviations: Cn — cancrinite, So — sodalite, P — perovskite, He — hematite, Hg — hydrogarnet, Po — portlandite, Gb — gibbsite, Cor — corundum (or other forms of Al_2O_3).........58

Figure 26. SEM-EDS elemental mapping of digester autoclave scale, where calcium (ferro)titanate (perovskite) crystals have intergrown into Na-Al-Si matrix, corresponding to cancrinite/sodalite. 59

Figure 27. Digester autoclave scale depicted on (a) optical microscope image with indicated points of LA-ICP-MS analysis spots. In graph (b) are given the main and trace elements distribution profiles, obtained by LA-ICP-MS. White spots on image (a) correspond to concentration values on graph (b). Standard element for LA-ICP-MS quantification was Fe. 61

Figure 28. Micro-areas of digester autoclave scale with (a) prevailing presence of perovskite (P) with cancrinite/sodalite (Cn) and some Fe particles as well as (b) cancrinite-dominant area. Perovskite area (a) corresponds to quantification shown in **Table 12.** 62

Figure 29. Trace elements distribution in different Bayer process materials. A reminder of sample names: SE-FI — security filtration solids, DG-SC — digester scale, TR-BX — Porto Trombetas bauxite, DC-BX mixed Greek Parnassos-Ghiona B3 horizon bauxite, RM-FP — bauxite residue, HY-AL — aluminium hydroxide, EL-DU — calciner dust from electrostatic filter. 63

Figure 30. Electron images of bauxite residue's minor phases: (a) Ca-Mg phase (dolomite?), (b) Ca-Mg-Al phase, (c) Ca phase that is likely portlandite ($Ca(OH)_2$), (d) Al-Si-K phase that could be a feldspar group phase, (e) Fe-Al-Si-Mg phase that could correspond to chamosite group phase, (f) Mn phase associated with minor cerium (Ce), (g) zircon, (h) copper sulphide that might correspond to chalcopyrite, (i) Fe-Cr phase that could correspond to chromite. All except for image (i) are BSE images from polished sections, but (i) is a secondary electron image of bauxite residue "as is", i.e. not in a polished condition...67

Figure 31. Backscattered electron images of (a) a fraction of metallic Fe containing Cr (denoted as Fe) compared with (b) typical bauxite residue's Fe oxide particle (denoted as FeO) and (c) their respective EDS spectra. Denotation of matrix refers to bauxite residue's Fe-Ca-Al-Si-Ti matrix. Note that the EDS spectrum of the metallic Fe particle does not possess the oxygen energy peak that Fe oxide particle has...68

Figure 32. Reacted titanium dioxide attached to calcium titanate (perovskite) reaction product, shown in (a) BSE image with EDS elemental maps and (b) respective EDS spectra. 70

Figure 33. HRTEM images of bauxite residue particles: (a) and (b) Fe particles corresponding to hematite, (c) agglomeration of Al-Na-Si particles corresponding to cancrinite or sodalite, (d) boehmite or diaspore together with Fe particles, (e) hexagonal Ca-Al-Si-Ti-Fe-Si phase that could correspond to titanium substituted hydrogarnet, (f) euhedral titanium dioxide particle corresponding to rutile based on electron diffraction pattern, (g) phyllosilicate phase and (h) chlorite group phase corresponding to chamosite. 72

Figure 34. Cerianite rich area in the second Parnassos-Ghiona B3 horizon bauxite sample (ST-BX) shown on (a) BSE image with respective EDS elemental maps, and (b) Raman spectra of cerianite and its surrounding matrix compared to reference Raman spectrum obtained from RRUFF database (Lafuente et al., 2015), with permission from RRUFF™. Raman spectrum is collected with a 532-nm wavelength laser. 75

Figure 35. REE phase in first Parnassos-Ghiona B3 horizon bauxite sample (DD-BX) associated with aluminosilicate (Al-Si). 76

Figure 36. In sub-figures (a-c) are shown florencite group LREE phases (Fl) and a zircon grain (Zr) and in (d) is a xenotime/churchite particle with a major composition of Y phosphate (YP), all contained in Ghanaian Awaso lateritic bauxite matrix. 77

Figure 37. Backscattered electron images of (a) La-Nd predominant REE particle, (b) intact Ce particle, (c) cracked Ce particle. In figure (d) is given the EDS spectrum corresponding to La-Nd particle (a). 78

Figure 38. Ce ferrotitanate phase observed in the karst bauxite preheating stage. The particle is mainly surrounded by the undigested Al phases matrix. 78

Figure 39. An ancylite group LREE carbonate phase depicted on (a) BSE image with its (b) EDS spectrum and (c) Raman spectrum compared to a reference spectrum of kozoite-(La) obtained from RRUFF database (Lafuente et al., 2015), with permission from RRUFF™. Raman spectrum is collected with a 532-nm wavelength laser. 79

Figure 40. Ce phosphate in bauxite residue matrix, shown on (a) BSE image with its (b) EDS spectrum. 80

Figure 41. BSE images of Ce ferrotitanate grains in bauxite residue matrix, (a), (b) and (c). The indicated quantification spots are reported in **Table 14**. 81

Figure 42. Nd-La predominant LREE particles, of which (a) is partly reacted, and (b) exhibits a zonation (I–III) relating to reaction stages with Bayer liquor. Within zone II of (b), deposition of a sodium aluminosilicate phase (Na-Al-Si) is indicated. Denoted measurement spots refer to **Table 15**. 82

Figure 43. Ce ferrotitanate particle shown on (a) secondary electron image with its (b) EDS spectrum; gold (Au) peak is from the coating layer on the sample. 84

Figure 44. LREE-bearing Ca ferrotitanate observed in the bright field imaging mode of HRTEM. SAED pattern of the particle is inserted to the upper right corner. The pattern is collected from [121] direction and corresponds to perovskite structure. 85

Figure 45. Morphological variations of Ca ferrotitanate (CTO) particles in nanoscale: (a) subhedral particles and a Fe oxide particle, (b) subhedral particles, (c) anhedral particle and (d) euhedral particles. 85

Figure 46. EPMA-WDS quantitative elemental mapping of a reacted LREE particle. The intensely reacted area is also intergrown with sodium aluminosilicate phase (indicated with Na-Al-Si). Mapped area corresponds to **Figure 42**b. 87

Figure 47. Raman spectrum collected from zone II of LREE ferrotitanate particle that is shown in **Figure 42**. 88

Figure 48. Various occurrences of Ca-Ti rims (a–c) with respective elemental maps and (d) EDS spectra. 89

Figure 49. Solid solution character of LREE ferrotitanate series, depicted as ionic proportions of the (a) substitutions of Ca and Na with REE on A site and (b) complete transformation, where (REE + Na + Th) + (Fe + Al) = Ca + Ti. Region annotated with I on (a) refers to the area of real solid solution, region annotated with II on (a) indicates to the measurements on transitional phases. Adapted after (Campbell et al., 1997; Nickel and McAdam, 1963). The equation is changed for a best description of present situation (i.e., Nb is left out of the equation whilst Th and Al are added to A and B sites, respectively). Figures are based on data from **Table 14** and **Table 15**. 90

Figure 50. Ce oxide/oxyhydroxide phase associated with Mn particle shown on (a) EDS elemental map with (b) respective spectra. 93

Figure 51. Ce oxide/oxyhydroxide phase associated with Mn shown on EDS elemental map. 94

Figure 52. Xenotime or churchite in undigested diaspore/boehmite matrix, depicted on (a) backscattered electron image with its (b) EDS spectrum. 95

Figure 53. A mixed type REE particle shown on (a) backscattered electron image with respective EDS elemental maps and (b) EDS spectrograms corresponding to indicated spot analyses. 96

Figure 54. Mixed LREE phases entrapped in Fe grain depicted on (a) BSE and respective EDS elemental maps and (b) the corresponding EDS spectra. Element maps are monochromatic, thus there is no colour intensity scale. 97

Figure 55. Qualitative identification of Sc peaks (in positions 97.05–97.20 mm) in different mineral matrices with PETH spectrometer of the EPMA-WDS instrument. Spectrum of goethite is retrieved from bauxite residue sample; the rest are from Parnassos-Ghiona B3 horizon bauxite samples. 102

Figure 56. Optical microscope image of bauxite DD hematite-dominant matrix area surrounded by multiphase bauxite matrix. The numbers indicate LA-ICP-MS measurement spots (**Table 18**) and "a)" is the spot of µ-Raman measurement depicted in **Figure 57**. 103

Figure 57. Raman spectrum of an example hematite matrix area of bauxite DD in relation to hematite reference. D — diaspore, Mgt — magnetite. Peaks with only numeric indexing are attributed to hematite. Reference spectrum is from RRUFF database (Lafuente et al., 2015). 103

Figure 58. BSE image of a selection of analysed spots of hematite-dominant grains in bauxite residue. Measurements are summarized in **Table 19** and individual measurements are reported in Table A.4. 106

Figure 59. Micro-area of Sc-rich goethite and Sc-depleted hematite contained in bauxite residue shown on backscattered electron image. Numbers 1–5 indicate to EPMA-WDS measurements (**Table 20**); letters “a)” and “b)” indicate the approximate areas of μ-Raman measurements (**Figure 60**). 108

Figure 60. Raman spectra of a) goethite area and b) hematite area contained in bauxite residue in relation to reference spectra. Analysed locations are indicated in **Figure 59**. He — hematite, D — diaspore, Mgt — magnetite; peaks with only numeric indexing are attributed to a) goethite, b) hematite. Reference spectra are from RRUFF database (Lafuente et al., 2015)........ 109

Figure 61. BSE image of an aluminium oxyhydroxide dominant particle observed in bauxite residue. Quantification of spot “2” is shown in **Table C 7**........ 110

Figure 62. BSE images of zircons observed in (a) Greek Parnassos-Ghiona bauxite (DD-BX), (b) bauxite residue, with (c) relative concentration profile measured on the dashed line shown in (a), and (d) respective EDS spectra corresponding to zircons in bauxite as well as in residue........ 112

Figure 63. Backscattered electron images of a) titanium dioxide (anatase/rutile) and b) iron titanate observed in Greek bauxite DD. The indicated quantification spots are reflected in a) **Table 24**, and b) in **Table 25**........ 113

Figure 64. Diffractogram of raw bauxite residue compared to diffractogram of residue after 3 h of leaching........ 118

List of Tables

Table 1. Requirements for the smelter grade alumina quality as specified for Australian alumina industries in Platt's Methodology and Specifications Guide (S&P Global Platts, a division of S&P Global Inc., 2018). 14

Table 2. Description of sampled materials. Refer to **Figure 3** to find the sampling points on the Bayer process flowsheet. 20

Table 3. Analytical methods and preparation techniques used for the determination of main and trace elements in the Bayer process solid and liquid samples. 22

Table 4. Standards used for the wavelength dispersive spectroscopy (WDS) quantification. 23

Table 5. Main chemical composition of the major materials interacting with the Bayer process. Description of the materials can be found in **Table 2** and the sampling points with respect to the Bayer process in **Figure 3**. 29

Table 6. Concentrations of selected trace elements (mg/kg) in the main Bayer process solid materials, based on a combination of ICP-MS, ICP-OES, XRF-st and INAA data. Extended overview of trace element concentrations can be found in **Table A 1** and **Table A 2**. 30

Table 7. Mineralogical composition of the main Bayer process materials, excluding products. The phase quantities represent the XRD-crystalline phases. In *italics* are indicated the Bayer process specific phases. 33

Table 8. Composition of Bayer process pregnant (PL) and spent (SL) liquors. Extended overview of Bayer process liquor composition is available in Appendix A **Table A 4**. 39

Table 9. Main oxide composition of minor Bayer process by-products (in wt%). 56

Table 10. Mineralogical composition of minor Bayer process by-products (in %). For security filtration material, only relative abundance is indicated. 57

Table 11. Trace element concentrations in minor Bayer process by-products (mg/kg). 60

Table 12. EPMA-WDS quantification of perovskite-dominant and cancrinite-dominant areas of digester autoclave scale sample. 63

Table 13. REE phases identified in the bauxites exploited by AoG. 74

Table 14. EPMA-WDS quantification (in wt %) of Ce-predominant ferrotitanate grains (**Figure 40**). Lower section of the table shows the number of ions in the mineral formula, following the ABO_3 perovskite structure. 82

Table 15. EPMA-WDS quantification (in wt %) of a Nd-La predominant partly reacted LREE grain (1–4) (**Figure 42**a) and a LREE ferrotitanate grain (5–10) (**Figure 42**b). Lower section of the table shows the number of ions in the mineral formula, following the ABO_3 perovskite structure. 83

Table 16. Summary of the physical parameters of the encountered REE particles in bauxite residue. 98

Table 17. Chemical composition of hematite-dominant matrices of bauxite samples determined by EPMA-WDS. In the category “Greek bauxite overall”, measurements of the two Greek Parnassos-Ghiona bauxite samples are combined. 104

Table 18. LA-ICP-MS analysis of bauxite hematite matrix sites. Fe was used as a standard element. Therefore, its content appears constant in all the analysed spots (see Materials and Methods section 2.4). SiO_2 measurements are from SEM-EDS. 105

Table 19. EPMA-WDS quantification of iron phase matrices of bauxite residue. 106

Table 20. EPMA-WDS quantification of goethite (1–3) and hematite (4–5) areas corresponding to **Figure 59**. 108

Table 21. EPMA-WDS quantification of aluminium oxyhydroxide matrices of bauxite samples (n = 14). 110

Table 22. LA-ICP-MS quantification of aluminium oxyhydroxide matrices of bauxite sample ST-BX. Al was used as a standard element. SiO_2 is from SEM-EDS. 111

Table 23. Sc concentration in zircons of bauxite (1–4) and its residue (5–10), quantified in EPMA-WDS* 113

Table 24. EPMA-WDS quantification of TiO_2 (anatase/rutile) particles in bauxite (ST-BX no. 1, DD-BX no.-s 1–7) and bauxite residue samples (8–9). 114

Table 25. EPMA-WDS quantification of iron titanite particles in bauxite DD sample. 114

Table 26. EPMA-WDS quantification of Sc-depleted mineral phases. Aluminosilicate, corresponding to kaolinite (1–6), is measured in Parnassos-Ghiona B3 sample (DD-BX). Hydrogarnet type phases (titanium- and iron-substituted; 7–8) and Ca-based phases (possibly calcite; 9–10) are measured in bauxite residue sample. 115

Table 27. Distribution of Sc between its host minerals. Titanium phases refer to anatase and rutile combined. 116

Introduction

The technological advance of the modern society has imposed new trends in the demand of raw materials, especially those that are required in the high-tech industry. More categories of specific commodities are needed than ever before in the history. Such commodities are, for example, the rare earth elements (REE), which are essential in the so-called smart devices as well as in green technologies like the wind turbines and electric vehicles. After the beginning of the 20th century which marks the start of a rapid growth in the exploitation of mineral resources, the usage of many raw materials has increased faster than the growth of the world's population and further growth follows an exponential curve. The demand for raw materials is not only dictated by the growth of the population, but a remarkable factor is also the proportion of the societies that are making transfers from developing to developed statuses. Examples of such regions include China, India and Brazil. The need for most of the raw materials in almost any industrial field is projected to increase and there are practically very few materials for which the production is decreasing (Binnemans et al., 2018; Christmann, 2018; Christmann et al., 2007; Frenzel et al., 2016; Vidal et al., 2017).

For the purposes of strategic planning and resource availability overviews, several economic and geographic regions such as Japan, USA and European Union have compiled lists of critical raw materials (Binnemans et al., 2018; European Commission et al., 2017). Criticality is generally defined as a function of numerically quantified supply risk and economic importance. European Commission lists currently 26 raw materials as critical (European Commission et al., 2017). Being categorised as a critical raw material or not, the accelerating growth of demand and relative scarcity of certain raw materials have impacts on the market prices of the commodities. On the one hand this can impose limitations in the accessibility of raw materials. On the other hand, it might motivate industries to start exploiting secondary resources that have so far not possessed economic prospects.

Besides the risks in the supply of raw materials and their increasing prices, the exploitation of non-renewable mineral resources can have an adverse impact on the ecological and environmental well-being of our planet. Aside of the anthropogenic-driven climate change about which there at least exists a consensus in the scientific community (Cook et al., 2013), the society has not yet adequately reacted to the implications that the Earth's ecosystems are in grave danger mostly due to human activities. The manifest that summarises the evidences in the form of a meta-study describing the difficult situation of the world's ecosystems and biodiversity in relation to human activities is signed by more than 15,000 scientists (Ripple et al., 2017). From the positive side, a good example exists which shows that if decisive actions are made, the situation of the planet can be improved. Such an example is the depletion of ozone in the atmosphere that was reversed upon the setting of regulations of the emissions of ozone-depleting substances (Ripple et al., 2017). It is an encouraging illustration that changes are possible. Unfortunately, there exist too many examples of the potentially harmful courses of behaviour relating to the minerals industry. It is a fact that the ratio of useful materials produced, and tailings created is in the favour of tailings as well as other by-products. Until this day the failures of tailings and residue stocking deposits happen that can release potentially harmful substances to the environment (Kossoff et al., 2014). Such was also the case with the dam failure in 2010, when about 1 million cubic meters of Bayer process red mud was spilled to the environment in Hungary, Ajka (Mayes et al., 2016). It is estimated that about 150 million tonnes of bauxite residue is being created annually worldwide (Evans, 2016), which has led to the accumulation of about 2.7 billion tonnes of residue (Power et al., 2011). In some cases, the environmental impact of mineral processing activities is difficult to be evaluated. However, it has been estimated that the largest worldwide producer of the REEs, Bayan Obo mine, is probably operating with a major impact to the environment (Ali, 2014). This indicates that there is room for developing the responsible sourcing of critical raw materials.

Despite the named difficulties, the minerals engineering community in a broad sense is not walking blind-folded through the current situation. Many solutions are being proposed and in general they have a common ground which often refers to closing the value loops or transferring to circular economy. This includes proposals and actions to obtain the virgin raw materials from the so-called responsible sources, reducing of the waste streams, exploiting residues or tailings as a secondary resource or recycling of the end-of-life products (Binnemans et al., 2015; Christmann, 2018; Kossoff et al., 2014; Krook et al., 2012; Wall et al., 2017).

It should be noted that REEs are a group of chemical elements known as the lanthanides as well as yttrium (Y). Sc is also considered often as a REE, but there is no conclusive consensus in this question. Based on the chemical properties, REEs are usually divided to light REEs (LREE, lanthanum to europium) and heavy REEs (HREE, gadolinium to lutetium and Y (Atwood, 2012), which is also the official IUPAC definition and used in the present work.

Following the previous discussion, also the alumina industry that mainly operates by using the well-established Bayer process has an important role to play. Bauxite that is used as the raw material of the Bayer process can contain typically more than 50 chemical elements above concentrations of 1 mg/kg, most of which can be considered as trace elements (Authier-Martin et al., 2001). Out of the bauxite trace elements, at least five chemical elements or groups of them are listed as critical raw materials in the report by the European Commission and at the same time their concentrations in Bayer process related materials occur in levels that are interesting from an economic point of view (Borra et al., 2016; European Commission et al., 2017; Evans, 2016). Such critical materials are the following: Ga, V, Sc, LREEs and HREEs (Binnemans et al., 2015; Borra et al., 2016; Davris et al., 2017; European Commission et al., 2017; Frenzel et al., 2016; Okudan et al., 2015).

Based on the discussion about responsible sourcing of critical raw materials, the Bayer process by-product bauxite residue has been highlighted as one of the potential future resources of critical metals, out of which mainly the REEs and Sc are considered (Wall et al., 2017). The attractiveness arises from the fact that the REEs and Sc mainly concentrate to bauxite residue after the Bayer process, giving rise to about two-fold increase in the concentration compared to bauxite (Derevyankin et al., 1981; Logomerac, 1971). Compared to other sources of the REEs, it should be admitted that bauxite residue does not have a very high concentration of REEs. Nevertheless, the competitiveness of bauxite residue has been emphasised mainly because of three reasons: (1) it does not need additional comminution because of its fine particle size, (2) it has low radioactivity levels compared to the conventional REE ores, and (3) it is a by-product and therefore no exploitation of virgin ores is necessary (Wall et al., 2017). Besides, when considering a ten-year perspective of REE demand in the context of the potential advantages of the deposit types, bauxite residue in addition to the ion adsorption clay deposits have been deemed to offer good opportunities to produce REEs (Goodenough et al., 2017).

The behaviour of the other critical metals occurring in the Bayer process related materials — Ga and V — is different compared to REEs and Sc. These metals (Ga and V) are digested along with bauxite aluminium (oxy)hydroxide minerals and tend to accumulate to Bayer process liquors. It is well-known that Ga is worldwide mainly produced as a by-product of the Bayer process and to a smaller extent as a by-product of the Zn production (Frenzel et al., 2016; Løvik et al., 2015). V is also produced as a by-product of the Bayer process to some extent (Evans, 2016; Gladyshev et al., 2015).

Dictated by the elevated concentrations of critical metals and the previously mentioned factors of competitiveness in the Bayer process materials, there exists a growing interest in the extraction of the relatively valuable REEs and Sc from bauxite residue by exploring various hydrometallurgical or combined pyro- and hydrometallurgical routes (Binnemans et al., 2015; Borra et al., 2016; Davris et al., 2017; Evans, 2016). The research and development is also taking place to recover more efficiently higher proportions of Ga and V mainly from Bayer process liquors, but also from some solid material streams of the Bayer process (Gladyshev et al., 2015; Habashi, 2006; Okudan et al., 2015). It has been indicated that the full potential of Ga production as a by-product of the Bayer process is not currently utilised and a growth of production is predicted (Frenzel et al., 2016). It was also summarised that only about 8–21% of the full capacity of Ga extraction was realised from the Bayer process in 2011 (Løvik et al., 2015).

Besides the opportunities to extract critical metals from bauxite residue, this material has also a good potential to be utilised in the extraction of Fe, Al or Ti. Other possibilities of re-use include the production of (low-carbon) construction materials from bauxite residue or using the material in soil amelioration, to name a few possible applications (Binnemans et al., 2015; Borra et al., 2016; Evans, 2016; Garau et al., 2007; Hertel et al., 2016; Pontikes, 2007; Power et al., 2011).

Aside of the prospects of recovering critical elements as by-products of the Bayer process, there are additional reasons why trace elements receive attention in the alumina industry. Firstly, there exists a need to control the levels of impurities in the aluminium hydroxide as well as alumina products, such as in the case of V (Teas and Kotte, 1980). Secondly, some trace elements require monitoring due to their possible impact on occupational health, which is the case for beryllium (Be) (Eyer et al., 2005; Suss et al., 2008). Thirdly, the fate of certain trace elements like arsenic (As) should be considered from the environmental point of view (Burke et al., 2012).

Although the relatively elevated presence of certain trace elements in bauxites as well as their economic potential has been acknowledged for decades (Bárdossy and Pantó, 1973; Blankova et al., 1977; Derevyankin et al., 1981; Logomerac, 1971), some gaps in the existing knowledge can be indicated. Despite of the long history of Ga research in alumina industry (Habashi, 2006; Hudson, 1965), it is not easy to retrieve published data of the distribution of Ga in the Bayer process. It has been emphasised that this missing knowledge in the accessible information has affected the compilation of worldwide resource estimation exercises, as there is no source available that relates the known Ga concentrations with actual material mass flows in the Bayer process (Frenzel et al., 2016; Løvik et al., 2015). Similar gaps exist for V, Cr, and the REEs. Some information can be retrieved about the distribution patterns of La and Sc in the Bayer process (Derevyankin et al., 1981), but given the date of this study it is useful to update and build new knowledge upon that existing study. For the rest of the elements considered in this work, at most the fractionation indexes between bauxite and derived residue or merely concentrations can be found (Mohapatra et al., 2012; Ochsenkühn-Petropulu et al., 1994; Wagh and Pinnock, 1987), and those are also often given based on lab-scale experiments (Feret and See, 2010; Logomerac, 1971). Comprehensive descriptions exist that provide the distribution patterns of other bauxite trace elements like molybdenum (Mo) and zinc (Zn) (Papp et al., 1971) as well as Be in the Bayer process (Eyer et al., 2005; Suss et al., 2008).

The mineralogical nature of the REEs in bauxite residue has so far not been established, while in bauxites their occurrence modes are relatively well known (Borra et al., 2016; Deady et al., 2016; Maksimovic and Pantó, 1996). The mineralogical characteristics relating to Sc in bauxites have been discussed only very briefly (Mongelli et al., 2017; Suss et al., 2017). The modes of occurrences of Sc in bauxite residue have been established to some extent, but only in the case of Chinese residues (Liu et al., 2018; Xiao, 1996; Zhang et al., 2017). However, the Chinese residues tend to be derived from the sintering or Bayer-sintering processes and the properties of the residues can differ from those of Bayer process bauxite residue (Evans, 2016; Songqing, 2017). From the other critical metals existing in bauxite residue, V has been well speciated with advanced techniques (Burke et al., 2012; Markus Gräfe et al., 2011b, 2011a). The same accounts for some other important trace elements (As, Cr, Mn) existing in bauxite residue (Burke et al., 2012; Markus Gräfe et al., 2011b, 2011a). The mineralogical characteristics of Ga are also relatively well known in bauxite and bauxite residue system, although the studies about this metal in residues are scarce (Liu et al., 2018; Maksimovic and Pantó, 1996; Shaw, 1957).

Based on the preceding, the aim of this dissertation is to (1) explain the distribution characteristics of trace elements (especially the REEs, Sc, Ga and V), and (2) elucidate the mineralogical characteristics of trace elements (especially the REEs and Sc) in the Bayer process materials including bauxite and the residues derived from it. Aside of the named trace elements that are interesting mainly due to their prospective economic value, attention is also paid to other trace elements like Cr, As, Th and U. It is of high interest to examine in particular the karst/diasporic bauxite trace elements distribution in the Bayer process, because these types of bauxites are relatively more enriched in trace elements compared to lateritic/gibbsitic bauxites (Bárdossy, 1982; Valeton, 1972).

The structure of the dissertation generally follows the progression of the material through the Bayer process, starting from raw bauxite and ending with the residue. In the major divisions, firstly the basic characteristics of the materials are described, then the distribution patterns of the trace elements are explained, and finally the specific microscale characteristics of the REEs and Sc are revealed.

1. Background

1.1 Bauxite

Bauxite is a type of alumina-rich rock, which is formed during the weathering of various kinds of aluminosilicate source rocks (Valeton, 1972). A major division is made between lateritic bauxite deposits (88% of the world's resources) and karst bauxite deposits (12% of world's resources) (Meyer, 2004). The former types of deposits are situated immediately on the source rocks mainly as weathered crusts. The prevailing alumina mineral there is gibbsite, in the form of aluminium hydroxide (Valeton, 1972). Karst bauxite deposits are associated with carbonate rocks, where bauxite bodies fill former karst cavities. Commonly, the source material of karst bauxite originates from a neighbouring area and has been transported during the formation of the deposit. The main alumina minerals in karst bauxite are diaspore and boehmite, in forms of aluminium oxyhydroxides. Due to the high content of alumina in bauxite, it is the main industrial ore source to obtain technically pure alumina and aluminium (Bárdossy, 1982). More than 50 chemical elements can be found in bauxites that occur in higher concentrations than 1 mg/kg (Authier-Martin et al., 2001). The trace elements that remain in the composition of bauxite are those which have some geochemical similarities mainly with the behaviour of Al, Fe and Ti. Such trace elements are, for example Ga, V and Sc, and they remain largely immobile during the source rock weathering (Valeton, 1972).

Parnassos-Ghiona bauxite deposit is located in Central Greece, north of the Gulf of Corinth, and named after the prominent peaks of Mount Parnassos and Mount Ghiona, around which numerous mining pits and mines are scattered. Tectonically, the area is controlled by the Parnassos-Ghiona zone consisting of orogenically uplifted Mesozoic limestones and dolomites. The bauxite deposit is of Jurassic to Cretaceous in age and consists of three consecutive horizons as layers, pockets or irregular bodies intercalated in Mesozoic limestone sequences (**Figure 1**). The upper horizon — B3 — being the youngest, most prevalent and suitable from processing aspects, is the primary bauxite exploited by AoG. The intermediate B2 layer is exploited to some minor extent. The formation of the deposit took place over the course of several transgressions and regressions of a shallow lagoon, while the regression periods and concurrent uplift provided a topography allowing the formation of karst cavities in the region. The karst cavities were further on filled with muddy sediments from the vicinity or transported several tens of kilometres across the landscape. Once deposited in the karst cavities, the sediments were turned into bauxite by chemical weathering, resulting in the depletion of silica components. Because the genesis of the deposit is related to limestones and karst phenomena, it is classified as a karst bauxite deposit. Parnassos-Ghiona bauxite deposit is a part of a wider Mediterranean karst bauxite belt, in which all deposits are related by their similar genesis and age (Bárdossy, 1982; Laskou and Economou-Eliopoulos, 2007; Petrascheck, 1989).

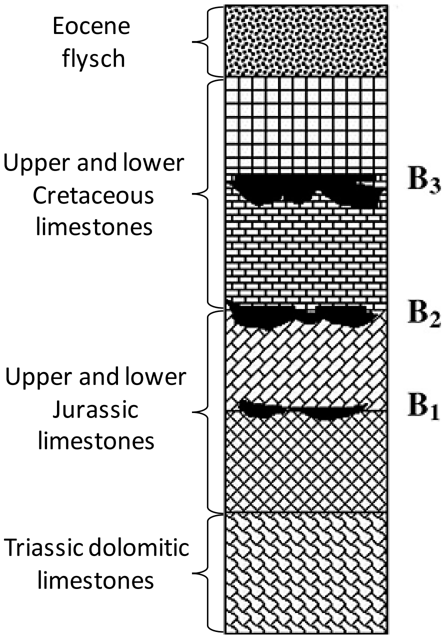

Figure 1. Stratigraphic column of Parnassos-Ghiona bauxite deposit showing the positions of first (B1), second (B2) and third (B3) bauxite horizons between the Mesozoic limestones. Modified after (Laskou and Economou-Eliopoulos, 2007).

Minor proportion of karst bauxite exploited by AoG and analysed also in present work is sourced from Turkey, Western Taurides mountains Milas area. In the context of Turkish bauxites, it is categorised as a diaspore deposit. It is explained that the Turkish diaspore deposits are associated mainly with metamorphosed material sourced from altered tuffs and other related rocks, situated on karst topography (Hatipoğlu et al., 2010; Patterson, 1967).

Lateritic bauxites from two locations are also considered in this study. First one is Porto Trombetas bauxite from Brazil. It belongs to the Amazonian bauxites category, which comprise 97% of total Brazilian bauxite reserves. The bauxite formation has occurred in warm and humid climate conditions which are typically necessary conditions for the creation of lateritic bauxite. Bauxite blanket is situated on top of clastic terrigenous sediments that are related to the Amazon river. In the complete bauxite profile, the principal bauxite layer (1–6 m thick) is situated between the lower kaolinitic layer and ferruginous nodular layer (~1 m thick) (**Figure 2**). The profile is capped by upper kaolinitic layer (Boulangé and Carvalho, 1997).

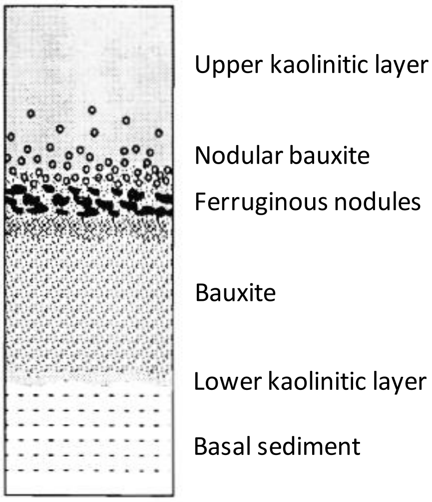

Figure 2. Typical profile of Porto Trombetas bauxite, showing the transition from basal sediment to upper kaolinitic layer. Adapted after (Boulangé and Carvalho, 1997).

The second lateritic bauxite discussed in present work originates from Awaso deposit in Ghana. It is one of the four major deposits in Ghana. Awaso deposit in particular has provided resources for European refineries for over 70 years (Gawu et al., 2012). The deposit is situated on hilltops from altitudes 450 to 550m above sea level. Generally, the bauxite deposits in western regions of Ghana including Awaso are formed on different kinds of source rocks, among which are named phyllites, tuffs, lavas and ashes, probably from Precambrian age (Patterson et al., 1986). The bauxite profile is petrographically sub-divided into three horizons, underlain by kaolinitic gibbsite-containing clay (Momade and Gawu, 2009).

1.1.1 REEs and Sc Geochemistry and Phase Composition in Bauxites

REEs are relatively more enriched in karst bauxite deposits compared to lateritic deposits (Valeton, 1972). In the bauxite profiles, REEs concentration increases towards the lower sections and is the highest immediately near the footwall limestone (Maksimović and Panto, 1991). Concentrations may differ by four magnitudes between the upper and lower parts of the profiles (Ochsenkühn-Petropoulou et al., 1991). In some instances, total REEs concentration near the carbonate footwall can reach a remarkable one weight percent (Ochsenkühn-Petropoulou et al., 1991; Ochsenkühn-Petropulu and Ochsenkühn, 1995). In such cases, REE minerals can even be identified by XRD analysis (Maksimović and Panto, 1980). This pattern is explained by the partial dissolution of REEs into the percolating pore fluids in the bauxite profile. Then, REEs are precipitated as secondary (authigenic) minerals near the carbonate footwall, where the fluids encounter an alkaline pH barrier. The migration is noted for both LREEs and HREEs (Maksimović and Panto, 1991). However, some fractionation in the REEs group is also noted. Namely, Ce is sometimes more concentrated in the upper sections of the profile. Ce can occur there in a tetravalent state under oxidative conditions. It precipitates as cerianite, $(Ce^{4+},Th)O_2$, in the upper parts of some bauxite profiles, while other Ce species like the fluorocarbonates are more often found in lower sections of the profiles (Maksimović and Panto, 1991; Mongelli, 1997).

First efforts to elucidate the characteristics of REE mineral species in bauxites were taken up in the 1970s (Bárdossy and Pantó, 1973). It was revealed that REEs can be found as detrital minerals, i.e., minerals in the same form as they occur in the bauxite parent rocks. In this category, mainly phosphate minerals like monazite ($(Ce,La,Nd,Th)PO_4$) and xenotime (YPO_4) have been identified (Bárdossy and Pantó, 1973; Laskou and Andreou, 2003). In bauxites, REEs also occur as authigenic phases, i.e., phases that have been precipitated in situ within the bauxite profile from percolating fluids. Such phases are commonly REE fluorocarbonates of the bastnäsite ($Ce(CO_3)F$) mineral group or phosphates of monazite group (Maksimovic and Pantó, 1996; Maksimović and Panto, 1980). Often, occurrences of hydroxylbastnäsite are reported, in which fluorine ion is substituted with hydroxyl ion ($REE(CO_3)(OH)$) (Maksimovic and Pantó, 1996; Maksimović and Panto, 1991; Ochsenkühn-Petropulu and Ochsenkühn, 1995). Moreover, hydroxylbastnäsite has been highlighted as the most frequently identified REE mineral in karst bauxites (Maksimovic and Pantó, 1996). Raman spectroscopy was successfully applied to aid the identification of authigenic monazite-Nd and authigenic xenotime in Zagrad karst bauxite deposit (Montenegro) (Radusinović et al., 2017). Ce can occur in the oxide form as authigenic cerianite (Mongelli, 1997). Some occurrences of REEs in bauxites are also attributed to the ion adsorption form on clay or diaspore surfaces (Wang et al., 2010). It has also been reported that REE mineral composition can be highly variable even in bauxite samples collected a few meters apart from each other (Maksimović and Panto, 1980). This list of REE minerals in bauxites is not exhaustive as there is a wide variety of REE phases described in bauxites. An increasing volume of research is being published about the mineralogy of REEs in bauxite deposits worldwide in the recent years (Li et al., 2013; Proenza et al., 2017; Radusinović et al., 2017; Wang et al., 2010). An overview and a case study of the REEs geochemistry in European bauxite deposits as well as in the derived residues is given by (Deady et al., 2016). As can be seen from the preceding reviews, REE minerals found in bauxite deposits are often like the ones that are commonly exploited in the existing REE mines, namely monazite, bastnäsite and xenotime (Habashi, 2013).

Within the geochemical cycle, Sc is known to be present in mafic and ultramafic rocks rather than in felsic rocks. Sedimentary rocks commonly exhibit a very low content of Sc. However, some bauxites and laterites are relatively rich in Sc (Chassé et al., 2017; Ochsenkühn-Petropulu et al., 1994). Its average concentration in continental crust is 22 mg/kg (Rudnick and Gao, 2003). Sc behaves as a lithophile element and is not affected by the redox conditions of the environment. Sc does not exhibit affinity towards ore forming anions. Because of that, it can be found in small quantities dispersed in many rock-forming minerals rather than concentrated in independent mineral phases. Such phases exist (e.g. kolbeckite, thortveitite), but are very rare. Since Sc is scattered in the Earth's crust and deposits with high Sc grade are not formed in natural processes, the production of Sc has relied on resources with Sc content around 100 mg/kg Sc (Das et al., 1971; Samson and Chassé, 2016).

When Sc is present in a bauxite deposit, its distribution is typically associated with REEs, like in south Italian and Sardinian karst bauxite deposits. This distribution pattern is interpreted as a covariance due to the chemical similarities of REEs and Sc rather than as an indication of the formation of any specific Sc-bearing mineral (Blankova et al., 1977; Mongelli et al., 2017). In the Zagrad bauxite deposit (Montenegro), Sc was enriched throughout the bauxite profiles, while some of the lower parts of profiles were particularly enriched in Sc as well as in REEs content (Radusinović et al., 2017).

As the result of direct investigation by electron microprobe, the first reports referring to Sc occurrence in certain bauxite minerals date back to 1973 and indicate its presence in detrital zircon (Bárdossy and Pantó, 1973). It is a well-established fact that Sc can be found in zircon, as reported in several bauxite deposits: Mazaugues (France), Campo Felice (Italy), bauxites of Southern

Apennines (Italy) (Bárdossy and Pantó, 1973; Boni et al., 2013; Mongelli et al., 2017; Radusinović et al., 2017). In Schugorsk deposit (Urals, Russia), zircon grains exhibit altered rims that contained up to 3.5 wt % Sc (Mordberg et al., 2001). Zircon can inorporate many "exotic" chemical elements such as Nb, Sc, U, Bi or HREEs. The multivalent substitution of Sc in zircon is commonly explained as $Zr^{4+} + Si^{4+} \leftrightarrow Sc^{3+} + P^{5+}$ (known as the pretulite type substitution). Sc^{3+} thus accommodates the Zr^{4+} site in zircon while P^{5+} substitutes Si^{4+} and the charges are compensated through the multivalent substitution. Pretulite is a scandium phosphate phase ($ScPO_4$) that can occur in solid solution with zircon, just as some other phosphate phases like yttrium phosphate. Such phosphate minerals are isostructural with zircon (Breiter et al., 2006; Moëlo et al., 2002).

Authigenic xenotime (YPO_4) of Zagrad bauxite deposit (Montenegro) has been shown to contain some amount of Sc (0.4–0.6 wt %) while residual xenotime did not contain any (Radusinović et al., 2017).

In Middle Timan bauxite (Urals, Russia), about 65 % of Sc is associated with diaspore and boehmite, where its concentration ranges from 80–100 mg/kg. The remaining part is found in zircon and chamosite, while the concentrations of Sc in these minerals are not known. During Bayer digestion, Sc is released from diaspore and boehmite and is thereafter assumed to be adsorbed on the surface of bauxite residue particles as ScO(OH) (Suss et al., 2017).

Several additional mineral hosts of Sc have been proposed for bauxite and its residue system. A correlation between Sc and P_2O_5 occurrence has been reported at least in three cases. Phosphate phases, like variscite, have been considered as Sc host minerals (Radusinović et al., 2017; Suss et al., 2017; Wagh and Pinnock, 1987).

Derevyankin et al. (1981) deduced from their analysis of Sc behaviour in the Bayer process that Sc is most likely bound with iron oxides and titanium dioxides in bauxite. Mongelli et al. (2017) suggested based on established association of Sc^{3+} with Fe^{3+} and geochemical data of several Italian bauxite deposits that Sc might occur in detrital iron minerals like titanomagnetite.

1.1.2 Ga and V Geochemistry in Bauxite Context

Ga and V together with Sc are among the few bauxite trace elements that tend to be associated with the main rock forming minerals such as boehmite or diaspore in bauxite deposits (Mordberg et al., 2001). Most of other trace elements such as the REEs, Cu or Zr are more often concentrated into discrete mineral phases that can be either detrital or authigenic (Bárdossy and Pantó, 1973; Maksimovic and Pantó, 1996). V has been shown to correlate with the distribution patterns of P, Ba, Sr and Bi (Mordberg et al., 2001), but these associations can be specific to a certain deposit and also depend on the source rock geochemistry. A strong positive correlation of V and Cr has been demonstrated in some cases, which has been interpreted as an indication and a result of the extent of bauxite formation and source rock weathering (Mordberg, 1993). In the context of multivariate statistical modelling of a large geochemical dataset of southern Italian bauxites, V has been grouped together with Sc, REEs and Cr (Mongelli et al., 2017). It has been assumed that because V has typically trivalent oxidation state, it likely behaves similarly to trivalent iron and therefore occurs either in detrital or rock-forming Fe minerals (Mongelli et al., 2017). However, thorough speciation studies of V in bauxite deposits do not mostly exist. A preliminary speciation of V suggested that in Parnassos-Ghiona bauxites, V appears likely in kaolinitic-type clays primarily as pentavalent V, whereas any occurrence together with Fe, Al or Ti minerals was excluded. However, this accounts only for the Fe-depleted sub-type of Parnassos-Ghiona bauxite (P. Gamaletsos et al., 2016).

Gallium possesses a close relation to aluminium. Similar properties include atomic radius, trivalent oxidation state, tetrahedral or octahedral coordination and amphotericity. Gallium is hosted in bauxites by Al-bearing minerals like gibbsite, boehmite, diaspore and kaolinite (Gray et al., 2013). High correlation with iron has been observed in ferruginous duricrusts and Fe-rich horizons of the bauxitic profiles due to gallium's different behaviour compared to aluminium under acidic conditions. In this situation, gallium is retained in Fe-oxyhydroxides and aluminium enriched horizons show low Ga/Al ratio (Hieronymus et al., 2001). U.S. Geological Survey (Schulte and Foley, 2014) reports that gallium concentrations in the world bauxites range from <10 ppm–812 ppm with an average of 57 ppm Ga. They also state that there are no significant differences between lateritic and karst bauxite deposits regarding Ga contents. Concentrations are said to be ranging from 12–52 ppm Ga with an average of 40 ppm in bauxite districts of Greece and Turkey (Schulte and Foley, 2014).

1.2 Bayer Process Description

Bayer process is a cyclic hydrometallurgical method that utilises sodium hydroxide leaching of bauxite ore to produce technically pure aluminium hydroxide that can be further calcined to obtain anhydrous alumina (Al_2O_3) (Adamson et al., 2013; Bayer, 1892, 1888; Chin, 1988; Power et al., 2011). Aluminium of Greece plant (Metallurgy Business Unit, Mytilineos S.A.; hereafter denoted as AoG) uses a set of processing conditions that are known in the industrial sector as high temperature digestion (HTD). These conditions (T >250 °C, elevated pressure) are dictated by the utilisation of mainly karst bauxite, in which primary alumina-containing minerals are diaspore (α-AlO(OH)) and boehmite (γ-AlO(OH)) that dissolve less readily than the more commonly exploited gibbsite minerals ($Al(OH)_3$) (M. Gräfe et al., 2011; Hudson et al., 2000).

Simplified flow diagram of AoG's process is shown in **Figure 3**. Because Parnassos-Ghiona bauxite in its natural position is situated between limestones, it is necessary to remove the contaminating limestone from the ore that inevitably is partly mined together with bauxite. Limestone, mineralogically composed mainly of calcite, is removed by gravimetric heavy media separation (HMS) in ferrosilicon medium (Lavalou et al., 1999; Papanastassiou et al., 2006), also referred as "decalcitation" (sic) process in the literature (Lavalou et al., 1999). This operation unit is shown in **Figure 3** as "HMS", marked by a dotted line, because it is not strictly a part of the conventional Bayer process (Lavalou et al., 1999). The primary output of this unit is mixed karst bauxite (also the main input to Bayer process, 73% of total bauxite mass during the present case study) and secondary output is "decalcitation residue". Karst bauxite is ground with the presence of concentrated leach liquor to achieve granulometry <315 µm and the resulting suspension is pre-heated at about 180 °C. Digestion of the karst bauxite suspension is performed at about 255 °C and a pressure of about 5.8–6.0 MPa during approximately one hour. To increase the productivity of the Bayer process, AoG also utilises an optimisation step that is termed as the "sweetening" process. In "sweetening" process, lateritic/gibbsitic bauxite is digested at a lower temperature aside of karst/diasporic bauxite. Lateritic bauxite suspension passes through a pre-desilication step with a residence time of about 24 h, to allow the formation of desilication products (mainly sodalite and cancrinite) and avoid the problems of reactive silica (i.e. kaolinite) during digestion. In the case of AoG, lateritic bauxite suspension is introduced to the main karstic bauxite slurry in the appropriate flash stage after the HTD of karst bauxite suspension. Lime is added to the process during digestion as a reaction catalyst, as well as during causticisation step that reduces soda losses and as a filter aid during the security filtration of pregnant leach solution after settling stage (liquor "polishing") (Lavalou et al., 1999; Whittington, 1996). From the leached effluent slurry after digestion, the solid fraction is separated as red mud (bauxite residue in a slurry form) by settling and washing. To obtain de-watered bauxite residue that helps to reduce the losses of soda and eases the stacking of residue, AoG utilises filter pressing of bauxite residue. The clear pregnant leach liquor, rich in sodium aluminate, passes to the next processing step where crystalline aluminium hydroxide ($Al(OH)_3$) is precipitated. Precipitation is initiated by the introduction of aluminium hydroxide seed crystals. The spent liquor after precipitation unit is concentrated in the evaporation unit, to create the necessary sodium hydroxide concentration level for the next processing cycle. Aluminium hydroxide, which is the final product of the Bayer process by formal definition, is calcined at >1000 °C to produce anhydrous alumina (Chin, 1988).

Sometimes, the Bayer process is divided into the "red side" to denote the units where bauxite and its residue are present, and to "white side" to indicate the stages after residue removal (clarification) until precipitation and evaporation stages (Bánvölgyi, 2016; Power et al., 2011).

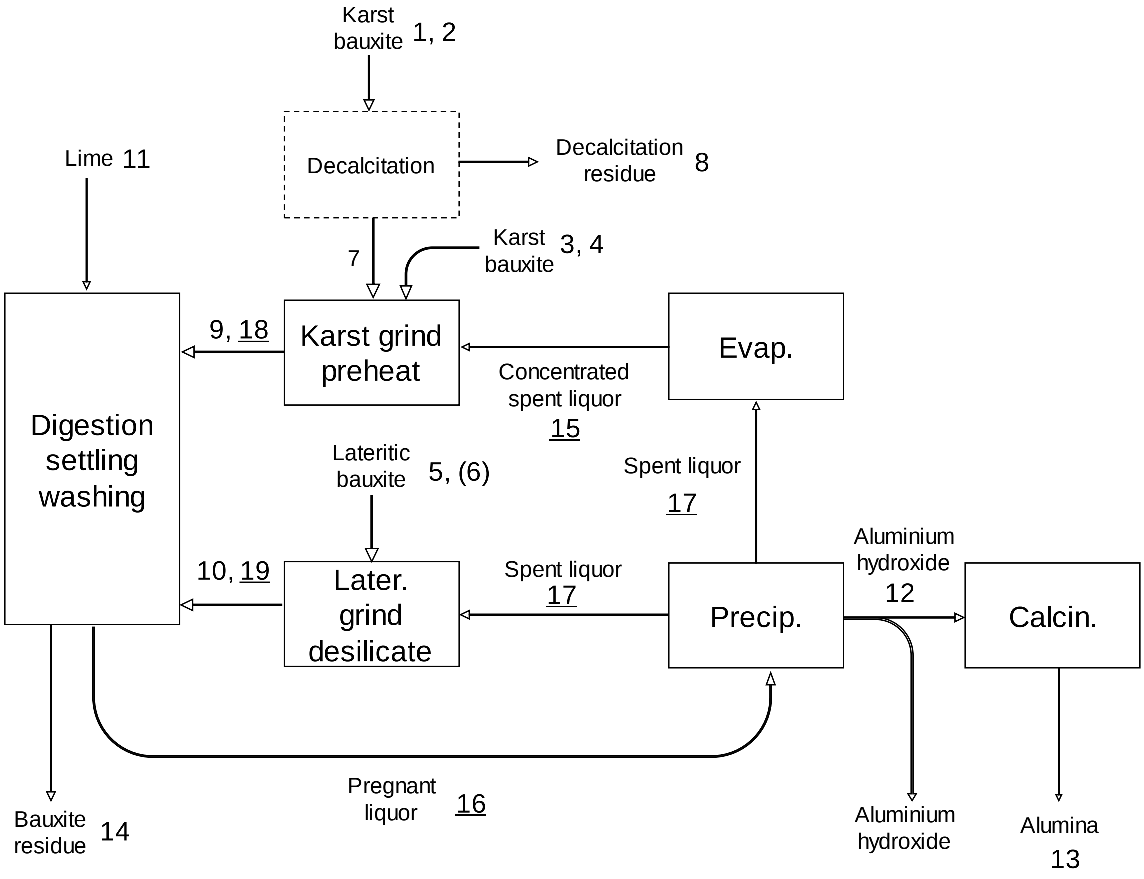

Figure 3. Simplified flowsheet of the Bayer process in AoG. Numbers indicate the sampled materials, while underlined numbers show samples in liquor form. Description of sampled materials can be found in Materials and Methods section 2.1, **Table 2**.

1.3 Trace Elements Behaviour Relating to the Bayer Circuit

Not all of the approximately 50 bauxite (trace) elements interact with the Bayer processing environment, but the following can react and accumulate to processing liquor to a greater or lesser extent: P, As, Mo, Ga, Cl, I, Br, K, Ge, Zn, U, Li, V, F, Be and Mg (Authier-Martin et al., 2001; Sato et al., 2013; Teas and Kotte, 1980).

Impurities which concentration in processing liquor drops across the line of precipitators compared to the concentration of impurity entering to precipitation unit, are generally unwanted, because they decrease the quality of aluminium hydroxide. The decrease in concentration means that the impurities are precipitated along with aluminium hydroxide. Such impurities are, for example, ZnO, Fe_2O_3, CaO, MgO and TiO_2 (Teas and Kotte, 1980; Whittington, 1996). In the alumina production and marketing, only a few of the many bauxite trace elements are monitored and kept as criteria for alumina purity, as can be seen from **Table 1**. Some impurities, such as Ga, are known to enter into the composition of alumina, but they do not pose problems for consecutive processing steps (like electrolysis to produce metallic aluminium) or other applications (Authier-Martin et al., 2001).

Table 1. Requirements for the smelter grade alumina quality as specified for Australian alumina industries in Platt's Methodology and Specifications Guide (S&P Global Platts, a division of S&P Global Inc., 2018).

Parameter	Quantity	Range
SiO_2 %	0.025	Max
Fe_2O_3 %	0.025	Max
TiO_2 %	0.007	Max
Na_2O %	0.55	Max
ZnO %	0.015	Max
P_2O_5 %	0.003	Max
CaO %	0.05	Max
V_2O_5 %	0.005	Max
LOI (300–1000 °C) %	1	Max
Alpha phase (alumina alpha or alpha content) %	12	Max
Specific surface area m^2/g	60–80	Min–Max
−45 µm %	12	Max
+45 µm %	88	Min

About 70% of the Ga contained in bauxite is digested during alumina refining and the remaining part is separated with bauxite residue (Figueiredo et al., 2002; Hudson, 1965). The reaction of digestion is described by **Equation 1** (Authier-Martin et al., 2001):

$$Ga_2O_3 + 6NaOH \rightarrow 2Na_3GaO_3 + 3H_2O \qquad \textbf{Equation 1}$$

The recyclable Bayer liquor reaches an equilibrium concentration of Ga in the range of 60–600 mg/L, yet typically shown values remain between 100–200 mg/L Ga (Figueiredo et al., 2002; Ilić and Mitrović, 1989; Lamerant, 1995, 1992; Riveros, 1990; Selvi et al., 2004). Some gallium enters to the crystal structure of aluminium hydroxide from the pregnant liquor and follows further to alumina after calcination. It has been demonstrated, that the quantity of Ga entering to aluminium hydroxide is basically a linear function with the concentration of Ga available in processing liquor (Hudson, 1965). As mentioned before, this impurity is not an issue for the alumina smelters (Authier-Martin et al., 2001). For producing gallium from Bayer liquor, a batch of it is separated from the circulation and one or more of the routes is followed: ion exchange, selective precipitation, electrochemical recovery or solvent extraction (Downs, 1993; Zhao et al., 2012b).

Authier-Martin et al., (2001) refer to earlier studies indicating that V is about 30 % soluble during Bayer digestion. Variable literature data indicates that V saturation levels in Bayer circuit liquors can range from 100–2800 mg/L (Figueiredo et al., 2002; Selvi et al., 2004; Teas and Kotte, 1980; Zhao et al., 2012a). In process liquors, V appears in the form of VO_4^{3-} (Zhao et al., 2012a). Some vanadium ends up in alumina, but this impurity has a negative impact due to its known property of decreasing the electric conductivity of metallic aluminium, causing a green hue in fused alumina, and the scale it can form in the piping of a Bayer refinery when precipitated from the liquor in the cooler parts of the circuit (Authier-Martin et al., 2001; Fenerty, 1960; Zhao et al., 2012a). The removal of V from process liquors is generally a side benefit of process lime addition. V precipitates as calcium vanadate, as an impurity in tri-calcium aluminate ($Ca_3Al_2(OH)_{12}$), or as $Na_7(VO_4)_2F{\cdot}19H_2O$ (Okudan et al., 2015; Smith, 2017; Zhao et al., 2012a). Sometimes, V is removed from the Bayer liquor as vanadium cake in the evaporation unit by cooling the liquor and crystallisation on vanadium salts (Gladyshev et al., 2015). This material has a concentration of 16–17% V_2O_5 and it can additionally contain other impurities such as Ga, As and Cr.

Behaviour of Sc and La in the Bayer process have been studied in two Russian alumina refineries by (Derevyankin et al., 1981). Back in the time of compiling the research, those refineries partially also utilised the sintering of bauxite feed, which deviates from the conventional Bayer method. It was reported that hardly any Sc and La is dissolved during wet grinding of bauxite. Concentrations of Sc and La are somewhat higher in the pregnant liquor compared to the spent liquor. During precipitation, the concentrations of La and Sc in the spent liquor remain constant which indicated to the authors that the mineralogical relations between Sc, La and Al are absent. During the growth of aluminium hydroxide on seed crystals, Sc and La probably do not enter the crystal lattice of this mineral. From the initial amount to the final aluminium hydroxide can enter 0–2% of Sc and up to 5% of La. These amounts depend on the thoroughness of washing of the hydroxide precipitate. Remaining part of Sc and La exits the process in the composition of bauxite residue, whereas Sc and La are thought to be present in both liquid and solid phases (Derevyankin et al., 1981). So far, distribution of the whole group of REEs has not been demonstrated in the Bayer process (Deady et al., 2016).

The radioactive element U is known dissolve and accumulate to minor extent in the Bayer process, achieving concentrations of about 1.4 mg/L in processing liquors. From there, U can also precipitate to aluminium hydroxide, which is an unwanted property. If the produced alumina is used in electronics industry the radioactivity of the material must be very low. It is known that the precipitation of U to aluminium hydroxide can be efficiently controlled and kept low by decreasing the quantity of organic compounds in the Bayer circuit (Sato et al., 2013). The other bauxite trace element that causes ionising radiation, Th (Adams and Richardson, 1960a, 1960b), does not interact with the Bayer process liquor and its bulk mass passes to bauxite residue (Sato et al., 2013).

1.4 REEs and Sc Abundance and Mineralogy in Bauxite Residue

1.4.1 REEs

Depending on the concentration of REEs in the bauxite ore, bauxite residue can have a concentration of total REEs up to 2500 mg/kg such as in the case of the example of Jamaican bauxite residue (Wagh and Pinnock, 1987). In AoG's bauxite residue, total REEs concentration ranges from 800 to 1100 mg/kg (Deady et al., 2016; Ochsenkühn-Petropulu et al., 1994). During a 15-year period, the REEs (including Sc) concentration in AoG's bauxite residue has fluctuated only about 8% (Davris et al., 2017). The noteworthy REE concentrations are commonly associated with bauxite residue derived from karstic bauxite (Borra et al., 2016; Logomerac, 1971).

So far, the REE occurrence modes and phases in bauxite residue have not been unambiguously explained (Borra et al., 2016). Several authors have expressed the difficulties of speciating the REE phases (Borra et al., 2015; Ochsenkühn-Petropulu et al., 1996). Regardless of the scarcity of information, some observations can be summarised. Doubtful identifications of allanite and dissakite have been reported from XRD diffractogram of an Indian bauxite residue sample. With only about 110 mg/kg concentration of cerium in the sample (Abhilash et al., 2014), it is not realistic that REE mineral phases result in XRD reflections. The authors also reported from EPMA analysis, that dispersed REEs presence was correlated with aluminium- and silicate-rich areas rather than with iron-rich areas of the sample (Abhilash et al., 2014). In a patent describing the recovery of REEs from bauxite residue, REEs have been indicated to occur in calcium titanate phases that were created in the Bayer process. According to the source, they correspond mineralogically to perovskite (Sugita et al., 2012). It was noted that in a Greek bauxite residue sample (from AoG), cerium presence might be related to the occurrence of a loparite type phase (belonging to perovskite group). The suggestion was based on a STEM-EDS investigation, where the presence of thorium and possibly some trace amount of cerium were identified in a mineralogically proven perovskite form ($Ca_{0.8}Na_{0.2}TiO_3$) (P. N. Gamaletsos et al., 2016). In a Canadian bauxite residue sample (Jonquière, Québec), REE-containing particles were noted as bright spots in electron backscatter imaging, sub-µm in size. A STEM-EDS elemental mapping also showed the presence of REE-containing particles, where cerium and titanium presence were correlated (Reid et al., 2017). Based on the observations of bauxite residue leaching behaviour, Bayer process secondary minerals like cancrinite and hydrogarnet have also been proposed as the possible hosts of REEs (Davris et al., 2016). Hematite has been proven to be able to incorporate tetravalent cerium into its lattice in experimental conditions. Based on that and the existence of cerium in hematite-enriched matrix of bauxite residue, hematite was suggested to contain cerium in its lattice as the potentially prevailing form of cerium occurrence in bauxite residue (Bolanz et al., 2018). In the same study, the heavy minerals fraction was found to contain some sporadic grains of bastnäsite and monazite, but they were considered as negligible carriers of REEs. Cerium was identified to occur in its tetravalent oxidation state in the bulk sample and therefore the common REE minerals (e.g., monazite) were excluded as the potential hosts of cerium (Bolanz et al., 2018). The authors admitted that cerium location in hematite lattice remains hypothetical, but they insisted that REEs occurrence in bauxite residue should be discussed in the context of main mineral phases rather than discrete REE phases (Bolanz et al., 2018). Summaries about the recovery of REEs from bauxite residue can be found from different publications (Akcil et al., 2017; Binnemans et al., 2015; Borra et al., 2016; Davris et al., 2017). In general, the methods follow a hydrometallurgical route or a combination of pyro- and hydrometallurgical routes. Recently developed technologies have successfully applied ionic liquid leaching on bauxite residue to selectively recover REEs from bauxite residue (Davris et al., 2017).

1.4.2 Sc

Sc concentrations detected in bauxite residues worldwide range generally from 41–254 mg/kg (Borra et al., 2016; Zhang et al., 2016). Based on various publications that used different analytical techniques, the average concentration of Sc in AoG's bauxite residue is 121 ± 16 mg/kg (n = 24) (Alkan et al., 2017; Borra et al., 2015; Davris et al., 2014; P. N. Gamaletsos et al., 2016; Laskou and Economou-Eliopoulos, 2007; Lymperopoulou et al., 2017; Ochsenkühn-Petropulu et al., 1994; Vind et al., 2017b; Yagmurlu et al., 2017). By year 2015, the volume of bauxite residue accumulated in Greece was estimated to be about 5 Mt, resulting from the yearly output of 0.7 Mt (Anagnostou, 2010; Deady et al., 2016). Based on the preceding information, the amount of Sc present in AoG's bauxite residue stocks could be about 600 tons in total.

It was hypothesized that Sc might be bound to iron oxides of bauxite residue, either by substituting Fe^{3+} or by its adsorption on iron oxides mineral surfaces, by analysing the behaviour of Sc during leaching experiments (Borra et al., 2015).

Correlations between Ti and Sc behaviour during leaching tests and the assumed mineralogical association of these metals have been reported at least three times for the case of AoG's bauxite residue (Bonomi et al., 2017; Ochsenkühn-Petropulu et al., 1994; Rivera et al., 2017).

Xiao has concluded after combining the results of leaching experiments and electron microprobe analyses of BR from Guizhou Alumina Production (China) that Sc in bauxite residue is associated with anatase, rutile, ilmenite, zircon and monazite by isomorphic substitution while other forms were excluded ((Xiao, 1996) cited in (Zhang et al., 2017)). On the other hand, Zhang et al., (2017) concluded based on bauxite residue from Shandong Alumina Refining Plant (China), that Sc is exclusively associated with iron oxides represented by hematite and goethite in the residue. In that assessment, no distinction is made between the two iron oxide phases (Zhang et al., 2017). The deficiencies in the explanations of the experimental setup might hinder the reproducibility of their work. In another bauxite residue sample from China (Chalco aluminium refinery, Shangdong), it was concluded based on Time of Flight Secondary Ion Mass Spectrometry and EPMA analysis that Sc is mostly bound with TiO_2 phases, followed by associations with Fe, Al and Si phases, ordered in the magnitude of occurrence intensity (Liu et al., 2018). Relatively frequently, the alumina plants in China deploy the Bayer-sintering process, which might produce residues with different characteristics compared to bauxite residue derived from the conventional Bayer process (Songqing, 2017).

The identified quantity of about 55–60% of Sc in Middle Timan (Urals, Russia) bauxites is in aluminium oxyhydroxide minerals. During Bayer digestion, Sc is thought to be released from diaspore and boehmite and is thereafter assumed to be adsorbed on the surface of bauxite residue particles as ScO(OH) or $Sc(OH)_3$. The remaining proportion of Sc in bauxite residue remains in the same form as in bauxite, namely in the composition of zircon and chamosite, while Bayer process specific solid phases like hydrogarnet do not capture Sc, for the case of this specific bauxite residue (Suss et al., 2017).

It can be concluded that Sc occurrences in bauxite residue are rather diverse in different locations and further development in the understanding of Sc mineralogy in this question is necessary.

2. Materials and Methods

2.1 Sampling and Technological Data

Sampling took place over a three-day period and materials were collected from key points in the process flow sheet to provide a snapshot of the whole process. The precondition of such sampling procedure is that all the input constituents should appear in the output materials of the process and sampled output material corresponds to the sampled input material. The sampling points are shown on **Figure 3**, and sample descriptions are detailed in **Table 2**. AoG uses largely two types of bauxite feed: locally mined karst (diasporic/boehmitic) bauxite and imported lateritic (gibbsitic) bauxite. The Greek karst bauxite samples originate from the Parnassos-Ghiona B3 stratigraphic horizon (**Figure 1**), which is the youngest and most exploited horizon of the deposit (Laskou and Economou-Eliopoulos, 2007). Minor amount of B2 stratigraphic horizon Parnassos-Ghiona bauxite was also used at the time of sampling, but the exploitation of this material is currently suspended. Another minor source of karst bauxite at the time of sampling was diasporic bauxite from Turkey, Milas area. The lateritic bauxites used at AoG originate from Brazil (Porto Trombetas) and Ghana (Awaso), while only Brazilian bauxite was processed in the period of sampling campaign.

Bauxite samples were collected from the one-tonne test batches to provide the best representation of the feed material. Bayer liquors, aluminium hydroxide, alumina and lime samples were collected from the appropriate sampling points according to the internal protocols of AoG. A composite sample of bauxite residue was collected after the filter pressing of the residues. Fresh sodium hydroxide addition to the process was negligible during the sampling period and was therefore excluded from the analysis. Process data for both solid and the liquid mass flows were acquired for the same period as the sampling took place.

Table 2. Description of sampled materials. Refer to **Figure 3** to find the sampling points on the Bayer process flowsheet.

Solid samples				
Input bauxite	Karst / diasporic	1	DD-BX	Parnassos-Ghiona bauxite from B3 horizon. Extracted by company Delphi-Distomon S.A., a subsidiary of Mytilineos S.A. In the plant jargon termed as "Delphi-Distomo" bauxite. This material is subjected to limestone removal before the Bayer process.
		2	ST-BX	Parnassos-Ghiona bauxite from B3 horizon. Extracted by S&B Industrial Minerals S.A. In the plant jargon termed as "standard" bauxite. This material is subjected to limestone removal before the Bayer process.
		3	HS-BX	Parnassos-Ghiona bauxite from horizon B2. It represents a minor input (1%) to the process. At present day, it is no longer exploited.
		4	TU-BX	Bauxite from Turkey, western Taurides range and Milas area.
	Lateritic / gibbsitic	5	TR-BX	Bauxite from Brazil, Porto Trombetas deposit. It represents the main input of lateritic bauxite to the process (21 % of total bauxite input). Input of lateritic bauxite alters between this (Trombetas) and Awaso bauxite.
		6	GH-BX	Bauxite from Ghana, Awaso deposit. At the time of the case study, this material was not exploited.
	HMS unit	7	DC-BX	Decalcitated karst/diasporic bauxite, from which limestone is separated. Inputs to this unit are DD-BX and ST-BX. Represents the main bauxite input (73 % of total bauxite input during the case study) to the Bayer process as a mixture of karst bauxite from two different mining locations that exploit B3 horizon Parnassos-Ghiona bauxite.
		8	DC-RE	HMS residue. Limestone residue that is separated from Parnassos-Ghiona B3 bauxite. Besides limestone, contains also a significant proportion of bauxite material.
Intermediate materials / additives		9	BF-DG	Solid fraction of karst bauxite slurry, from grinding and preheating unit of karst bauxite.
		10	SW-DS	Solid fraction of lateritic/gibbsitic bauxite slurry from desilication unit.
		11	CA-OX	Lime, CaO.
Products / by-products		12	HY-AL	Aluminium hydroxide, $Al(OH)_3$, output from precipitation unit.
		13	CA-AL	Calcined alumina, Al_2O_3, output from calcination unit.
		14	RM-FP	Bauxite residue (red mud) after the filterpressing of thick bauxite residue slurry
Liquid samples				
Liquors		15	CL	Concentrated spent liquor, from the output of evaporation unit, routed to karst bauxite grinding
		16	PL	Pregnant liquor, from the outlet of settling and security filtration
		17	SL	Spent liquor, from the outlet of precipitation. Largest proportion is routed to evaporation and a small proportion to lateritic bauxite grinding.
Slurries		18	BF	Liquid phase from grinding and preheating unit of karst bauxite, corresponds to sampling point 9 and solid sample “BF-DG”
		19	SW	Liquid phase from grinding and desilication unit of lateritic bauxite, corresponds to sampling point of 10 “SW-DS”

2.2 Compiling of the Mass Balance

The results from chemical analysis were used in combination with mass flow data of the plant and normalised to the mass of produced aluminium hydroxide (on dry calcined basis) according to Equation 2. The mass balance approach to describing trace element distribution were based on the method given by Papp et al. (Papp et al., 1971). Original mass flow data was corrected only for the output units of “grinding and preheating of karst bauxite” and “grinding and desilication of lateritic bauxite”, assuming a constant Fe_2O_3 total mass in solids (Papp et al., 1971).

$$C = \frac{c \times m_1}{m_2} \qquad \text{Equation 2}$$

Where: C normalised concentration of trace element, mg/kg;

c measured concentration of trace element in solid, mg/kg; or liquid, mg/L;

m_1 mass flow of material on dry basis, kg/d; or liquor flow m^3/d;

m_2 mass flow of aluminium hydroxide on dry calcined basis, kg/d.

2.3 Analytical Methods for Bulk Material Characterisation

Solid samples were prepared for the analysis using standard techniques (drying, crushing, splitting, grinding). Elemental compositions of the samples were determined by a combination of techniques listed in **Table 3**. Lithium borate fusion was chosen as the appropriate method prior to inductively coupled plasma mass spectrometry (ICP-MS) that ensures with high efficiency the total dissolution of bauxite and bauxite residue mineral matrix (Adam and Krüger, 2017; Feret and See, 2010). Instrumental neutron activation analysis (INAA) has been outlined as a good analytical technique for determining trace element concentration in bauxite and bauxite residue as it is a non-destructive method and does not require any sample pre-treatment. Also, chemical interferences such as matrix effect are avoided (Feret and See, 2010; Ochsenkühn-Petropoulou et al., 1991). On the other hand, INAA is a relatively slow technique and not all the trace elements can be measured by this method. The quality of the trace element analysis was assessed by measuring certified bauxite reference material BX-N (Govindaraju, 1982; Govindaraju and Roelandts, 1989) with both methods, ICP-MS and INAA. INAA measurements were also verified with certified reference material DMMAS 120.

Bayer liquors were prepared for analyses either by (1) simply dilution, (2) acidification with concentrated HNO_3 (Singh and Mishra, 2012), or (3) dewatering the liquors to obtain dry pulps of the liquor (**Table 3**). The latter method also provides a guarantee that trace constituents are not precipitated out from the liquid phase during sample preparation. Besides, dewatering enhances the concentration of each component contained in the sample.

Table 3. Analytical methods and preparation techniques used for the determination of main and trace elements in the Bayer process solid and liquid samples.

	Abbr.	Method	Preparation and specifications
Solid samples	XRF-st	X-ray fluorescence, standardised	Fusion of solids with $Li_2B_4O_7/LiBO_2$ (66:33) flux, sample to flux ratio 1:11 (Yamada, 2010). Standardised with appropriate standard materials.
	ICP-MS	Inductively coupled plasma mass spectrometry	Fusion of solids with $Li_2B_4O_7/LiBO_2$ (66:33) flux, sample to flux ratio 1:20, glass bead dissolved in 10% v/v nitric acid
	INAA	Instrumental neutron activation analysis	About 2 g of sample is inserted in a polyethylene vial
Liquor samples	titr.	Thermometric acid-base titration	Details given in method description (Metrohm, 2018). Metrohm 855 Robotic Titrosampler
	AAS	Atomic absorption spectroscopy	Appropriate dilution with deionised water.
	ICP-MS	Inductively coupled plasma mass spectrometry	Sample is diluted with deionised water and then acidified with concentrated nitric acid while gently heating the sample in proportions 1:10:1, additional dilutions are made
	ICP-OES	Inductively coupled plasma optical emission spectroscopy	Sample is diluted with deionised water and then acidified with concentrated nitric acid while gently heating the sample in proportions 1:10:1, additional dilutions are made
	INAA	Instrumental neutron activation analysis	Dewatering of liquor until the creation of dry pulps (Büchi Syncore, vacuum pump Büchi V-700, controller Büchi V-850; Flawil, Switzerland). Then, about 2 g of sample is inserted in a polyethylene vial.
	XRF	X-ray fluorescence, no standardisation, semi-quantitative	Dewatering of liquor until the creation of dry pulps (Büchi Syncore, vacuum pump Büchi V-700, controller Büchi V-850)
	UV	UV Photometer	Acidification with conc. HCl and dilution with deionised water in proportions 1:3:20; only for analysing Fe.

Mineralogical composition of the samples was determined by X-ray diffraction (XRD, Bruker, USA) with Bruker D8 Focus. Identification and phase quantification of mineral phases was performed with XDB Powder Diffraction Phase Analytical System version 3.107 that is specifically designed for analysing bauxite and bauxite residue (Sajó, 2008, 2005).

2.4 Microanalytical Methods

The parts of samples subjected to microscale investigation were embedded in resin, polished and coated with carbon (qualitative investigations) or platinum (quantitative investigations), all in duplicate. Bauxite residue “as is” was attached to sample holder and coated with gold for secondary electron imaging. Bauxite residue subsample (~0.5 g) that was analysed in nanoscale, was suspended in acetone and treated with ultrasound to disaggregate the coagulated particles. The sample was then placed on a 300-mesh carbon coated copper grid and air-dried overnight.

Qualitative microscale investigations were performed by electron probe microanalysis (EPMA) with energy dispersive spectroscopy (EDS) with (1) EVO MA15 (ZEISS, Oberkochen, Germany) coupled with AZtec X-MAX 80 (Oxford Instruments, Abingdon, UK), and (2) JEOL 6380 LV (JEOL, Tokyo, Japan). EMPA-EDS instruments were operated at 20 kV. Microscale quantitative analyses were performed with a field emission microprobe JEOL JXA-8530F (JEOL, Tokyo, Japan) coupled with wavelength dispersive spectrometers (WDS): (1) TAP/LDE1, (2) LIF/PET, (3) LDE2H/TAPH, (4) LIFH/PETH, (5) LIFH/PETH. It was operated at 15 kV with a probe current of 30 nA. The standards used are listed in **Table 4**. For a regular WDS quantification, counting time on peak was 60 s and on background 10 s. For the case of Sc WDS quantification, different operational parameters were used. Long counting times (60 s), high beam current (100 nA) and usage of the H-type spectrometers resulted in an estimated detection limit of Sc of about 10 mg/kg.

Table 4. Standards used for the wavelength dispersive spectroscopy (WDS) quantification.

Element	Name	Formula
Al	Albite	Na($AlSi_3O_8$)
Ca	Diopside	$CaMgSi_2O_6$
Ce	Monazite	(Ce,La,Nd,Th)PO_4
Cr	Chromium (III) oxide	Cr_2O_3
Fe	Hematite	Fe_2O_3
Hf	Internal standard	
La	Monazite	(Ce,La,Nd,Th)PO_4
Mg	Periclase	MgO
Mn	Willemite	$(Zn,Mn)_2SiO_4$
Na	Albite	Na($AlSi_3O_8$)
Nd	Neodymium glass	SiO_2-CaO-Al_2O_3-Nd_2O_3
Pr	Praseodymium glass	SiO_2-CaO-Al_2O_3-Pr_2O_3
Sc	Scandium metal	Sc
Si	Diopside	$CaMgSi_2O_6$
Zr	Ziconia cubic	ZrO_2
Th	Monazite	(Ce,La,Nd,Th)PO_4
Ti	Rutile	TiO_2
U	Internal standard	
V	Vanadium (III) oxide	V_2O_3

Nanoscale investigation of bauxite residue was performed with a high resolution JEOL JEM-2100 LaB6 transmission electron microscope (HRTEM) (JEOL, Tokyo, Japan), operating at 200 kV. Grain microstructure was also studied using a bright field detector in scanning (STEM) mode of JEM-2100 instrument. Elemental analyses were carried out using an Oxford X-Max 100 Silicon Drift Energy Dispersive X-ray spectrometer (Oxford Instruments, Abingdon, UK), connected to TEM, with a probe size ranging from 2 to 5 nm in STEM mode.

Microscale in-situ Raman spectroscopy was performed using Renishaw inVia confocal Raman microscope (Renishaw, Wotton-under-Edge, UK), operated with a 532-nm or a 785-nm laser at a power of 25–50 mW at the laser source. Raman spectra were processed with Spectragryph 1.0.7 software. For presenting purposes, some EDS spectra were smoothed with Spectragryph 1.0.7

(Menges, 2017). Retrieved Raman spectra were compared with reference data from RRUFF database (Lafuente et al., 2015).

Complementary in-situ Sc and Ga content quantification was performed by laser ablation (LA) ICP-MS (Cetac LSX-213 G2+ LA, HelEx 2-volume ablation cell, coupled to Agilent 8800 ICP-MS). Helium was used as carrier gas at combined flow of 0.8 L/min. USGS GSD-1G standard was used for quantification and BHVO-2G and NIST612 were used for quality control measurements. Fe was used as an internal standard element for the analysis of hematite matrices and Al in the case of Al oxyhydroxide matrices. Internal standard element concentrations were determined by SEM-EDS quantitative measurements as average values of the representative sample areas. Single spot analysis with spot size of 40 µm, laser energy output of 1.46–1.48 J/cm^2 at a frequency of 10 Hz were used.

2.4.1 Challenges in the Microanalysis of Bauxite Residue

When performing microscale analysis of bauxite residue, some limiting conditions should be considered. First, the particle size of bauxite residue is very fine. In AoG's bauxite residue, 80 % of the particles are below 1 µm in dimensions (Borra et al., 2015). The fineness of the residue material is partly caused by the crushing and milling of bauxite during the pre-processing of bauxite feed (e.g. Chin, 1988). The need for fine particle size is crucial during the exploitation of especially karst (diasporic/boehmitic) bauxites (Lavalou et al., 1999). The minimum particle size that can readily be studied in EPMA is about 1 µm. Therefore, about 20 % of the particles can be analysed with this technique. It is reported, however, that there is no significant partitioning of mineral phases between the different size fractions in AoG's bauxite residue. A slightly higher amount of gibbsite and diaspore may be present in the coarser fractions and a higher amount of hydrogarnet group phases in the finest fractions (<32 µm) (Pontikes, 2007). Besides, it has been reported from the beneficiation experiments of different bauxite residues that there is only a slight enrichment of Sc in the finest fraction (<20 µm) of the material while the other fractions have relatively even distribution of Sc (Gu et al., 2016; Petrakova et al., 2014). To partly overcome the problem of fineness of bauxite residue, bauxite samples were studied which have not undergone crushing and grinding and therefore are not disturbed materials like the residue is. To analyse larger crystals of the specific Bayer process secondary minerals, a sample of scale from the digester autoclave was collected, which contained perovskite and cancrinite phases. Perovskite-based scales, for instance, have been previously shown to contain trace elements like Y, Nb and Zr (Zhong-Lin and Song-Qing, 1995). It has been also shown in other studies, that the investigation of Bayer process scales can provide advantageous information regarding the various properties of the secondary Bayer process mineral phases (Bánvölgyi, 2016; Kawashima et al., 2016). Besides that, bauxite was preliminarily investigated with transmission electron microscopy (TEM), which has the capability to make observations of nano-scaled materials. Unfortunately, the EDS device attached to TEM did not provide the required sensitivity to detect the low quantities of Sc in bauxite residue's fine particulates.

The second limiting condition for analysing bauxite residue is that it can be a mixture of raw materials from different origins, as in the present case of AoG. Thus, it can be difficult to distinguish the origin of a particle. Also, for this reason were the significantly Sc-enriched source bauxites examined that provide the characteristics of the source material of bauxite residue. Considering the preceding reasoning, it is concluded that current analysis is mostly representative for the bulk of AoG’s bauxite residue.

3. General Characteristics of the Materials

3.1 Chemical and Mineralogical Composition of Solid Materials

The analysed karst bauxite samples are dark brown with an oolitic/pisolitic texture (DD-BX, ST-BX, HS-BX, TU-BX; **Figure 4**). Sample ST-BX is vesicular (porous), while DD-BX, HS-BX and TU-BX are more massive than porous. Lateritic bauxite samples (TR-BX, GH-BX) are brownish red in colour and their texture is earthy, while Porto Trombetas bauxite is more lithified than the Ghanaian Awaso bauxite. Both lateritic bauxites exhibit segregation of darker brown or reddish (probably hematite-predominant) and whitish fragments (probably gibbsite-predominant).

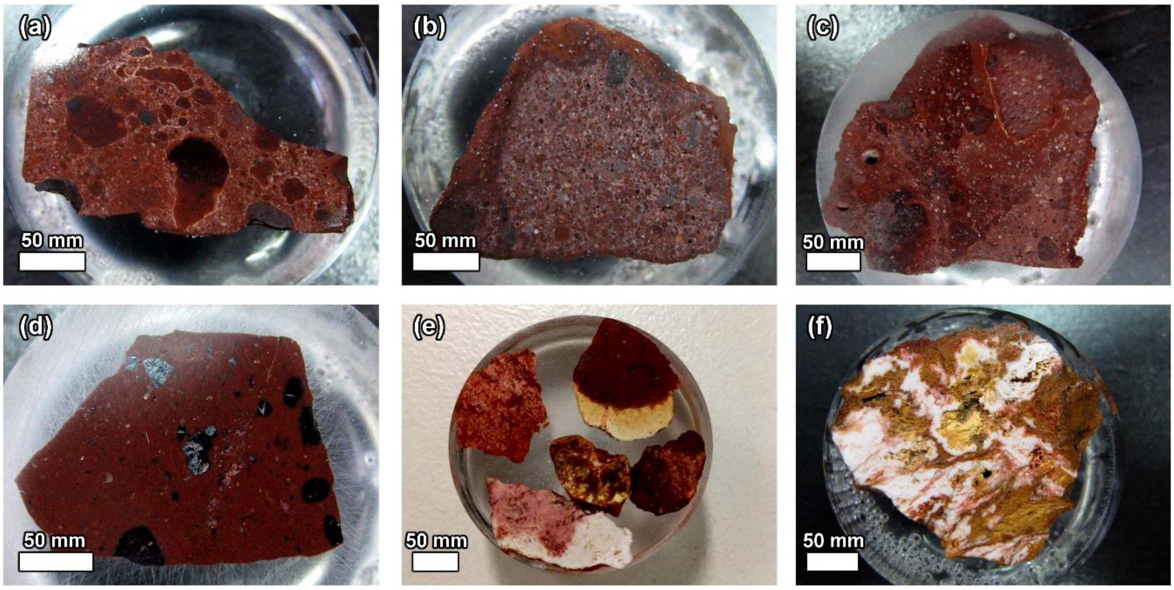

Figure 4. Macroscale photographs of bauxite samples: (a) first Greek Parnassos-Ghiona B3 horizon bauxite, DD-BX; (b) second Greek Parnassos-Ghiona B3 horizon bauxite, ST-BX; (c) Greek Parnassos-Ghiona B2 horizon bauxite, HS-BX; (d) Turkish bauxite from Milas area, TU-BX; (e) Brazilian bauxite from Porto Trombetas deposit, TR-BX; and (f) Ghanaian bauxite from Awaso deposit, GH-BX.

Bauxite samples are chemically mainly composed of aluminium, iron, silicon and titanium oxides, while aluminium and iron oxides embody most of the materials (**Table 5**). Lateritic bauxites have a higher proportion of LOI compared to karstic ones, which reports mainly to the crystalline water of gibbsite mineral. Calcium oxide is present in the Greek karstic bauxite sample and not in the Ghanaian and Brazilian lateritic bauxites. The mixed karst bauxite after HMS unit (where the limestone is separated) has an increased concentration of Al_2O_3 and decreased concentration of CaO.

Bauxite residue is a dark red thick muddy material with moisture content about 26 % in its initial state after exiting the Bayer process (**Figure 5**). As a contrast to bauxite samples, bauxite residue's main chemical components are iron oxides, but there is also present an appreciable amount of unrecovered aluminium oxide (**Table 5**). The relatively high amount of calcium oxide is mainly attributed to lime addition in the Bayer process. Sodium oxide content appears from the losses of sodium hydroxide that binds with secondary minerals created during bauxite processing, due to transformation of clay minerals to desilication products and reaction of quartz resulting in the same (M. Gräfe et al., 2011).

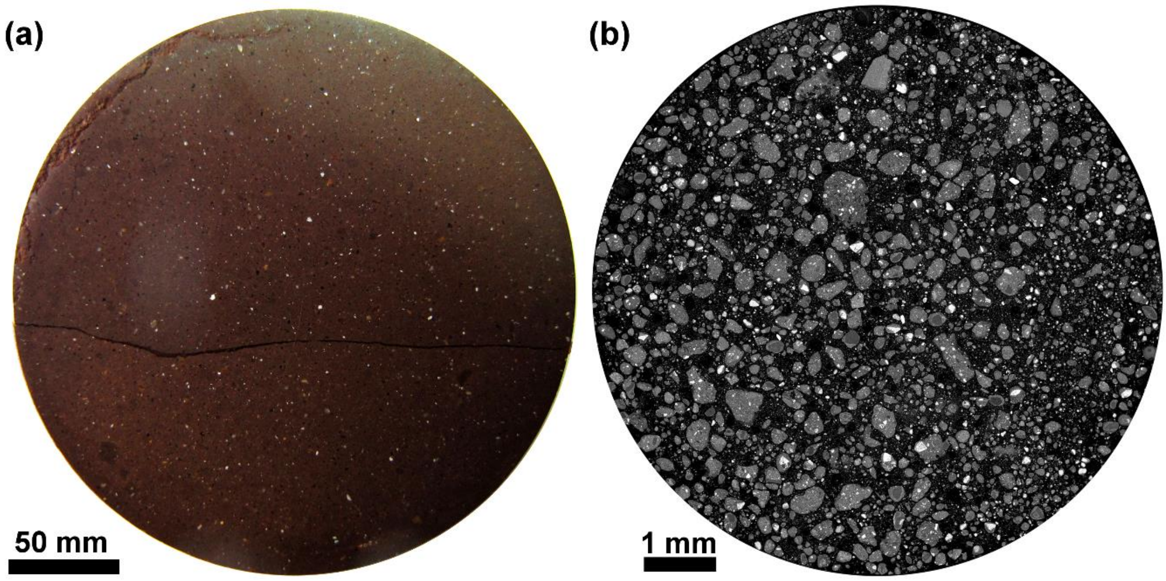

Figure 5. Appearance of bauxite residue shown on (a) macroscale photograph of a sample prepared in the manner of XRF pressed pellet impregnated with resin and polished, and (b) BSE composite image of a polished section of residue sample in resin. The images do not correspond to each other. On image (b), brighter particles are generally Fe oxides and greyish areas are generally composed of Al-Ca-Si-Ti matrix while black colour represents resin.

Aluminium hydroxide ($Al(OH)_3$, HY-AL) and calcined alumina (Al_2O_3, CA-AL) are regular products of the Bayer process with some common detectable impurities, such as Fe_2O_3 SiO_2 CaO and Na_2O, while TiO_2 is not detected.

Table 5. Main chemical composition of the major materials interacting with the Bayer process. Description of the materials can be found in **Table 2** and the sampling points with respect to the Bayer process in **Figure 3**.

Sample type	Code	LOI % (1000 °C)	Al_2O_3 wt%	Fe_2O_3 wt%	SiO_2 wt%	TiO_2 wt%	CaO wt%	Na_2O wt%	SUM wt%
Input bauxite	DD-BX	12.80	60.62	19.59	2.17	2.9	0.86	-	98.94
	ST-BX	14.28	56.54	19.79	2.33	2.64	3.78	-	99.36
	HS-BX	12.88	61.40	20.04	1.04	2.91	0.5	-	98.77
	TU-BX	11.24	53.88	24.72	4.59	2.99	0.97	-	98.39
	TR-BX	26.59	53.73	11.19	4.96	1.35	<0.01	-	97.82
	GH-BX	26.48	52.73	13.54	4.29	1.49	<0.01	-	98.53
	DC-BX	12.87	61.94	19.21	1.62	2.77	1.25	-	99.66
	DC-RE	17.85	52.04	12.88	3.14	2.26	9.67	-	97.84
Intermediate	BF-DG	19.41	50.41	17.02	1.30	2.24	4.94	6.11	101.43
	SW-DS	24.82	46.67	13.22	4.82	1.69	1.09	5.32	97.63
Product / by-product	HY-AL	39.2*	60.8*	0.0104§	0.0037§	<0.0016§	0.0123§	-	100.00
	CA-AL	1.15⊥	98.4‖	0.0115	0.0044	<0.0016	0.0018	0.3610	100.00
	RM-FP	10.38	20.64	41.65	6.76	5.32	10.07	2.87	97.69

* on wet hydrate basis
§ on calcined basis
⊥ on dry basis
‖ calculated

An overview of some of the key trace elements in the main Bayer process materials is presented in **Table 6**. An extended overview of the trace elements in Bayer process solid materials can be found in Appendix A, **Table A 1** and **Table A 2**. It can be noted that higher concentrations of Ce, La and Y can be found in Turkish Milas bauxite, when comparing the different karst bauxites. Lateritic bauxite samples and especially the one from Porto Trombetas have low concentrations of Ce, La and Y. The concentrations of Ga are similar in all bauxites, but again the Turkish Milas bauxite displays a slightly higher value. Ga is also the only detectable trace element in this selection of analytes that is enriched in aluminium hydroxide and oxide products compared to bauxites. Karst bauxites contain approximately 6 times higher quantity of Sc compared to lateritic bauxites, implying their high importance in the influx of Sc to the system even without presenting detailed mass balance calculations. The higher abundance of the REEs in karst bauxites coincides with the higher quantity of Th in the analysed samples. The most prominent trace elements, or even secondary elements depending on the definition, are Cr and V. There is about two times higher concentration of V found in karst bauxites compared to lateritic ones, but this does not render the amount of V in lateritic bauxite insignificant. Present data supports the relative enrichment of trace elements into karst bauxites as opposed to lateritic bauxites (Valeton, 1972) and the indicated similarities in Ga concentrations independent of the bauxite type (Schulte and Foley, 2014).

Table 6. Concentrations of selected trace elements (mg/kg) in the main Bayer process solid materials, based on a combination of ICP-MS, ICP-OES, XRF-st and INAA data. Extended overview of trace element concentrations can be found in **Table A 1** and **Table A 2**.

Description		Name	Ce	Cr	Ga	La	Nd	Sc	Th	V	Y
Karst	B3	DD-BX	208	693	58	58	53.5	53.7	51.2	398	47.5
		ST-BX	177	588	60	63	53.8	43.1	53.0	558	46.7
	B3 mix	DC-BX	195	768	60	67	42.5	50.0	51.2	471	44.8
	B2	HS-BX	177	590	66	46.7	31.9	43.1	54.4	650	46.1
	Turkey	TU-BX	265	442	69	145	92.3	56.0	44.9	487	92.7
Lateritic		TR-BX	9	138	60	5.0	<5	7.1	24.7	258	11.4
		GH-BX	29	521	57	19.1	12.0	8.4	16.7	247	17.2
Residue		RM-FP	363	1429	41	135	86.5	97.7	105.0	1020	89.5
		DC-RE	137	450	55	56	45.3	27.3	37.7	179	39.9
Product	Al(OH)3	HY-AL	<3	<5	85	<0.5	<5	<0.1	<0.2	<10	<10
	Al2O3	CA-AL	<2	<5	83	<0.5	<5	<0.1	<0.2	<10	<10

The chondrite-normalised plot of REE-enriched Bayer process materials is given in **Figure 6** (Anders and Grevesse, 1989). Such plotting is often used in geochemistry to eliminate the so-called Oddo-Harkins effect according to which the even-numbered chemical elements are more abundant than the odd-numbered ones and therefore the plots would otherwise possess a zig-zag pattern (Rollinson, 1993). It can be seen from the graph that in Parnassos-Ghiona bauxites there is a positive Ce anomaly. This is in accordance with a previous case study (Deady et al., 2016). The authors of that study proposed that it could be an artefact of the samples originating from the upper parts of the bauxite profiles with relatively oxidising conditions that favour the abundant occurrence of tetravalent Ce (Deady et al., 2016). However, present case study suggests the Ce positive anomaly to be a more systematic effect in the Parnassos-Ghiona deposit, observed both in B2 and B3 horizon bauxites. Ce anomaly is not observed in the Turkish Milas bauxite and in the lateritic bauxite samples. Bauxite residue in both samples from 2010 and 2016 has inherited the positive Ce anomaly from bauxite feed. All karst bauxites display a minor negative Eu anomaly, but the Brazilian Porto Trombetas bauxite seems to have a positive Eu anomaly. Small enrichment of Gd, can be seen in all karst bauxite as well as bauxite residue samples, which is also consistent with previous observations (Deady et al., 2016). Bauxite residue is clearly enriched in REEs compared to Parnassos-Ghiona bauxite, but the enrichment level of Turkish Milas bauxite is practically the same as for the current bauxite residue. The HMS residue from limestone separation unit is slightly depleted in REEs compared to the bauxites from which it is derived from and the Ce anomaly is less pronounced.

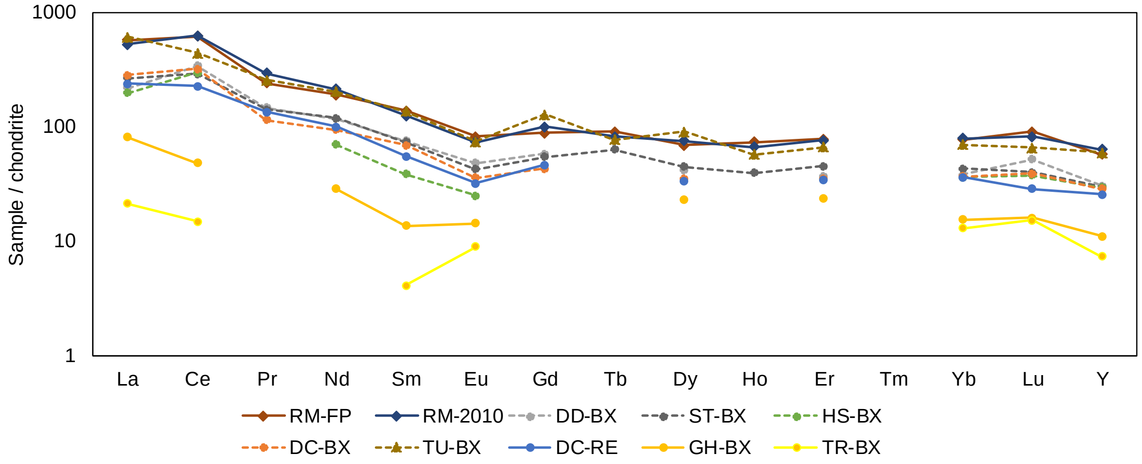

Figure 6. Chondrite-normalised plot of bauxites and bauxite residue. In the positions with gaps, the REE concentrations are below detection limit. Chondrite data is adapted from Anders and Grevesse, (1989). Gaps mark the analyses where the analyte concentration is below the available detection limit.

Main mineral phases of the karst bauxites are diaspore, boehmite and hematite, while for the lateritic bauxites they are gibbsite, goethite and hematite (**Figure 7**, **Table 7**). Brazilian Porto Trombetas bauxite has also a relatively high kaolinite content, 10.5%.

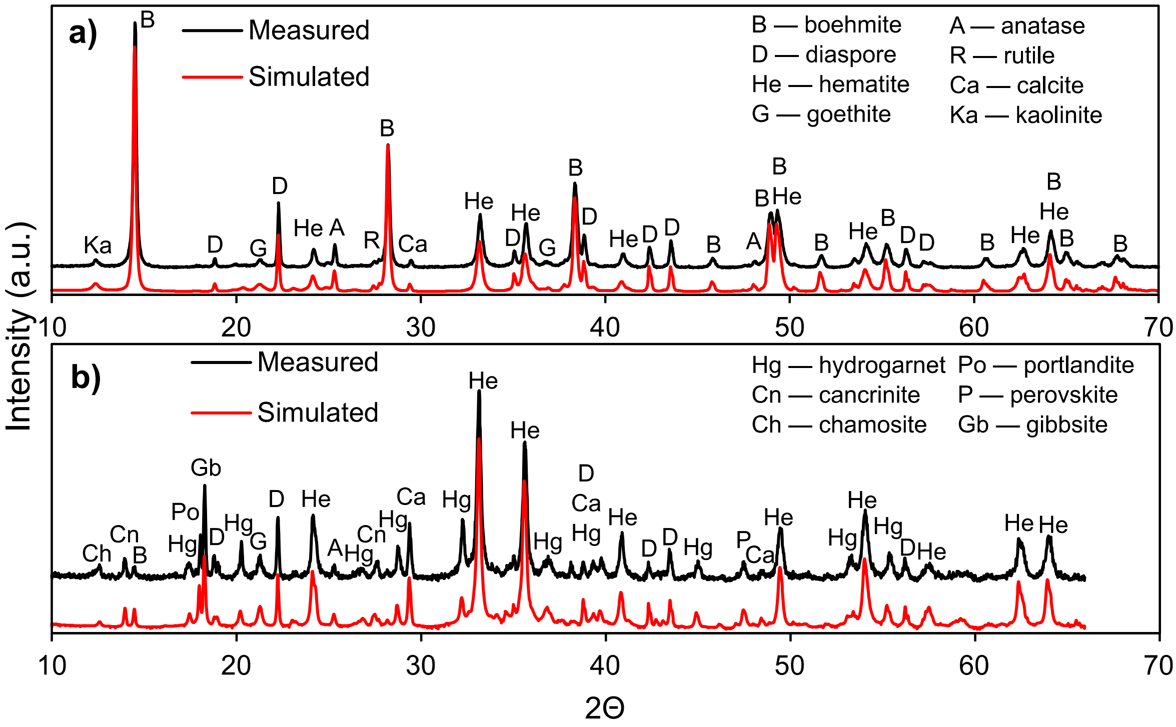

Figure 7. Examples of diffractograms and simulated patterns of (a) Greek Parnassos-Ghiona B3 horizon bauxite, DD-BX; and (b) bauxite residue. Intensity scale is linear.

While bauxites are composed of well crystallized phases judging by the narrow peaks of XRD scans, the crystallinity of bauxite residue phases is less developed as seen from the wider XRD peaks (**Figure 7**). The most abundant mineral phase in bauxite residue is hematite (31%), followed by hydrogarnet group phases (14.5%). These are then followed by diaspore (13%), cancrinite (11%) and goethite (7.5%), while diaspore represents the unrecovered alumina. Several minor mineral phases exist in the residue in addition to the major ones, such as calcite, perovskite, chamosite (a chlorite group phase), gibbsite, boehmite, portlandite, rutile and anatase. According to a previous work, about 10 % of AoG's bauxite residue could be XRD amorphous (Hertel et al., 2016). Chamosite was detected only in the bauxite residue and intermediate karst bauxite slurry samples (BF-DG), but its presence has been reported earlier in Parnassos-Ghiona bauxite, based on microanalysis (Laskou and Economou-Eliopoulos, 2007). Generally, chamosite is a commonly encountered chlorite group phase in bauxites (Bárdossy, 1982; Valeton, 1972). The 2Θ positions of kaolinite and chamosite main peaks coincide in diffractograms of bauxites. Chamosite reacts very slowly in the Bayer process and does so at temperatures above 280 °C (Songqing and Zhonglin, 2016). Therefore, its presence in bauxite residue is expected. In the intermediate karst bauxite slurry (BF-DG), kaolinite has already been reacted, supported by the existence of Si-containing hydrogarnet phases (9%) and minor amount of cancrinite (1%) in this material. Kaolinite starts to react in the temperature 95–100 °C (Songqing and Zhonglin, 2016), therefore its absence in the solids in the preheating stage is expected.

Bauxite processing results in the formation of secondary minerals like hydrogarnet group phases. In the present bauxite residue sample it was identified being an iron substituted hydrogarnet ($Ca_3[Al,Fe]_2(SiO_4)n\cdot(OH)_{12-4n}$) (Sajó, 2005; Smith, 2017). Nevertheless, it is reasonable to assume that several of the hydrogarnet group endmembers exist in bauxite residue since their XRD peak positions are similar. Perovskite phase ($CaTiO_3$) is the result of titanium dioxides, mainly anatase, reacting with NaOH and then with lime (Smith, 2017; Suss and Rydashevsky, 1996). The reaction between sodium aluminate and dissolved silica forms cancrinite ($Na_8(Al,Si)_{12}O_{24}(OH)_2\cdot 3H_2O$) (Sajó, 2005; Whittington, 1996).

A rough indirect estimate of zircon phase quantity in the studied materials resulted in a value of 0.1% in bauxite and 0.2% in bauxite residue. This estimate was based on bulk zirconium (Zr) elemental concentration (0.12% Zr in bauxite residue) (P. N. Gamaletsos et al., 2016), assuming that all of the elemental Zr is attributed to zircon mineral phase. Zircon phase quantity becomes important in the context of estimating trace element inventory (especially Sc) in different mineral phases.

Aluminium hydroxide is mineralogically mainly composed of gibbsite. Alumina sample is mainly composed of theta alumina, which is one stage before the alpha alumina in the decomposition reaction series from aluminium hydroxide to alumina (Hudson et al., 2000).

Table 7. Mineralogical composition of the main Bayer process materials, excluding products. The phase quantities represent the XRD-crystalline phases. In *italics* are indicated the Bayer process specific phases.

Sample	**Phase**														
Bauxite	Boehmite	Diaspore	Gibbsite	Hematite	Goethite	Anatase	Rutile	Calcite	Quartz	Kaolinite	Chamosite	*Hydrogarnet*	*Cancrinite*	*Perovskite*	*$Na_2Al_2O_4·3H_2O$*	*Total*
DD-BX	53	14.5		17.5	3	2.2	0.7	0.8		6.5						98.2
ST-BX	32	36		17	4.5	2	0.7	3	0.5	3.5						99.2
HS-BX	59	10		21	3.5	2	1	0.6		2.5						99.6
TU-BX*		58		19	5	0.8	2	3	1	5						100.3
TR-BX			76	6	5.5	0.9	0.4			10.5						99.3
GH-BX§	1.5	1	80	3.5	9	0.4	1.2		0.3	2						99.4
DC-BX	28	42		13	9	2	0.7	0.6		4						99.3
Intermediate																
BF-DG	10	43	1.5	10	6	1.2	0.8	1			4	9	1		2.5	90.0⊥
SW-DS	0.5	1	63	11	2	1.2	0.5	1		1.5		3	10			94.7⊥
By-products																
RM-FP	2	13	2.5	31	7.5	0.6	0.7	5	0.3		3.7	14.5	11	4		95.8
DC-RE	30	28		9	4.5	1.5	0.8	17		7						97.8

* Also 5% illite/illite-montmorillonite and 1.5% corundum.

§ Also 0.5% lithiophorite.

⊥ Missing proportion could account to non-crystalline sodium in the sample as chemical and mineralogical analysis cannot be matched with Na_2O concentration.

Bauxite residue phase composition was compared in samples collected from 2010–2016 (**Figure 8**). The diffractograms that were used for phase quantification originate from: 2010 — present; 2011a — C. Bonomi & C. Cardenia; 2011b — P. Tam; 2015 — present; 2016a D. Ariño Montoya, 2016b — present. It can be therefore indicated that hematite content varies in AoG's bauxite residue from 26 to 35%, hydrogarnet phases varies from 14 to 18%, chamosite from 3 to 7%, goethite is quite stable and varies from 7.5 to 9%, cancrinite has quite high variations from 6 to 11%. It should be noted, though, that the method used for current phase quantification can inherit the errors in the chemical analysis of the samples, if they are present (Sajó, 2008). **Figure 9** depicts the average phase concentration of AoG's bauxite residue based on the data described previously.

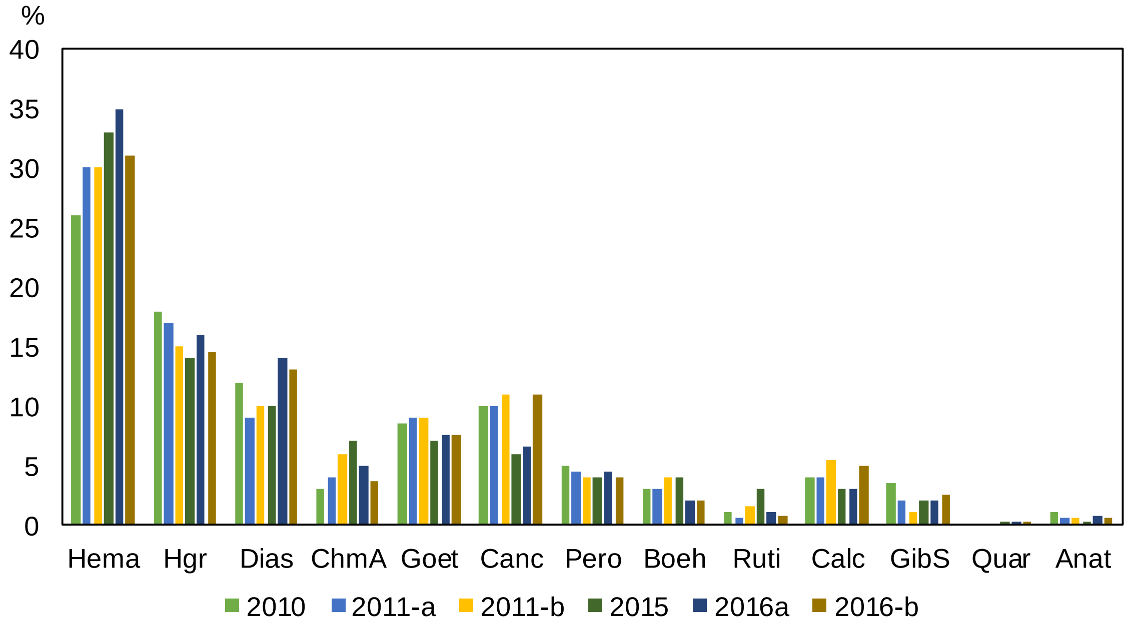

Figure 8. Comparison of AoG's bauxite residue phase composition deposited in different years. Abbreviations: hematite (Hema), hydrogarnet (Hgr), diaspore (Dias), Chamosite (ChmA), goethite (Goet), cancrinite (Canc), perovskite (Pero), boehmite (Boeh), rutile (Ruti), calcite (Calc), gibbsite (GibS), quartz (Quar), anatase (Anat).

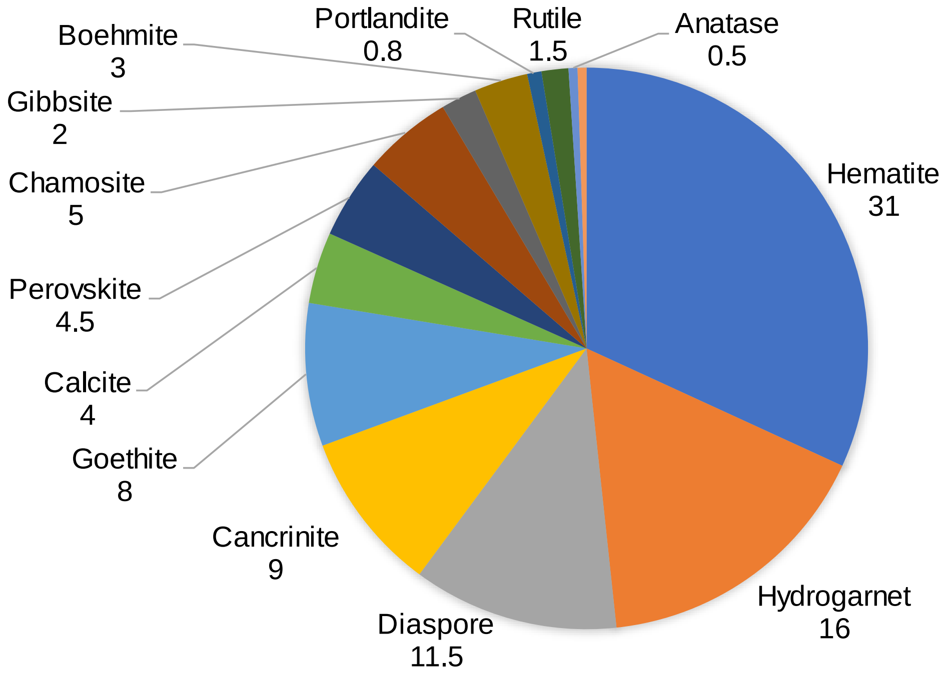

Figure 9. Average AoG's bauxite residue mineralogical phase composition based on 6 residue samples.

The chemical and mineralogical composition of bauxite materials is quite typical with respect to both analysed bauxites, karstic and lateritic, compared those described in the literature (Bárdossy, 1982; Valeton, 1972). It can be said that also the bauxite residue from AoG is with a typical composition, but different residues around the world have quite varying ranges of compositions (Evans, 2016).

3.2 Basic Microscale Characteristics

3.2.1 Bauxites

Greek Parnassos-Ghiona bauxites are dominated by oolitic/pisolitic textures (**Figure 10**, a–c). Three principal textures are commonly present: (1) Al-dominated ooids/pisolites that are dark gray on BSE images, (2) Fe-dominated ooids/pisolites that are bright and whitish in the BSE images, and (3) matrix that fills the areas between the ooids/pisolites that has about equal content of Al and Fe and appears light grey in BSE images. Second Parnassos-Ghiona B3 horizon bauxite (ST-BX, **Figure 10**, b) has distinct hollow vesicles or pores and it is more fractured than the other two Parnassos-Ghiona bauxites. Turkish Milas diasporic karst bauxite is more massive and homogeneous with rather distinct Al- and Fe-dominant formations compared to Greek bauxites (**Figure 10**, d). Brazilian Porto Trombetas bauxite has rather diverse textural characteristics, with relatively large areas dominated by Al as well as large areas dominated by Fe oxides. It is more compact compared to the other lateritic bauxite from Ghana. In the image in **Figure 10** (e), the depicted area is dominated by Al-rich matrix, whereas on the left side of the image, some globular formations of Fe oxides are present. As indicated from the macroscale characteristics of Ghanaian lateritic bauxite, also its micro-texture is fractured, implying to poor lithification (**Figure 10**, f). Al- and Fe-rich areas are relatively homogeneously distributed, while Fe oxides have the tendency of seemingly filling the fractures. Some minor phases are also seen in the images shown here, like a Ti phase in **Figure 10** (a) and a zircon grain in **Figure 10** (f).

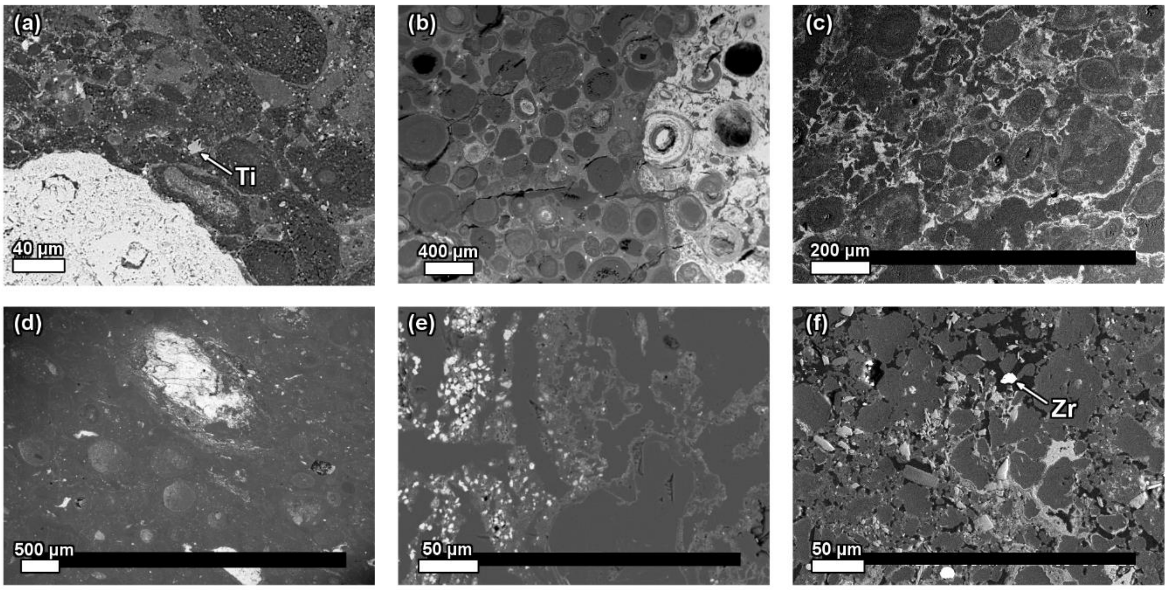

Figure 10. Microstructure of bauxite samples shown on BSE images: (a) first Greek Parnassos-Ghiona B3 horizon bauxite, DD-BX; (b) second Greek Parnassos-Ghiona B3 horizon bauxite, ST-BX; (c) Greek Parnassos-Ghiona B2 horizon bauxite, HS-BX; (d) Turkish bauxite from Milas area, TU-BX; (e) Brazilian bauxite from Porto Trombetas deposit, TR-BX; and (f) Ghanaian bauxite from Awaso deposit, GH-BX. Ti — titanium dioxide particle, Zr — zircon particle. Generally, the darker greyish areas are Al-dominant and brighter areas are Fe-dominant.

3.2.2 Bauxite Residue

Although bauxite residue is generally a very fine material, it does not prevent from making distinction between its main as well as minor mineral phases in microscale analysis. This can be seen in **Figure 11**, where examples of practically all bauxite residue’s main mineral phases also detected with XRD are shown. Commonly, relatively large fragments (10–100 µm) of Al-rich, Fe-rich or Ca-Al-Si containing particles found embedded inside a matrix of the residue’s fine particulates (**Figure 11**, a). Al-rich fragments generally correspond to undigested diaspore/boehmite, Fe-rich particles to hematite or goethite and Ca-Al-Si particles are probably hydrogarnet group phases, when comparing the XRD phase quantification and microscale analyses and the known occurrence of such phases in bauxite residue (M. Gräfe et al., 2011; Smith, 2017; Zoldi et al., 1987).

Fe oxide/oxyhydroxide particles occur in very wide range of sizes, as emphasised in **Figure 11** (b). Sometimes, hematite particles are attached with goethite (**Figure 11**c). The identity of such Fe oxide occurrences was identified with Raman microscopy (refer to section 7.1.2). It is characteristic to goethite phases analysed in bauxite residue that the sum of total oxides measured by WDS is around 90 wt%, from where the missing 10 wt% accounts for crystalline water of goethite (refer to section 7.1.2, **Table 19**). Both evidences, based on Raman spectroscopy and WDS, will be addressed more thoroughly in further chapters (section 7.1.2). Also, the Al-rich particles, corresponding to boehmite/diaspore, can be relatively large, exceeding 50 µm-s. Differently from Fe oxide particles, Al oxyhydroxide particles tend to be fractured, probably because of bauxite grinding (**Figure 11**d). In the example of Al oxyhydroxide in **Figure 11**e, the rims of the particle are eroded as a result of the caustic leaching, but the dissolution has not been finished, leaving most of the particle intact. Particles composed almost exclusively of Ca can be linked with calcite phase identified in XRD (**Figure 11**f). Ti dioxide phases, such as shown in **Figure 11**g, that have comparatively large sizes (>20 µm) are encountered in SEM analysis quite rarely. It was noted that some Ti phases exhibit properties indicating that a reaction has occurred (**Figure 11**h). Ti dioxide phase, probably anatase, is attached in **Figure 11**h to a calcium titanate phase that is likely a reaction product of anatase reacting with caustic soda and the dissolved Ca ions (discussed further in section 5, **Figure 32**). In **Figure 11**i is shown a Ca-Al-Fe-Si phase that could correspond to iron substituted hydrogarnet identified by XRD and discussed in several publications (Smith, 2017; Whittington, 1996; Zoldi et al., 1987).

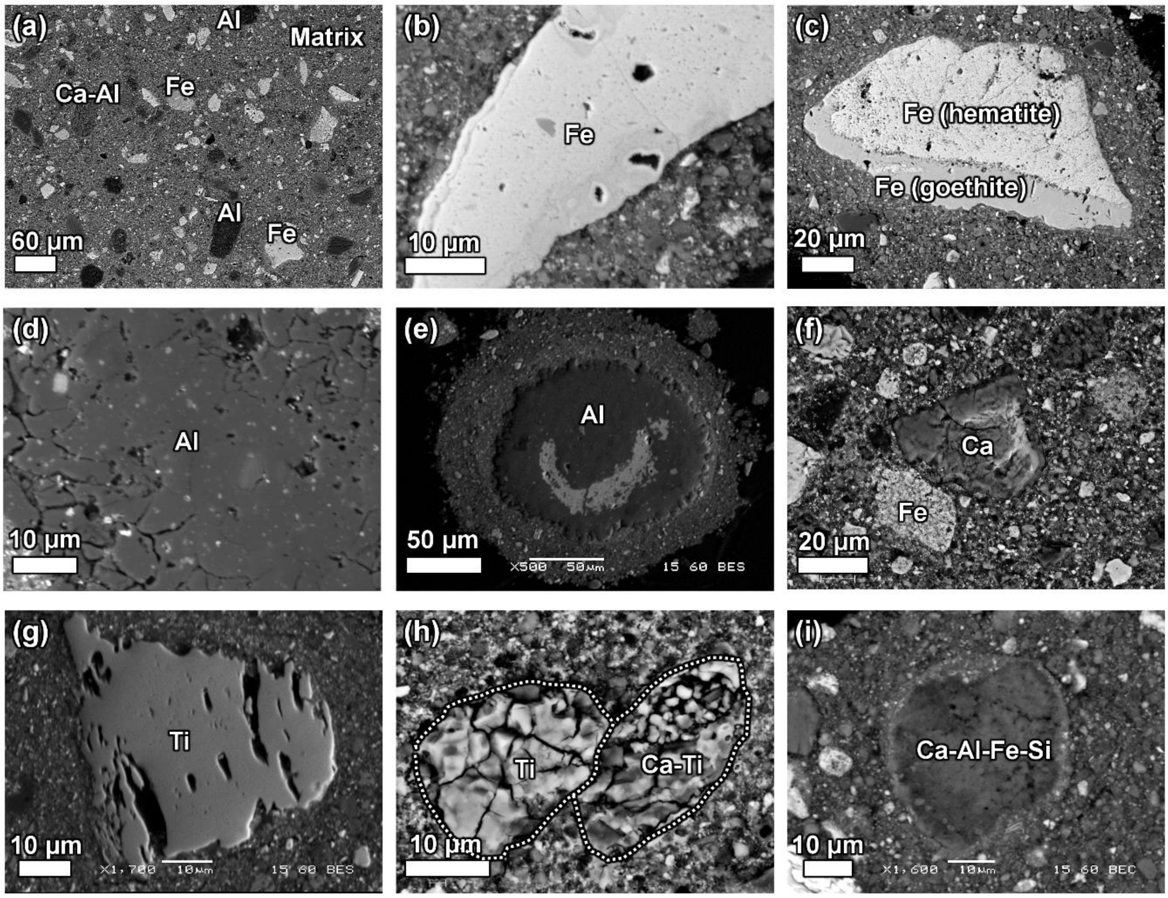

Figure 11. Microscale BSE images of bauxite residue's main mineral phases: (a) particles of Fe oxides (Fe) and undigested boehmite/diaspore (Al) particles as well as calcium aluminate particle in fine homogeneous Fe-Al-Ca-Si-Ti matrix of the residue, (b) fragment of an Fe oxide particle, (c) two Fe phases attached to each other, corresponding to hematite and goethite as identified by µ-Raman spectroscopy, (d) undigested boehmite/diaspore, (e) undigested boehmite/diaspore which edge areas are affected by the caustic leaching, (f) Ca phase corresponding to calcite, (g) titanium dioxide corresponding to anatase or rutile, (h) titanium dioxide, likely anatase, and a newly formed calcium titanate phase on the account of reacted anatase, and (i) calcium aluminium ferro-silicate phase probably corresponding to iron substituted hydrogarnet.

3.2.3 Aluminium Hydroxide and Alumina

In addition to bauxite and bauxite residue, also the Bayer process products aluminium hydroxide as well as calcined alumina were examined microscopically (**Figure 12**). It is the purpose of the Bayer process to produce technically pure alumina, therefore significant impurities are not present in the products, as seen in the homogeneous character of BSE images in **Figure 12** (a), (d) and (e). Those impurities which were detected, are all silicate-based. They include Fe-Al-Mg-Si particles, Na-Al-Si particles that could correspond to cancrinite and K-Al-Si particles. However, such impurities are very scarce which is in accordance with the chemical analysis of Bayer process products (**Table 5**, **Table A 3**).

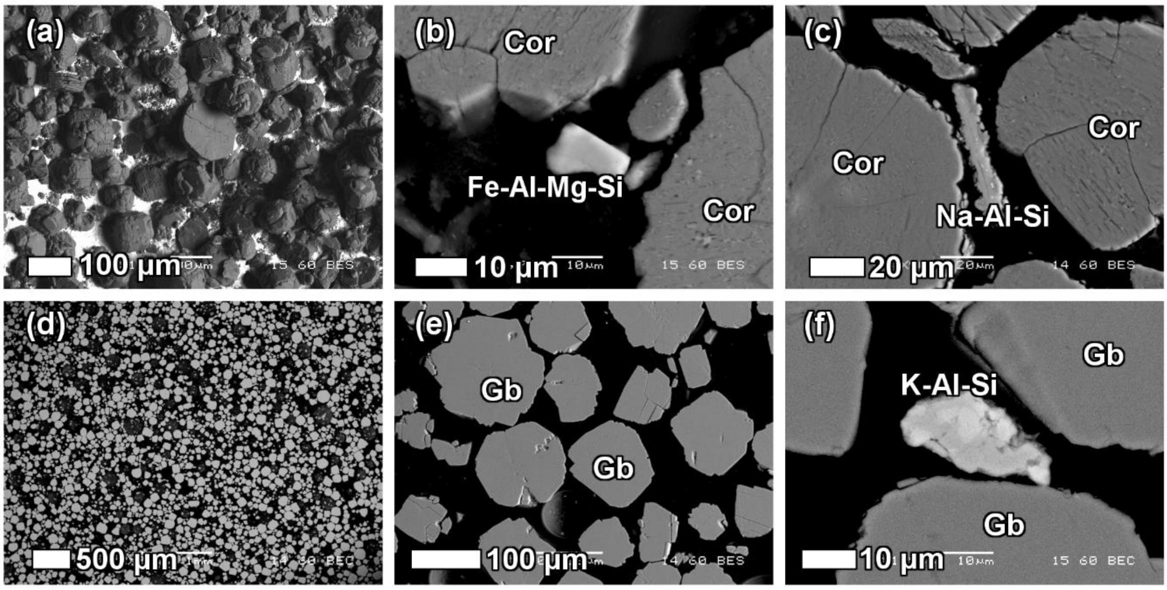

Figure 12. Microstructure of alumina (a–c) and aluminium hydroxide (d–f) with impurities. Cor — corundum (or other forms of Al_2O_3), Gb — gibbsite.

3.3 Chemical Composition of the Bayer Liquors

Bayer liquor from various production stages is relatively enriched in the concentration of Ga, V, As and K (**Table 8**, Appendix A **Table A 4**). Ga, V, As and K concentrations in various Bayer plants are relatively well known, while K is considered highly soluble in the process liquors and Ga, V as well as As medium soluble (Teas and Kotte, 1980). Note that the concentration of some analytes, like Ga and V, is higher in the spent liquor compared to pregnant liquor. This is because the total volume of spent liquor is smaller than the total volume of pregnant liquor and therefore the concentrations appear higher. At the same time, the mass balances of these elements are in equilibrium, as explained further (section 4.1). The same accounts for the concentration of total caustic. Mo was also accumulated to process liquor, but the behaviour and mass balance of this element in Bayer process is already given by Papp et al. (Papp et al., 1971). Detectable concentrations of Cr and Ni are also present in Bayer liquor, but these metals are not particularly accumulated into Bayer liquor compared to their concentration in bauxite feed. Other metals, such as Ce, La or Y that were of high interest within the scope of this study, do not occur in dissolved form in Bayer liquor in detectable concentrations (**Table 8**). This is a possible result as the REEs are not predicted to have soluble species in highly alkaline conditions (pH >14) (Brookins, 1988, 1983), which is further supported by the mineralogical observations indicating the REEs remain in solid forms during the Bayer digestion (section 6.3). For the case of Sc, ICP-MS indicated the presence of some dissolved Sc in process liquors (0.2–0.4 mg/L), but INAA did not confirm its presence in these samples. Suss et al. report that Sc concentration in Bayer liquor remains <1 mg/L (Suss et al., 2017). Bayer liquor also contains low concentrations of U (about 1.3 mg/L), which is in accordance with previously known facts (Sato et al., 2013). It is interesting to note that 20–30 mg/L concentration of tungsten (W) was also found in process liquors by INAA and XRF. Previous studies that have compared W concentrations in bauxite and derived residue have indicated a depletion of W in bauxite residue compared to bauxite feed, suggesting that current detection of W in Bayer liquor is realistic (Feret and See, 2010; Gamaletsos, 2014).

Table 8. Composition of Bayer process pregnant (PL) and spent (SL) liquors. Extended overview of Bayer process liquor composition is available in Appendix A **Table A 4**.

	Al_2O_3*	**Na_2O**[§]	**As**	**Br**	**Ca**	**Ce**	**Cr**	**Fe**	**Ga**	**Gd**	**K**
	g/l	g/l	mg/L	mg/L	mg/L	mg/L	mg/L	mg/L	mg/L	mg/L	g/l
	titr.	titr.	INAA	INAA	AAS	ICP-MS	ICP-MS	UV	ICP-OES	ICP-MS	AAS
PL	192.2	159.4	110.8	33.6	14.9	<0.04	1.4	9.6	267.2	<0.04	13.7
SL	108.6	171.7	99.6	31.4	16.5	<0.04	1.3	3.4	279.7	<0.04	13.8

	La	**Mg**	**Mo**	**Ni**	**Sc**	**Si**	**Th**	**U**	**V**	**W**	**Y**
	mg/L	mg/L	mg/L	mg/L	mg/L	mg/L	mg/L	mg/L	mg/L	mg/L	mg/L
	ICP-MS	AAS	INAA	AAS	INAA	AAS	INAA	ICP-MS	ICP-OES	INAA	ICP-MS
PL	<0.04	<0.1	318	4.8	<0.05	544	<0.1	1.28	295.2	27	<0.04
SL	<0.04	<0.1	273	<4	<0.05	520	<0.1	1.27	314.7	21	<0.04

* The aluminate content of the liquor, expressed as Al_2O_3 (Wellington and Valcin, 2007).

[§] Total caustic, the sum of the free Na(OH) and Na bound with sodium aluminate, expressed as Na_2O (Wellington and Valcin, 2007).

4. Distribution of Trace Elements in the Bayer Process

Chapter 4 is based on the following publication: Vind, J., Alexandri, A., Vassiliadou, V., Panias, D., 2018. Distribution of selected trace elements in the Bayer process. Metals 8 (5), 327.

Based on the information about trace element concentrations in process liquors (**Table 8**), the mass distribution descriptions of the trace elements were divided into two main categories. The first one describes the metals (and metalloids) that accumulate to Bayer liquor or dissolve sparingly (V, Ga, As, Cr, U) while the second one describes the metals for which the distribution is controlled only by solid materials (REEs, Sc, Th).

Full data describing the distribution and mass balance inventory of all analysed trace elements is given in Appendix A (**Table A 5**, **Table A 6**, **Table A 7**). Processing steps are divided into seven principal units: (I) heavy media separation (HMS), (II) grinding and preheating of karst bauxite, (III) grinding and pre-desilication of lateritic bauxite, (IV) digestion, settling and washing, (V) precipitation, (VI) evaporation and (VII) calcination. Overall mass balance is summarised in "internal balance" which includes the process liquors in addition to solids and "external balance" that includes only solid materials input and output. For the metals which do not occur in process liquors, units V–VII are omitted, because the metal concentrations relating to those units were below detection limits (which are specified in Table A3).

4.1 Metals (and Metalloids) that Accumulate to Processing Liquor

There was insignificant difference in the Ga concentrations when comparing lateritic and karst bauxites (Appendix A, Table A2). This is in line with the report by U.S. Geological Survey, where they concluded a similar presence of Ga in karstic and lateritic bauxites. They summarise the world average Ga concentration in all analysed bauxite deposits as being 57 mg/kg (Schulte and Foley, 2014), which is comparable to present analysis — 57 to 66 mg/kg in all currently analysed bauxites.

Concentrations are said to be ranging from 12 to 52 mg/kg Ga with an average of 40 mg/kg in bauxite districts of Greece and Turkey (Schulte and Foley, 2014).

Gallium possesses a close relation to Al and therefore occurs prevalently in Al-minerals. Similar properties include atomic radius, trivalent oxidation state, tetrahedral or octahedral coordination and amphotericity (Gray et al., 2013; Shaw, 1957). The mass distribution of Ga is mainly controlled by process liquors (**Figure 13**). During bauxite digestion, Ga is released from aluminium-bearing minerals like gibbsite, boehmite and diaspore (Gray et al., 2013). The Ga digestion reaction is described by **Equation 1** (Authier-Martin et al., 2001).

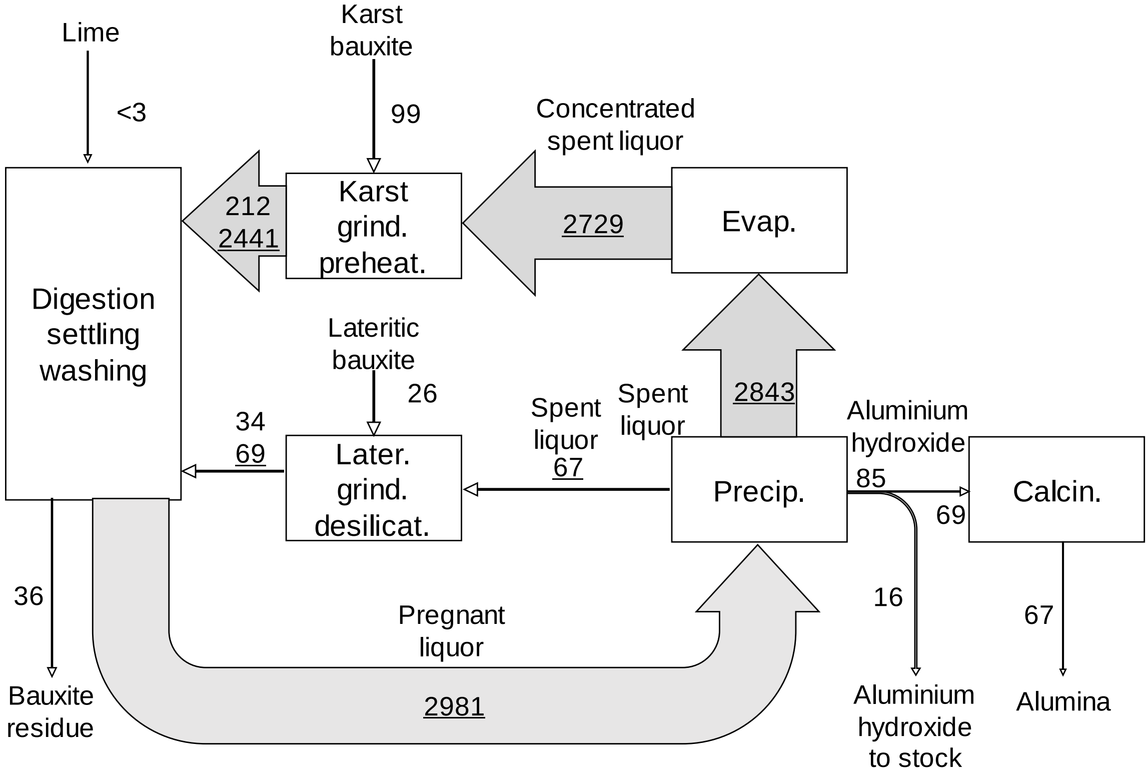

Figure 13. Mass distribution of Ga (mg/kg) normalised to mass of aluminium hydroxide produced, based on ICP-MS (solids) and ICP-OES (liquors) data.

Ga accumulates in process liquors, achieving saturation at levels exceeding 300 mg/L. This is about the average of that reported across earlier publications (60–600 mg/L Ga), yet typically shown values remain between 100–200 mg/L Ga (Figueiredo et al., 2002; Ilić and Mitrović, 1989; Lamerant, 1995, 1992; Riveros, 1990; Selvi et al., 2004). The present Ga saturation levels are prospective for economic extraction given that Frenzel et al. suggest a conservative cut-off concentration for profitable production of Ga from process liquor being 240 mg/L (Frenzel et al., 2016). Ga is about 25 times enriched into pregnant liquor compared to bauxite input. Even though the highest concentration of Ga was detected in concentrated spent liquor, the highest relative amount of Ga (allowing for volumetric changes from gibbsite precipitation and liquor evaporation) was found in pregnant liquor. This is because freshly leached Ga in digestion is present in pregnant liquor, while some Ga is precipitated along with gibbsite during precipitation and so removed from the concentrated spent liquor stream.

From the pregnant liquor, 68% of Ga entering the process is precipitated with aluminium hydroxide, resulting in the concentration of 85 mg/kg. This impurity, however, has no adverse effect on the quality of smelter grade alumina (Authier-Martin et al., 2001). A smaller proportion of 29% reports to bauxite residue (36 mg/kg on product-normalised basis). The mass difference between the entering and exiting portion of Ga is negligible (3%). Note that the normalised concentration of Ga in liquid fraction decreases from spent liquor to concentrated spent liquor and then to the slurry after preheating stage. In the latter, the decrease of concentration in liquid fraction is accompanied by the simultaneous increase in the solid fraction. Since this is a systematic observation occurring also in the distribution of other trace elements, it will be discussed further in the text.

For the purposes of theoretical modelling of Ga distribution, Hudson (Hudson, 1965) has indicated, and Frenzel et al. (Frenzel et al., 2016) have applied the partitioning of Ga as 35% going to bauxite residue and 65% to hydrate product (Frenzel et al., 2016; Hudson, 1965). From this analysis, the partitioning is more in line with that reported by Figueiredo et al., (2002), suggesting 30% of Ga going to bauxite residue, and 70% to hydroxide product, although Figueiredo et al., (2002) do not refer to the source of their data. This case study therefore supports the literature that suggests about 70% of bauxite Ga is digested in the Bayer process, and this part is subsequently precipitated into aluminium hydroxide. About 30% of Ga is separated from the process with bauxite residue.

Almost twice as much V is contained in the karst bauxite (336–650 mg/kg) compared to the lateritic bauxite (201–258 mg/kg). Given the different proportions of bauxites in the feed, the major input of V is therefore from karst bauxite (87%). Mass distribution of V is given based on XRF-st data since it provided considerably better fit in the mass balance model compared to ICP-MS data (**Figure 14**).

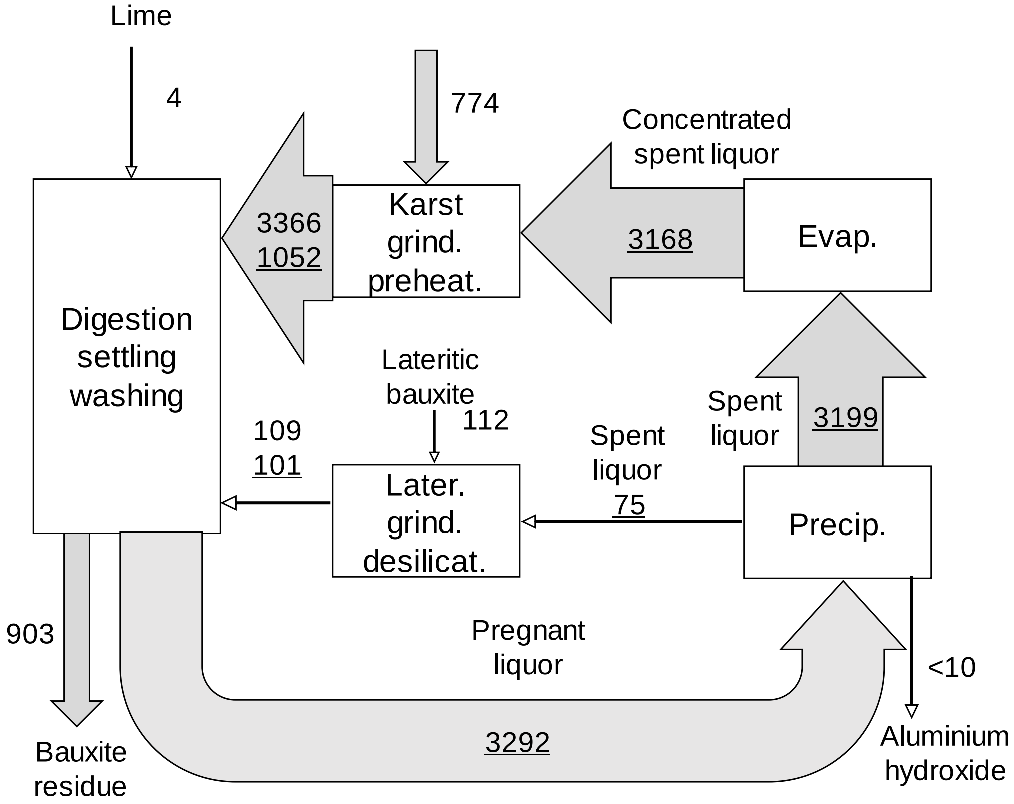

Figure 14. Mass distribution of V (mg/kg) normalised to mass of aluminium hydroxide produced, based on XRF-st and ICP-OES data.

The mass distribution of V is again mainly regulated by process liquors, where the concentration of V exceeds 400 mg/L in concentrated spent liquor. This is in accordance with the range of V saturation levels in Bayer liquors reported elsewhere in publications (100–2800 mg/L V) (Figueiredo et al., 2002; Selvi et al., 2004; Teas and Kotte, 1980; Zhao et al., 2012a). Authier-Martin et al. refer to earlier studies indicating that V is about 30% soluble during Bayer digestion (Authier-Martin et al., 2001). Compared to bauxite feed on alumina normalised basis, V is enriched in pregnant liquor up to 4 times in this study. In process liquors, V appears in the form of VO_4^{3-} (Zhao et al., 2012a). This impurity is unwanted in hydroxide and metal production due to its known property of decreasing the electric conductivity of metallic Al, causing a green hue in fused Al, and the scale it can form in the piping of a Bayer refinery when precipitated from the liquor in the cooler parts of the circuit (Authier-Martin et al., 2001; Fenerty, 1960; Zhao et al., 2012a). The removal of V from process liquors is a side benefit of process lime addition. V precipitates as calcium vanadate, as an impurity in tri-calcium aluminate ($Ca_3Al_2(OH)_{12}$), or as $Na_7(VO_4)_2F{\cdot}19H_2O$(Okudan et al., 2015; Smith, 2017; Zhao et al., 2012a). Present study as well as the regular monitoring in the plant materials did not detect any V in the aluminium hydroxide product (<10 mg/kg). Therefore, lime addition that mainly reduces soda losses among other beneficial effects, is simultaneously providing a way to remove excess V from the Bayer cycle and preventing V precipitation to product. Besides, V impurities that pass to product are more commonly related to the existence of V in the fuel used to calcine aluminium hydroxide (Teas and Kotte, 1980). In the existing case study, V is separated from the process and is accumulated in the bauxite residue.

The input of As to the system from lateritic bauxite is negligible compared to karst bauxite. Once again, the accumulation of As to the liquor-based circuit is evident, as seen from the diagram in **Figure 15**. The saturation of As to process liquor is achieved at about 130 mg/L concentration. In earlier studies, As has been detected in the alkaline liquor of bauxite residue suspension as well as in Bayer liquors (Burke et al., 2012; Teas and Kotte, 1980). Teas & Kotte have classified As as a medium soluble impurity in the Bayer process with a similar behaviour to V (Teas and Kotte, 1980), which is evident also from this case study.

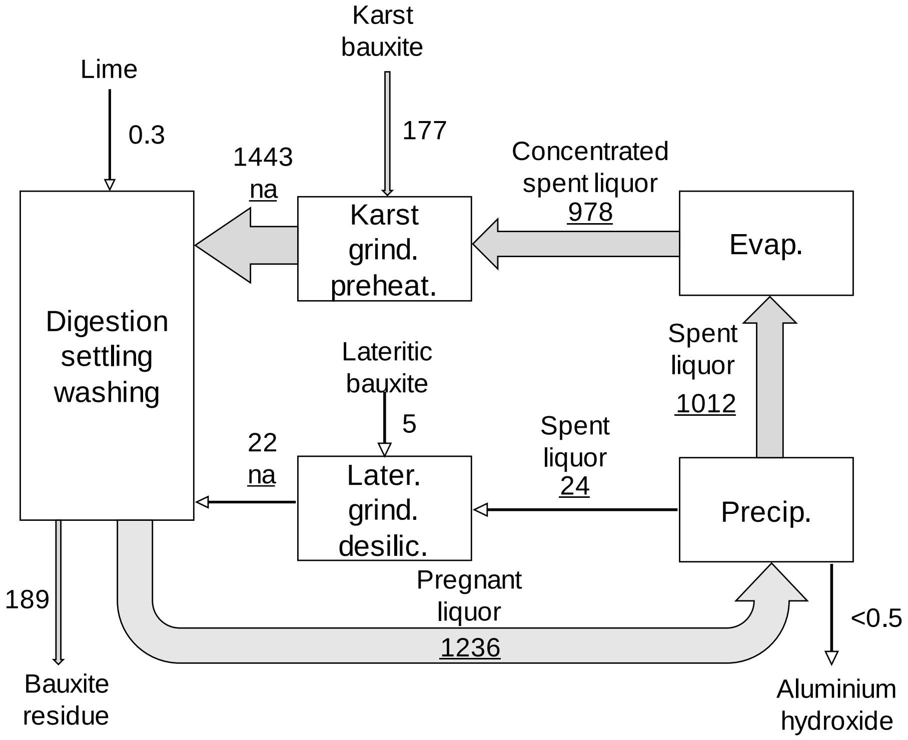

Figure 15. Mass distribution of As (mg/kg) normalised to mass of aluminium hydroxide produced, based on ICP-MS (solids) and INAA (liquors) data.

Higher than usual discrepancies in the input and output masses of As in different units are noted compared to other analysed elements. This could be an indication to the need of further developing analytical techniques relating to As in Bayer process materials. However, dissolved As must exist in the system when we observe the "karst bauxite grinding and preheating" unit. It is apparent from there that As concentration increases significantly when comparing the solids entering and exiting the unit. This implies that the entering of As to solid fraction must originate from the concentrated spent liquor. In any case, in the end of the processing cycle, all As in found in bauxite residue and in the context of available detection limits does not enter to aluminium hydroxide product (<0.5 mg/kg).

The majority of Cr input (95%) originates from karst bauxite. A minor fraction of Cr, about 1% of input, can be dissolved into process liquor giving rise to a concentration of 1.4 mg/L (**Figure 16**). During precipitation, Cr was not detected to enter product (<5 mg/kg), or it does in a very small quantity (~ 2 mg/kg), as could be suggested from difference in the balance of precipitation stage and the small deficiency (1%) of Cr mass in the output material. An earlier study has pointed out a 5 mg/kg concentration of Cr in hydroxide product (Mohapatra et al., 2012). All the quantity of Cr that entered to the process is found in bauxite residue as the sole output carrier of this metal.

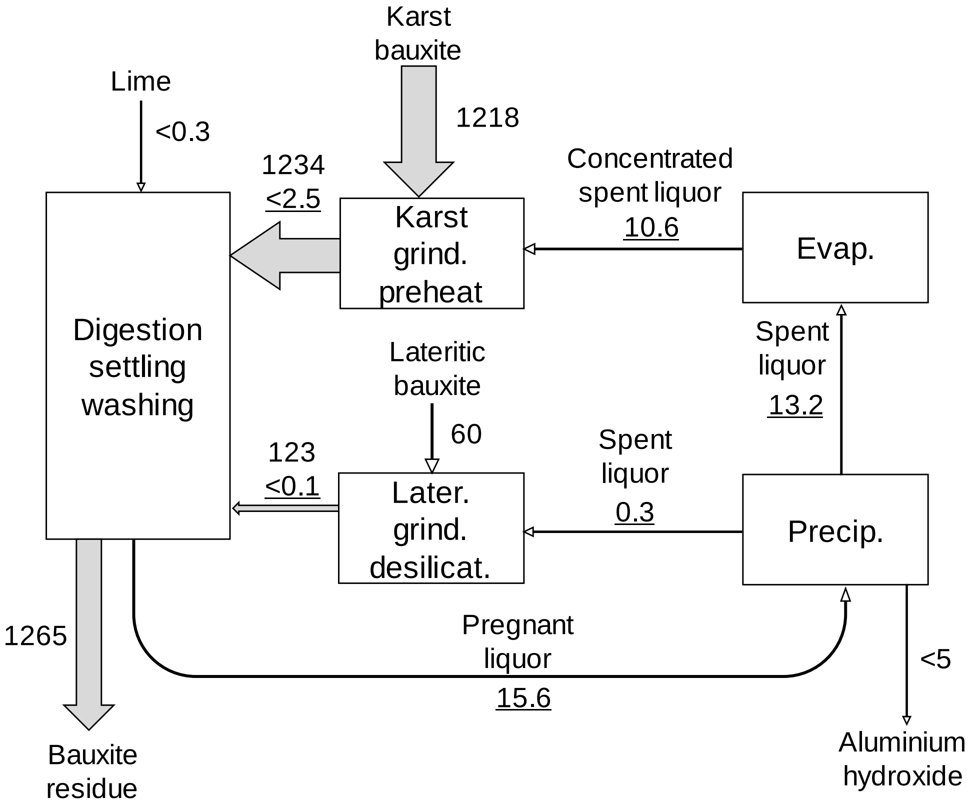

Figure 16. Mass distribution of Cr (mg/kg) normalised to mass of aluminium hydroxide produced, based on ICP-MS (solids and liquors) data.

Uranium is another bauxite trace element that occurs in bauxite deposits in very low quantities (in present bauxites 3–8 mg/kg) but is known to dissolve to some extent in Bayer liquor (**Figure 17**).

Approximately an equal quantity of product-normalised U is introduced to the process via the composition of bauxite as well as concentrated spent liquor. After digestion stage, additional quantity of U is dissolved into the liquid phase and the pregnant liquor achieves the highest level of normalised quantity (14.3 mg/kg $Al(OH)_3$). As far as the measured concentration is concerned, the saturation level of U in pregnant liquor is 1.28 mg/L, which is comparable to that reported in the literature — 1.4 mg/kg U (Sato et al., 2013). It can be therefore indicated that about one-to-one ratio of product-normalised U exists in the system when comparing the input bauxite feed and the process liquor. In the precipitation stage, approximately 8% of the initial quantity of U exits the process in the composition of aluminium hydroxide which then passes also to calcined alumina. It has been reported previously that 10% of initial U can end up in aluminium hydroxide (Sato et al., 2013). The rest of the U is separated from the system in the composition of bauxite residue, while present mass balance has a small deficiency of 4% in the end of the process when comparing the input and output solid materials. U is an unwanted impurity in certain applications of alumina, such as some electronical applications, because of its property to produce ionising radiation and the emitted alpha particles can therefore affect memory devices (Sato et al., 2013). The main controlling factor of U precipitation to aluminium hydroxide is primarily the surface area of the seed crystals and then the precipitation temperature. Therefore, increased surface area of seed and higher precipitation temperature decreases the quantity of U precipitating to hydroxide product. Another way to reduce U in product is explained to be the removal of organic compounds from the pregnant liquor (Sato et al., 2013).

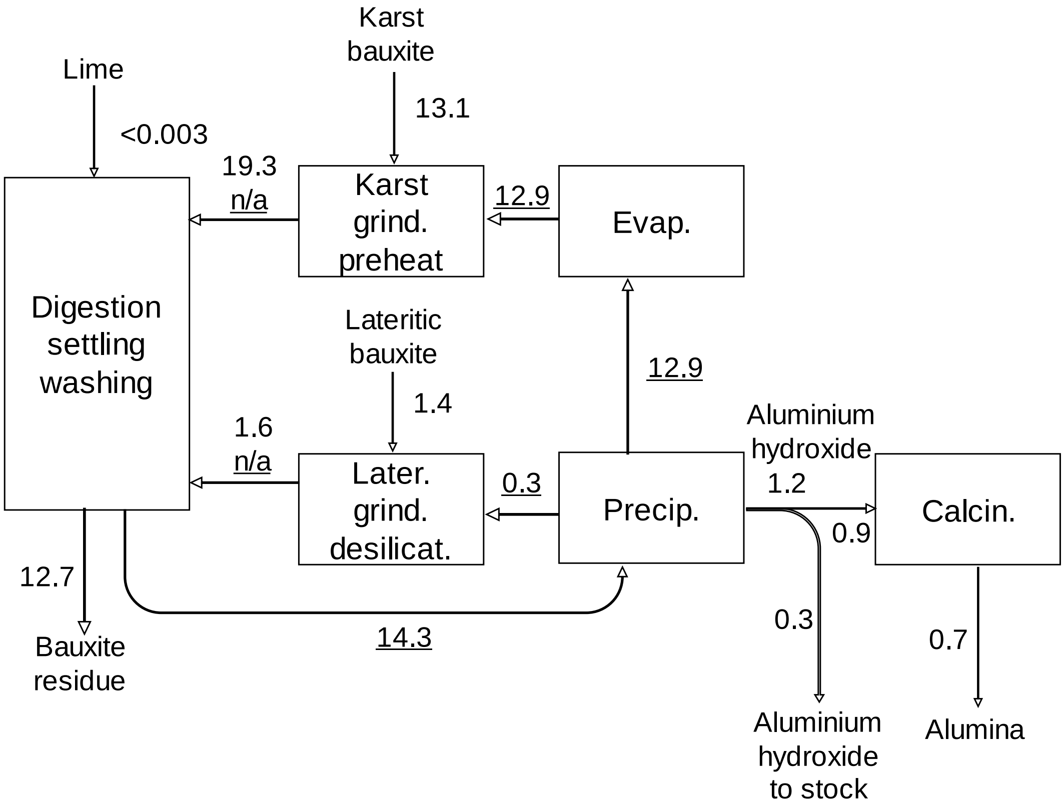

Figure 17. Mass distribution of U (mg/kg) normalised to mass of aluminium hydroxide produced, based on ICP-MS (solids and liquors) data.

In the mass balance models of Ga, V, As, Cr as well as U it can be noted that during the "karst bauxite grinding and preheating" as well as in smaller scale during "lateritic bauxite desilication", a pronounced increase in trace element concentration is observed in the solid fraction flows. This increase of trace constituents is occurring with the simultaneous decrease in concentrations in liquid flows. Thus, the trace constituents appear to precipitate during these processing phases. Probably, the trace elements precipitate in the composition of Bayer process characteristic solid phases, that are a group of Ca-, Al-, Na- and Si-containing phases, including desilication products (sodalite and cancrinite), hydrogarnet (hydrogrossular) type phases as well as calcium titanate in the form of perovskite ($CaTiO_3$) (M. Gräfe et al., 2011; Smith, 2017). Calcium vanadate or $Ca_3Al_2(OH)_{12}$ are already known species that contain V in Bayer process specific solid phases (Smith, 2017; Zhao et al., 2012a). As mentioned before, lime addition position on the schemes is a simplification and it is added in more processing steps, including the preheating, thus the possibility of forming Ca-containing species is not limited to the digestion stage. Therefore, during the preheating stage, the trace elements occurring in the spent liquor (Ga, V, As and Cr) are thought to precipitate in the composition of Bayer process characteristic solid phases. While this effect occurs, the trace element concentration in the liquid fraction decreases and in the solid fraction increases. At the same time, the mass balance equilibrium of the trace elements is maintained. During digestion, the pregnant process liquor becomes saturated again in the trace elements on the account of leaching of the newly added bauxite feed.

Another characteristic that can be observed from the mass distributions of Ga, V, As and Cr is that their product-normalised content shows a decreasing trend from pregnant liquor to spent liquor and then to concentrated spent liquor. Only for Ga it is evident that part of its mass is removed from the liquor during precipitation. Since it is observed in the distribution patterns of all the named trace elements, it can be concluded being a systematic behaviour. The working hypothesis is that minor deposition of the trace constituents occurs throughout the mentioned production steps in the form of secondary precipitates or solid formations like scales in the cooler parts of piping or in the solids of filter cakes (e.g. from security filtration of pregnant liquor, "liquor polishing") (Bánvölgyi, 2016; Lavalou et al., 1999; Teas and Kotte, 1980). Like already mentioned, some trace elements (Y, Nb, Zr) have been detected in perovskite-based scales in the Bayer circuit (Zhong-Lin and Song-Qing, 1995). Enhanced concentrations of trace elements like Ni, Cr and V in the range of 700–4900 mg/kg were detected in perovskite-dominated matrix of a scale sample formed in the AoG's digestion autoclave. The cancrinite-dominated matrix of the same sample was, however, relatively depleted in trace elements (e.g. 140–170 mg/kg V) (Vind et al., 2017a). Sometimes, enhanced concentrations of V (112 mg/kg) and Ga (28 mg/kg) have been identified in the alumina dust from calciner electrostatic filters, making this material an attractive source of V and Ga (Gladyshev et al., 2015). The former examples therefore support the hypothesis that a proportion of trace elements is deposited to minor by-products of the Bayer process. Scales, filter cakes and electrostatic filter dust are regularly cleaned during the production. The volumes of these materials being created are not easily quantifiable, but an assumption can be made that the decrease in the trace element concentrations in the liquor stream can account to the passing of the trace elements to the formerly mentioned minor by-products of the Bayer process as result of the described systematic behaviour.

For the previously discussed elements (Ga, V, As and Cr), it can be concluded that they first accumulate to Bayer process liquor (although Cr in very small extent) and once their saturation level in liquor is achieved, their input and output flows equilibrate. Minor output of those trace elements probably occurs into minor Bayer process by-products from the liquor-based circuit as the concentrations in liquors drop systematically in the consecutive production steps.

4.2 Metals that do not Accumulate to Liquor

Distribution of Ce is presented as the representative of LREE elements due to its highest concentration in analysed materials and good analytical stability (**Figure 18**, Appendix A Table A1). The rest of the mass balances of REEs can be found in Appendix A, Tables A5 and A6. The input of Ce from lateritic bauxite is practically insignificant and almost the sole source of it is karst bauxite. Cerium distribution is dictated by solid materials only. On the "white side" of the Bayer process, all the analysed concentrations of Ce are below detection limits (aluminium hydroxide <3 mg/kg, process liquors <0.04 mg/L). Ce content remains steady from bauxite to intermediate suspension solid fraction and then to bauxite residue. In the end of the process, there is only 1% difference in the input and output quantities.

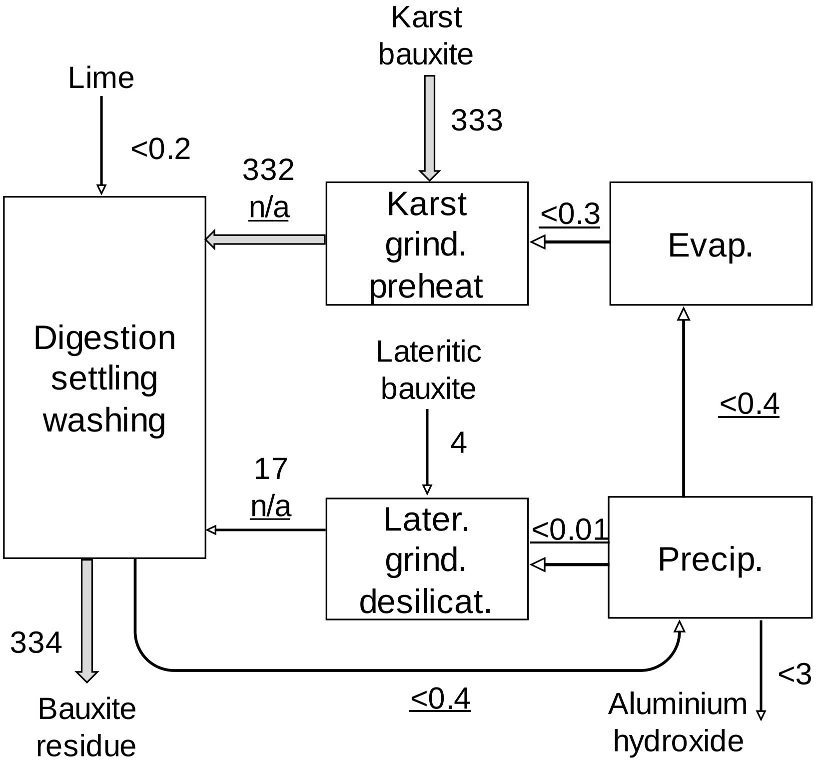

Figure 18. Mass distribution of Ce (mg/kg) normalised to mass of aluminium hydroxide produced, based on INAA (solids) and ICP-MS (liquors) data.

The distribution of Y is presented as the representative of HREEs given its highest concentration among this group of elements (**Figure 19**). Except for the quantities, the distribution of Y is identical to the one of Ce. In all processing stages, its distribution follows the solid materials and Y does not dissolve in the process liquor and thus does not enter to aluminium hydroxide product. The difference in the quantity of input and output of Y (4%) is higher than for most of the REEs, but still acceptable for presenting its mass balance model.

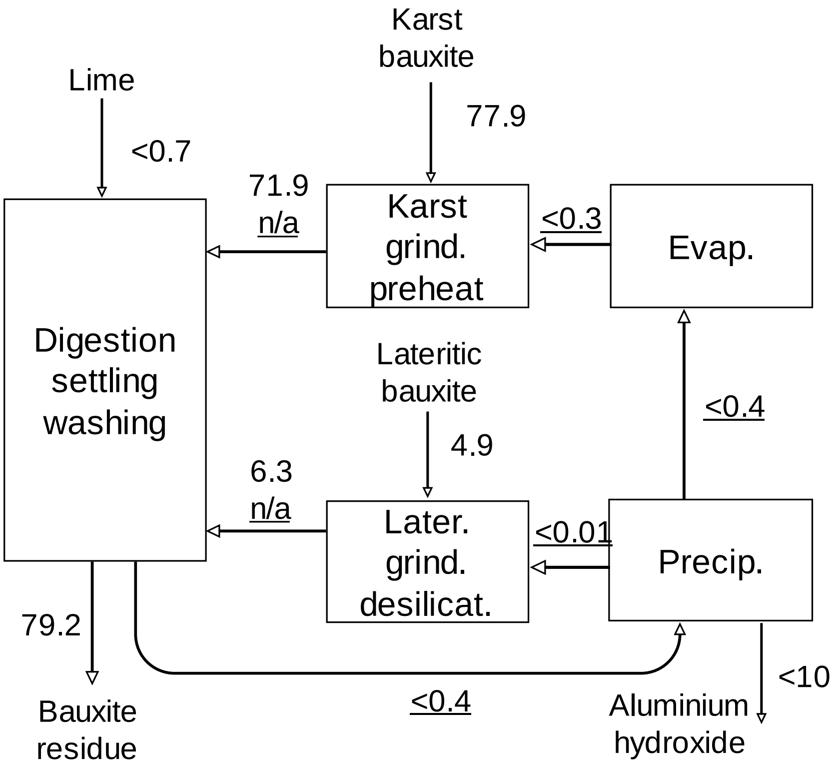

Figure 19. Mass distribution of Y (mg/kg) normalised to mass of aluminium hydroxide produced, based on ICP-MS (solids and liquors).

The distribution of Sc is presented in **Figure 20**. Note that the concentrations of Sc were analysed by INAA method.

Suss et al. (2017) report that Sc is expected to occur in dissolved form during Bayer digestion, but, it probably precipitates rapidly in an unknown form that might be ScO(OH) or $Sc(OH)_3$ (Suss et al., 2017). The progression of Sc through the process is once more regulated by solid material matrix from bauxite to intermediate solids and then to residue. There is no missing quantity of Sc in the end of the cycle. Present result is slightly different from previous results of Sc distribution patterns, where 0.6–1.5 mg/kg bauxite-feed-normalised concentration of Sc was detected in aluminium hydroxide products in Alumina Plant of Urals and Bogoslovski Alumina Plant (Derevyankin et al., 1981). It can be noted, though, that the processing conditions between the Russian alumina plants and AoG are different, since the former also partly included sintering of the bauxite ore, although it was not performed for the total amount of bauxite feed.

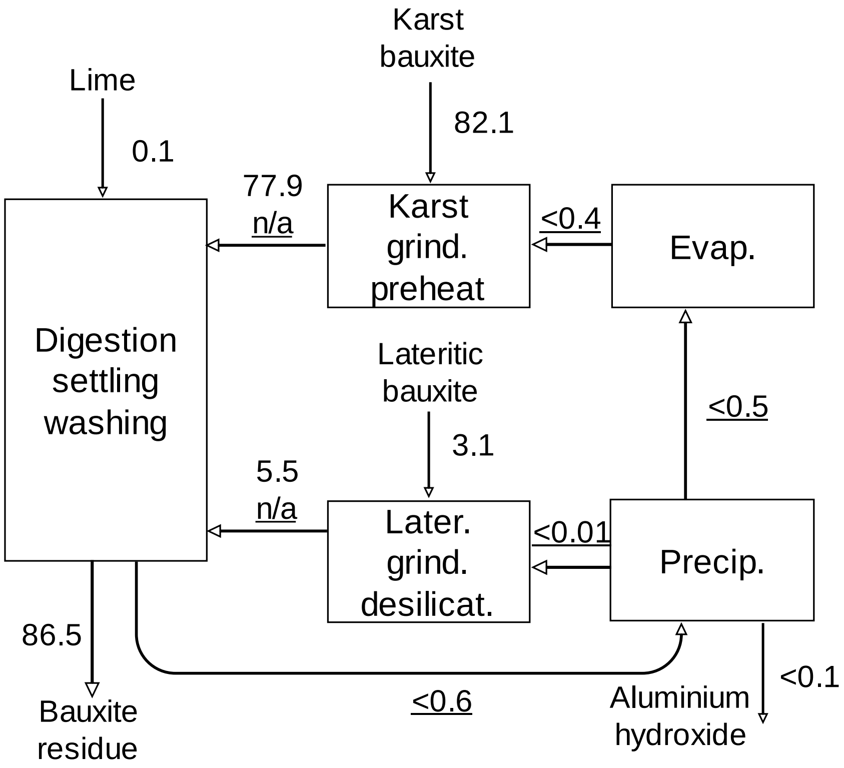

Figure 20. Mass distribution of Sc (mg/kg) normalised to mass of aluminium hydroxide produced, based on INAA (solids and liquors).

Analogously to the REEs, the transportation of Th through the Bayer process takes place in the composition of solid mineral matrix so that Th is found only in the "red side" of the process (**Figure 21**). This is in accordance with previous studies that considered the fate of radioactive elements in the Bayer process. However, the publication did not discuss the behaviour of Th further than reporting its concentration in Bayer process materials, because no ionising radiation related to Th was detected in the hydroxide product (Sato et al., 2013). Practically all Th is recovered in bauxite residue and the measured mass balance model has an insignificant 1% of Th mass loss.

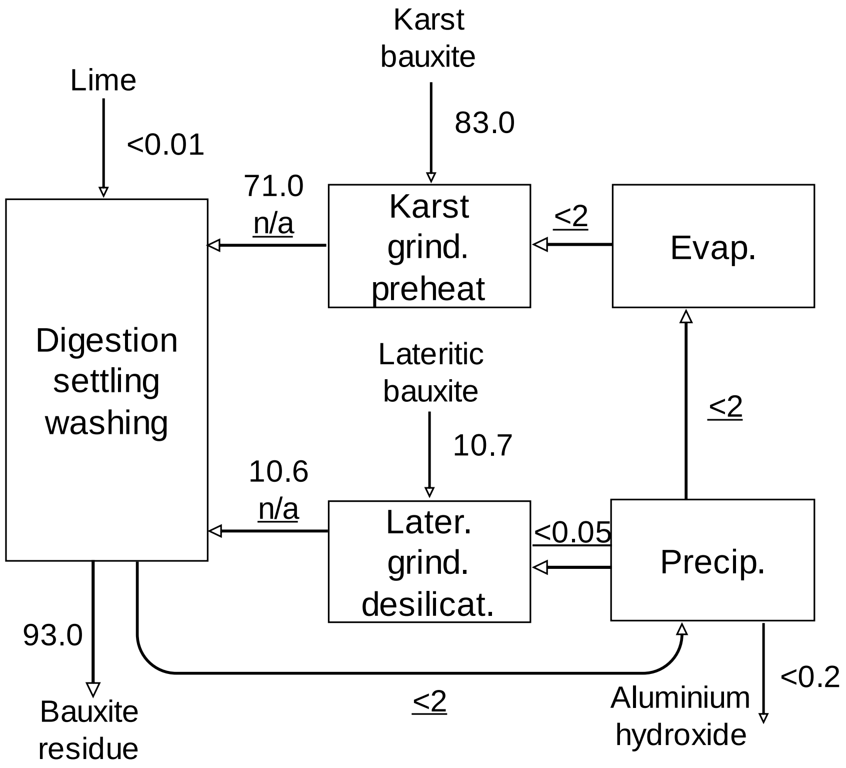

Figure 21. Mass distribution of Th (mg/kg) normalised to mass of aluminium hydroxide produced, based on ICP-MS data (solids and liquors).

For most the REEs, Sc as well as for Th distribution, a deficiency in the mass balance in the output of limestone separation HMS unit is noted (-8% on average). This can be regarded as a problem of material representativeness. However, since this is a pre-processing step, it does not affect the mass balance models of the Bayer process.

Besides the REEs distributions presented graphically (**Figures 18–19**), all the mass balance inventories of the REEs (except for Tb, Ho and Tm due to low concentrations) are available in the compiled dataset (Appendix A, Tables A5 and A6). Even lutetium (Lu), the last chemical element in the lanthanides group, mass balance was possible to be quantified given the very low detection limit available in INAA method for this element (**Figure 22**). The data shows consistently that all the analysed REEs behave similarly during bauxite processing and at least 95 % of the REEs entering to Bayer process are transferred in the composition of solid matrix to bauxite residue. Even more, in most of cases the transfer rate of REEs to bauxite residue is more than 98 %. None of the REEs or Sc enter to aluminium hydroxide, following the available detection limits, e.g., La <0.5 mg/kg, Sm <0.1 mg/kg or Sc <0.1 mg/kg (Appendix A Table A2). The fact that REEs and Sc are transferred to bauxite residue only in the composition of solid material is also supported by mineralogical studies. Present thesis explains (Paragraph 1), that the form of Sc occurrence mainly in the composition of hematite remains the same after bauxite processing. On the other hand, the precursor REE phases found in bauxite are affected by the Bayer process conditions and REE ferrotitanate type compounds are created, but the transformations taking place seem to occur in situ on mineral grain surfaces without the dissolution of the precursor REE phases (Paragraph 6). Present case study was not able to repeat the result that up to 5 % of total La content can be passed to aluminium hydroxide product (Derevyankin et al., 1981). This difference can be again explained by the differences between the operational conditions of refineries, as mentioned above. It can be noted, however, that low La presence has been semi-quantitatively found in some 2 w/v% aluminium hydroxide suspensions (Chemtrade Rehydragel® LV and SPI Pharma Aluminum hydroxide wetgel VAC 20; 0.14 and 0.72 mg/L La, respectively) that are used as adjuvants in vaccines by applying very sensitive ICP-MS techniques. At the same time, the concentrations of Ce, Nd and Sc were below detection limits, <0.0005 mg/L, <0.002 mg/L and <0.01 mg/L, respectively (Schlegl et al., 2015).

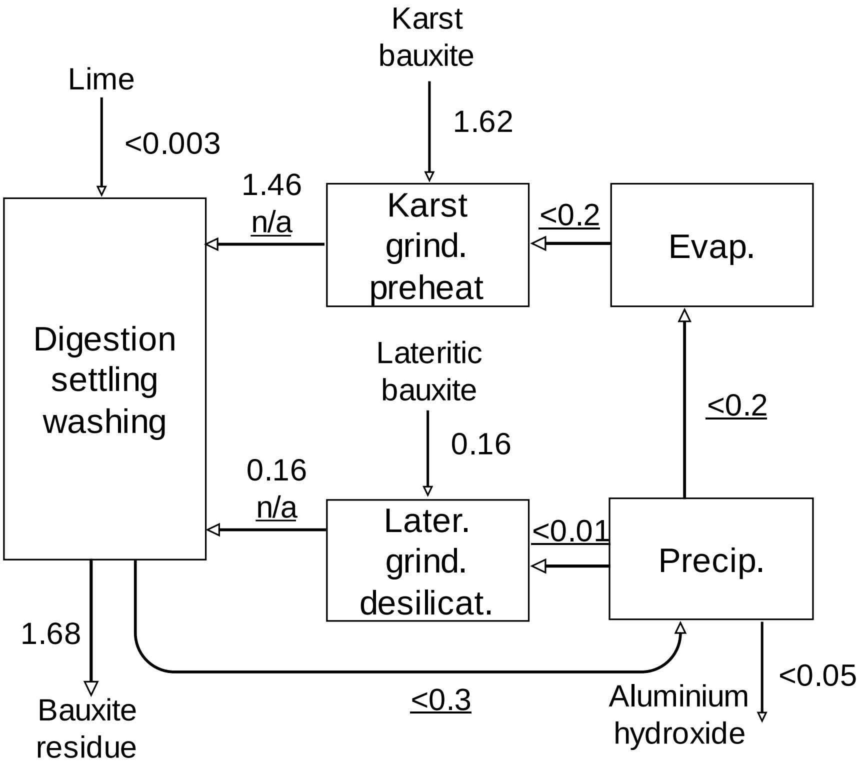

Figure 22. Mass distribution of Lu (mg/kg) normalised to mass of aluminium hydroxide produced, based on INAA (solids and liquors).

Inconsistencies in the mass balance of some REEs such as Ce can be noted in the “lateritic bauxite grinding and desilication” unit (**Figure 18**). Such situation is best explained with the possibility that during sampling, some contribution of the other lateritic bauxite from Ghana was also present in the lateritic bauxite slurry. Presently sampled Ghanaian bauxite contains higher concentration of REEs and Sc compared to the existing Brazilian bauxite and by hypothetically replacing the two bauxites in the mass balance calculation resolves the inconsistency. However, in broad sense this discrepancy is not an issue because total input and output flows are well in acceptable balance and besides, the input of REEs and Sc from lateritic bauxites has a minor magnitude regardless of the two lateritic bauxite types.

4.3 Fractionation Indexes and Systemic Predictions

All the analysed elements except for Ga are enriched by more than a factor of two to bauxite residue. This can be emphasised by calculating the fractionation indexes by dividing trace element concentration in bauxite residue with the same parameter in the bauxite feed (**Figure 23**). The fractionation indexes of all the elements except for Ga are like the (1) ratio of bauxite feed mass to bauxite residue mass created during sampling period (2.33), (2) fractionation index of Fe_2O_3 during sampling period (2.34), and (3) fractionation index of Fe_2O_3 during one-year period (2.31). Iron oxide fractionation index is considered for a comparison here because it represents a largely inert oxide in the Bayer process, as well as because it has been used for a similar comparison before (Feret and See, 2010). All the indexes of trace elements (except Ga) differ from the three major indexes by a maximum of 6% and for most of cases less than 2%. The differences are essentially negligible and probably account for errors in sample representativeness and/or analytical variations. This similarity of indexes is well-reasoned, because raw-material-to-residue ratio or Fe_2O_3 fractionation index set a logical boundary, what can be the maximum possible fractionation index of a constituent in the process. Basically, new material cannot be created during the process and if the constituent does not fraction to aluminium hydroxide product, then the fractionation index must be like the one of Fe_2O_3 or the bauxite-feed-to-residue coefficient. Present result is similar to what was concluded in lab-scale testing of trace element enrichment from bauxite to bauxite residue, although higher variations were noted in lab testing (Feret and See, 2010).

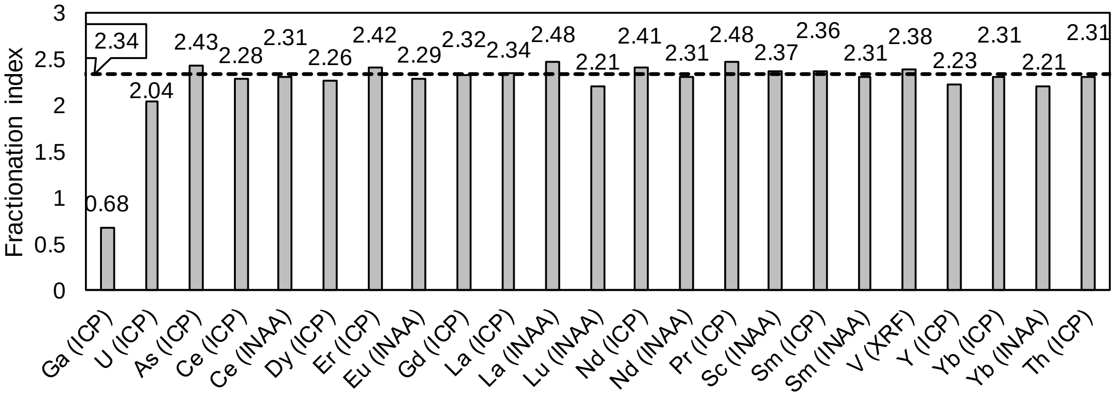

Figure 23. Fractionation indexes of trace elements calculated as trace element concentration in bauxite residue divided by trace element concentration in bauxite. Fractionation indexes are compared to the one of Fe_2O_3 during sampling period (horizontal dashed line).

The former reasoning provides opportunities for predicting the trace element concentrations in bauxite residue based on existing information about bauxite feed. First option is based on Fe_2O_3 concentration in bauxite and bauxite residue, as shown in **Equation 3**. It is not uncommon, that the conditionally inert Fe_2O_3 is used as an aid in mass balance estimations relating to the Bayer process (Santana and Tartarotti, 2012; Sato et al., 2013).

$$C_{BR} = \frac{C_{Fe\_BR}}{C_{Fe\_BX}} \times C_{BX}, \qquad \textbf{Equation 3}$$

Where: C_{BR} Predicted concentration of trace element in bauxite residue, mg/kg;

C_{Fe_BR} Fe_2O_3 concentration in bauxite residue, %;

C_{Fe_BX} Fe_2O_3 concentration in bauxite, %;

C_{BX} Average concentration of trace element in bauxite feed, mg/kg.

Another option is to consider just the mass flows of bauxite feed and the resulting residue created, as shown in **Equation 4** and combine it with trace element concentration in bauxite feed. In any case, care must be taken on the representativeness of the bauxite trace element concentration values, because considerably high variations can occur in some bauxite deposits (Ochsenkühn-Petropulu et al., 1994).

$$C_{BR} = \frac{M_{tot\_BX}}{M_{tot\_BR}} \times C_{BX} \qquad \textbf{Equation 4}$$

Where: C_{BR} Predicted concentration of trace element in bauxite residue, mg/kg;

M_{tot_BX} Total dry mass of bauxite fed into system (t);

M_{tot_BR} Total dry mass of bauxite residue leaving the system (t);

C_{BX} Average concentration of trace element in bauxite feed, mg/kg.

The **Equations 3** and **4** can be used only for the trace elements which do not fraction to aluminium hydroxide product, therefore it is not applicable for such metals as Ga or U.

4.4 Trace Elements Distribution in Minor By-Products (Scales, Filtered Solids)

It is well known that scales can be formed in several parts of the Bayer plant piping and tanks. These are unwanted materials, because they can cause clogging and other negative effects like bad heat transfer during the production of alumina (Bánvölgyi, 2016; Zhong-Lin and Song-Qing, 1995). However, from research perspective, scales can be considered as useful materials in the investigation of several phenomena relating to the Bayer process, for example for specifying parameters of Bayer process derived secondary minerals or the mechanisms of scale formation (Bánvölgyi, 2016; Kawashima et al., 2016). The composition of scales can be very diverse and include several Na, Al, Si, Ti and Fe oxide and hydroxide phases as well as phosphates in crystalline or amorphous form. Scaling mechanisms are complex and include multiple reaction steps. Commonly, aluminium hydroxide-based scales are found in precipitators. DSP-based scales are found in pre-desilication units, preheaters, digesters and evaporators. Calcium titanate predominant scales are more often related to preheaters and digesters in the high temperature processes. In relation to trace elements, it has been reported that some amounts of Zr, Y and Nb (concentrations not reported) have been found in calcium titanate scales, implying the isomorphous substitution of these metals into calcium titanate structure (Zhong-Lin and Song-Qing, 1995). In addition to scales, other minor by-products of the Bayer process have been examined to propose new alternative material flows for recovering minor metals like Ga and V from alumina dust accumulated to electrostatic filter or V from secondary precipitates (Gladyshev et al., 2015).

Based on the former indications relating to trace elements in such materials, it was investigated, whether any minor Bayer process solid could act as a sink or a point of accumulation for trace elements. In addition, indications to the mineralogy of trace elements in relation to Bayer process specific solid phases were examined. Samples were collected from both the “red side” as well as “white side” of the process. Generally, sections prone to scaling as well as filters are cleaned regularly in the plant or upon need. Calciner dust accumulated in electrostatic filter is not a by-product in the sense that it is usually recycled in electrolysis plant along with calcined alumina, if it meets the required quality, or is fed again to calcination. The following materials were sampled to fulfil present sub-task:

(1) evaporator scale from Escher-Wyss evaporator, divided into two sub-samples based on colour hue (white and red);

(2) digester autoclave scale, line 1, digester no. 9;
(3) precipitation tank scale;
(4) solid cake from security filtration of pregnant liquor (“polishing”), after settling and washing;
(5) dust from calciner electrostatic filter.

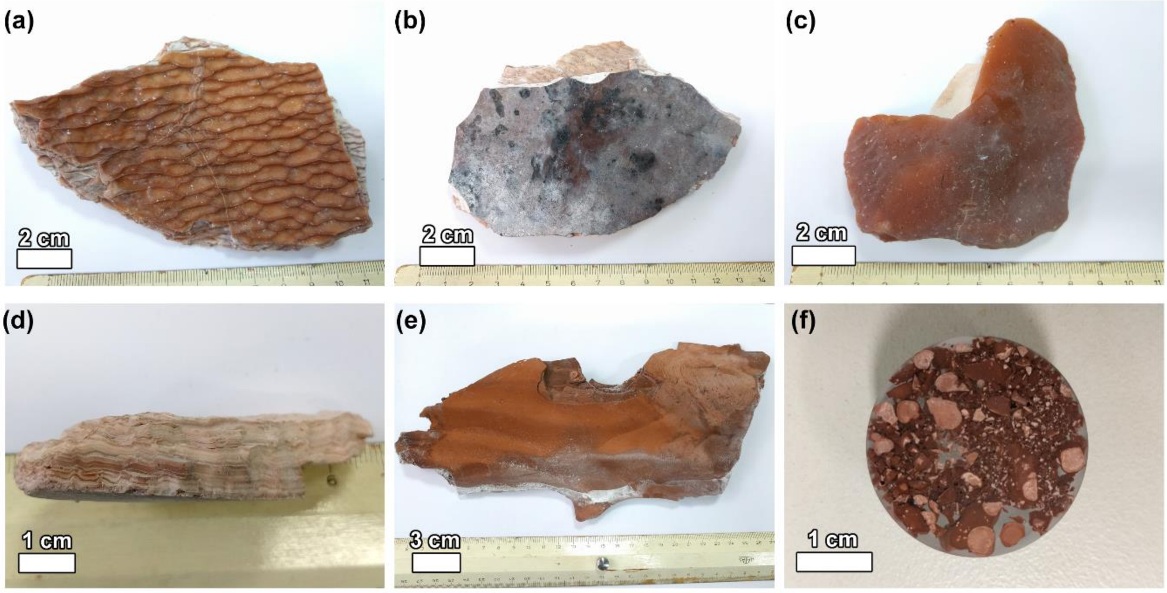

Figure 24. Macroscopic photographs of minor by-products: (a) evaporator scale shown from the side that has been in contact with process liquor, (b) evaporator scale shown from the side that has been in contact with the plant tubing, (c) fragment of the red fraction of evaporator scale, (d) cross section view of the white fraction of evaporator scale, (e) digester autoclave scale, and (f) solids from security filtration embedded in resin (prepared for microscale analysis).

Minor by-products are characterised by high concentrations of Al_2O_3 and Na_2O, except for alumina dust and precipitator scale which do not and are not expected to contain a notable quantity of Na_2O (**Table 9**). In addition, materials deposited as scales tend to have a high concentration of SiO_2. This is because dissolved silica and its depositions as DSP in Bayer circuit is one of the main reasons of scale formation in Bayer process (Bánvölgyi, 2016). The most diverse chemical composition is noted in the scale collected from digester autoclave. In addition to Al_2O_3 and Na_2O, it contains also Fe_2O_3, TiO_2, CaO as well as SO_3. This is because during bauxite digestion, many reactions take place and due to the saturated state of the Bayer liquor, lower temperature near the digester wall and a lower flow rate, several compounds deposit on the digester walls (Bánvölgyi, 2016; Whittington, 1996; Zhong-Lin and Song-Qing, 1995). Sulphur trioxide content in the scale samples is explained by the fact of the partial dissolution and accumulation of sulphur compounds to Bayer liquor. In scales, sulphate ions are captured commonly to the composition of cancrinite and/or sodalite due to the ability of these phases to incorporate anions like Cl^-, SO_4^{2-} and CO_3^{2-} into their lattice (Whittington, 1996). Security filtration solids have the highest concentration of CaO, because of the usage of lime as a filter aid (Whittington, 1996). It is an expected conclusion that alumina dust as well as scales from precipitator are mainly composed of Al_2O_3, and other major oxides occur as minor impurities in these materials.

In calciner dust, 96.2% of particles are <106 µm and 53.0 % of particles are <45 µm. For a comparison, calcined alumina has only 9.2% of the particles <45 µm, thus the categorisation of this material as „dust."

Table 9. Main oxide composition of minor Bayer process by-products (in wt%).

Oxide	Digester scale	Evaporator scale		Security filtration solids	Calciner dust	Precipitator scale
		white	red			
Al_2O_3	25.77	29.93	31.16	27.13	92.85*	66.72*
Fe_2O_3	7.55	0.17	0.18	2.07	0.0121	0.105
SiO_2	25.60	33.19	32.48	1.53	0.0094	0.194
TiO_2	4.39	0.02	0.02	0.32	0.003	0.011
CaO	3.67	0.07	0.06	25.20	0.0161	0.146
Na_2O	19.67	24.11	23.92	15.47	0.2957	0.3977
SO_3	4.30	3.68	2.75	0.13	<0.006	0.015
MgO	0.40	0.20	0.17	0.31	-	-
K_2O	0.44	0.60	0.57	0.71	0.0069	0.016
MnO	0.02	0.01	0.01	0.01	<0.0017	<0.0017
P_2O_5	0.02	0.01	0.01	0.08	<0.0012	<0.0012
LOI	7.79	8.59	9.21	25.48	6.80	32.40
Total	99.62	100.58	100.54	98.44	100.00	100.00

*calculated

Mineralogically, scales are mainly composed of cancrinite and sodalite (76–99%), i.e. DSPs (**Table 10**). Like the chemical composition, also the mineralogical constituents of digester scale are diverse, including perovskite, hematite and hydrogarnet. Security filtration solids are composed of hydrogarnet, portlandite and bayerite, but it was not feasible to quantify these phases due to complex diffraction patterns and deviations from available reference patterns. The dominating contents of Al_2O_3, Na_2O and SiO_2 are consistent with the prevailing presence of hydrogarnet. Precipitator scale as well as calciner dust are mainly composed of gibbsite, while for precipitator scale this is practically the only mineralogical phase. Calciner dust phase composition indicates that aluminium hydroxide in this material has been calcined only to a minor extent, given the low corundum concentration of 9%. Two fractions of evaporator scale, white and red, differ mainly with the very low content of hematite and diaspore in the red fraction, that do not occur in white fraction. The red hue of this sample can be thus attributed to the small presence of hematite. Because there were no other considerable differences in these two fractions, and the chemical composition was also very similar, only the white fraction of evaporator scale was subjected to further trace element analysis.

Table 10. Mineralogical composition of minor Bayer process by-products (in %). For security filtration material, only relative abundance is indicated.

Phase	Evaporator scale	Evaporator scale	Digester scale	Calciner dust	Security filtration	Precipitator scale
	white	red				
Cancrinite	88	85	74			
Sodalite	11.5	11	2.5			
Hematite		0.2	6.5			
Diaspore		1	1.5			
Boehmite				3		
Gibbsite			0.7	85		98
Bayerite					+	
Corundum				9		
Portlandite					++	
Perovskite			7.5			
Hydrogarnet			4		+++	
$Na_2SO_4 \cdot 10H_2O$			3.5			
$Ca_4Al_2O_6(SO_4) \cdot 14H_2O$				2		2
Total	99.5	97.2	100.2	99		100

General microstructure of the minor by-products is shown in **Figure 25**. Both analysed evaporator scale sub-samples have a homogeneous microstructure composed of cancrinite/sodalite matrix (**Figure 25** a and b). The difference is that in white scale (a), the crystal morphology is fibrous and for red scale (b), it is rather massive and compact. The scale from digester autoclave (**Figure 25**, c) is composed of finely intergrown crystals of cancrinite/sodalite and perovskite with sporadic individual Fe oxide particles that appear as bright spots in the backscattered electron image. Solid material from security filtration (**Figure 25**, d) is the only minor by-product, where discrete mineral particles exist that contain considerable content of bauxite trace elements, namely Cr. Within the very fine matrix of the filtered material composed mainly of hydrogarnet and portlandite phases occur the particles with the presence of Fe, Cr and Mn. From the previously known observations of bauxite it can be suggested that these particles could possibly be grains of chromite (Laskou, 2001). The presence of Cr-containing grains in this sample is in accordance to the bulk analysis of the security filtration solids (186 mg/kg Cr, **Table 11**). The microscopic view of calciner dust is dominated by crystals of gibbsite and corundum grains (or other forms of Al_2O_3) can be discerned more scarcely (**Figure 25**, e). The two phases can be distinguished from each other by the difference in relative brightness level, because brightness level in the backscattered electron imaging mode corresponds to the weight of atoms, and gibbsite contains crystalline water that makes the particles to appear relatively darker. The morphology of electrofilter dust particles is irregular with several different shapes and fractured particles (compare with **Figure 12** that depicts alumina and aluminium hydroxide). On the second image of calciner dust (**Figure 25**, e) are shown prismatic or elongated particles that are uncommon for both aluminium hydroxide and calcined alumina products (compare with **Figure 12**). The formation of elongated prisms during aluminium hydroxide crystal formation has been linked with the presence of organic compounds, they can also grow from potassium aluminate solutions or can be caused by other factors (Sweegers et al., 2001).

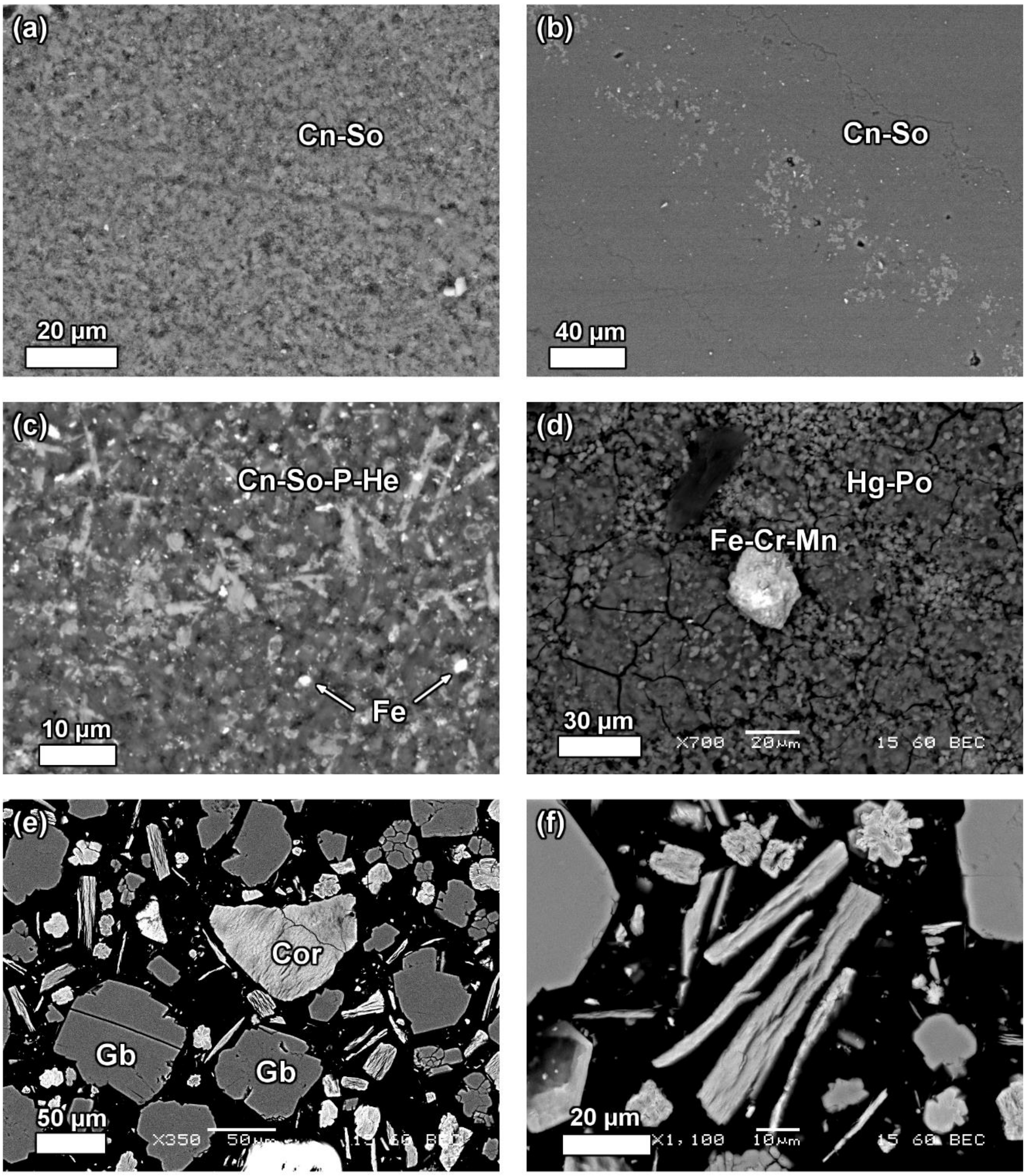

Figure 25. Microstructure of Bayer process minor by-products shown in BSE images: (a) white evaporator scale, (b) red evaporator scale, (c) digester scale, (d) security filtration solid material with Fe-Cr-Mn particle in the middle, (e) calciner electrofilter dust overview image, and (f) elongated particles of calciner dust that are irregular compared to aluminium hydroxide or calcined alumina. Abbreviations: Cn — cancrinite, So — sodalite, P — perovskite, He — hematite, Hg — hydrogarnet, Po — portlandite, Gb — gibbsite, Cor — corundum (or other forms of Al_2O_3).

Some areas of digester autoclave scale are particularly intergrown with calcium titanate crystals, as can be seen in **Figure 26**. From the XRD analysis it is known that calcium titanate in this sample corresponds to perovskite. It appears that acicular and dendritic perovskite crystals have been formed into a matrix of Na, Al and Si, corresponding to cancrinite and/or sodalite, also known from XRD. The formation of perovskite as seen in this scale sample likely corresponds to the reaction mechanism, in which titanium dioxide (especially anatase) phases react with Bayer liquor and lime under high temperature digestion conditions. As a result, perovskite crystals form from the dissolved Ti and Ca ions (Smith, 2017). Presently observed morphology of perovskite clearly indicates to the deposition of the newly formed phase from dissolved Ca and Ti ions. Perovskite also contains a small amount of Mg. Some Al also occurs as individual spots that could be undigested particles of diaspore or boehmite. The presence of Fe is mainly seen as individual spots in its distribution map. This is in accordance with the previous reports that Fe occurs in digester scales mainly as entrapped Fe particles that were formerly suspended in digestion suspension (Bánvölgyi, 2016). However, a part of Fe is also found in the composition of perovskite, which is in accordance with the perovskite composition quantification further in the text (**Table 12**). This implies to partial incorporation of dissolved Fe into perovskite composition.

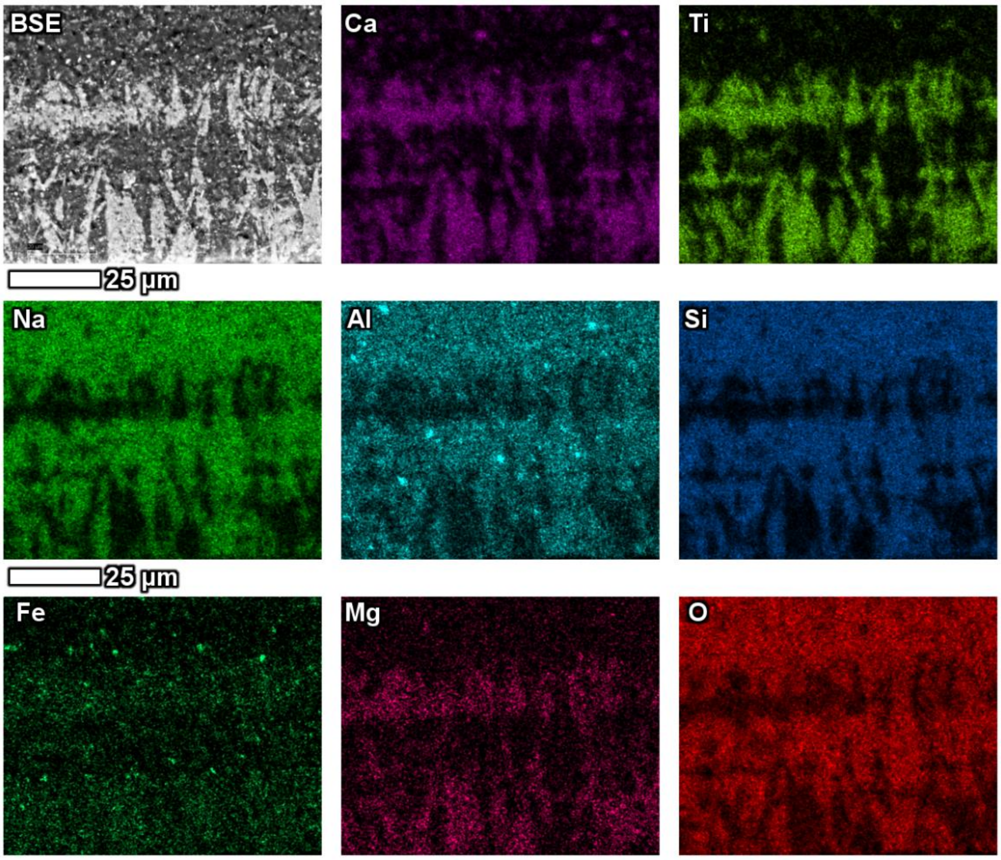

Figure 26. SEM-EDS elemental mapping of digester autoclave scale, where calcium (ferro)titanate (perovskite) crystals have intergrown into Na-Al-Si matrix, corresponding to cancrinite/sodalite.

Trace element concentrations in Bayer process minor by-products are given in **Table 11**. Higher trace element concentrations are associated with the „red side“ (represented by materials like digester scale or security filtration solids, for terminology refer to paragraph 1.2) of the Bayer process, represented here by digester scale and security filtration solids. To the „white side“ (represented by materials evaporator scale, calciner dust or precipitator scale) of the process can migrate such metals like Ga, V and Cr that have been identified to occur in dissolved form in Bayer liquor and can deposit further in the composition of precipitator scale, calciner dust and evaporator scale (section 4.1). Other metals like the REEs, Th and Sc don’t migrate to the “white side” of the process because of their limited or absent property of dissolving in processing liquor (section 4.2). Thus, it can be assumed that their presence in digester scale and security filtration solids could be controlled by deposition and/or capture of very fine solid particles.

Table 11. Trace element concentrations in minor Bayer process by-products (mg/kg).

Analyte	Method	Digester scale	Security filtration	Evaporator scale (white)	Calciner dust	Precipitator scale
As	INAA	39.3	-	10.3	-	-
Ce	ICP-OES/MS	76 ± 0	275 ± 4	<20	-	-
Ce	INAA	79	-	<3	-	-
Cr	XRF	256	123	-	-	-
Cr	ICP-OES	398 ± 4	186 ± 1	<40	47 ± 0	-
Cr	INAA	376	-	33	-	-
Ga	ICP-OES	92 ± 1	302 ± 2	58 ± 0	95 ± 0	69
La	ICP-OES	65 ± 0	51 ± 1	<50	<25	-
La	INAA	22.9	-	<0.5	-	-
Nd	ICP-OES/MS	25 ± 1	<50	<20	<25	-
Nd	INAA	5	-	<5	-	-
Sc	INAA	19.7	-	0.2	-	-
Sm	INAA	3.5	-	0.1	-	-
Th	INAA	12.1	-	<0.2	-	-
U	INAA	6.2	-	0.6	-	-
V	ICP-OES	225 ± 1	143 ± 3	82 ± 2	<10*	<10*
Y	ICP-OES/MS	25 ± 0	65 ± 1	<20	-	-
Yb	INAA	3.0	-	<0.2	-	-

* based on standardised XRF

In the cake from the security filtration is found the highest concentration of Ga across all sampled solid materials (302 mg/kg Ga) relating to Bayer process. This is about five times higher than in bauxite, three times higher than in alumina, and comparable to the concentration of Ga in Bayer liquor. Since the material under discussion is mainly composed of hydrogarnet, it can be assumed that this mineralogical phase might capture dissolved Ga^{3+} to its composition by isomorphously substituting Al^{3+}, given the notable similarity of these metals (Gray et al., 2013; Shaw, 1957). In aluminium hydroxide analysed in present work, Ga concentration is much lower (85 mg/kg), thus the property of gibbsite to include Ga to its composition might be lower than that of hydrogarnet. Also, the use of lime as a filter aid in security filtration might facilitate the more intense precipitation of Ga compared to other parts of the Bayer process. Ga is also present in evaporator scale (58 mg/kg), where its concentration is higher than in bauxite residue (41 mg/kg), but lower than in aluminium hydroxide and security filtration solids. This provides an indication that Ga could be potentially incorporated to cancrinite and/or sodalite, as these are almost the only mineral phases in evaporator scale. In naturally occurring cancrinite, a mean concentration of 59 mg/kg Ga has been reported (Shaw, 1957), which is notably similar in currently analysed cancrinite-dominant evaporator scale (58 mg/kg). Again, the likely form is the isomorphous substitution of Al^{3+} with Ga^{3+}. The former reasoning leads to a conclusion that the affinity of Al-containing Bayer process secondary phases to incorporate Ga into their composition follows the relative intensity of hydrogarnet >gibbsite >cancrinite.

What can be seen in **Figure 27** (a) is a part of the cross section of digestion autoclave scale sample, cut at a right angle with scale layering for demonstrating the trace element distribution patterns in this material. Considerable concentrations of Cr and V can accumulate to digester autoclave scale, while Cr concentration can be about twice the amount of V concentration, as seen from the LA-ICP-MS profiles measured in the scale sample (**Figure 27**, b). The trends of Cr and V in the distribution profiles are roughly similar, both element concentrations increase towards the upper parts of the profile. At the same time, the trend is the opposite for Al concentration, implying that Cr and V do not accumulate in association with Al minerals. However, the trends are similar for Ga and Al distribution, indicating once again the close association of these metals (Gray et al., 2013). Therefore, Ga seems to have been deposited into this scale sample within the composition of Al minerals. There is no considerable presence of Sc in this material, its concentration is consistently low in all analysed spots, ranging from 16–37 mg/kg, which is consistent with the bulk concentration of Sc in this sample (19.7 mg/kg). The indicated concentration is lower than Sc content in bauxite and its residue. However, the lower Sc concentrations are consistent with the lower Al_2O_3 presence. Similar trend is noted in all Bayer process solid materials, where Sc is present, which is further explained in following paragraphs where the occurrences of Sc are discussed in the context of microanalysis (paragraph 7). Considering main oxides in this sample, the concentrations of TiO_2 and Fe_2O_3 also remain low in the analysed profile section.

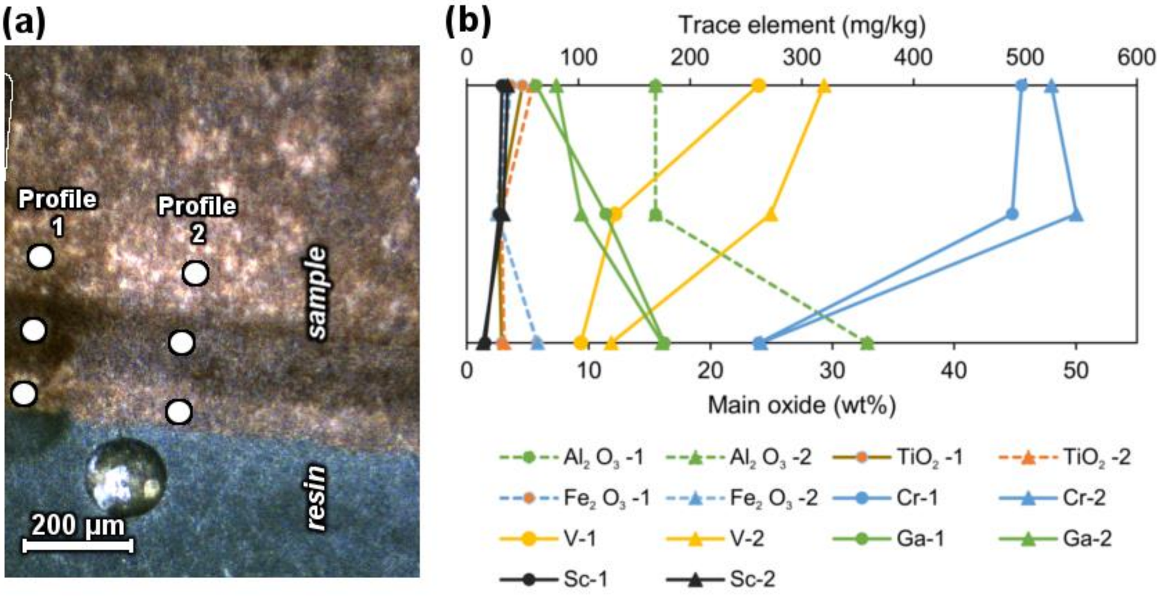

Figure 27. Digester autoclave scale depicted on (a) optical microscope image with indicated points of LA-ICP-MS analysis spots. In graph (b) are given the main and trace elements distribution profiles, obtained by LA-ICP-MS. White spots on image (a) correspond to concentration values on graph (b). Standard element for LA-ICP-MS quantification was Fe.

Given the indications that Sc might be associated with titanium phases including perovskite in the bauxite residue (Bonomi et al., 2017b; Ochsenkühn-Petropulu et al., 1994), it was examined whether Sc can be detected in the perovskite intergrowths in the digester scale sample (**Figure 28**). Perovskite-dominant matrix did not detect any presence of Sc, while cancrinite-dominant matrix indicated 20–90 mg/kg of Sc, based on EPMA-WDS (**Table 12**). There is a partial overlap in the WDS energy lines of Ca and Sc. To overcome that, the scale sample was also subjected to LA-ICP-MS measurements, as already shown before (**Figure 27**). It provided evidence for the same conclusion that perovskite and cancrinite are depleted in Sc, but still the detected quantities ranged from 12 to 37 mg/kg Sc on different spots. Unfortunately, the LA-ICP-MS spot size (40 µm) is larger than the individual perovskite crystals (about 5 µm), therefore a single crystal cannot be targeted with this experimental method. The analysed minerals (perovskite and cancrinite) might contain only a minor amount of Sc (<30 mg/kg), as suggested by the bulk (**Table 6**) as well as spot Sc analysis (**Table 12**) of the scale sample, whereas cancrinite is a more probable host for Sc. However, the detected quantities can also be attributed to the presence of minute iron oxide particles in the scale sample ("Fe" in **Figure 28**). It can be noted that other minor and trace elements such as Mg, Cr, V and Ni are significantly enriched into the perovskite-dominant matrix compared to cancrinite matrix (**Table 12**). The concentrations can be as high as about 0.6 wt% on the example of NiO. This indicates that perovskite can entrap several minor and trace metals that are introduced to the Bayer process. The evidence has been also presented that the named elements, Mg, Cr V and Ni, also occur in the dissolved form in process liquor (**Table 8**), therefore their migration to newly formed perovskite includes them being dissolved in the Bayer liquor and then precipitating into perovskite composition. It is a well-known fact that perovskite structure in a broad sense is very versatile and can incorporate a wide number of cations into its lattice (Mitchell et al., 2017).

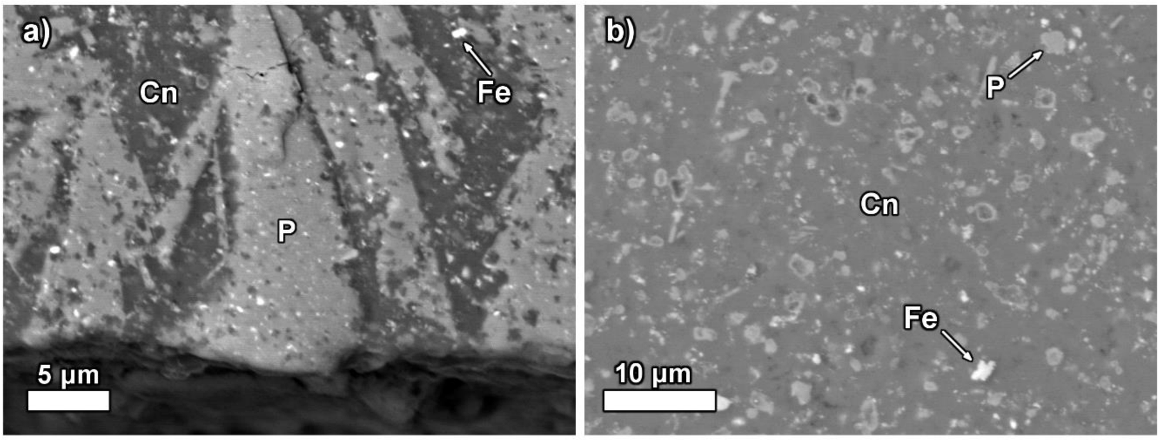

Figure 28. Micro-areas of digester autoclave scale with (a) prevailing presence of perovskite (P) with cancrinite/sodalite (Cn) and some Fe particles as well as (b) cancrinite-dominant area. Perovskite area (a) corresponds to quantification shown in **Table 12.**

Table 12. EPMA-WDS quantification of perovskite-dominant and cancrinite-dominant areas of digester autoclave scale sample.

Analyte		**Perovskite-dominant**			**Cancrinite-dominant**	
Fe_2O_3	wt%	9.69	10.18	9.30	2.30	4.41
TiO_2	wt%	34.39	30.71	36.19	0.55	2.19
Al_2O_3	wt%	14.18	15.83	13.21	34.72	28.30
SiO_2	wt%	1.61	2.07	0.84	22.54	19.62
Na_2O	wt%	2.07	1.97	1.72	12.84	18.42
CaO	wt%	17.83	16.81	18.05	1.35	3.61
MgO	wt%	2.26	1.95	2.34	0.00	0.05
K_2O	wt%	0.04	0.07	0.05	0.40	0.52
Cr_2O_3	wt%	0.256	0.220	0.211	0.031	0.036
V_2O_3	wt%	0.186	0.128	0.130	0.025	0.031
NiO	wt%	0.619	0.565	0.630	0.052	0.038
Sc	mg/kg	0	0	0	90	20
Total	wt%	83.13	80.50	82.67	74.80	77.23

4.5 Summary of the Trace Elements Distribution

A summarising comparison of selected trace element concentrations in different Bayer process solid materials is shown in **Figure 29**. It depicts a general trend that the investigated karst bauxites are more enriched in trace elements among bauxite samples and typically the highest concentrations in solid materials are found in bauxite residue. For Ga, the trend is different as bauxite residue is relatively depleted in the element and the products collect the highest proportion of Ga. A minor material that shows a relative enrichment of some trace elements (Ce, Ga) is the solid cake from security filtration (liquor “polishing”).

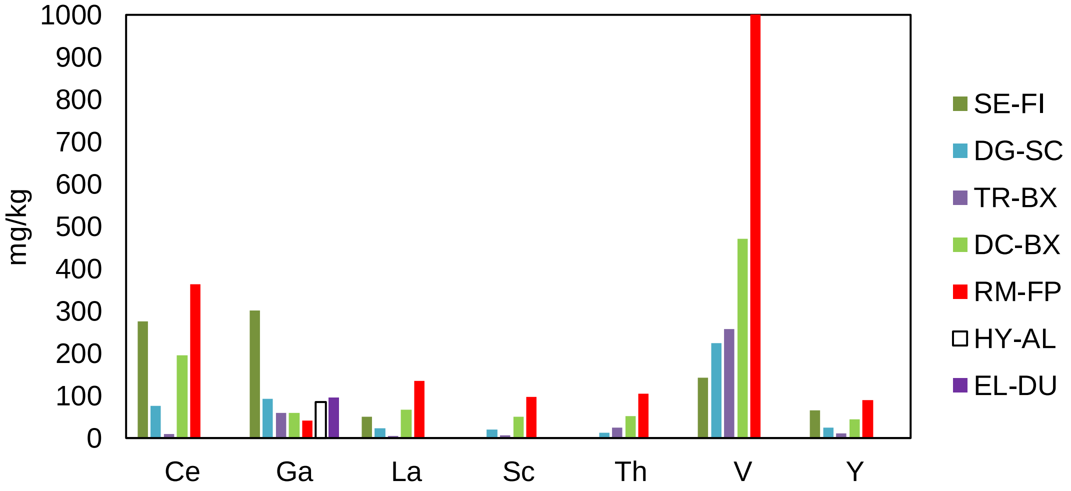

Figure 29. Trace elements distribution in different Bayer process materials. A reminder of sample names: SE-FI — security filtration solids, DG-SC — digester scale, TR-BX — Porto Trombetas bauxite, DC-BX mixed Greek Parnassos-Ghiona B3 horizon bauxite, RM-FP — bauxite residue, HY-AL — aluminium hydroxide, EL-DU — calciner dust from electrostatic filter.

Bauxite trace elements under the focus of this study were divided into two main categories: (1) those that dissolve completely or sparingly in the process liquor (Ga, V, Cr, U), and (2) those that pass through the process in the composition of solid material flows (REEs, Sc, Th).

The trace element analysis of Bayer process scales and minor by-products showed that these materials are not particularly significant collectors of trace elements. Even more when considering that the quantity of production of these materials, though difficult to estimate, is substantially smaller than the quantity of bauxite residue produced. However, since they do contain several trace elements such as Ga, V and Cr, they can be used to explain the effect seen in the mass balance models of the trace elements distribution where a decrease of concentration was observed in the consecutive processing steps (section 4.1). An interesting material for further extraction experiments could be the solid cake from security filtration of pregnant liquor with respect to its Ga content (**Figure 29**). With its concentration of 302 mg/kg of Ga, it represents a significant enrichment point of Ga compared to about 60 mg/kg Ga concentration in bauxite feed. Further work is encouraged for investigating Bayer process scale samples in relation to trace elements or other aspects, because it is possible to find isolated crystals of Bayer process specific solid phases that are challenging to be analysed directly in bauxite residue.

5. Minor and Nano-Scaled Phases in Bauxite Residue

A range of minor mineral phases have been observed in bauxite residue, as depicted in **Figure 30**. Oxidic phases have been identified where the metallic components are Ca and Mg as well as Ca, Mg and Al (**Figure 30** a, b). Notably, there is no or very low presence of Si in these phases. It could be that the Ca-Mg-containing phases are dolomite, since minerals with these two constituents are commonly carbonates (Gregg et al., 2015). Besides, carbonate phases in the example of calcite do occur in bauxite residue, based on current and literature information (M. Gräfe et al., 2011). On the other hand, the typical rhombohedral habit of dolomite cannot be seen in present electron image (**Figure 30**a) (Gregg et al., 2015). In any case, it seems that these Ca-Mg-Al oxidic phases together with chamosite (chlorite group silicate) type phases (**Figure 30** e) are the main carriers of Mg in current bauxite residue. The Ca-predominant particle in **Figure 30** (c) can be identified as portlandite ($Ca(OH)_2$), based on the positive identification of this phase from XRD diffractogram and its hexagonal habit that is photographed and indicated in the electron image. Portlandite has been reported to occur sometimes in bauxite residue (Evans, 2016). Some Al-Si-K particles were discerned also in bauxite residue (**Figure 30** d). In the literature, the presence of muscovite has been reported in bauxite residue, which roughly corresponds to such Al-Si-K composition, while other phases with similar composition especially with respect to K have not been noted to occur in bauxite residue (M. Gräfe et al., 2011; Newson et al., 2006; Santini, 2015). Muscovite is categorised in the context of bauxite residue as a residual phase inherited from bauxite (Santini, 2015). More rarely, another K-containing phyllosilicate phase, biotite, has been identified in bauxite residue (Markus Gräfe et al., 2011a). Phases having major compositions of Fe-Al-Si-Mg should correspond to the chamosite phase identified by XRD. Higher localised microscale concentrations of Mg are usually associated with chlorite phases such as chamosite in bauxite deposits (Bárdossy and Pantó, 1971). As already mentioned, chamosite largely endures Bayer digestion and can occur in the residues (Songqing and Zhonglin, 2016). Occurrences of Mn phases are also noted in bauxite residue (**Figure 30** f). Following the presence of Co and Ni in addition to Mn, the phase could correspond to asbolane ($Mn(O,OH)_2(Ni,Co)_x(O,OH)_2 \cdot nH_2O$) (Manceau et al., 1992). Note that Ce is also associated with this Mn phase. This phenomenon will be discussed further in the text (section 6.3.3). Zircon ($ZrSiO_4$) grains (**Figure 30** g) are encountered relatively frequently in bauxite residue, given that they are discrete phases with relatively high atomic weight and therefore they stand out bright in the BSE mode of SEM analysis, which is sensitive to atomic weight of chemical elements. Zircon concentrate is one of the many proposed possible value-added products that could be derived from bauxite residue (Logomerac, 1971; Mohapatra et al., 2012). As a rare representative of sulphide phases, Cu-Fe sulphide was discerned in bauxite residue (**Figure 30** h). It could likely correspond to chalcopyrite. Chalcopyrite has not been found in Parnassos-Ghiona bauxite knowingly to the author of this work. However, in other bauxite deposits (e.g. bauxites form Northern Urals and Mazaugues deposit in France), chalcopyrite has been noted as the only Cu-enriched mineral phase (Bárdossy and Pantó, 1973, 1971). Therefore, chalcopyrite can be regarded as a phase that endures Bayer process and represents a Cu carrier phase in bauxite residue. Some grains of pyrite have also been encountered in bauxite residue (not shown here). The Fe-Cr particles seen in the residue probably correspond to chromite type phases, that are known to be present in Parnassos-Ghiona bauxite deposit (Gamaletsos, 2014; Laskou, 2001). Commonly, the trace elements speciation studies (focussing mainly on Cr, As, Ti, Mn and V) of different bauxite residues have not noted the presence of chromite in bauxite residue (Burke et al., 2012; Markus Gräfe et al., 2011a). Perhaps this is because chromite is more abundant in Parnassos-Ghiona ores given the close association with basic and ultrabasic rocks via its genesis, compared to other bauxite deposits (Bárdossy and Pantó, 1973; Laskou et al., 2010; Valeton et al., 1987). In any case, chromite is certainly not the only location of Cr in present bauxite residue.

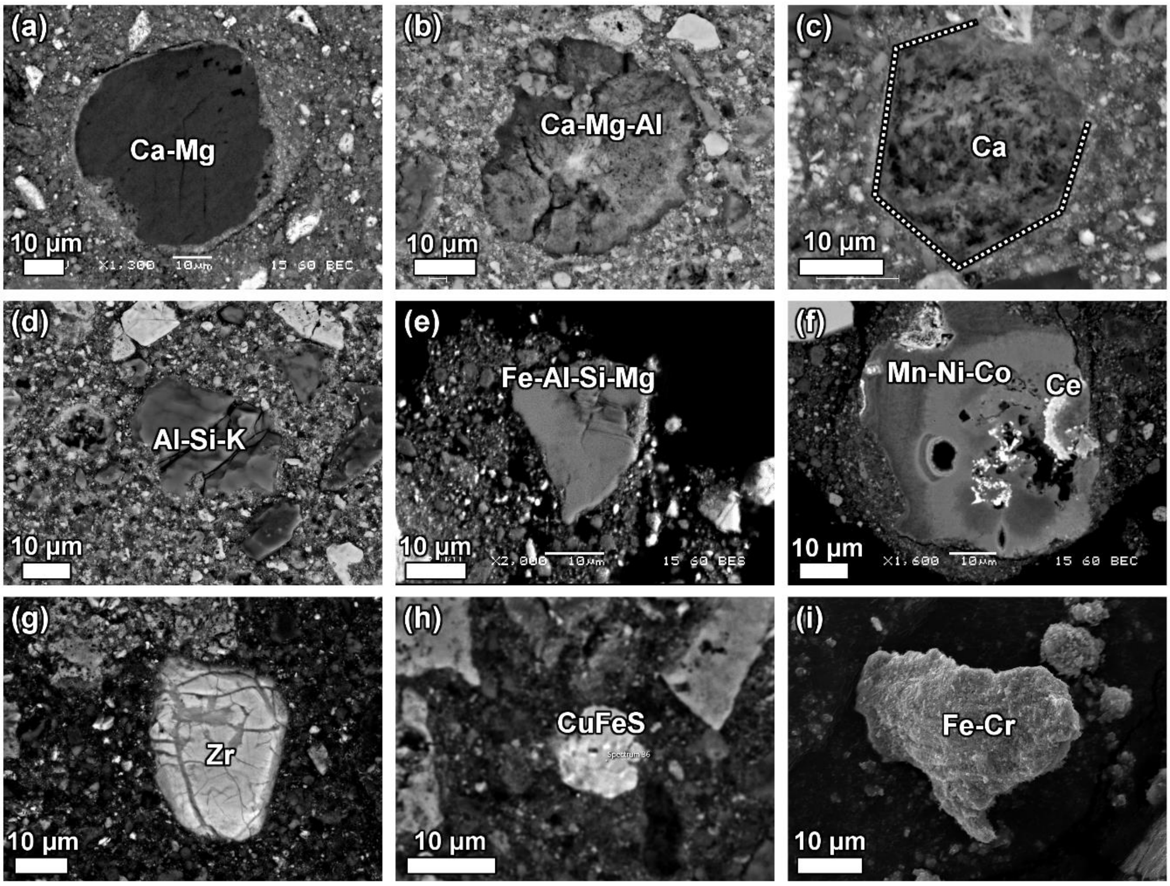

Figure 30. Electron images of bauxite residue's minor phases: (a) Ca-Mg phase (dolomite?), (b) Ca-Mg-Al phase, (c) Ca phase that is likely portlandite ($Ca(OH)_2$), (d) Al-Si-K phase that could be a feldspar group phase, (e) Fe-Al-Si-Mg phase that could correspond to chamosite group phase, (f) Mn phase associated with minor cerium (Ce), (g) zircon, (h) copper sulphide that might correspond to chalcopyrite, (i) Fe-Cr phase that could correspond to chromite. All except for image (i) are BSE images from polished sections, but (i) is a secondary electron image of bauxite residue "as is", i.e. not in a polished condition.

Certain Cr-containing Fe particles were seen in the residue (**Figure 31**). They are unlike the common Fe particles because they do not exhibit oxygen energy peaks in the EDS spectra, compared to typical Fe oxide particles (**Figure 31**c). Therefore, they seem to be fragments of metallic Fe. They probably come from metal bars and/or balls of the grinding mills. Therefore, Bayer process equipment might act as an additional input of Cr to the system.

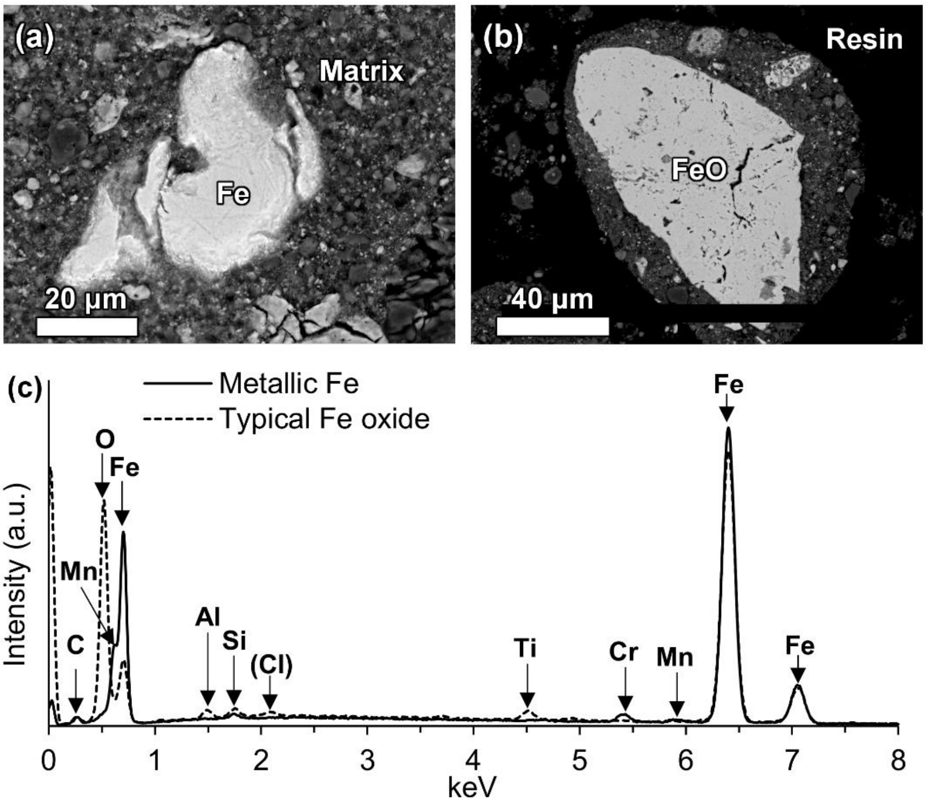

Figure 31. Backscattered electron images of (a) a fraction of metallic Fe containing Cr (denoted as Fe) compared with (b) typical bauxite residue's Fe oxide particle (denoted as FeO) and (c) their respective EDS spectra. Denotation of matrix refers to bauxite residue's Fe-Ca-Al-Si-Ti matrix. Note that the EDS spectrum of the metallic Fe particle does not possess the oxygen energy peak that Fe oxide particle has.

It is worth pointing out that during microscale characterisation of bauxite residue, a titanium dioxide particle was located that exhibited indications to a specific reaction behaviour (**Figure 32**). Titanium is considered being a major constituent of bauxites, but it's interactions with minor elements necessitate its mentioning here. The principal titanium minerals in bauxites are TiO_2 isomorphic forms anatase and rutile. Titanium poses many challenges to alumina refineries, like scale formation, inhibition of boehmite extraction and titanium impurities in alumina (Chester et al., 2009). The currently observed particle is composed mainly of two principal phases. The first one, located on left in **Figure 32**, is with a major composition of titanium dioxide (**Figure 32**b). The second one, located on right, is with a major composition of calcium titanate. The first one corresponds probably to anatase, although XRD has identified also rutile in current bauxite residue. The reason for assuming it is anatase is derived from the fact that anatase reacts more favourably in HTD conditions and rutile almost doesn't (Chester et al., 2009; Suss and Rydashevsky, 1996). The second phase likely corresponds to perovskite, as it is also detected in XRD and it is a generally acknowledged titanium phase to occur in Bayer process system (Chester et al., 2009; Smith, 2017). From the elemental mapping of the particle (**Figure 32**) it seems that perovskite has been formed in situ on the account of titanium dioxide particle as they are attached to each other. In the left side of the particle, the concentration of Ti is relatively lower than on the left side while Ca is clearly present only on the right side. Calcium has also penetrated the small fractures of titanium dioxide particle (Ca map in **Figure 32**). The EDS measurements (**Figure 32**b) indicate an almost pure titanium dioxide on the left side and almost pure calcium titanate on the right side with some impurities of Na, Al and Si are also detected. The newly formed perovskite contains also partly Na and Mg, while the locations of these two elements do not coincide. Generally, all the previous explanations of Ti phases reactions in the Bayer process describe the formation of perovskite through the reaction of dissolved ions in the liquor (Chester et al., 2009; Riley et al., n.d.; Suss et al., 2002; Suss and Rydashevsky, 1996). In general, titanium phases are explained to react first with sodium aluminate liquor and then with lime added to the process. Different interpretations have proposed various intermediate phases before the formation of perovskite, which is most commonly amorphous sodium titanate (indicative stoichiometry $Na_2O \cdot 3TiO_2 \cdot 2.5H_2O$) (Smith, 2017 and references therein). There are indications also to calcium hydroxy-titanate type as well as titanium substituted hydrogarnet type intermediate phases that further form the perovskite end-product (Smith, 2017). In any case, an in-situ transformation of titanium dioxide to perovskite has not been described to occur in the Bayer process. The described transformation is in broad terms analogous to the in-situ reaction of kaolinite to sodium aluminium hydrosilicate DSP at 100 °C without the dissolution of the components to process liquor (Bánvölgyi et al., 1991).

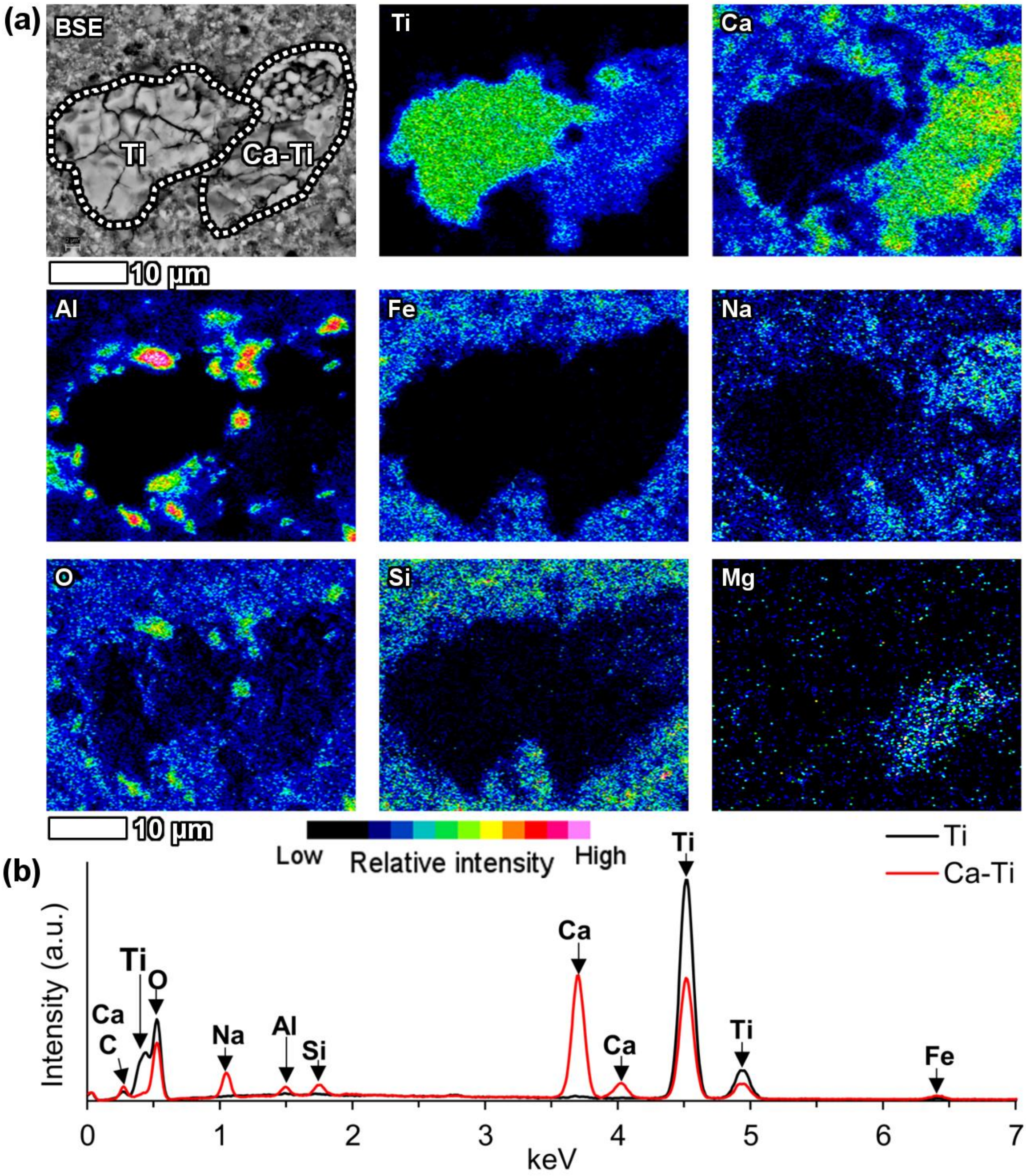

Figure 32. Reacted titanium dioxide attached to calcium titanate (perovskite) reaction product, shown in (a) BSE image with EDS elemental maps and (b) respective EDS spectra.

Since bauxite residue from AoG is a fine material with about 80% of the particles having particle sizes <1 µm (Borra et al., 2015), the material was subjected to HRTEM investigation that provides superior nanoscale magnification conditions (**Figure 33**). This approach has been applied also earlier to investigate bauxite residue from different sources and with different objectives (Burke et al., 2012; P. N. Gamaletsos et al., 2016; Gelencsér et al., 2011; Gu and Wang, 2013). In nanoscale, bauxite residue particulates can occur as a complex of agglomerated particles (**Figure 33** c), but clear distinctions can be made between different mineral phases by applying EDS chemical analysis as well as electron diffraction method. In most of the cases, the particles are anhedral, while some euhedral particles also occur (e.g. **Figure 33** e and f). Much of the material is composed of Fe particles (**Figure 33** a, **Figure 33** b), as suggested also by bulk phase quantification of current material (31% hematite). The electron diffraction patterns of **Figure 33** a and **Figure 33** b suggested them to correspond to hematite. In **Figure 33** c, a complex of small particles is shown, which resemble cancrinite or sodalite phases based on their chemical composition (Al-Na-Si as well as minor S). In **Figure 33** d an aluminium oxyhydroxide phase is shown that corresponds either to boehmite or diaspore. Hexagonal hydrogarnet type phase observed in bauxite residue is shown in **Figure 33** e. Due to hydrogarnet group highest level symmetry of cubic class it is possible for hydrogarnets to appear in hexagonal shape. Hexagonal hydrogarnets were also observed in the experiments of (Kanehira et al., 2013). Chemical analyses of this mineral type show consistently the presence of Al and Si as well as Fe, but there is always a higher concentration of Ca present compared to Ti (Ti:Ca ratio 0.3 to 0.6). The described chemistry as well as the morphology of the phases does not allow to identify them as calcium titanates. In fact, the phase is likely a titanium and iron substituted hydrogarnet (Suss et al., 2002; Zoldi et al., 1987). The euhedral titanium dioxide particle in **Figure 33** f was matched with rutile reference card (PDF 000-01-1292) based on electron diffraction pattern. The particle in **Figure 33** g can be termed broadly as a phyllosilicate phase. It is largely composed of Al and Si without a significant presence of other components. In the last image (**Figure 33** h), a Mg-containing chlorite group phase is shown, that was matched with a chamosite (berthierine) reference card (PDF 07-0315). There were no obvious clues relating to trace element occurrences in the nano-scaled fraction of the sample besides Ce and La that were associated with calcium titanates. These forms, however, are thoroughly discussed in a further chapter (section 6.3.2).

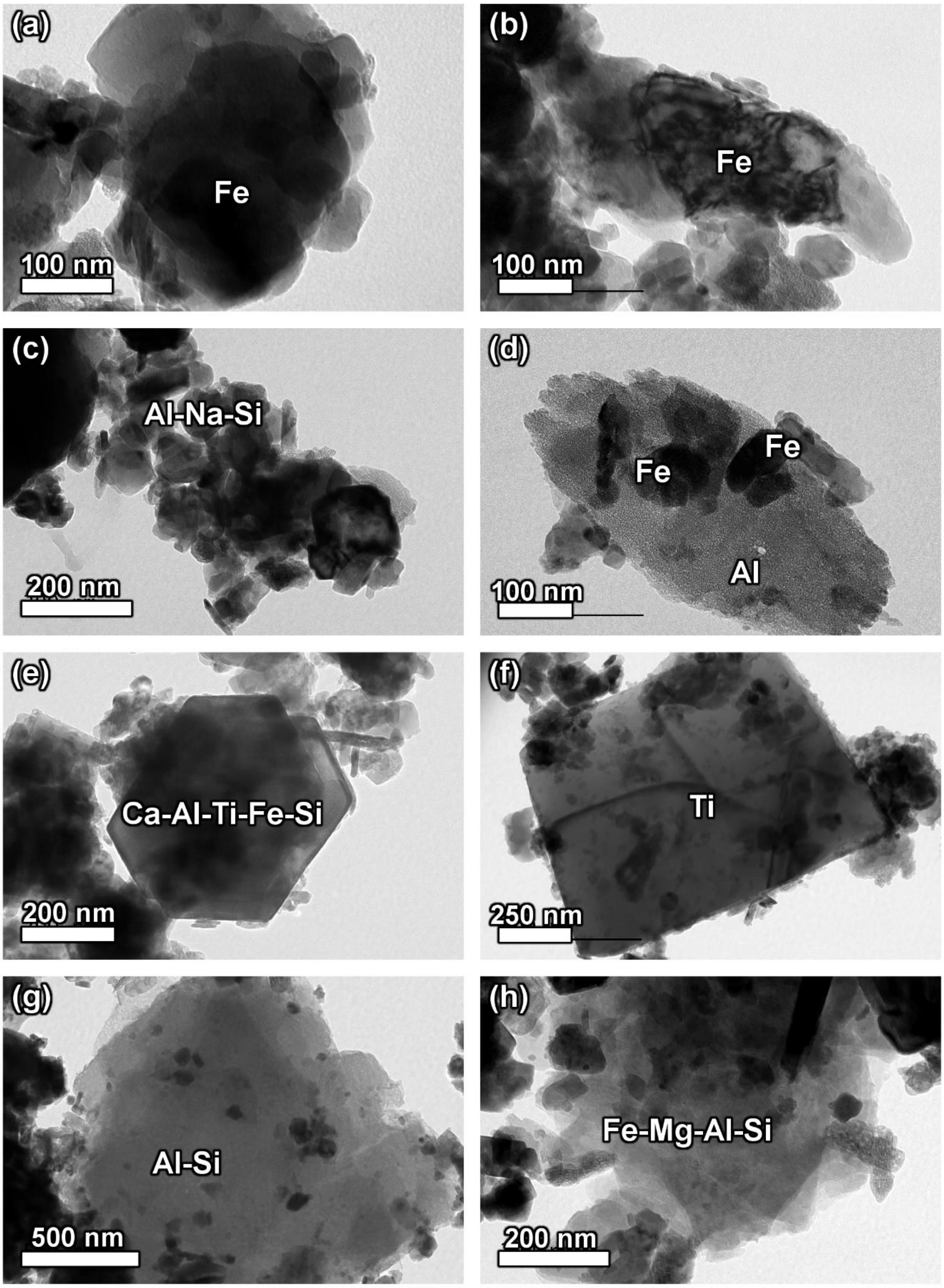

Figure 33. HRTEM images of bauxite residue particles: (a) and (b) Fe particles corresponding to hematite, (c) agglomeration of Al-Na-Si particles corresponding to cancrinite or sodalite, (d) boehmite or diaspore together with Fe particles, (e) hexagonal Ca-Al-Si-Ti-Fe-Si phase that could correspond to titanium substituted hydrogarnet, (f) euhedral titanium dioxide particle corresponding to rutile based on electron diffraction pattern, (g) phyllosilicate phase and (h) chlorite group phase corresponding to chamosite.

6. REEs Mineralogy in Bauxite and Bauxite Residue

Chapter 6 except for 6.2 is based on the following publication: Vind, J., Malfliet, A., Blanpain, B., Tsakiridis, P.E., Tkaczyk, A.H., Vassiliadou, V., Panias, D., 2018. Rare Earth Element Phases in Bauxite Residue. Minerals 8, 77.

6.1 Precursor REE phases in bauxite feed

In **Table 13** are shown the REE phases that are likely to be introduced to AoG's production line via the composition of bauxite feed. In Parnassos-Ghiona bauxite profiles (Prossorema and Frussia), detrital rhabdophane and florencite have been identified as LREE phases, whereas detrital churchite and xenotime represent HREE phases (Laskou and Andreou, 2003). Hydroxylbastnäsite-(La) and -(Nd) were identified in the lowermost bauxite profile samples of Parnassos-Ghiona deposit (Mandri Tsakni) as the only contribution that deployed WDS quantification (Ochsenkühn-Petropulu and Ochsenkühn, 1995). Authigenic bastnäsite and parisite group phases were further reported as representatives of authigenic fluorocarbonate LREE minerals in Parnassos-Ghiona bauxite (Pera Lakkos) (Gamaletsos, 2014; P. N. Gamaletsos et al., 2016). As it is not clear on what basis was the distinction of parisite group from the rest of calcium-bearing REE groups made, it is categorised together with other calcium containing LREE fluorocarbonates, synchysite and röntgenite (Grice et al., 2007). A recent report questions the earlier identifications of cerium-predominant REE phases, that they could be rather cerium oxides or carbonates, because of the absence of phosphorus and fluorine. Due to the absence of other lanthanides, even the identification as hydroxylbastnäsite-Ce is being questioned (Evangelos Mouchos et al., 2017).

Table 13. REE phases identified in the bauxites exploited by AoG.

Phase	Formula	Parnassos-Ghiona, Greece					Awaso Ghana
		*	§	⊥	‖	Present	Present
LREE							
rhabdophane-(Ce)	$(Ce)(PO_4)\cdot H_2O$		+				
florencite-(Ce)	$CeAl_3(PO_4)_2(OH)_6$		+	+			+
bastnäsite group	$Ce(CO_3)F$			+			
parisite/ synchysite/ röntgenite	$Ca_{1-2}REE_{1-3}(CO_3)_{2-5}F_{1-3}$			+		+	
hydroxylbastnäsite-(Nd) and -(La)	$(Nd,La)(CO_3)(OH)$	+					
cerianite	CeO_2				?	+	
HREE							
churchite	$YPO_4\cdot 2H_2O$		+				
xenotime	YPO_4		+				+

* (Ochsenkühn-Petropulu and Ochsenkühn, 1995)
§ (Laskou and Andreou, 2003)
⊥ (Gamaletsos, 2014; P. N. Gamaletsos et al., 2016)
‖ (Evangelos Mouchos et al., 2017)

In the studied Parnassos-Ghiona bauxite samples, some areas are particularly rich in REE phases (**Figure 34**). Authigenic cerium-predominant LREE phases in sizes over 10 µm are concentrated into iron and aluminium oxide matrix rather than to alumina-rich pisolitic textures. This is in line with the observations made by Mongelli, (1997), where he noted that Ce is more fractioned to the bauxite matrix as opposed to ooids (pisolites). However, the ooids described by Mongelli (1997) are controlled by hematite matrix which is different from present observation. This textural fractionation has not been reported in the case of Parnassos-Ghiona bauxite deposit. The LREE phases were identified by µ-Raman spectroscopy being cerianite (CeO_2), following the main band at 457 cm^{-1}, when comparing with the reference spectrum R050379 from RRUFF database and those spectra given in the literature sources (**Figure 34** b) (Lafuente et al., 2015; Zaitsev et al., 2011). Based on the analysis of synthetic and natural cerianite specimens, this band can be attributed to the symmetric breathing mode of Ce–O–Ce bond (Cui and Hope, 2015; Zaitsev et al., 2011). The band at 396 cm^{-1} present on the reference spectrum R050379, but missing in current experimental spectrum, is rarely noted in different cerianite Raman spectra (Cui and Hope, 2015; Zaitsev et al., 2011). The band at 396 cm^{-1} could also be hidden due to the broadening of 457 cm^{-1} band. Broadening as well as shifting of cerianite main band is noted to occur along with decreasing particle size (Weber et al., 1993). Notably, the acquired spectrum lacks the presence of Raman bands that could be associated with the occurrence of carbonate (around 1100 cm^{-1}) or hydroxide ions (3400–3600 cm^{-1}) (Yang et al., 2008; Zaitsev et al., 2011). The matrix where cerianite is situated, is mainly controlled by hematite, following the Raman bands at 225, 293 and 409 cm^{-1} (De Faria et al., 1997; Lafuente et al., 2015). Zaitsev et al., (2011) have demonstrated that F can also be present in cerianite, and F is also present in cerianite of Parnassos-Ghiona bauxite (**Figure 34**a). Some of the previously reported REE phases might have been erroneously identified as bastnäsite group phases on qualitative basis when judged only by the presence of F. Thus, current results support the doubts of Mouchos et al., (2017) regarding the cerium-predominant phases and evidence is provided for the identification of cerianite in Parnassos-Ghiona bauxite.

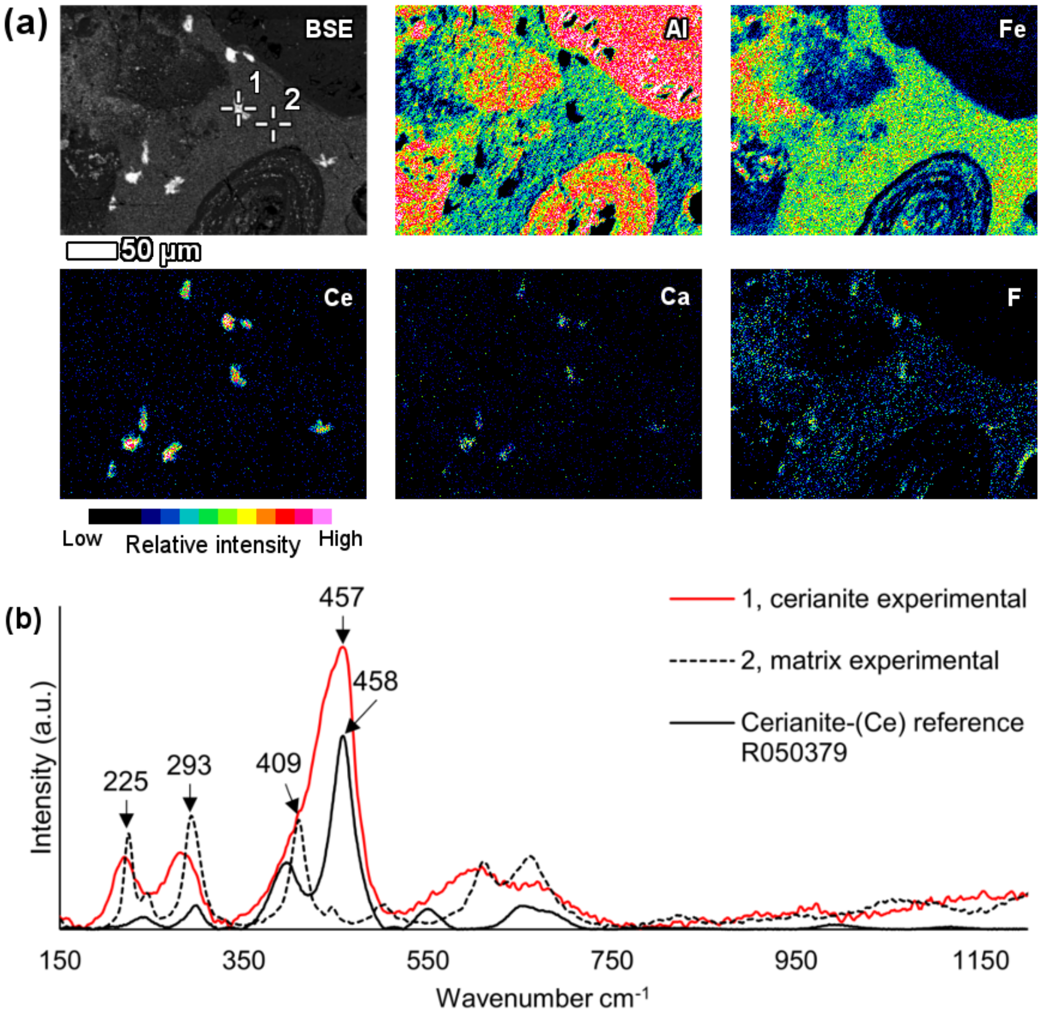

Figure 34. Cerianite rich area in the second Parnassos-Ghiona B3 horizon bauxite sample (ST-BX) shown on (a) BSE image with respective EDS elemental maps, and (b) Raman spectra of cerianite and its surrounding matrix compared to reference Raman spectrum obtained from RRUFF database (Lafuente et al., 2015), with permission from RRUFF™. Raman spectrum is collected with a 532-nm wavelength laser.

Authigenic cerium-predominant REE phases were noted to be associated with fissures filled with aluminosilicate matrix that is likely kaolinite (**Figure 35**). Kaolinite-associated authigenic REE phases have not been reported before, but their presence has been assumed in Parnassos-Ghiona bauxite due to the easily leachable proportion of REEs (E. Mouchos et al., 2017). It was noted previously, however, that some detrital florencite crystals were encased within clay fragments (Laskou and Andreou, 2003).

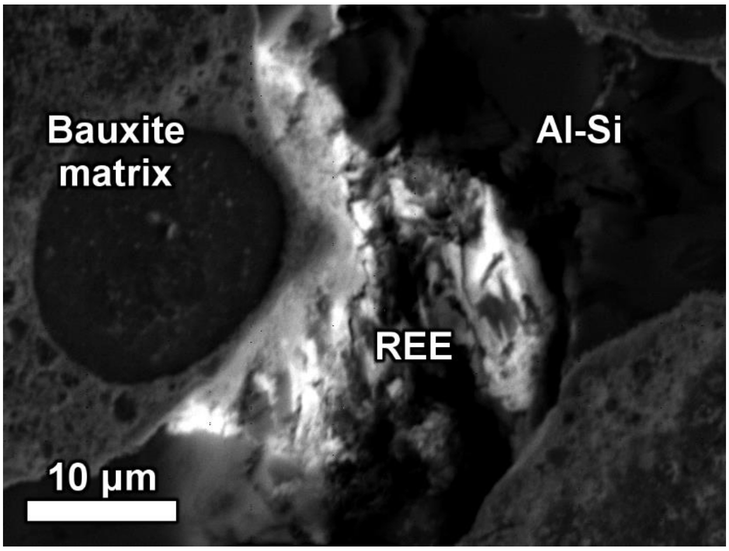

Figure 35. REE phase in first Parnassos-Ghiona B3 horizon bauxite sample (DD-BX) associated with aluminosilicate (Al-Si).

Regardless of the low REEs concentration in Ghanaian bauxite (e.g. 29 mg/kg Ce), distinct detrital REE phases are also contained within this lateritic bauxite (**Figure 36**). The REE minerals have a prevailing content of aluminium, followed by cerium, phosphorus and then other LREEs. Thus, these REE phases can be identified as belonging to the florencite group. In addition, detrital xenotime was identified in the Ghanaian bauxite. Florencite grains are significantly larger (20–60 µm) than xenotime grains (1–3 µm). The presence of florencite and xenotime group phases in Ghanaian lateritic bauxite implies granitic origin of the bauxite parent material. The other analysed lateritic bauxite from Brazilian Porto Trombetas deposit did not contain any detectable REE phases. This is in line with the low REEs concentration in this sample (e.g. 9 mg/kg Ce), which is even lower than that of the Ghanaian bauxite.

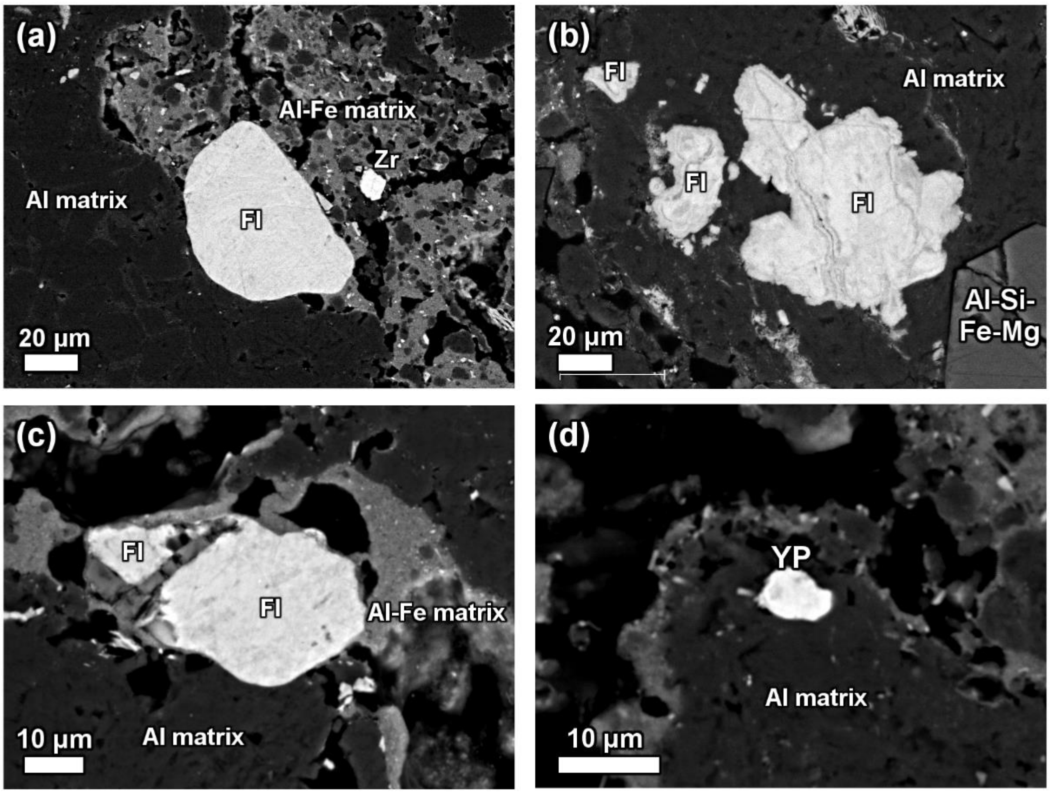

Figure 36. In sub-figures (a-c) are shown florencite group LREE phases (Fl) and a zircon grain (Zr) and in (d) is a xenotime/churchite particle with a major composition of Y phosphate (YP), all contained in Ghanaian Awaso lateritic bauxite matrix.

The main input of LREE phases introduced to the Bayer process in AoG along with the bauxite feed therefore appear to be LREE fluorocarbonates of the bastnäsite group as well as cerianite. Minor LREE input is from phosphate phases. Heavy REEs enter the process as phosphate-based groups. Elucidating the REE mineralogy in the Parnassos-Ghiona bauxite deposit deserves a thorough investigation in terms of clearly defining the mineral phases and their spatial distribution along the bauxite profiles. The currently existing information is scattered and not uniform.

6.2 Preheating Stage

In this production stage, karst bauxite has been ground and suspended in caustic soda. Additionally, the suspension has passed through the preheating stage, where a temperature of 180 °C has been reached. In this material, La-Nd as well as Ce predominant REE phases were observed (**Figure 37, Figure 38**). The La-Nd particle **Figure 37** (a) contains F, providing an indication that its form could be a bastnäsite group phase. It can be proposed that REE phases in this production stage resemble mostly bauxite REE phases and they might correspond to bastnäsite group phases on the example of La-Nd phases and cerianite following the Ce-predominant particles. The La-Nd predominant particle in **Figure 37** (a) also contains Y and P, indicating to minor contribution from xenotime/churchite phase. The Ce-predominant particles in **Figure 37** (b) and (c) are mostly without the presence of other elements, suggesting possibly an oxide or oxyhydroxide form. All the observed REE phases in this production stage are with a free surface or surrounded by crushed bauxite matrix. The particle in **Figure 37** (c) appears to be fractured, likely because of the crushing and grinding phase of bauxite in the beginning of bauxite processing. Other observed particles are mostly intact without a clear sign of mechanical destruction. Presumably, all the REE particles in

Figure 37 occur in the original forms like in bauxite, because no chemical alteration was noticed compared to precursor REE phases.

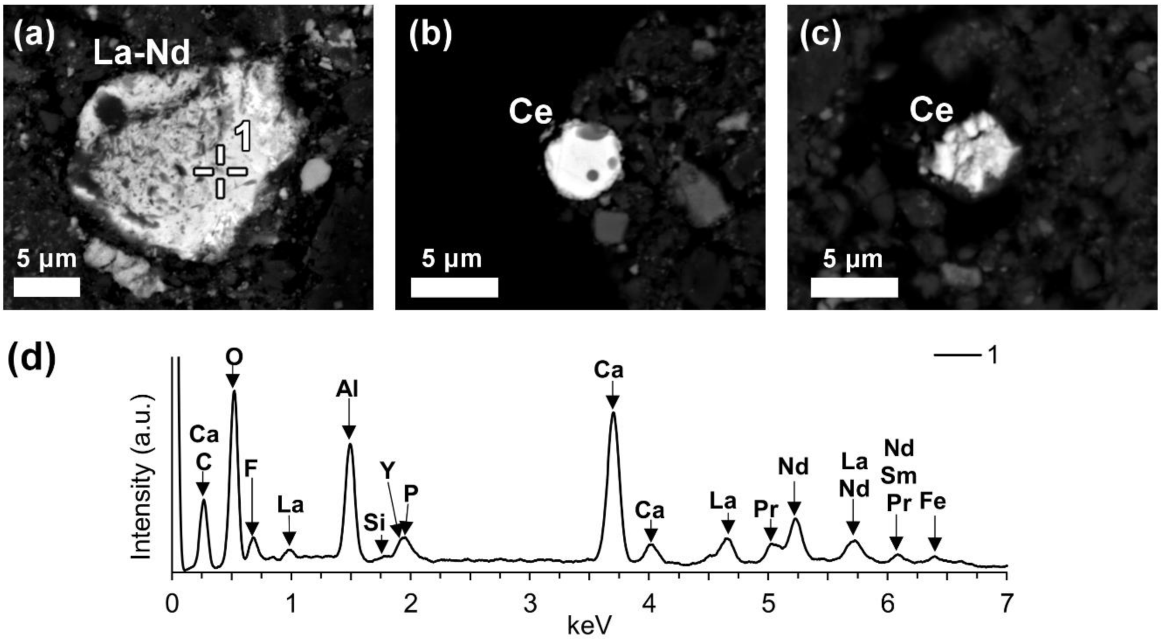

Figure 37. Backscattered electron images of (a) La-Nd predominant REE particle, (b) intact Ce particle, (c) cracked Ce particle. In figure (d) is given the EDS spectrum corresponding to La-Nd particle (a).

Besides the unaffected REE particles, an observation was made that revealed a chemically changed Ce predominant REE phase, as can be seen in **Figure 38**. Besides Ce, this particle also contains Ti and Fe whilst it is surrounded mainly by undigested crushed Al and Fe phases matrix. The characteristics of such REE ferrotitanate species are further discussed in the chapter explaining REE phases in bauxite residue (section 6.3.2).

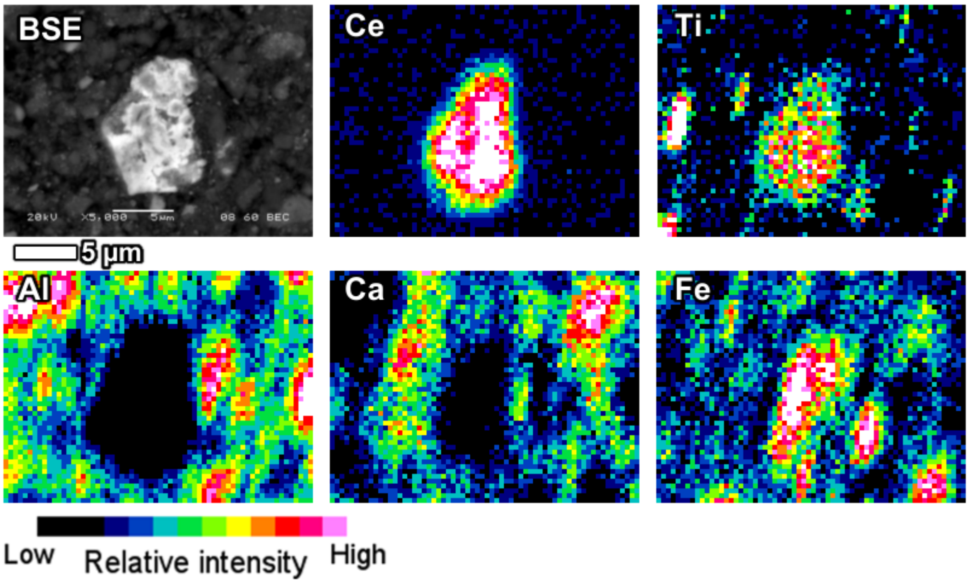

Figure 38. Ce ferrotitanate phase observed in the karst bauxite preheating stage. The particle is mainly surrounded by the undigested Al phases matrix.

The former observations (**Figure 37**, **Figure 38**) provided insight, that while the majority of REE phases seem to occur in their original form, some chemical transformation of REE minerals already starts during the preheating of karst bauxite suspension at 180 °C under atmospheric pressure.

6.3 REE Phases in Bauxite Residue

In bauxite residue, REE mineral particles appear in the BSE imaging mode as bright particles. They are contrasting in their brightness from other bauxite residue phases like hematite, diaspore/boehmite, hydrogarnet, titanium dioxides, cancrinite or perovskite (e.g. **Figure 11**). At a similar brightness level as the REE particles, occur other heavy mineral particles such as for instance, zircon, chromite and chalcopyrite (chapter 5, **Figure 30**).

6.3.1 REE Carbonate and Phosphate Species

In the investigated bauxite residue sample, a Nd and La predominant particle with the presence of C was revealed (**Figure 39**). Other LREEs like Pr and Gd are also present. The specific particle is notably large, more than 40 µm in its longest dimension and exhibits a blocky crystal habit.

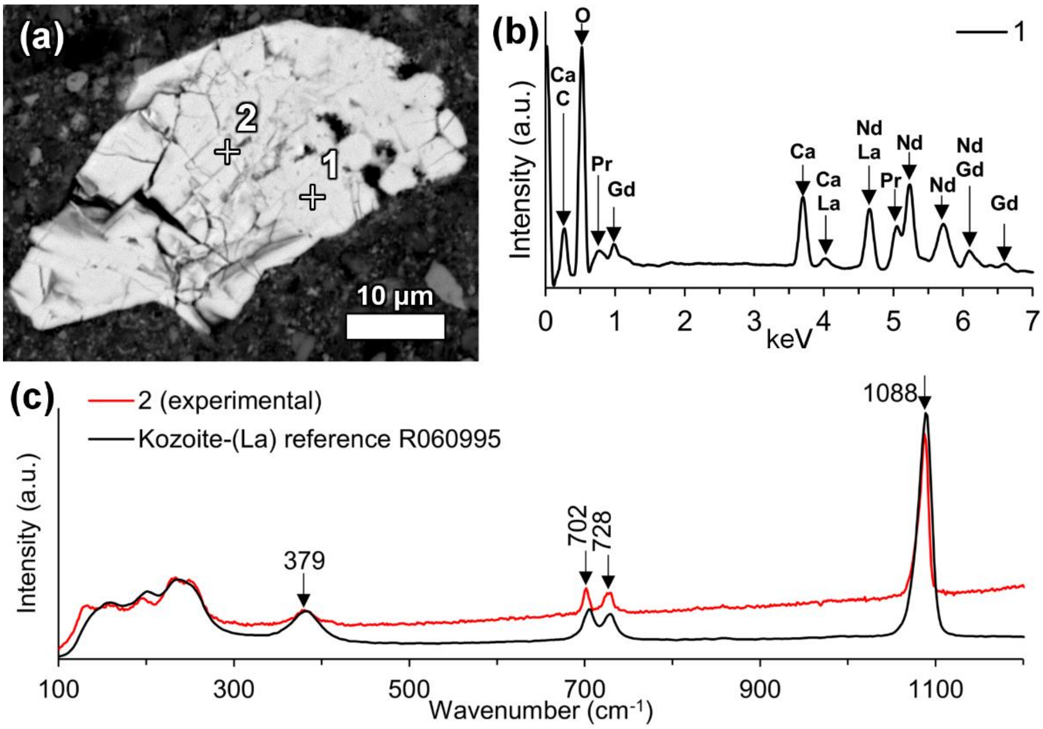

Figure 39. An ancylite group LREE carbonate phase depicted on (a) BSE image with its (b) EDS spectrum and (c) Raman spectrum compared to a reference spectrum of kozoite-(La) obtained from RRUFF database (Lafuente et al., 2015), with permission from RRUFF™. Raman spectrum is collected with a 532-nm wavelength laser.

Raman investigation of this grain resulted in a spectrogram showing a major peak at 1088 cm^{-1}, that can be attributed to symmetric C–O stretching of CO_3^{2-} (**Figure 39**c) (Buzgar and Apopei, 2009; Zhuk, 2017). Comparison with reference data from RRUFF database resulted in a notably similar match with the kozoite-(La) ($La(CO_3)(OH)$) Raman spectrum (Lafuente et al., 2015). The observed peak at 1088 cm^{-1} is the most characteristic one for the ancylite group phases (Lafuente et al., 2015; Zhuk, 2017). Kozoite, belonging to the ancylite mineral group, is dimorphous with hydroxylbastnäsite. In other words, it has identical chemical composition, but different mineral structure. The former occurs in orthorhombic crystal system and the latter in hexagonal (Miyawaki et al., 2000). The kozoite-(La) reference spectrum given in the RRUFF database has not yet been confirmed by other identification methods. Therefore, the present identification cannot be regarded as conclusive. However, the absence of other matching spectra and the relative similarity with other ancylite group minerals Raman spectra (Lafuente et al., 2015) allows at least suggesting that the investigated particle belongs to ancylite mineral group.

The formerly described evidence shows that a part of LREEs can occur as carbonate phases in bauxite residue. Ancylite group minerals have not been identified in any bauxite sample. It could be that they have been reported as hydroxylbastnäsite species because of their identical chemical composition. Generally, REE carbonate phases are expected to be dissolved during sodium hydroxide digestion (Habashi, 2013). Based on the abovementioned evidence, it is difficult to define whether the LREE carbonate phase is a primary mineral inherited from bauxite that withstood Bayer digestion conditions or is a secondary precipitate form created in the Bayer process. In any case, it is a very rare occurrence type in bauxite residue.

In a few cases, LREEs are found as calcium containing phosphate phases in bauxite residue, more specifically as Ce phosphates. It can be seen from the EDS spectrum of an analysed particle, exhibiting a pronounced P X-ray peak (**Figure 40**). This and other similar observed grains are Ce-predominant. The low amount of LREE phosphate species in bauxite residue is in line with the relative scarcity of phosphate phases in the AoG's bauxite feed. The composition of these grains resembles rhabdophane-(Ce) that has been detected in Parnassos-Ghiona bauxite (**Table 13**) (Laskou and Andreou, 2003). It is an indication that REE phosphates endure, at least partly, the Bayer process. This is an expected behaviour as REE phosphates do not dissolve easily in sodium hydroxide, although there are processes that apply sodium hydroxide leaching to recover REEs from phosphate minerals like monazite and xenotime (Habashi, 2013). In such processes, sodium hydroxide is more concentrated (40%–50% NaOH) (Habashi, 2013) than in the Bayer process (12%–22% NaOH) (Authier-Martin et al., 2001).

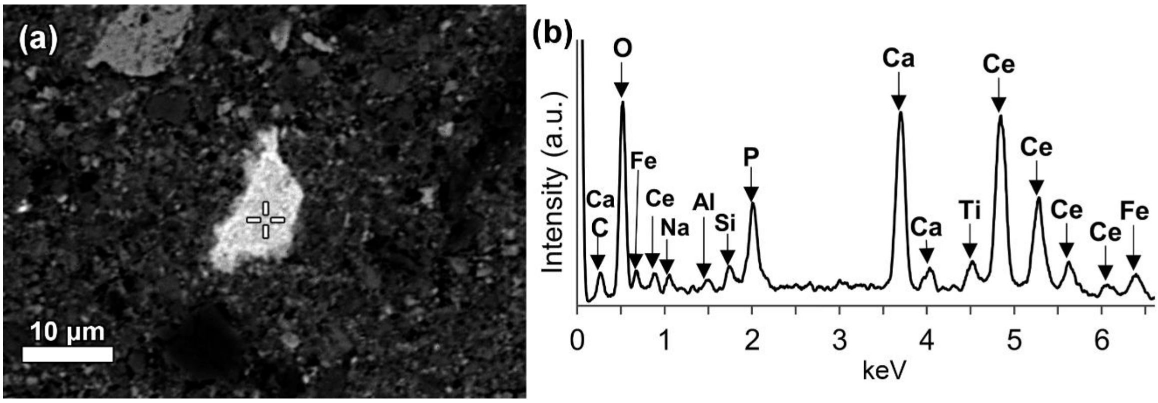

Figure 40. Ce phosphate in bauxite residue matrix, shown on (a) BSE image with its (b) EDS spectrum.

6.3.2 LREE Ferrotitanate Species, (REE,Ca,Na)(Ti,Fe)O_3

In bauxite residue, LREE mineral particles that contain Ca, Ti, Fe and Na (**Figure 41**, **Figure 42**, **Table 14**, **Table 15**) are also found. They further divide into Ce-predominant (**Figure 41**, **Table 14**) and Nd-La-predominant particles (**Figure 42**, **Table 15**). The number of ions in the mineral formula shown in **Table 14** and **Table 15** have been calculated based on a perovskite stoichiometry with three oxygen atoms (ABO_3). Alternatively, the number of ions could be calculated by adopting the double perovskite structure with the composition $A_2B_2O_6$ (Mitchell et al., 2017). Division of the ions between A and B sites is based on previous literature, considering their charges and relative ionic radii (Campbell et al., 1997; Mitchell et al., 2017). The chemical composition of these particles is variable, for instance Ce_2O_3 content ranges from about 34 to 51 wt% while TiO_2 content ranges from 9 to 24 wt% (Table 5). It can be noted that measurements 1–6 in **Table 15** are relatively depleted in Fe_2O_3 content, although the title of this section refers to ferrotitanate species. This effect is explained further in the text below. Such chemical composition which is uncommon for REE phases in bauxite, especially the appreciable presence of Na, clearly indicates that the LREE ferrotitanates are formed during the Bayer process.

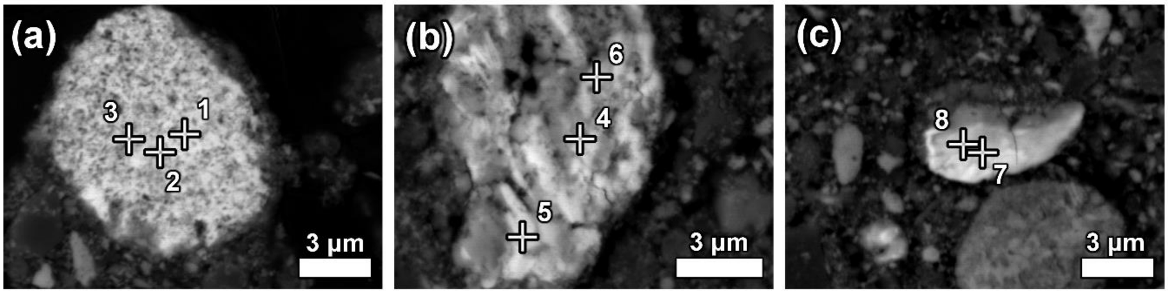

Figure 41. BSE images of Ce ferrotitanate grains in bauxite residue matrix, (a), (b) and (c). The indicated quantification spots are reported in **Table 14**.

Table 14. EPMA-WDS quantification (in wt %) of Ce-predominant ferrotitanate grains (**Figure 40**). Lower section of the table shows the number of ions in the mineral formula, following the ABO_3 perovskite structure.

Oxide	**Figure 41 Quantification**							
No.	1	2	3	4	5	6	7	8
La_2O_3	1.65	1.21	1.31	0.09	0.10	0.11	1.28	1.10
Ce_2O_3	51.25	45.36	48.13	47.22	44.67	34.48	45.52	47.27
Pr_2O_3	1.30	0.82	0.86	0.00	0.10	0.07	1.31	1.24
Nd_2O_3	2.48	1.93	2.00	1.41	1.54	1.00	3.30	2.99
TiO_2	9.00	9.16	9.44	14.84	21.78	18.56	21.37	23.86
Fe_2O_3	17.85	22.33	21.98	14.84	8.77	22.87	7.80	7.32
CaO	4.34	4.01	4.13	6.56	8.78	9.91	7.93	9.59
MgO	0.02	0.05	0.03	0.01	0.02	0.22	0.03	0.01
SiO_2	0.98	0.97	0.98	1.00	1.21	2.09	1.53	1.59
Na_2O	0.90	1.32	0.92	0.92	1.49	2.16	2.01	3.21
Al_2O_3	1.39	1.43	1.30	1.13	1.12	2.01	1.50	1.39
ThO_2	2.68	1.99	2.21	1.36	1.36	1.21	0.02	0.02
Total	93.83	90.58	93.28	89.36	90.94	94.70	93.60	99.58
No. of ions per ABO_3 formula								
La	0.03	0.02	0.02	0.00	0.00	0.00	0.02	0.01
Ce	0.81	0.73	0.75	0.71	0.61	0.44	0.61	0.58
Pr	0.02	0.01	0.01	0.00	0.00	0.00	0.02	0.02
Nd	0.04	0.03	0.03	0.02	0.02	0.01	0.04	0.04
Ti	0.29	0.30	0.30	0.46	0.61	0.49	0.58	0.60
Fe	0.58	0.73	0.71	0.46	0.25	0.60	0.21	0.18
Ca	0.20	0.19	0.19	0.29	0.35	0.37	0.31	0.35
Mg	0.00	0.00	0.00	0.00	0.00	0.01	0.00	0.00
Si	0.04	0.04	0.04	0.04	0.05	0.07	0.06	0.05
Na	0.08	0.11	0.08	0.07	0.11	0.15	0.14	0.21
Al	0.07	0.07	0.07	0.06	0.05	0.08	0.06	0.06
Th	0.03	0.02	0.02	0.01	0.01	0.01	0.00	0.00
Structural formulas following the ABO_3 structure								
A (REE, Ca, Na, Th)	1.20	1.11	1.11	1.11	1.10	0.99	1.14	1.20
B (Ti, Fe, Al, Si)	0.99	1.15	1.12	1.02	0.95	1.24	0.92	0.90

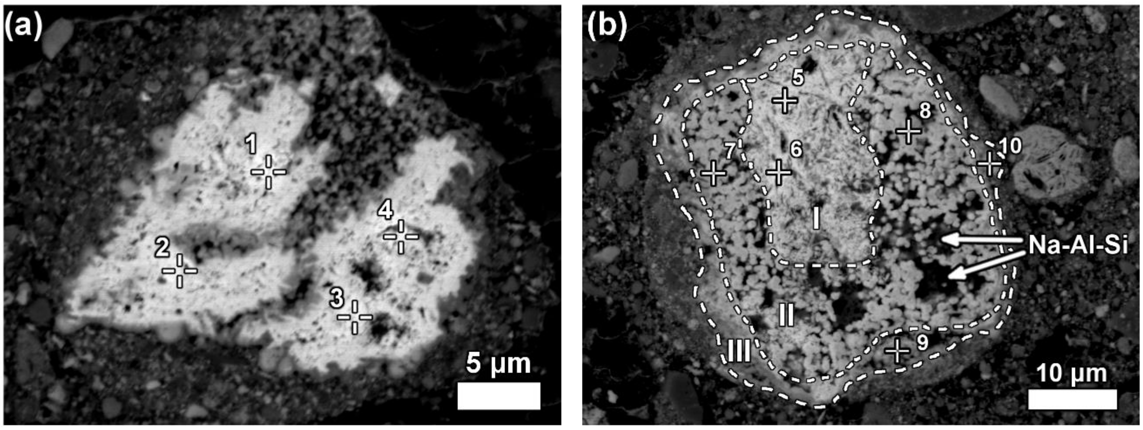

Figure 42. Nd-La predominant LREE particles, of which (a) is partly reacted, and (b) exhibits a zonation (I–III) relating to reaction stages with Bayer liquor. Within zone II of (b), deposition of a sodium aluminosilicate phase (Na-Al-Si) is indicated. Denoted measurement spots refer to **Table 15**.

Table 15. EPMA-WDS quantification (in wt %) of a Nd-La predominant partly reacted LREE grain (1–4) (**Figure 42**a) and a LREE ferrotitanate grain (5–10) (**Figure 42**b). Lower section of the table shows the number of ions in the mineral formula, following the ABO_3 perovskite structure.

Oxide	**Figure 42 Quantification**									
No.	1	2	3	4	5	6	7	8	9	10
La_2O_3	23.21	24.93	25.99	25.49	23.89	23.89	10.25	13.87	1.06	7.41
Ce_2O_3	7.87	8.87	10.57	10.47	5.99	5.46	2.71	3.49	0.58	1.29
Pr_2O_3	21.91	20.56	20.79	21.90	22.02	20.78	9.41	8.45	1.03	5.60
Nd_2O_3	35.10	33.73	33.59	34.02	34.92	34.19	14.37	17.22	1.71	8.53
TiO_2	3.87	5.85	0.83	3.08	1.44	2.03	27.48	24.13	32.60	40.35
Fe_2O_3	2.61	2.35	2.20	3.27	6.67	4.07	10.71	12.21	42.44	12.26
CaO	2.11	3.07	1.93	2.56	1.46	1.12	4.42	5.64	17.92	14.16
MgO	0.00	0.00	0.01	0.00	0.11	0.08	0.99	0.02	0.03	0.03
SiO_2	0.16	0.29	0.17	0.20	0.38	0.54	2.93	1.25	1.57	2.30
Na_2O	0.16	0.62	0.00	0.14	0.00	0.00	5.65	4.46	2.87	6.93
Al_2O_3	0.28	0.34	0.33	0.25	0.66	0.88	3.21	1.36	1.07	2.13
ThO_2	0.00	0.00	0.00	0.00	0.09	0.07	0.05	0.02	0.01	0.04
Total	97.28	100.62	96.40	101.37	97.62	93.11	92.17	92.12	102.89	101.02
	No. of atoms per ABO_3 formula									
La	0.44	0.43	0.52	0.46	0.45	0.47	0.12	0.18	0.01	0.07
Ce	0.15	0.15	0.21	0.19	0.11	0.11	0.03	0.05	0.01	0.01
Pr	0.41	0.35	0.41	0.39	0.41	0.41	0.11	0.11	0.01	0.05
Nd	0.64	0.57	0.65	0.60	0.64	0.65	0.17	0.22	0.02	0.08
Ti	0.15	0.21	0.03	0.11	0.06	0.08	0.67	0.65	0.67	0.81
Fe	0.10	0.08	0.09	0.13	0.26	0.16	0.26	0.33	0.87	0.25
Ca	0.12	0.16	0.11	0.13	0.08	0.06	0.15	0.22	0.52	0.40
Mg	0.00	0.00	0.00	0.00	0.01	0.01	0.05	0.00	0.00	0.00
Si	0.01	0.01	0.01	0.01	0.02	0.03	0.09	0.04	0.04	0.06
Na	0.02	0.06	0.00	0.01	0.00	0.00	0.35	0.31	0.15	0.36
Al	0.02	0.02	0.02	0.01	0.04	0.06	0.12	0.06	0.03	0.07
Th	0.00	0.00	0.00	0.00	0.00	0.00	0.00	0.00	0.00	0.00
	Structural formulas following the ABO_3 structure									
A (REE, Ca, Na)	1.76	1.72	1.90	1.79	1.72	1.71	0.99	1.08	0.72	0.98
B (Ti, Fe, Al, Si)	0.27	0.32	0.15	0.27	0.37	0.33	1.15	1.08	1.61	1.18

Some LREE particles were observed that have a relatively small percentage of Fe, Ti and Na oxide content (**Figure 42**a, **Table 15**). Others showed distinct zonation expressed in wide variation in chemical composition as well as in morphological features (**Figure 42**b, **Table 15**).

The texture of LREE ferrotitanate grains is mostly anhedral. Secondary electron imaging of bauxite residue “as is” revealed that LREE ferrotitanate grains are partly covered with submicron-sized bauxite residue matrix particulate (**Figure 43**). At most, aggregates of anhedral globular crystallites can be observed when examining larger particles that exhibit different reaction stages. This can be seen in **Figure 42**b, especially in the zone II.

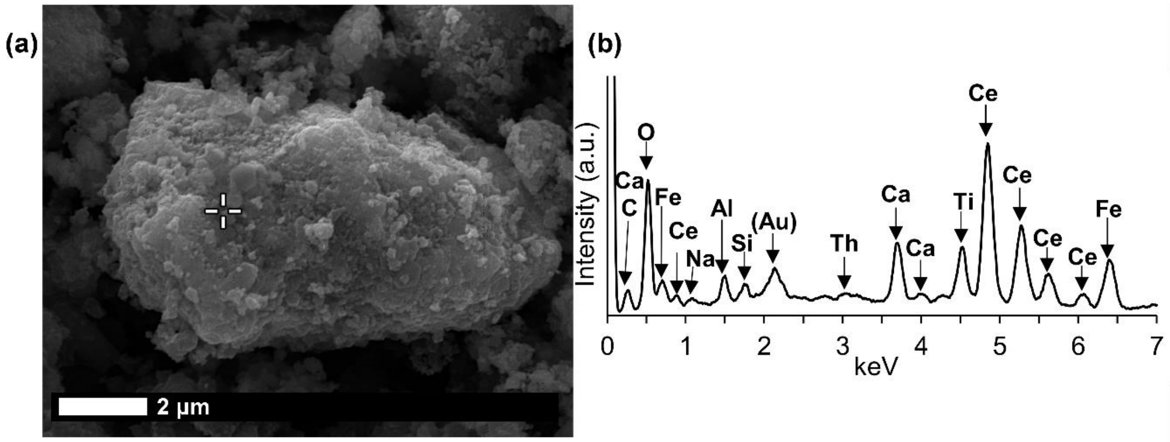

Figure 43. Ce ferrotitanate particle shown on (a) secondary electron image with its (b) EDS spectrum; gold (Au) peak is from the coating layer on the sample.

In addition, LREE-containing globular Ca ferrotitanate particles were discerned in nanoscale investigation with HRTEM (**Figure 44**, Appendix B **Table B 1**). The morphological variations of anhedral to subhedral and euhedral Ca titanate phases are shown in **Figure 45**. The maximum concentrations of REEs measured in EDS were about 3 wt % of cerium and about 2.5 wt % of lanthanum (Appendix B, **Table B 1**). The quantities of REEs below 1 wt % were regarded as unreliable due to the poor ability of EDS to measure trace constituents. Selected area electron diffraction (SAED) of a LREE bearing particle resulted in a reflection pattern indicating to a well crystallised character. The d-values (d = 0.2564 nm) measured form the patterns resemble the ones of conventional perovskite reference (d = 0.2710 nm) from [121] direction (**Figure 44**). Most of the Ca ferrotitanate particles were, however, REE-depleted. The nanoscale Ca ferrotitanates observed here are similar to those analysed in the work that elucidated the characteristics of Th contained in perovskite structure found in bauxite residue (P. N. Gamaletsos et al., 2016). Other REE-containing phases were not confidently discerned among the fine particulates of bauxite residue during nanoscale HRTEM investigation.

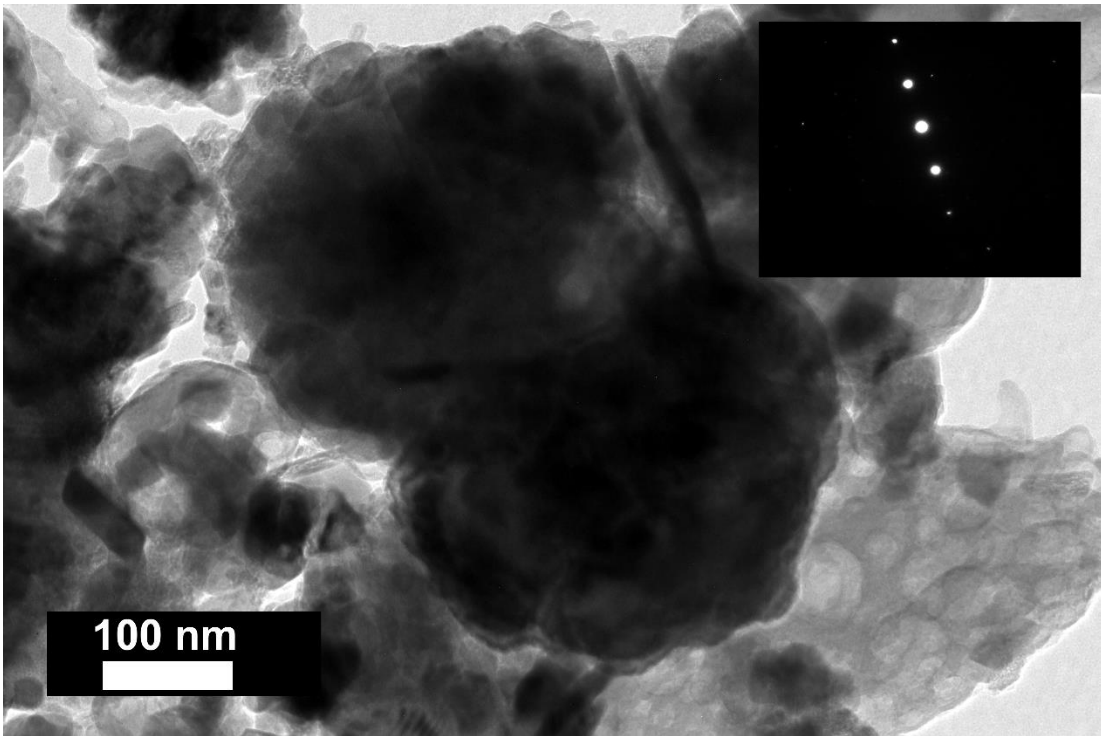

Figure 44. LREE-bearing Ca ferrotitanate observed in the bright field imaging mode of HRTEM. SAED pattern of the particle is inserted to the upper right corner. The pattern is collected from [121] direction and corresponds to perovskite structure.

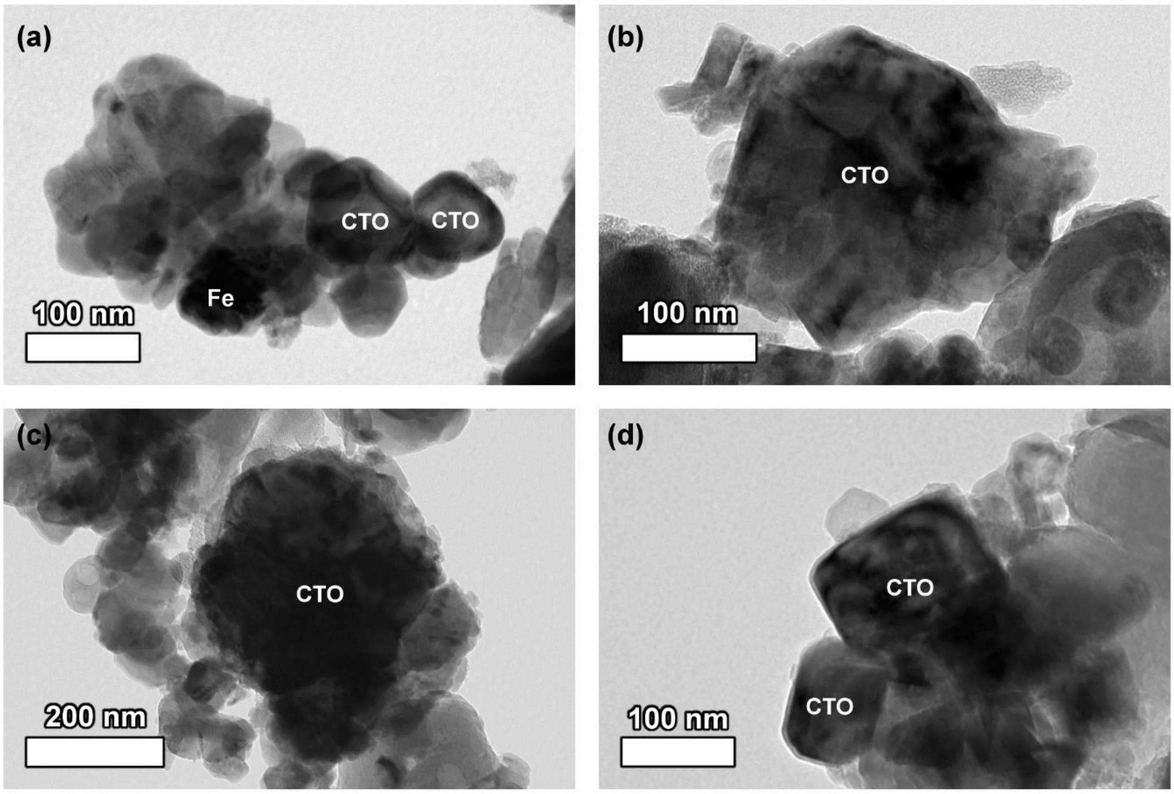

Figure 45. Morphological variations of Ca ferrotitanate (CTO) particles in nanoscale: (a) subhedral particles and a Fe oxide particle, (b) subhedral particles, (c) anhedral particle and (d) euhedral particles.

From the previously noted observations, an important conclusion should be made. Ca ferrotitanate species, likely corresponding mineralogically to perovskite, with low LREE concentration, should not be confused with the REE-barren perovskite sensu stricto ($CaTiO_3$) that is also found in bauxite residue, as detected in XRD phase quantification (**Table 7**). Such perovskite is created by a different reaction route. Namely, titanium dioxide phases, especially anatase, react partially with sodium hydroxide and then with lime added to Bayer process and as a result form perovskite sensu stricto (Smith, 2017).

When the LREE ferrotitanate particles are relatively large (20–30 µm), the variations in their chemical composition can be drawn out by elemental mapping (**Figure 46**). It is seen in **Figure 46**, that the highest REEs concentrations are found in the core of the particle. REE concentration decreases towards the edges of the particle. In the bauxite residue matrix surrounding the particle, there are no presence of REEs. The trend is the opposite for Ti, Ca and Na. Their concentration increases towards the edges of the particle. While the change in Ti concentration is quite gradual from core to edge, there is a more sudden increase of Ca concentration on the rim of the particle. The gradual change of the chemical composition refers to the existence of a solid solution between the LREE predominant and Ca-predominant end-members. Another characteristic feature of the reacted LREE ferrotitanate particles is that the outer layer tends to form a distinct Ca ferrotitanate shell around the particle, where LREEs concentrations are low (Ti, Ca and Fe maps on **Figure 46**). The zone that contains about an equal amount of Ti and REEs (corresponding to zone II on **Figure 42**b, or silica rich area in **Figure 46**, indicated with Na-Al-Si), is also intergrown with a sodium aluminium silicate phase. This likely corresponds to a secondary Bayer process phase, sodalite or cancrinite.

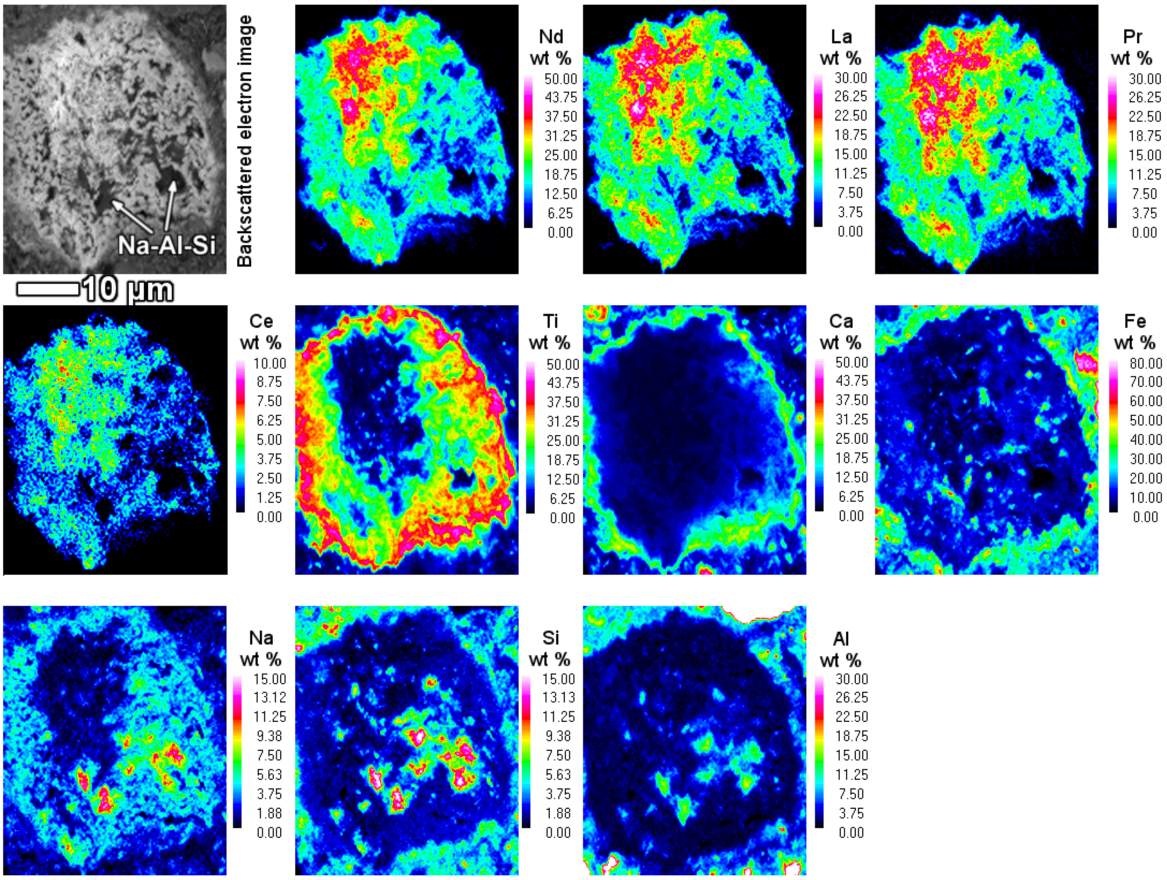

Figure 46. EPMA-WDS quantitative elemental mapping of a reacted LREE particle. The intensely reacted area is also intergrown with sodium aluminosilicate phase (indicated with Na-Al-Si). Mapped area corresponds to **Figure 42**b.

Raman spectroscopy of LREE ferrotitanate particles did not provide easily interpretable spectrograms, as shown on an example in **Figure 47**. It has been noted that certain loparite minerals result in anomalously wide Raman scattering peaks (Popova E. A. et al., 2015). In other resources such as the RRUFF database (RRUFF id: R070251), the wide wave-like features in loparite-(Ce) Raman spectra have been interpreted as fluorescence that has been induced by the laser beam. Nevertheless, the measurements made with Raman microscope provide the means to exclude that these kind of phases are not carbonates, as there is no peak observed in the range of about 1000–1100 cm^{-1}, where the carbonate C-O stretching usually occurs (Buzgar and Apopei, 2009; Yang et al., 2008). A conclusion can also be made that the occurrences termed here as LREE ferrotitanates do not contain hydroxyl ions because of the absence of characteristic bands in the region of 3200–3800 cm^{-1}, that are present for example in hydroxylbastnäsite phases (Yang et al., 2008). The minor band seen in 286 cm^{-1} could be attributed to hematite from a nearby area as in this region is commonly located the most intense band of hematite (293 cm^{-1}) (De Faria et al., 1997).

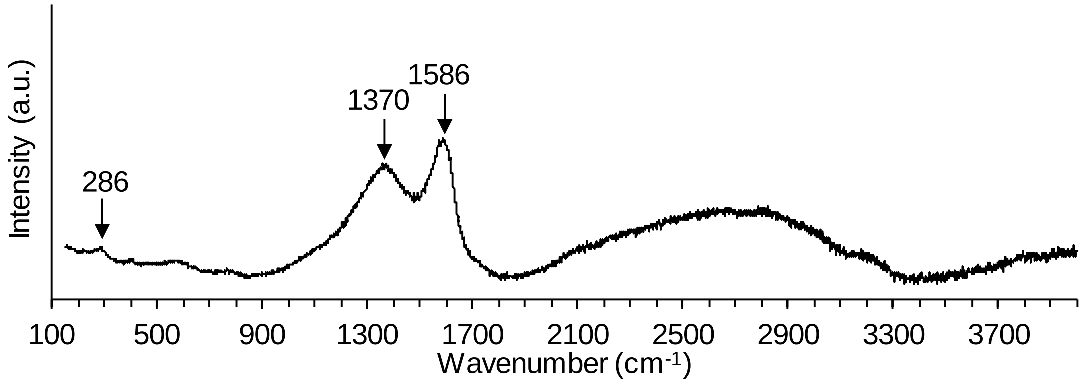

Figure 47. Raman spectrum collected from zone II of LREE ferrotitanate particle that is shown in **Figure 42**.

A few considerations can be given about the formation mechanism of such LREE ferrotitanate phases. As mentioned before, the LREE ferrotitanate phases are clearly formed during the Bayer process. The primary LREE phases interact with the Bayer process liquor. The precursor phases possibly belong to the bastnäsite mineral group of REE fluorocarbonates or cerianite as they are the most frequently encountered LREE phases in bauxite feed. Bayer liquor consists mainly of sodium aluminate and free sodium in the form of sodium hydroxide (Wellington and Valcin, 2007). There is commonly, at least in the high temperature process, also a small proportion of dissolved iron (3–50 mg/L Fe_2O_3) and titanium (1–10 mg/L TiO_2) present (Authier-Martin et al., 2001; Singh and Mishra, 2012; Teas and Kotte, 1980). In the current process, Fe concentration ranges from 2–10 mg/L and Ti concentration is about 1 mg/L (**Table 8**). The reaction appears to take place in-situ on the outer part of the REE particles (III on **Figure 42**b). There is no indication if the newly formed phases would be precipitated from the process liquor. The ions taking part in the reaction (Na, Fe, Ti, Ca) diffuse into deeper parts of the particles as the reaction progresses. Ti ions diffusion seems to be the most intense. The inner part of the particle (I on **Figure 42**b) seems to be only slightly affected by the reaction, as there is only a minor part of Ti and Fe present while no Na is detected. Similarly, the particle on **Figure 42**a has very low content of Ti and Fe as well as Na. The presence of Ca might be already inherited from the precursor mineral (**Table 13**). Thus, the complete particle on **Figure 42**a as well as inner part (I) of **Figure 42**b are neither entirely a primary REE phases nor newly created LREE ferrotitanates, but intermediate phases with a deficiency of titanium and iron. The intensely reacted zones II and III (**Figure 42**b, **Figure 46**) are also intergrown with sodium aluminium silicate phases. This might indicate to a gel-like state in the reaction front that allows also other mineral species to be nucleated and formed.

The morphology of the inner part of **Figure 42**b resembles the fibrous or acicular radiating morphology described in the case of authigenic LREE phases in bauxites (Mongelli, 1997). The middle and outer parts (**Figure 42**b II and III) exhibit a different morphology with globular crystallites, which are characteristic to the newly formed LREE ferrotitanates. They indicate also to a newly formed mineralogical character. The outer part (**Figure 42**b, III) of the particle represents the last stage of the transformation, where a high amount of Ca and Ti have been deposited with 4–23 wt% of REEs also present (**Table 15**). This latest deposition forms a distinct (ferro)titanate shell around many of the observed LREE particles, which is also emphasised in **Figure 48**. The shells are present in La- as well as Ce-predominant particles.

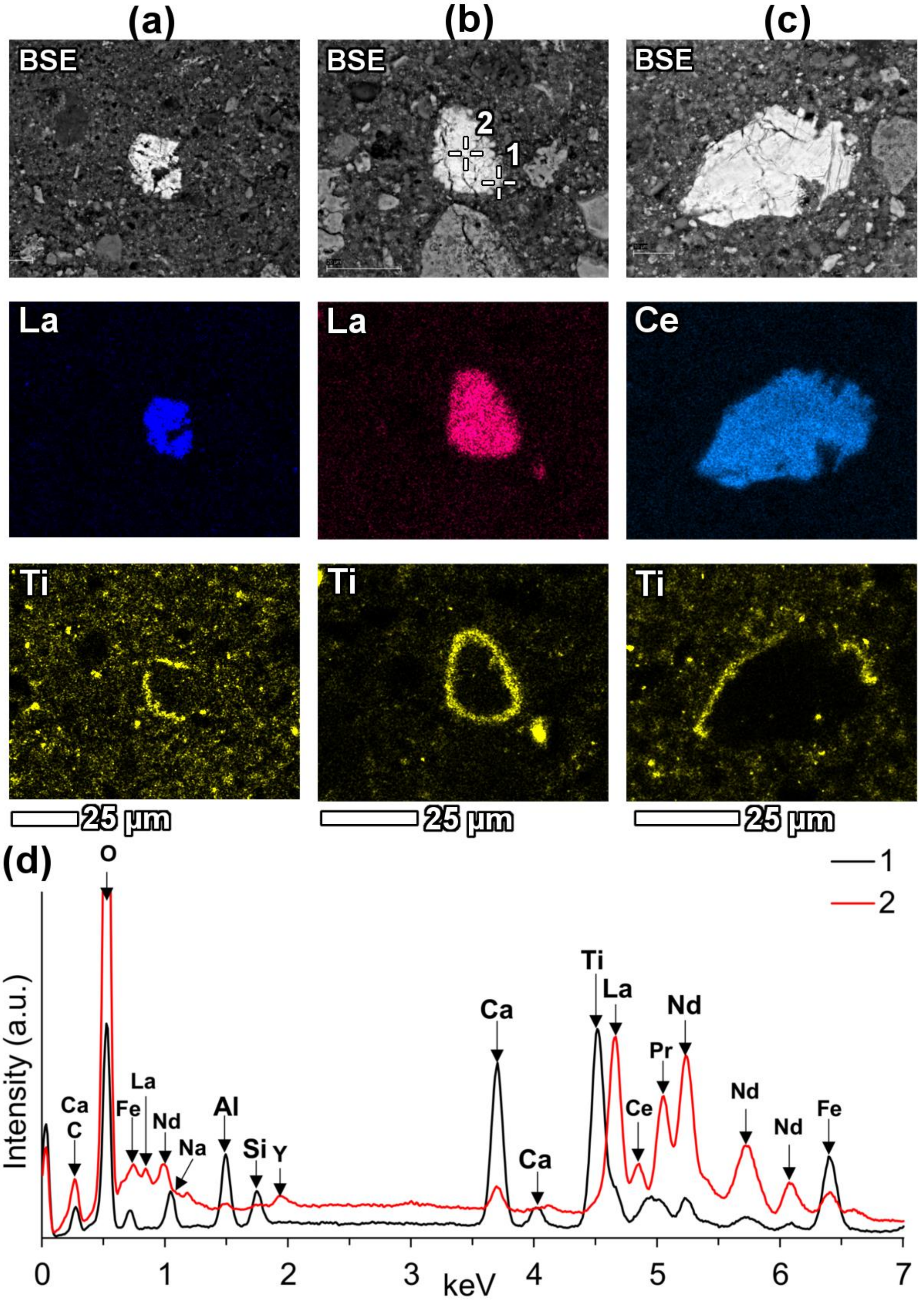

Figure 48. Various occurrences of Ca-Ti rims surrounding REE particles (a–c) with respective elemental maps and (d) EDS spectra.

Considering that the grains in **Figure 42** are relatively large, it can be assumed that smaller REE particles react entirely and their final products should be something like what is observed in the zone III on **Figure 42**b, with Ca prevailing ferrotitanates alongside some presence of REEs. Evidences have been shown in support of this claim from the nanoscale HRTEM investigation, where the maximum REE concentrations per particle did not exceed 5 wt%. The particles seen in nanoscale have a similar composition as well as morphology to the area seen in highly reacted zone III on **Figure 42**b.

In support of the in-situ transformation of LREE minerals in the Bayer process stands the fact that LREEs do not possess soluble species in highly alkaline conditions (Brookins, 1988, 1983). In a broad sense, an analogous in situ transformation of kaolinite to sodium aluminium hydrosilicate has been described to take place during Bayer process (Bánvölgyi et al., 1991).

It was observed that the LREE species containing Na, Ca, Ti and Fe in variable proportions form a solid solution. The characteristics of the solid solution are expressed on **Figure 49**, where the ionic proportions of the cations are plotted. Region denoted with I on (a) refers to the measurements reflecting the real solid solution. Region denoted with II on (a) are the measurements performed on the transitional phases that are not the final LREE ferrotitanate products. The solid solution characteristic is the most recognizable on A site, where Ca and Na substitute REEs. The correlation coefficient between the substituting cations is 0.947 (b on **Figure 49**). The endmembers of the series have ideal compositions of $(Ca,Na)(Ti,Fe)O_3$ and $(REE,Ca,Na)(Ti,Fe)O_3$. Because the measured compositions are highly variable, it is not reasonable to report any average chemical composition or formula of the LREE ferrotitanates. Some examples of the formulas can be shown that approach the ideal stochiometric end-members of the series. For the neodymium-lanthanum predominant phases they can be $(Ca_{0.40}Na_{0.36}REE_{0.22})_{\Sigma 0.98}$ $(Ti_{0.81}Fe_{0.25})_{\Sigma 1.05}O_3$ (spot 10 in **Table 15**) and $(REE_{0.56}$ $Na_{0.31}Ca_{0.22})_{\Sigma 1.08}(Ti_{0.65}Fe_{0.33})_{\Sigma 0.97}O_3$ (spot 8 in **Table 15**).

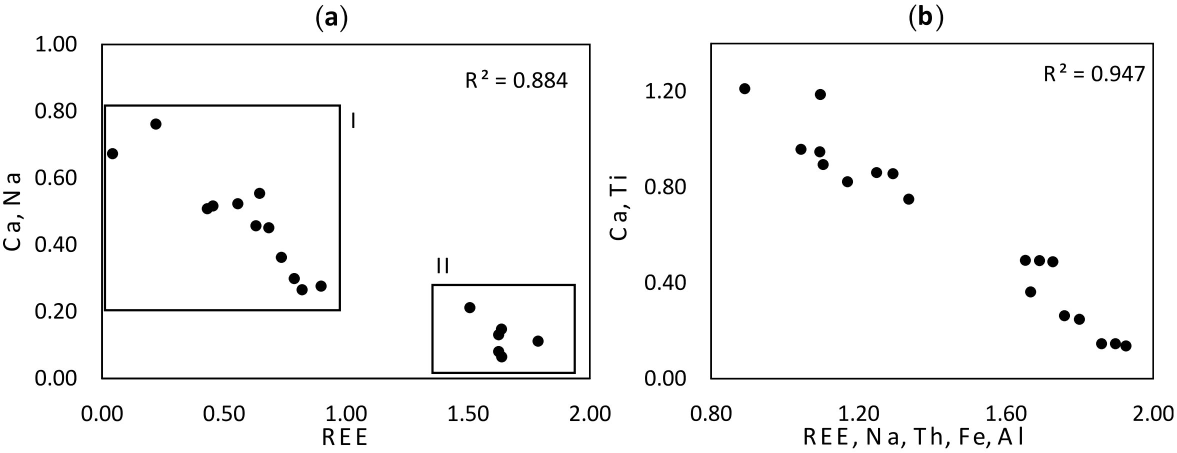
(**a**) (**b**)

Figure 49. Solid solution character of LREE ferrotitanate series, depicted as ionic proportions of the (a) substitutions of Ca and Na with REE on A site and (b) complete transformation, where (REE + Na + Th) + (Fe + Al) = Ca + Ti. Region annotated with I on (a) refers to the area of real solid solution, region annotated with II on (a) indicates to the measurements on transitional phases. Adapted after (Campbell et al., 1997; Nickel and McAdam, 1963). The equation is changed for a best description of present situation (i.e., Nb is left out of the equation whilst Th and Al are added to A and B sites, respectively). Figures are based on data from **Table 14** and **Table 15**.

The only mineral group containing species corresponding to the currently presented chemical composition (**Table 14**, **Table 15**) is the perovskite sensu lato. Perovskite group, also termed as the perovskite supergroup refers to the basic structure of ABX_3, where A is a relatively large cation, B is relatively small cation and X is oxygen or another anion (Mitchell, 1996; Mitchell et al., 2017). It's aristotypic mineral structure is cubic. However, due to the extremely wide compositional variations, many structures are possible. Perovskites exhibit extensive solid solutions, where diverse cations can occupy the A and B sites. REE-containing perovskites are well known from the natural systems and there have been many REE perovskites synthesized for several applications (Atta et al., 2016; Mitchell, 1996; Mitchell et al., 2017). The compositions measured in present work resemble the end-members of the perovskite sensu stricto ($CaTiO_3$) and loparite ($(REE,Na,Ca)(Ti,Nb)O_3$) (Castor and Hedrick, 2006) solid solution series (Mitchell et al., 2017). Loparite typically occurs in peralkaline igneous rocks, especially in nepheline syenite (Castor and Hedrick, 2006). As in the peralkaline rocks, there is an excess of sodium in the present investigated system of Bayer process. It can be noted from **Table 14** and **Table 15**, that the currently calculated mineral formulas don't have an ideal stoichiometry as there are deficiencies and excesses of ions on A and B sites. This is a regularly encountered observation for perovskites, as they are considered "defect" structures (Campbell et al., 1997; Mitchell et al., 2017). Excess and deficiency are compensated with the different ion proportions on A and B sites considering the charge balance as well as excess or deficiency of oxygen molecules (Campbell et al., 1997; Mitchell, 1996; Mitchell et al., 2017). As many of currently analysed spots show approximately 1:1 ratio of A:B sites, oxygen deficiency can be hypothesised to exist. One of the deviations compared to perovskite-loparite natural system, however, is that in current observations, there is no presence of niobium detected. Typically, niobium is a ubiquitous constituent in the natural occurrences of loparite (Mitchell et al., 2017). This is explained by the fact that present LREE ferrotitanates are formed in-situ and thus inherit partly the chemical composition of their precursor phases. In the precursor minerals, there is no niobium present (**Table 13**). Thus, niobium is not expected to appear in the reaction product either. A second slight deviation is, that the presence of iron was also observed in the discussed particles. However, iron can generally exist together with titanium on the B site of perovskite/loparite (Campbell et al., 1997), but the nomenclature of iron containing perovskites has not yet been established (Mitchell et al., 2017). Regardless of the incomplete nomenclature, perovskites with composition $LaFeO_3$ have been synthesized and characterised (Thirumalairajan et al., 2013). Since the currently investigated system is a technogenic and not a natural one, it is not uncommon to find some rarely encountered mineral types. Perovskites matching with the currently defined chemical composition have not yet been synthesised, but similar ones are for example $NaLaTi_2O_6$ or $NaCeTi_2O_6$ (Mitchell et al., 2017). Moreover, endmembers of perovskite-loparite series with formulas $Na_{0.5}Ce_{0.5}TiO_3$ and $Na_{0.5}La_{0.5}TiO_3$ have been identified as thermodynamically stable (Feng et al., 2016). Among a variety of perovskite synthesizing methods, there exist the wet chemical processes, such as hydroxide-based sol-gel process (Atta et al., 2016). Cerium titanates ($CeTi_2O_6$) with brannerite structure have been also synthesized (Valeš et al., 2014). Those titanates, however, do not match with the stoichiometry of current REE ferrotitanates because they have two moles of Ti per one mole of Ce while in the present case the A and B sites have approximately one-to-one ratio.

Present findings can also be related to some of the previously existing knowledge about REE phases in bauxite residue. During a nanoscale investigation, a perovskite phase with a general composition of $Ca_{0.8}Na_{0.2}TiO_3$ was described to contain trace amounts of Th as well possibly Ce and some other trace elements (P. N. Gamaletsos et al., 2016). The authors proposed a minor contribution from a loparite phase related to perovskite to explain the observations. That information compares well with the present analysis. The mentioned perovskite was also crystallographically characterised and matched with perovskite structure reference with some deviations from the conventional data, possibly due to the incorporation of sodium on the A site of perovskite (P. N. Gamaletsos et al., 2016). Ce and Ti correlating presence was found in a Canadian bauxite residue sample (Jonquière, Québec) (Reid et al., 2017). Bayer process derived REE-containing titanate compounds were mentioned in a patent describing the recovery of REEs from bauxite residue (Sugita et al., 2012). A recent contribution that investigated strictly the forms of Ce in bauxite residue, did not refer to any relations between Ce and Ti (Bolanz et al., 2018). The former comparison allows to suggest, that the observed LREE ferrotitanate phases presented in this study are not isolated cases for only AoG (Greek) bauxite residue, but instead seem to be a more generic characteristic that occurs in bauxite residues originating from different alumina refineries. The exception presented by Bolanz et al., (2018) who hypothesize that the main carrier of Ce is hematite, indicates to the need of examining rare earth phases in relation to Bayer process conditions as well as in relation to bauxite feed and REE occurrence forms within bauxite.

Current data supports the existence of Th in perovskite type phases contained in bauxite residue (P. N. Gamaletsos et al., 2016). In fact, compared to the 700 mg/kg Th concentration estimated in the report by Gamaletsos et al., (2016) based on EDS analysis, current WDS quantification results show that Th concentration in cerium predominant LREE ferrotitanates can reach as high as 2.7 wt% ThO_2 (**Table 14**). Also, Th is mainly associated with Ce predominant phases instead of Nd and La predominant ones. This can be explained by the possible existence of Ce in tetravalent oxidation state, which is the same as for Th. At the same time, practically all the other REEs occur only in the trivalent oxidation state. That inhibits the incorporation of Th to the mineral structure of Nd and La predominant phases. The amount of Th incorporated to LREE ferrotitanate phases is probably highly dependent on the precursor REE phases in bauxite and the content of Th within them.

Present observations deviate with the work of Gamaletsos et al., (2016) in the fact that no Nb or Zr were detected in the LREE ferrotitanate particles analysed in this work. Considering the reaction mechanism that forms the LREE ferrotitanates, it is a reasonable observation that the aforementioned elements are not present in the reacted REE particles since neither of them is a component of the precursor REE phases. Current work also disagrees with the statement of Gamaletsos et al., (2016), that bauxite residue is a very homogeneous material, for which microscale investigations, especially with regards of trace elements, are not feasible to be conducted. As shown in present work, microscale investigations, combined with nanoscale analysis, provide very detailed information about the fate of REE minerals in the Bayer process.

6.3.3 Manganese-Associated Ce Oxide or Oxyhydroxide

A part of LREE phases were found to be associated with Mn in bauxite residue. In **Figure 50** and similar observations, LREEs occur as surface adsorbed phases on manganese mineral particles. It may be assumed that they are manganese oxyhydroxides. In the case of the particles depicted on **Figure 50** as well as **Figure 51**, the Mn particle is also associated with Co and Ni as well as some Mg. Following its chemical composition, the Mn phase could be asbolane ($Mn(O,OH)_2(Ni,Co)_x(O,OH)_2 \cdot nH_2O$) (Manceau et al., 1992).

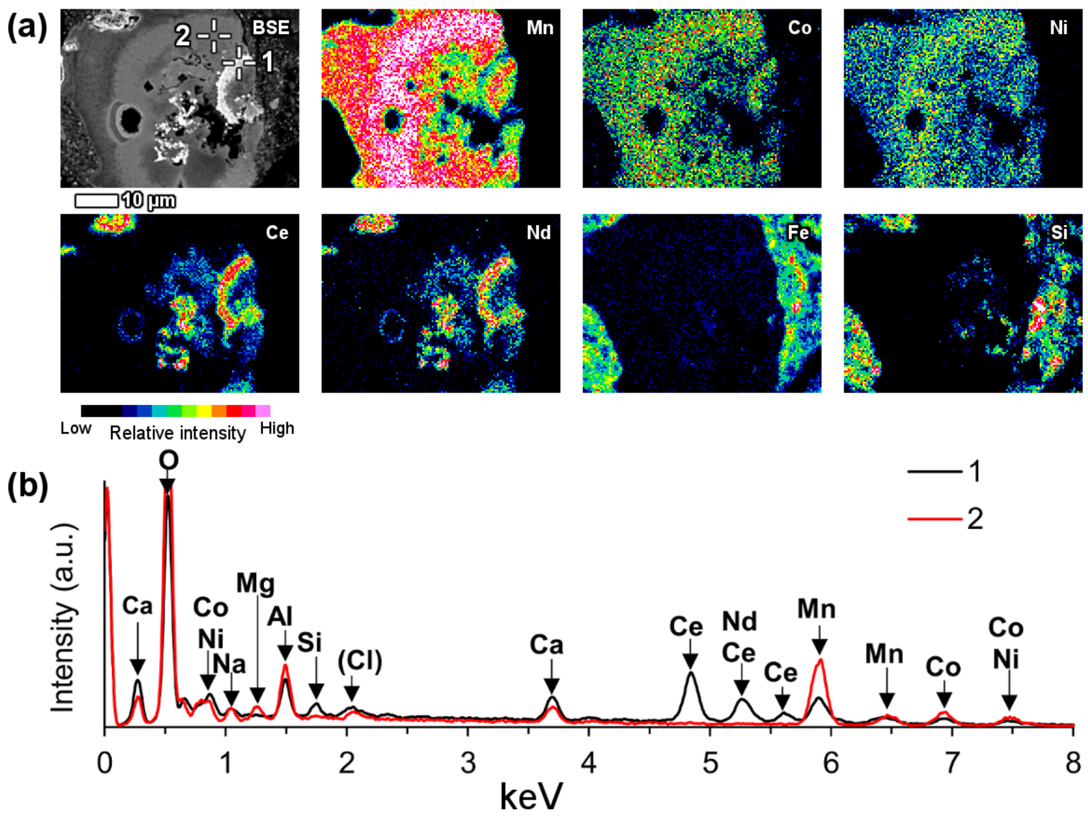

Figure 50. Ce oxide/oxyhydroxide phase associated with Mn particle shown on (a) EDS elemental map with (b) respective spectra.

It is common that the mentioned LREE formations have a circular morphology that follows the circular cavities of Mn particles or they surround the Mn grains. The referred LREE phases contain Ce as the prevailing element, but other lanthanides as well as Ca were discerned to be present also (**Figure 50**). Based on semi-quantitative EDS estimation, Ce concentration in this LREE occurrence form is about 35–40 wt%.

Individual Mn-associated LREE particles are small, about 1 µm in size, but agglomerated particles are over 10 µm in dimensions. On occasions, Mn-associated LREE phases exhibit remarkable sizes exceeding 50 µm (**Figure 51**). On the example of the particle depicted on **Figure 51**, it may be assumed that the growth of this LREE particle was nucleated on a Mn-Ni-Co particle and continued to form a Ce- and Ca-predominant particle. The fine acicular morphology of the particle on **Figure 51** indicates that the growth rate of this particle has been relatively fast.

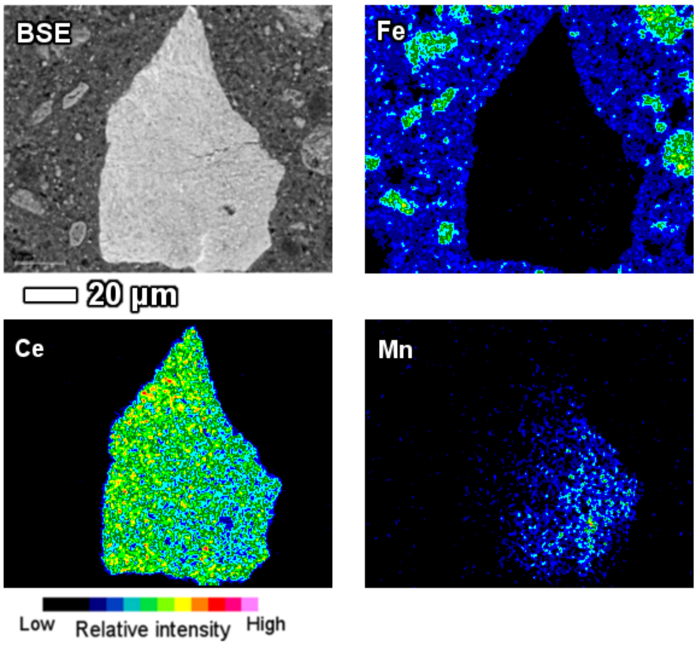

Figure 51. Ce oxide/oxyhydroxide phase associated with Mn shown on EDS elemental map.

LREE phases of this category do not exhibit the presence of phosphorus or carbon (measured in Pt-coated sample). Therefore, the occurrence form as phosphate or carbonate can be excluded. The absence of titanium, iron or sodium and a different morphology compared to LREE ferrotitanates (section 6.3.2) rules out the linkages between the LREE ferrotitanate forms. As a conclusion, these LREE phases can be termed as oxides or oxyhydroxides, which might correspond to cerianite.

Laskou and Andreou (Laskou and Andreou, 2003) have referred to the existence of minor amounts of Mn oxyhydroxides, as well as lithiophorite and brindleyite, in the Parnassos-Ghiona bauxite profiles. It is possible that these are the precursor Mn phases for the kinds observed in bauxite residue in present study. Higher REE concentrations have been noted to occur together with higher Mn concentrations in Parnassos-Ghiona bauxite profiles (Eliopoulos et al., 2014), while some authors have noted a negative correlation between the REEs and manganese contents (Laskou and Andreou, 2003). Nevertheless, relations of these Mn phases with specific REE minerals in Parnassos-Ghiona bauxites have not been noted. Even more, such Mn-associated REE occurrences have not been referred in any bauxite deposit.

Mn and REEs are chemically similar and in natural systems, Mn-adsorbed REEs are not uncommonly encountered, especially in marine environment (Pourret and Davranche, 2013). There, REEs occur in the form of adsorption onto ferro-manganese crusts and nodules (Astakhova and Sattarova, 2012; Dubinin, 2004). It is worth mentioning that similar Ce occurrence form has been revealed in Ni laterites in the Dominican Republic. Rings of cerianite in the sizes of about 5 µm or larger aggregates up to 30 µm were associated with Mn oxyhydroxides (Aiglsperger et al., 2016). The morphology of those Ce occurrence forms resembles the morphology seen in present work.

Considering that the described LREE occurrence form has only been observed in bauxite residue and its morphology indicates to a relatively fast crystallisation, it is assumed that this might be a secondary form of LREE occurrence, created during the Bayer process. An easily leachable REE occurrence form by ion-adsorption, related possibly to kaolinite, illite or chamosite, has been speculated to exist in Parnassos-Ghiona bauxites (E. Mouchos et al., 2017). This claim has some support from present investigation (**Figure 35**). It might be that the ion-adsorbed REEs are leached during the Bayer digestion and are thereafter precipitated in association with Mn particles. From the relative abundance of Ce compared to other lanthanides in these specimens, it can be assumed that Ce occurs in the tetravalent oxidation state. Similarly, the most common oxidation state of manganese is 4^+ (also 2^+), allowing a more favourable co-occurrence of these metals.

6.3.4 Heavy REE Phosphates

Heavy REE phosphates with the major constituent being Y were found in bauxite residue (**Figure 52**). Other HREEs like gadolinium, dysprosium and erbium are also present. These phases correspond to xenotime or churchite. Xenotime particles are a few µm in size. They can be either contained in a diaspore/boehmite particle (**Figure 52**) or with a free surface inside bauxite residue matrix. Either way, shielded by another particle or not, xenotime/churchite endures the Bayer digestion conditions. It appears in bauxite residue in its original form just as in bauxite ores (Laskou and Andreou, 2003).

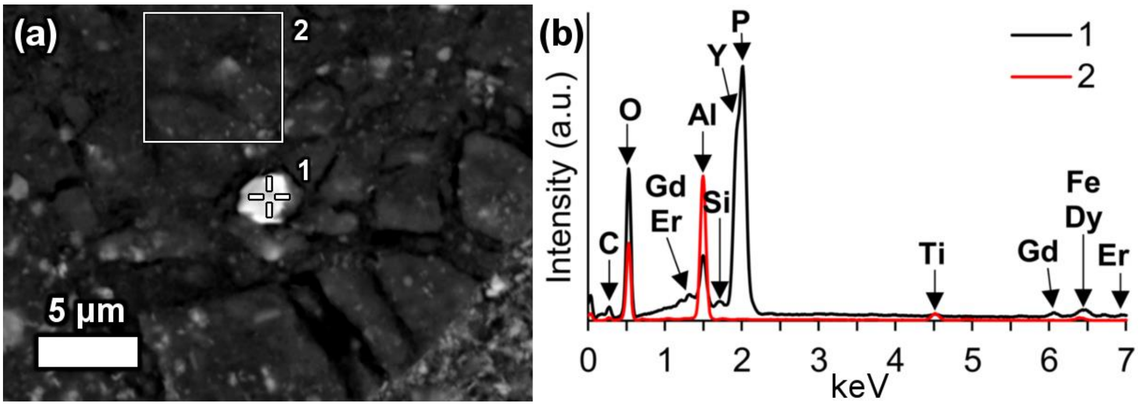

Figure 52. Xenotime or churchite in undigested diaspore/boehmite matrix, depicted on (a) backscattered electron image with its (b) EDS spectrum.

6.3.5 Mixed REE Occurrences

Some REE particles were found as mixtures of different REE species. One example of such particle is depicted in **Figure 53**. It contains Ce as the prevailing REE, while it also contains Nd, La, Ca as well as minor Y and Th (**Figure 53**b). The particle could be either a LREE carbonate or an oxide/oxyhydroxide phase. What makes it different from the formerly described observations is that it also contains phosphorus, indicating to the presence of REE phosphate phases within a mixed type of REE particle.

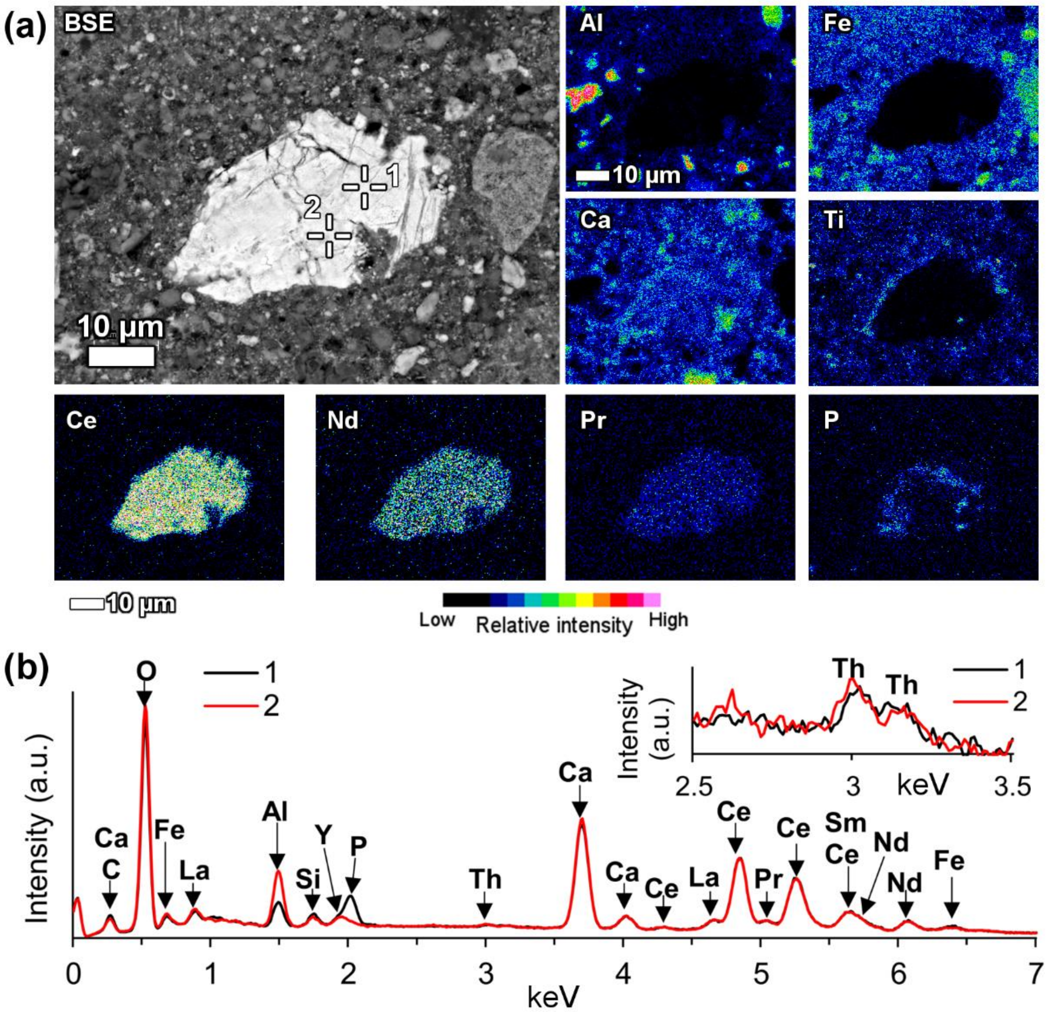

Figure 53. A mixed type REE particle shown on (a) backscattered electron image with respective EDS elemental maps and (b) EDS spectrograms corresponding to indicated spot analyses.

Another example of a mixed REE particle is depicted in **Figure 54**. The important characteristic of this particle is that the REEs are contained within the pores and fissures of a large Fe particle. The Fe particle has acted as a protective shield from the Bayer liquor and therefore the REE phases contained within it are thought to be primary ones, inherited from bauxite. In present case, Nd is the prevailing metal in the regions of REEs presence, seconded by La. Like the previously described particle in **Figure 53**, this particle (**Figure 54**) also exhibits the partial presence of phosphorous. The total area with Nd presence does not coincide with the presence of phosphorus, but all areas shown to contain phosphorus, coincide with the occurrence of Nd. Therefore, the primary LREE phases contained within the fissures and pores of the Fe particle are LREE phosphates and possibly carbonates.

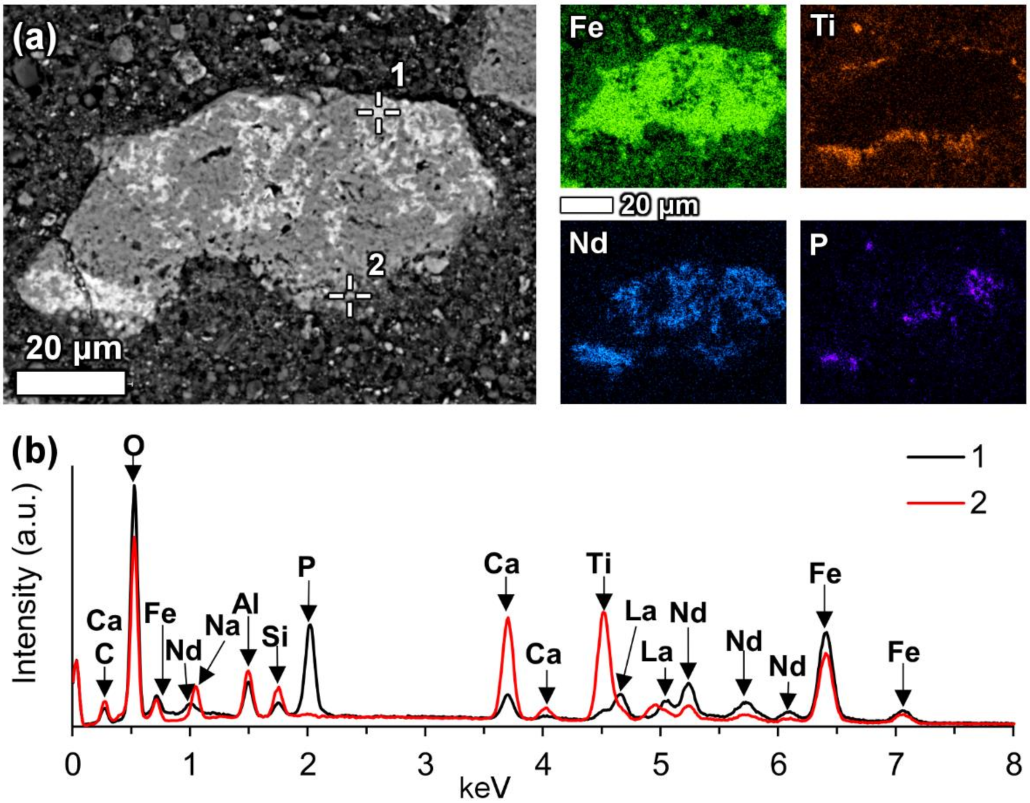

Figure 54. Mixed LREE phases entrapped in Fe grain depicted on (a) BSE and respective EDS elemental maps and (b) the corresponding EDS spectra. Element maps are monochromatic, thus there is no colour intensity scale.

Both previously described particles share the characteristic that they are partially surrounded by a calcium ferrotitanate shell or a rim, where minor LREE content is also present (**Figure 53**, **Figure 54**b). This indicates that the particles passing through the Bayer process are slightly affected by the caustic digestion. It also concludes that the majority of LREE particles found in bauxite residue are surrounded by a calcium ferrotitanate rim that has been formed during the Bayer process.

6.4 Summary of the REE Phases Physical Parameters

It is not feasible to quantify how much of each REE phase is present in bauxite residue. However, hereby the observations are summarised in **Table 16** and classified according to previously presented categories (section 6.3). The most frequently encountered REE particles are LREE ferrotitanates. This concludes that the majority of REE particles entering to the process are affected by Bayer digestion. The typical sizes of the LREE particles are 5–10 µm. HREE particles tend to be smaller, 2–3 µm. Low REEs content ferrotitanate category refers to observations with REE concentration below 5 wt %. They are mainly encountered in the very fine particulate (<1 µm) of bauxite residue, revealed by HRTEM-EDS.

Table 16. Summary of the physical parameters of the encountered REE particles in bauxite residue.

Phase	Count	Typical size (µm)	Free Surface/Total Count
LREE carbonate	1	20–30	1/1
Y phosphate (xenotime/churchite)	3	2–3	2/3
Ce phosphate	3	5–10	2/3
Partly reacted LREE ferrotitanate	4	10	4/4
High LREE content (>5 wt %) ferrotitanate	16	5–10	15/16
Low LREE content (<5 wt %) ferrotitanate	6	<1	6/6
Ce oxide/oxyhydroxide	1	5	0/1
Ce oxide/oxyhydroxide associated with Mn	3	irregular	2/3
Mixed	3	20–40	1/3

The proportions of the REE particles having a free surface were also summarised. This excludes the fact that many of the observed particles are surrounded by a calcium ferrotitanate rim. It was concluded that the majority of REE particles have a free surface. The particles might be covered only by a fine bauxite residue particulate coating, but this is likely not a chemical association. Occurrences that are categorized as “mixed” tend to be more entrapped in some other major mineral particle, such as seen in **Figure 54**.

Microscale investigation resulted in finding a remarkable number of discrete REE particles with substantially higher REEs concentration in relation to their bulk concentration in the sample. Nanoscale assessment discerned the existence of calcium ferrotitanate phases with several weight percent REEs concentrations, that also surpass REEs bulk concentration in bauxite residue. Current work does not provide support for the suggestion by Bolanz et al. (Bolanz et al., 2018) who speculated that tetravalent cerium could theoretically be located in bauxite residue within hematite lattice. Neither does present work disprove the existence of such occurrence forms.

6.5 Considerations for the Recovery of REEs from Bauxite Residue

Since the mineralogical character of REEs in bauxite residue has been elucidated, some considerations for the recovery of REEs can be suggested. The most abundant REE type identified in this work is LREE ferrotitanate. It resembles mostly the naturally occurring loparite mineral, (REE,Ca)(Ti,Nb)O_3. Loparite is currently exploited only in the Lovozero massif (Kola peninsula, Russia) (Castor and Hedrick, 2006). This mineral is being beneficiated there with the combination of density and magnetic separation methods (Jordens et al., 2013). Thus, additional physical beneficiation methods could be explored also for bauxite residue, based on the existing knowledge about loparite beneficiation. In support of this proposal is the fact that the majority of REE particles in bauxite residue are not attached to other mineral particles, i.e., they have a free surface. However, the beneficiation trials so far have not been very encouraging (Borra et al., 2016) and a likely restriction is the similar density of hematite (5.26–5.30 g/cm^3) and loparite (4.77 g/cm^3)

known from natural systems. The recovery of REEs from Lovozero loparite is performed via pyrometallurgical route by chlorination (Castor and Hedrick, 2006). Chlorination has been trialled in the case of bauxite residue (Borra et al., 2016), but this route could be developed further.

On the one hand, the observed REE particles have commonly a free surface, therefore they should be immediately affected by any treatment performed targeting the leaching of REE phases from bauxite residue. Nevertheless, the newly formed LREE ferrotitanate particles tend to have a calcium ferrotitanate shell surrounding them. The named shells might hinder the effectiveness of leaching performance due to the need of dissolving the titanate shell before the reaction reaches to the area with high REEs concentrations.

Another approach for discussing these matters is to compare REE phases found in bauxite and in bauxite residue. In metallurgical terms, the REE fluorocarbonates that are found in bauxites should be easier to be processed compared to the complex LREE ferrotitanate phases in bauxite residue. Thus, the route of recovering REEs from crushed bauxite before Bayer digestion is encouraged to be tested. In support of the latter, it has been demonstrated that between 19% and 47% of REEs in bauxite are easily leachable, in fact ion exchangeable, using ammonium sulphate. The authors also proposed an option to selectively mine the REE-enriched lower parts of bauxite deposits and thus recover REEs prior to the Bayer process (E. Mouchos et al., 2017). Present mineralogical assessment supports such an approach, as the REE phases in bauxite are less complex than in bauxite residue.

The fact that Th is associated with LREE phases, particularly with Ce predominant ferrotitanates, indicates to a possible route of removing Th from the system. If REE leaching from bauxite residue is performed, Th should also be leached because of its presence in the same mineral phases as the REEs. The simultaneous dissolution of REEs and Th is a well-documented behaviour in the REEs industry (Habashi, 2013). This so far has not been identified in the case of bauxite residue (Borra et al., 2016). The possible leaching of Th along with REEs could be potentially beneficial for the use of leached bauxite residue in construction materials. Naturally occurring Th with its radionuclide series is the main source of ionising radiation related to bauxite residue, that puts certain limits to the re-use of this material in construction applications in its raw form (Goronovski et al., 2018; Nuccetelli et al., 2015).

7. Modes of Occurrences of Sc in Bauxite and Bauxite Residue

Chapter 7 is based on the following publication: Vind, J., Malfliet, A., Bonomi, C., Paiste, P., Sajó, I.E., Blanpain, B., Tkaczyk, A.H., Vassiliadou, V., Panias, D., 2018. Modes of occurrences of scandium in Greek bauxite and bauxite residue. Minerals Engineering 123, 35–48.

Based on the elevated Sc concentration of karst bauxites (43–56 mg/kg Sc; **Table A 1**) compared to the currently assessed lateritic bauxites (7–8 mg/kg Sc), a detailed microscale speciation of Sc was focused on the Sc-enriched Parnassos-Ghiona bauxite samples representing the major input of Sc to the Bayer process system (96% of total Sc). Once again, bauxite residue was subjected to detailed microscale speciation of Sc that represents the major output carrier of Sc from the Bayer process (refer to section 4.2).

7.1 Sc Hosted in Hematite and Goethite

7.1.1 Bauxite Samples

Iron phases are represented by hematite and goethite in the assessed Parnassos-Ghiona bauxite samples, as detected by XRD (**Table 7**). It was determined qualitatively and quantitatively by EPMA-WDS that iron oxide matrices contain Sc in elevated concentrations when compared to the bulk Sc concentrations of the respective samples (**Figure 55**, **Table 17**, **Table 18**). The rest of the mineral matrix measurements shown in **Figure 55** will be addressed further on in the text. The analysed areas containing mainly iron phases were chosen as those with the highest possible purity (e.g. **Figure 56** showing the area of LA-ICP-MS measurements). However, minor contribution from other compounds might have occurred because Al_2O_3, TiO_2 and SiO_2 impurities were also detected with both EPMA-WDS and LA-ICP-MS techniques. Al_2O_3 content might be from finely dispersed aluminium oxyhydroxide phases, SiO_2 because of kaolinite group phases contribution, and TiO_2 can be either because of the occurrence of Ti in hematite mineral lattice or due to the occurrence of nanoscale titanium dioxide phases in the matrix. The latter have been proven to exist in the diaspore matrix of Parnassos-Ghiona Fe-depleted bauxite (Gamaletsos et al., 2017).

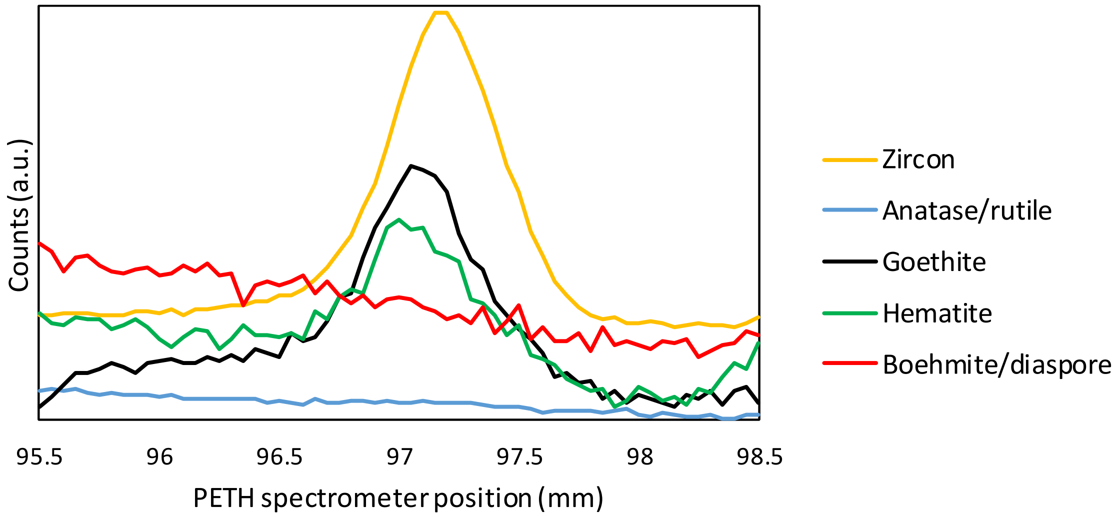

Figure 55. Qualitative identification of Sc peaks (in positions 97.05–97.20 mm) in different mineral matrices with PETH spectrometer of the EPMA-WDS instrument. Spectrum of goethite is retrieved from bauxite residue sample; the rest are from Parnassos-Ghiona B3 horizon bauxite samples.

A representative area of the iron oxide dominant matrix was identified to be hematite-dominant by μ-Raman spectroscopy (**Figure 57**). It is possible to conclude that Raman bands at wavenumbers 225, 245, 292, 411, 496 and 610 cm^{-1} are attributed to hematite, when comparing the spectra with those presented in the literature and reference patterns measured with the same exciting laser wavelength (785 nm) reported by different authors (De Faria et al., 1997; Gamaletsos et al., 2007; Lafuente et al., 2015). Minor band at 450 cm^{-1} could represent diaspore (Gamaletsos et al., 2007; Ruan et al., 2001) and a band at 661 cm^{-1} could be attributed to magnetite. Because of its gaussian shape, the latter could also be a fluorescence peak. Magnetite has not been confirmed to appear in the bulk sample by XRD, but it might occur under the detection limit of this technique.

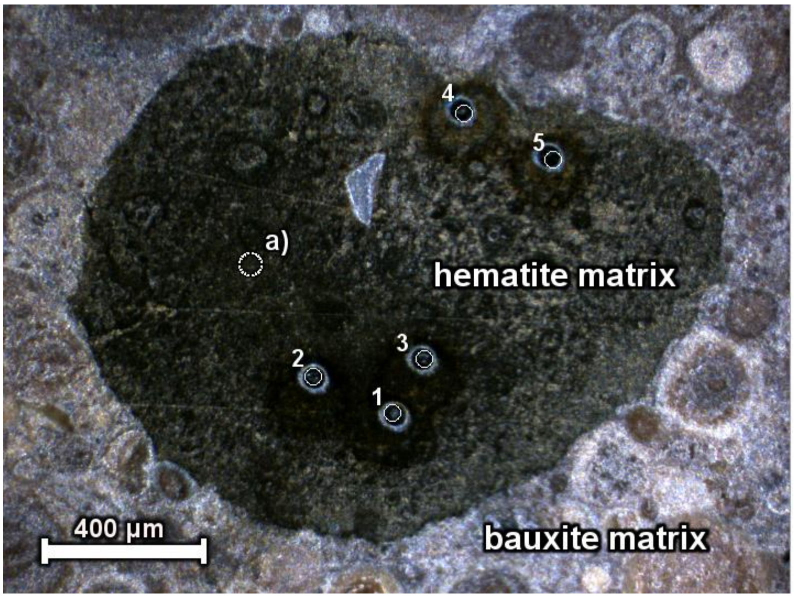

Figure 56. Optical microscope image of bauxite DD hematite-dominant matrix area surrounded by multiphase bauxite matrix. The numbers indicate LA-ICP-MS measurement spots (**Table 18**) and "a)" is the spot of µ-Raman measurement depicted in **Figure 57**.

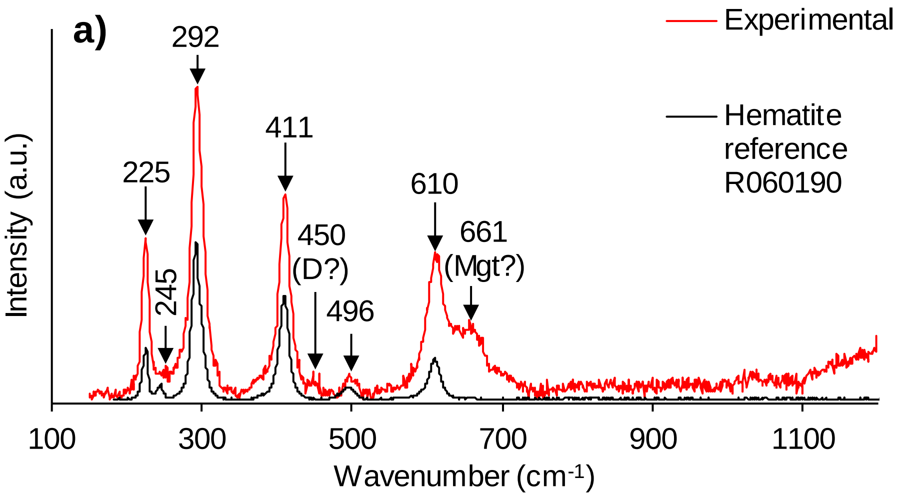

Figure 57. Raman spectrum of an example hematite matrix area of bauxite DD in relation to hematite reference. D — diaspore, Mgt — magnetite. Peaks with only numeric indexing are attributed to hematite. Reference spectrum is from RRUFF database (Lafuente et al., 2015).

The average Sc concentration in the DD-BX sample hematite-dominant matrices was higher (260 mg/kg) than that of the ST-BX sample (170 mg/kg) (**Table 17**), measured by EPMA-WDS. Full data of the quantification are displayed in Appendix B, **Table C 1** and **Table C 2**. The standard deviation (S.D.) in **Table 17** and in the following tables is calculated as the *sample standard deviation* for a better representation of the whole sample, considering the small number of performed measurements. The occasional high S.D. values in **Table 17** and in following tables are due to the high spread of the measured values.

The presence of Sc in hematite matrices of bauxite was further confirmed by LA-ICP-MS measurements (**Table 18**). The two methods produced constant values for both samples. Sample DD-BX with higher Sc contents in hematite areas yields also higher bulk concentration of Sc (**Table A 1**). When comparing two methods, the average concentration of Sc in the hematite matrix of 200 mg/kg measured by EPMA-WDS was almost identical to the average value determined by LA-ICP-MS on both bauxite samples, 199 mg/kg (n = 9). The average Sc concentration contained in the hematite matrix equals to that of an Australian laterite deposit, where Sc content in hematite was also shown to be 200 mg/kg on average (Chassé et al., 2017). The most probable form of occurrence of Sc in hematite is by the known substitution of Fe^{3+} with Sc^{3+} (Chassé et al., 2017; Horovitz, 1975; Samson and Chassé, 2016). The occurrence of goethite was not revealed during microscale analysis of bauxite samples. Therefore, it was not possible to establish whether goethite hosts any Sc in bauxites or not. It could be that goethite occurs in these samples in sub-µm size. Laskou and Economou-Eliopoulos, (2007) as well as Laskou and Economou-Eliopoulos, (2013) have noted the presence of goethite in Parnassos-Ghiona bauxites in association with pyrite and diaspore in veins crosscutting the bauxite matrix as well as in small (~10 µm) cavities.

Table 17. Chemical composition of hematite-dominant matrices of bauxite samples determined by EPMA-WDS. In the category "Greek bauxite overall", measurements of the two Greek Parnassos-Ghiona bauxite samples are combined.

Analyte	**Bauxite DD-BX (n = 12)**			**Bauxite ST-BX (n = 16)**			**Parnassos-Ghiona overall (n = 28)**		
	Median	Average	S.D.	Median	Average	S.D.	Median	Average	S.D.
Fe_2O_3 (wt %)	88.12	85.84	7.66	96.13	95.97	1.32	94.13	91.63	7.14
TiO_2 (wt %)	2.82	2.82	0.51	2.52	2.53	0.38	2.57	2.66	0.46
Al_2O_3 (wt %)	9.58	11.83	8.36	1.98	2.47	1.82	3.00	6.48	7.25
SiO_2 (wt %)	1.12	1.14	0.11	0.57	0.64	0.33	0.80	0.85	0.36
Na_2O (wt %)	0.00	0.01	0.01	0.02	0.02	0.01	0.01	0.01	0.01
CaO (wt %)	0.15	0.15	0.03	0.11	0.11	0.04	0.13	0.13	0.04
Cr_2O_3 (wt %)	0.22	0.22	0.04	0.18	0.20	0.06	0.20	0.21	0.05
V_2O_3 (wt %)	0.09	0.09	0.01	0.23	0.24	0.04	0.20	0.18	0.08
Sc (mg/kg)	260	260	20	180	170	40	200	200	60
Total (wt %)	102.11	102.16	0.92	102.18	102.21	1.37	102.14	102.19	0.04

Table 18. LA-ICP-MS analysis of bauxite hematite matrix sites. Fe was used as a standard element. Therefore, its content appears constant in all the analysed spots (see Materials and Methods section 2.4). SiO_2 measurements are from SEM-EDS.

Analyte	**Bauxite DD-BX**							**Bauxite ST-BX**			
	1	2	3	4	5	6	7	8	9	**Average**	**S.D.**
Fe_2O_3 (wt %)	91.86	91.86	91.86	91.86	91.86	91.86	91.86	91.99	91.99	91.89	0.06
TiO_2 (wt %)	2.61	2.65	2.47	2.62	2.59	2.57	2.71	3.27	3.19	2.74	0.29
Al_2O_3 (wt %)	3.11	3.97	4.37	8.81	4.66	5.23	5.81	4.35	9.66	5.55	2.23
SiO_2 (wt %)	0.60	0.60	0.60	0.00	0.60	0.60	0.00	0.30	0.30	0.40	0.26
Cr_2O_3 (wt %)	0.25	0.26	0.25	0.30	0.26	0.25	0.27	0.33	0.37	0.28	0.04
V_2O_3 (wt %)	0.19	0.20	0.19	0.18	0.19	0.19	0.17	0.24	0.26	0.20	0.03
Sc (mg/kg)	220	220	214	204	214	209	205	146	157	199	28
Total (wt %)	98.62	99.54	99.74	103.77	100.15	100.70	100.82	100.48	105.76	101.06	2.26

7.1.2 Bauxite Residue Sample

As in bauxite samples the most commonly encountered Sc-containing particle type in its residues is hematite-dominant (**Figure 58**, **Table 19**). Two populations of hematite-dominant particles were categorized as Sc-hosting and Sc-depleted (**Table 19**). The population of Sc-depleted material (average 30 mg/kg) was defined by categorizing Sc concentrations below the lowest measured content of Sc in bauxite samples hematite matrices, <100 mg/kg (**Table C 1**). This category is thought to represent material derived from lateritic bauxite feed, which has a negligible bulk Sc content (7–8 mg/kg). It is not possible to propose any other sources for this population of Sc-depleted hematite. The Sc-hosting category has a similar average Sc concentration (190 mg/kg, **Table 19**) as the examined population of Greek bauxite hematite matrices (200 mg/kg, **Table 17**). The bauxite feed proportion in the production is 80 % karst and 20 % lateritic and the hematite input is therefore 90 % from karst and 10 % lateritic bauxite (calculated by combining phase quantities in **Table 7** and the feed proportions). This reasoning allows an overall estimation of average Sc content in hematite-dominant particles of bauxite residue to be reported as 170 mg/kg.

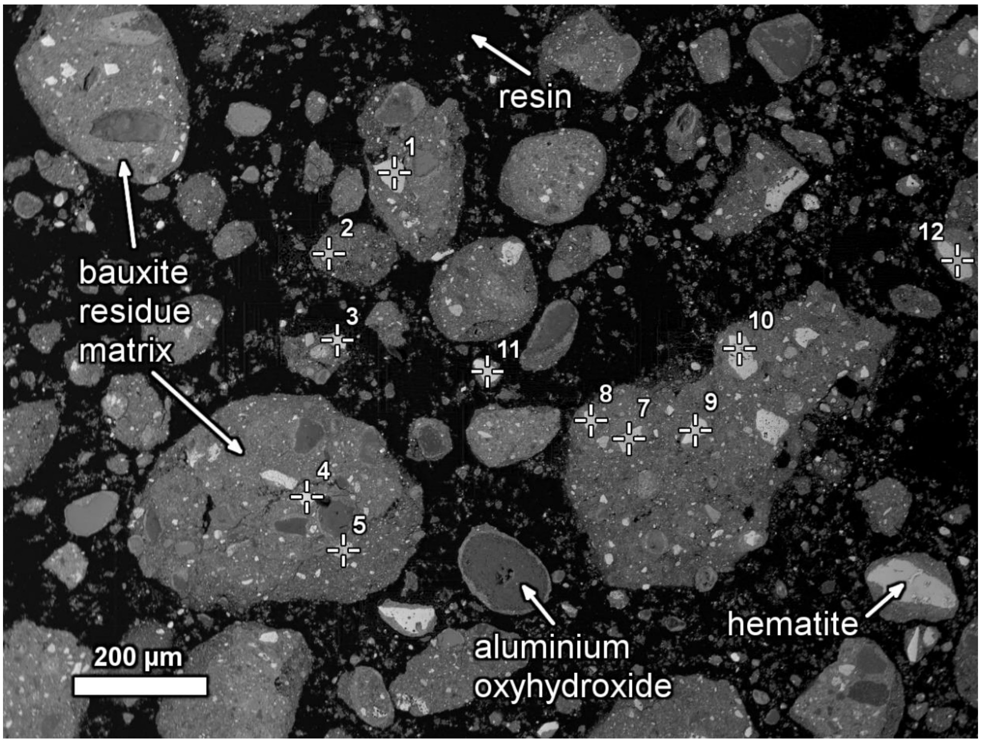

Figure 58. BSE image of a selection of analysed spots of hematite-dominant grains in bauxite residue. Measurements are summarized in **Table 19** and individual measurements are reported in Table A.4.

Table 19. EPMA-WDS quantification of iron phase matrices of bauxite residue.

Analyte	**Sc-hosting hematite (n = 24)**			**Sc-depleted hematite (n = 32)**			**Goethite (n = 12)**		
	Median	Average	S.D.	Median	Average	S.D.	Median	Average	S.D.
Fe_2O_3 (wt%)	93.55	92.02	4.06	93.93	93.81	3.49	84.86	85.89	4.84
TiO_2 (wt%)	3.52	3.98	2.17	0.94	1.02	0.82	0.72	2.36	3.34
Al_2O_3 (wt%)	1.82	1.79	0.60	1.66	1.91	1.47	0.61	0.75	0.72
SiO_2 (wt%)	0.45	0.71	0.60	1.14	1.11	0.68	1.76	1.84	0.43
Na_2O (wt%)	0.21	0.29	0.26	0.40	0.43	0.27	0.37	0.36	0.23
CaO (wt%)	0.42	0.49	0.32	0.42	0.44	0.17	0.20	0.29	0.20
Cr_2O_3 (wt%)	0.18	0.24	0.12	0.03	0.05	0.05	0.03	0.05	0.04
V_2O_3 (wt%)	0.14	0.17	0.11	0.03	0.07	0.12	0.04	0.05	0.03
Sc (mg/kg)	180	190	70	30	30	20	300	330	240
Total (wt%)	101.05	99.74	3.39	99.26	98.99	2.28	90.80	91.73	3.15

In the bauxite residue sample, another iron phase was distinguished from hematite by its darker hue in the backscattered electron imaging mode (**Figure 59**), its distinctively high WDS peak in qualitative scanning (**Figure 55**), and its higher Sc content (**Table 19**, **Table 20**, **Table C 5**). Quantitative EPMA-WDS analysis resulted in a deficiency of about 10 % in total oxide values, and this is attributed to hydroxyl content. This iron oxyhydroxide phase was identified as goethite in µ-Raman spectroscopic analysis (bands 204, 221, 240, 296, 396, 472, 546 cm^{-1}), sometimes associated with hematite in the same particle (bands 224, 246, 291, 410, 495, 609 cm^{-1}) (**Figure 59**, **Figure 60**) (De Faria et al., 1997; Lafuente et al., 2015). Raman identification of Sc-bearing goethite was repeated on several particles. The claimed goethite phase contains 330 mg/kg of Sc on average and maximum values exceed 800 mg/kg while the standard deviation is high because of the high spread of the measured values. Often, but not always, goethite is associated to Sc-depleted hematite containing no or very low amounts of Sc (**Figure 59**, **Table 20**).

A potential scenario explaining the observed complex goethite/hematite structures as the one shown in **Figure 59** assumes that the mixed goethite/hematite particles originate from the lateritic bauxite instead of the karstic one and therefore are initially Sc-depleted. During the bauxite digestion stage, Sc might be partially dissolved from some Sc-bearing minerals into the Bayer process liquor and subsequently adsorbed on the goethite surface giving rise to goethite particles with high Sc concentration. The above hypothesis is not uncommon as Chassé et al. (2017) have revealed in a high Sc grade Australian laterite deposit that Sc is adsorbed on the surface of goethite, giving rise to an average concentration of about 1300 mg/kg associated with this phase. By contrast, in hematite Sc is held in the mineral lattice with a lower concentration of approximately 200 mg/kg (Chassé et al., 2017). In broad terms, a similar partitioning between hematite and goethite with regards to Sc contents is also evident in our investigated system of Bayer process derived residue. If this analogy holds true, the occurrence mode of Sc in goethite of present study could also be attributed to Sc adsorption phenomena.

Another scenario explaining the formation of complex goethite/hematite structures is based on the transformation of goethite to hematite that is induced through a reaction with lime. The reaction path includes the formation of iron hydrogarnet as an intermediate product which is further decomposed into hematite (Smith, 2017). During the transformation of the originally Sc-contained goethite phases to iron hydrogarnets, Sc is liberated because it cannot enter to the intermediate hydrogarnet phase, as indicated below (section 7.3.2) and also reported in the literature (Suss et al., 2017), giving rise to the formation of a new Sc-depleted hematite phase.

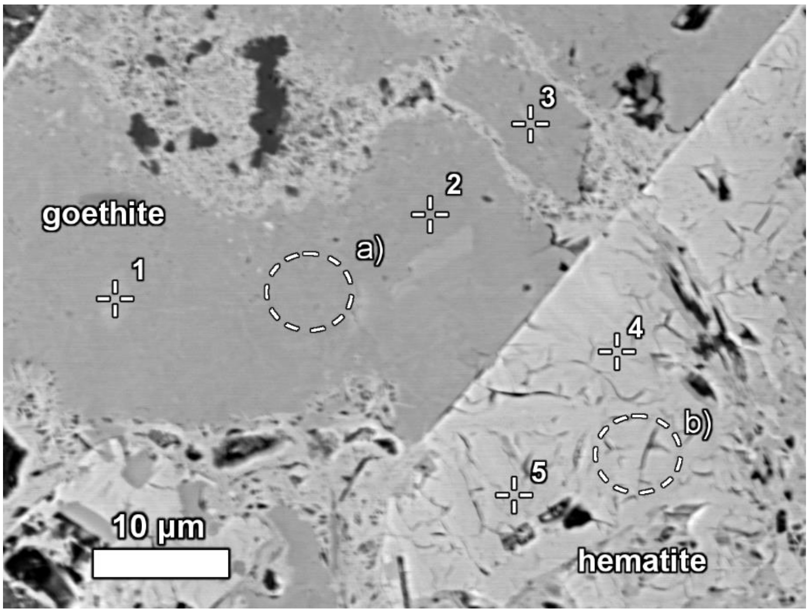

Figure 59. Micro-area of Sc-rich goethite and Sc-depleted hematite contained in bauxite residue shown on backscattered electron image. Numbers 1–5 indicate to EPMA-WDS measurements (**Table 20**); letters "a)" and "b)" indicate the approximate areas of µ-Raman measurements (**Figure 60**).

Table 20. EPMA-WDS quantification of goethite (1–3) and hematite (4–5) areas corresponding to **Figure 59**.

Analyte	**Goethite**			**Hematite**	
	1	2	3	4	5
Fe_2O_3 (wt%)	88.91	80.13	83.07	101.11	100.80
TiO_2 (wt%)	0.33	7.81	9.33	1.56	1.52
Al_2O_3 (wt%)	0.15	0.51	0.69	0.11	0.15
SiO_2 (wt%)	1.70	1.39	1.59	0.07	0.10
Na_2O (wt%)	0.20	0.15	0.46	0.03	0.01
CaO (wt%)	0.14	0.10	0.17	0.10	0.13
Cr_2O_3 (wt%)	0.00	0.02	0.07	0.08	0.09
V_2O_3 (wt%)	0.01	0.08	0.11	0.28	0.28
Sc (mg/kg)	300	400	290	0	10
Total (wt%)	91.47	90.26	95.53	103.34	103.08

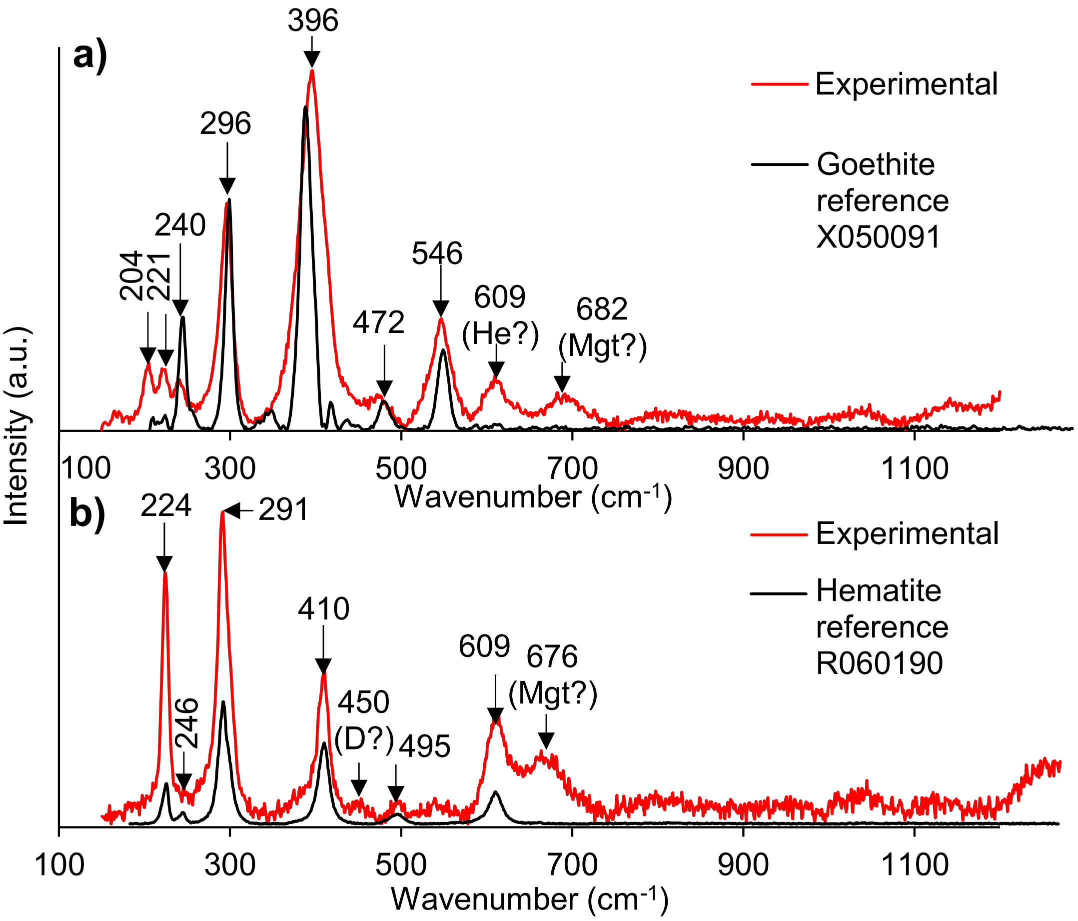

Figure 60. Raman spectra of a) goethite area and b) hematite area contained in bauxite residue in relation to reference spectra. Analysed locations are indicated in **Figure 59**. He — hematite, D — diaspore, Mgt — magnetite; peaks with only numeric indexing are attributed to a) goethite, b) hematite. Reference spectra are from RRUFF database (Lafuente et al., 2015).

7.2 Aluminium Oxyhydroxides as Minor Sc Hosts

Diaspore and boehmite, the respective aluminium oxyhydroxide phases contained in bauxites as well as in the residues, are relatively depleted in Sc (**Figure 55**, **Figure 61**, **Table 21**, **Table 22**). As in the case of iron oxide matrices, it is considered that the analysed spots are not completely pure aluminium oxyhydroxides, but rather matrices of different phases with a high and prevailing content of Al_2O_3. Minor peaks of Sc could be identified on some of the qualitatively analysed spots (**Figure 55**). The Sc amount that could be quantified was right on or slightly above the detection limit of EPMA-WDS method with an average of about 10 mg/kg (**Table 21**) in both bauxite (**Table C 6**) and bauxite residue aluminium oxyhydroxide particles (**Table C 7**). LA-ICP-MS measurements on the bauxite ST-BX aluminium oxyhydroxide locations indicated an average of 16 mg/kg Sc (**Table 22**).

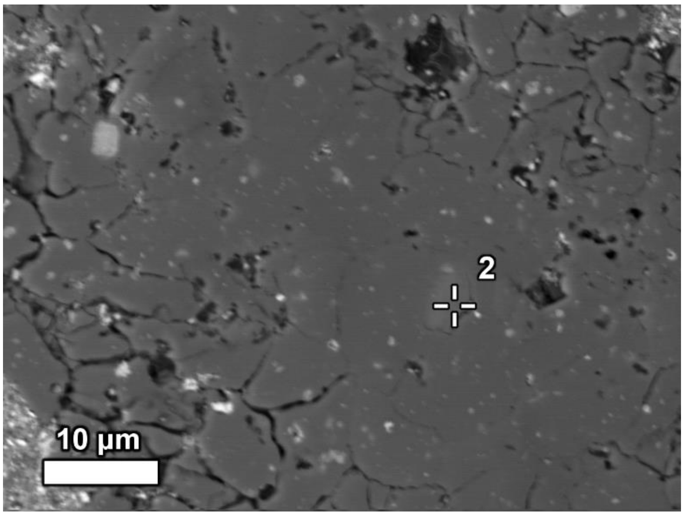

Figure 61. BSE image of an aluminium oxyhydroxide dominant particle observed in bauxite residue. Quantification of spot “2” is shown in **Table C 7**.

The results of this work prove once more the preference of Sc substitution towards iron phases instead of aluminium ones, due to the relative similarity of Sc^{3+} with Fe^{3+} rather than with Al^{3+}. The latter should not be excluded as the substitution of Al^{3+} by Sc^{3+} has also been described to take place (Horovitz, 1975) and in Middle Timan bauxite (Urals, Russia), this is the primary form of Sc occurrence (Suss et al., 2017). Consequently, a small proportion of Sc could possibly be released from diaspore/boehmite minerals to processing liquor during Bayer digestion.

Table 21. EPMA-WDS quantification of aluminium oxyhydroxide matrices of bauxite samples (n = 14).

Analyte	Median	Average	S.D.
Fe_2O_3 (wt %)	3.53	4.03	1.88
TiO_2 (wt %)	0.18	0.42	0.46
Al_2O_3 (wt %)	88.40	89.02	2.18
SiO_2 (wt %)	0.45	0.44	0.25
Na_2O (wt %)	0.01	0.01	0.01
CaO (wt %)	0.04	0.06	0.09
Sc (mg/kg)	10	10	10
Total (wt %)	94.87	93.98	2.91

Table 22. LA-ICP-MS quantification of aluminium oxyhydroxide matrices of bauxite sample ST-BX. Al was used as a standard element. SiO_2 is from SEM-EDS.

Analyte	1	2	3	4	5	6	7	Average	S.D.
Fe_2O_3 (wt %)	2.52	2.66	3.21	2.43	3.15	3.22	3.51	2.96	0.42
TiO_2 (wt %)	1.91	1.82	1.86	1.53	0.11	0.12	0.13	1.07	0.89
Al_2O_3 (wt %)	82.14	82.13	82.13	82.13	81.38	82.51	82.51	82.13	0.38
SiO_2 (wt %)	0.00	0.00	0.00	0.00	1.07	0.86	0.86	0.40	0.50
Cr_2O_3 (wt %)	0.02	0.02	0.02	0.02	0.01	0.01	0.02	0.02	0.00
V_2O_3 (wt %)	0.04	0.04	0.05	0.05	0.03	0.03	0.03	0.04	0.01
Sc (mg/kg)	23	20	20	15	10	10	11	16	6
Total (wt %)	86.68	86.74	87.33	86.20	85.79	86.78	87.09	86.66	0.52

7.3 Minor and Secondary Phases

7.3.1 Sc-Hosting

Zircon ($ZrSiO_4$), detected in bauxite and its residue samples, was found to contain the highest concentration of Sc throughout the analysed mineral species with an average of about 3600 mg/kg (**Table 23**). Sc peaks were also identified both in WDS (**Figure 55**) and in EDS spectra (**Figure 62**). In the observed grains, zones with higher Sc and Ca contents can be detected, visualized in backscattered electron imaging by darker tones (**Figure 62**). Very high heterogeneity of Sc contents in zircon is evident, probably because of Sc-depleted zircons originating from lateritic bauxite and/or because of the zonation of the Sc presence in zircon. This results also in a very high standard deviation. Sc bearing zircon, containing also Hf, U and Ca consistent with present observations, was detected in karst bauxite in the Southern Apennines, Italy (Boni et al., 2013). It seems that in bauxite residue, the highest values of Sc in zircon are correlated with the higher concentrations of Ca, Al as well as U when comparing with the measurements with low Sc concentration. However, the Sc concentration does not seem to be dependent on Hf concentrations. This regularity is also emphasised in the relative elemental concentration profiles shown in **Figure 62**c, where higher concentrations of Sc and Ca coincide with the decreased concentrations of Zr and Si. The former example is another case of the heterogeneity of Sc presence inside zircon. Therefore, a multivalent substitution in zircon involving Ca, Al, U and Sc can be hypothesized to exist in these occurrences of zircon in bauxite and its residue. Resulting from the preceding, it can also be inferred that parts of Hf and U in bauxite residue are associated with zircon. The zonation of zircon with Sc-enriched areas has been explained to occur as a result of zircon alteration in some bauxite deposits, giving rise to a partly amorphized structure (Mordberg et al., 2001). In present case, such features indicating to alteration or amorphousness of zircon were not observed, but the morphology of the crystals rather indicates to fracturing and a subsequent filling of the fractures with Sc-enriched zircon. More insight into zircon occurrence in bauxite and its properties in relation to Sc content can be found from Mordberg et al., (2001). The Bayer process is expected to have no or minimum effect on zircon because of its well-known high chemical durability (e.g. Hanchar, 2015), which is also evident from current observations.

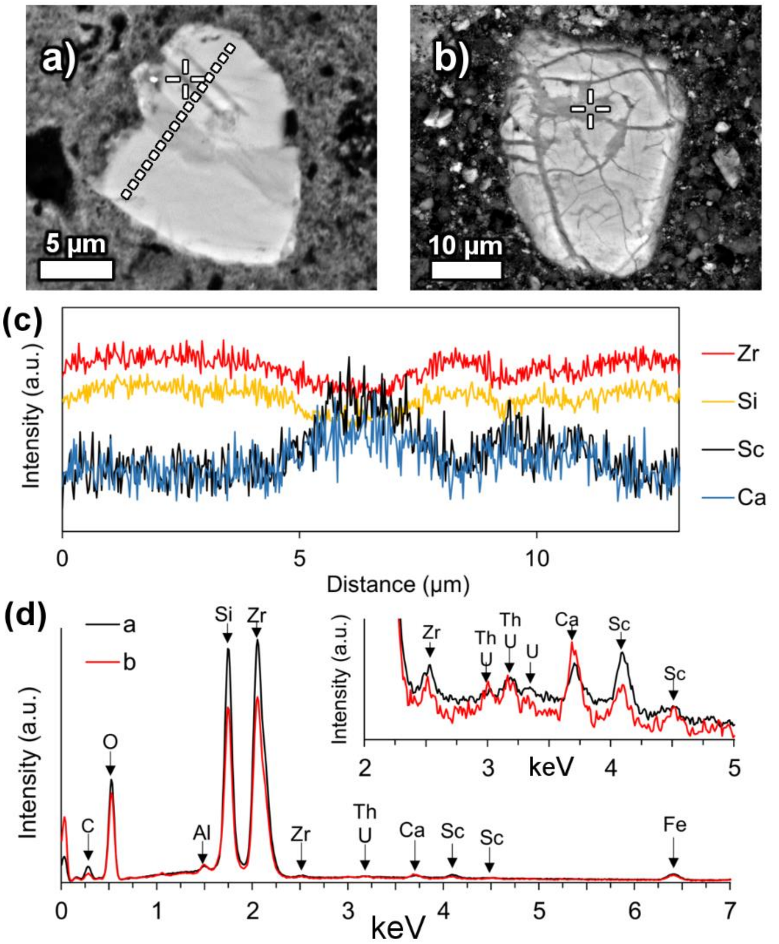

Figure 62. BSE images of zircons observed in (a) Greek Parnassos-Ghiona bauxite (DD-BX), (b) bauxite residue, with (c) relative concentration profile measured on the dashed line shown in (a), and (d) respective EDS spectra corresponding to zircons in bauxite as well as in residue.

Table 23. Sc concentration in zircons of bauxite (1–4) and its residue (5–10), quantified in EPMA-WDS*.

Analyte	Bauxites ST and DD				Bauxite residue							
	1	2	3	4	5	6	7	8	9	10	Average	S.D.
ZrO_2 (wt %)	56.80	59.02	55.06	61.10	56.53	61.82	57.73	57.98	62.52	57.45	58.60	2.46
SiO_2 (wt %)	24.78	26.01	30.20	31.86	30.07	32.65	30.37	30.53	32.70	30.23	29.94	2.61
Fe_2O_3 (wt %)	3.82	3.05	4.30	3.20	3.97	3.52	4.10	3.95	3.27	3.98	3.72	0.43
HfO_2 (wt %)	n/a	n/a	n/a	n/a	1.14	1.48	1.14	1.15	1.50	1.16	1.26	0.18
CaO (wt %)	0.50	0.02	0.42	0.02	0.64	0.00	0.54	0.65	0.01	0.69	0.35	0.30
UO_2 (wt %)	n/a	n/a	n/a	n/a	0.82	0.33	0.79	0.86	0.21	0.87	0.65	0.29
Al_2O_3 (wt %)	n/a	n/a	n/a	n/a	n/a	n/a	n/a	0.72	0.02	0.82	0.52	0.44
Sc (mg/kg)	1860	350	3100	540	7240	80	7180	7230	50	8400	3600	3500
Total (wt %)	86.20	88.14	90.45	96.27	94.28	99.82	95.77	96.94	100.24	96.48	94.46	4.73

* For a part of the measurements, Al_2O_3, HfO_2 and UO_2 contents were overlooked, but for a wider overview of Sc contents in zircon, these measurements were included as a part of this summary.

7.3.2 Sc-Depleted

Titanium dioxide polymorphs anatase and/or rutile do not contain a significant amount of Sc (**Table 24**). Anatase and rutile can't be distinguished from each other in EPMA-WDS because of their identical chemical composition (**Figure 63**a). The concentrations of Sc in titanium dioxides of bauxite and its residue materials were similar, a summarising concentration of about 40 mg/kg (n = 9) can be given for the two phases combined. Iron titanates, corresponding to either ilmenite or titanomagnetite (not detected in XRD) show variable contents of Sc from 0 to 260 mg/kg, but are commonly completely barren in Sc content (**Figure 63**b, **Table 25**). They were identified only in DD-BX sample.

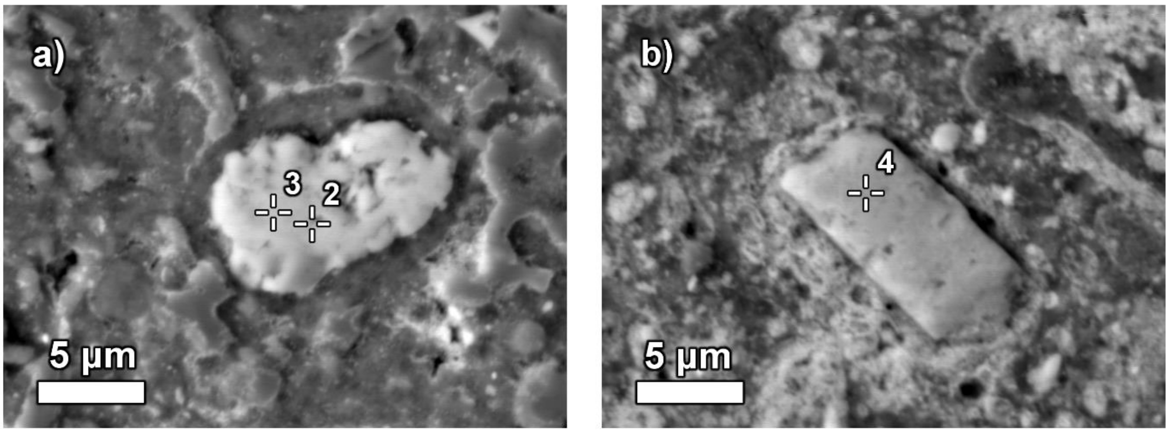

Figure 63. Backscattered electron images of a) titanium dioxide (anatase/rutile) and b) iron titanate observed in Greek bauxite DD. The indicated quantification spots are reflected in a) **Table 24**, and b) in **Table 25**.

Table 24. EPMA-WDS quantification of TiO_2 (anatase/rutile) particles in bauxite (ST-BX no. 1, DD-BX no.-s 1–7) and bauxite residue samples (8–9).

Analyte	ST-BX	DD-BX						Bauxite residue		Average	S.D.
	1	2	3	4	5	6	7	8	9		
TiO_2 (wt %)	93.94	92.39	89.75	92.90	84.59	86.52	88.01	100.85	93.41	91.37	4.84
Fe_2O_3 (wt %)	1.43	0.93	1.03	1.25	6.12	1.40	1.68	1.92	4.53	2.25	1.81
Al_2O_3 (wt %)	n/a	0.56	0.80	0.55	5.33	0.59	1.14	0.94	2.03	1.49	1.63
SiO_2 (wt %)	1.04	0.95	1.37	0.22	0.42	0.32	0.57	0.29	1.34	0.72	0.46
Na_2O (wt %)	0.07	0.02	0.04	0.01	0.00	0.06	0.01	0.04	0.07	0.03	0.03
CaO (wt %)	1.28	0.06	0.07	0.06	0.10	0.08	0.11	0.74	0.70	0.35	0.45
Cr_2O_3 (wt %)	n/a	n/a	n/a	n/a	n/a	n/a	n/a	0.03	0.03	0.03	0.00
V_2O_3 (wt %)	n/a	n/a	n/a	n/a	n/a	n/a	n/a	0.63	0.45	0.54	0.13
Sc (mg/kg)	40	70	150	10	40	0	0	30	20	40	50
Total (wt %)	97.75	94.93	93.07	94.98	96.58	88.97	91.55	105.44	102.57	96.20	5.19

Table 25. EPMA-WDS quantification of iron titanite particles in bauxite DD sample.

Analyte	1	2	3	4	5	Average	S.D.
TiO_2 (wt %)	32.32	53.59	53.75	58.78	52.54	50.20	10.28
Fe_2O_3 (wt %)	34.37	43.55	42.08	37.11	42.43	39.91	3.96
Al_2O_3 (wt %)	10.64	0.33	0.10	0.74	0.17	2.40	4.61
SiO_2 (wt %)	0.62	0.01	0.01	0.04	0.01	0.14	0.27
Na_2O (wt %)	0.00	0.01	0.02	0.01	0.01	0.01	0.01
CaO (wt %)	0.14	0.04	0.02	0.05	0.02	0.05	0.05
MgO (wt %)	n/a	n/a	n/a	n/a	0.08	0.08	n/a
MnO (wt %)	n/a	n/a	n/a	n/a	3.61	3.61	n/a
Sc (mg/kg)	260	0	0	10	0	50	120
Total (wt %)	78.1	97.5	96.0	96.7	98.9	93.44	8.63

There are no indications suggesting to the existence of any discrete phases of Sc in bauxite or its residue. Rare earth phases and aluminosilicate phases, latter corresponding to kaolinite group clay minerals, did not reveal any content of Sc (**Table 26**). Sometimes, kaolinite-associated Sc has been referred to occur (Lavrenchuk et al., 2004). The chlorite group phase chamosite, detected in XRD scan of bauxite residue, was not discerned during EPMA investigation. Neither observation derived any conclusions about the relations between phosphates and Sc.

Table 26. EPMA-WDS quantification of Sc-depleted mineral phases. Aluminosilicate, corresponding to kaolinite (1–6), is measured in Parnassos-Ghiona B3 sample (DD-BX). Hydrogarnet type phases (titanium- and iron-substituted; 7–8) and Ca-based phases (possibly calcite; 9–10) are measured in bauxite residue sample.

Analyte	Aluminosilicate (kaolinite)						Hydrogarnet		Ca-based phase	
	1	2	3	4	5	6	7	8	9	10
SiO_2 (wt %)	25.85	25.11	25.64	26.39	27.31	26.59	9.73	9.94	2.08	0.27
MgO (wt %)	0.37	0.37	0.37	0.40	0.20	0.79	0.01	0.02	0.07	0.66
Al_2O_3 (wt %)	35.48	35.48	35.48	38.16	39.22	39.57	13.07	11.22	3.81	1.52
Na_2O (wt %)	0.05	0.05	0.05	0.05	0.05	0.11	0.73	0.22	0.35	0.04
Fe_2O_3 (wt %)	1.65	1.65	1.65	1.74	1.47	4.03	11.07	12.24	15.48	2.14
CaO (wt %)	0.05	0.05	0.05	0.05	0.05	0.12	36.78	33.62	50.53	56.31
TiO_2 (wt %)	-	-	-	-	-	-	21.21	18.48	1.51	0.12
Cr_2O_3 (wt %)	-	-	-	-	-	-	0.31	0.30	0.08	0.00
V_2O_3 (wt %)	-	-	-	-	-	-	2.56	2.24	0.17	0.02
Sc (mg/kg)	0	0	0	0	0	0	0	10	0	0
Total (wt %)	63.44	62.71	63.24	66.79	68.30	71.21	95.47	98.27	74.08	61.08

The Bayer process secondary minerals of the hydrogarnet group, cancrinite or perovskite did not detect the presence of Sc, when analysing them in bauxite residue samples or scales (**Table 12**, **Table 26**). Note that the analysed hydrogarnet type phases contain substantial quantities of Ti and Fe. This makes it possible to identify them as Ti and Fe substituted hydrogarnet phases that are also noted in other studies, sometimes given with the formula $Ca_3(Al,Fe)_2[(Si,Ti)O_4]_n(H_2O)_{(6-2n)}$ (Suss et al., 2002; Zoldi et al., 1987). They may also contain a considerable quantity of V (about 2.5 wt% V_2O_5). This is the highest V concentration per spot analysis detected in this study. Only a few small perovskite grains were possible to be analysed by EPMA-WDS in bauxite residue sample. Therefore, due to the very fine size of cancrinite and perovskite grains in bauxite residue, these phases were investigated on a sample of scale formed in the Bayer process autoclave (74 % cancrinite, 7.5 % perovskite, 6.5 % hematite, 12 % other; 19.7 mg/kg Sc; **Table 6**, **Table 7**). For the full description of this material, the reader is referred to paragraph 4.4 (**Table 12**, **Figure 28**), which discusses the characteristics of minor Bayer process by-products, such as scales. In the studied autoclave scale, the crystals exhibit larger sizes while representing Bayer process secondary mineral phases (**Figure 28**). It was concluded previously from the investigation of the scale sample (paragraph 4.4) that perovskite is not a likely host of Sc, while cancrinite can be associated with minor quantities of Sc (20–90 mg/kg, **Table 12**). Nevertheless, this indication cannot be regarded as conclusive because the analysed cancrinite-predominant matrix also contains sub-micron sized grains of iron oxides, thus the indicated quantity of Sc might be related to those Fe particles. If Sc presence in cancrinite or perovskite is to be assumed, then cancrinite is a more probable host for Sc than perovskite. To confirm whether cancrinite can incorporate Sc to its composition, a purer source of cancrinite phase should be isolated. In any case, even if cancrinite contains roughly about 30 mg/kg of Sc, it cannot account for more than 3% of the total Sc budget in bauxite residue, rendering its importance as a Sc host minimum.

7.4 Distribution of Scandium Between its Host Minerals

Having quantified the phase compositions (**Table 7**), Sc bulk concentrations (**Table 6**) and the contents in its host minerals (sections 7.1, 7.2, 7.3), we can compile the data into a mass balance estimation to indicate the amount of the total Sc each phase contains. Higher and lower limits are determined by the standard deviations of Sc quantification. The estimation is based on EPMA-WDS data, values of major phases are rounded to a multiple of 5. For the bauxite residue, the most significant Sc host is hematite, containing 55 ± 20 % of total Sc, followed by goethite with 25 ± 20 % of contribution (**Table 27**). A lesser amount is associated with zircon and a quantity of 10 ± 5 % Sc hosted by this mineral can be estimated. The primary change from bauxite to bauxite residue is that boehmite/diaspore lose their role of hosting Sc, because they are dissolved in the Bayer process (e.g. Authier-Martin et al., 2001). Other authors have arrived to the same conclusion, that some Sc is released from diaspore/boehmite, but in their case the boehmite/diaspore-associated proportion of Sc in bauxite is reportedly substantially higher (100–110 mg/kg Sc; 55–60 % of total Sc) than in present case (Suss et al., 2017). The released proportion of Sc could be scattered in bauxite residue in the form of adsorbed ions on mineral surfaces or on the goethite surface. Goethite was not distinctively observed in bauxite samples and the presence of Sc in them could not be identified. Therefore, goethite related mass balance figure can only be given for bauxite residue.

Table 27. Distribution of Sc between its host minerals. Titanium phases refer to anatase and rutile combined.

Phase	Bauxite	Bauxite residue
	% of total Sc	
Hematite	70 ± 20	55 ± 20
Goethite	?	25 ± 20
Diaspore/boehmite	15 ± 15	2 ± 2
Zircon	10 ± 5	10 ± 5
Titanium phases	2 ± 2	1 ± 1
Cancrinite		3?

7.5 The Route of Scandium Enrichment into Bauxite Residue

There are two main parent lithologies from where Parnassos-Ghiona bauxite material is thought to originate. First are the ultramafic and mafic rocks. They are linked to the bauxite deposit primarily by relating the contents of chromium and chromite mineral species as well as other compatible elements (P. Gamaletsos et al., 2016; Laskou, 2001; Petrascheck, 1989; Valeton et al., 1987). Second are felsic rocks of igneous origin, linked to the bauxite deposit by the elevated content of REEs and incompatible elements of the high field strength elements group (e.g. Th) as well as the presence of detrital zircon (P. Gamaletsos et al., 2016; Valeton et al., 1987). Scandium source in the analysed system can be assumed to be associated with the mafic and ultramafic rocks rather than the felsic ones because of the known relative abundance of Sc in mafic types of rocks (Jaireth et al., 2014; Samson and Chassé, 2016). The proportion of Sc reporting to zircon could be originating from the felsic rocks.

During source rock weathering, Sc^{3+} is released from its initial host minerals. Sc then often follows the behaviour of Fe^{3+} because of the similarities in the Eh-pH stability field of hematite and Sc_2O_3 (Brookins, 1988; Hoatson et al., 2011; Jaireth et al., 2014). Furthermore, the ionic radii of six-coordinated Sc^{3+} and Fe^{3+} are similar, but still different enough to limit the maximum amount of Sc entering to hematite lattice (Chassé et al., 2017). Sc^{3+} and Fe^{3+} isomorphous substitution is a common scenario in various lithologies and expected also in present case (Samson and Chassé, 2016).

During the Bayer process, the concentration of Sc in bauxite residue compared to material feed is further increased by a factor of 2.37 (**Figure 23**), achieving its maximum concentration in the investigated system, while the mineralogical occurrence remains practically the same as in bauxite.

7.6 Linkages Between the Sc Occurrences and its Leaching Behaviour

As already mentioned in the Introduction, several experimental studies have been carried out for exploring the opportunities of recovering Sc from bauxite residue (Akcil et al., 2017; Borra et al., 2016; Davris et al., 2017; Zhang et al., 2016).

Borra et al. (2015) reported that during mineral acid leaching of bauxite residue, recovering 30–40 % of Sc results in the leaching of only a minor part of Fe whereas recovering more than 50 % of Sc unavoidably results in the dissolution of a major part of Fe. From the leaching correlation curves, they proposed that Sc is not homogeneously distributed between the iron phases. Eventually, the recovery of Sc does not exceed 80 % (Borra et al., 2015). During functionalized hydrophobic ionic liquid leaching of bauxite residue, Sc recovery reaches up to 45 % while less than 3 % of Fe is leached (Davris et al., 2016). The former examples agree with the conclusion of the present assessment that Sc is distributed mainly between goethite and hematite. The more easily leachable proportion of Sc (30–40 %) is probably associated with goethite. Recovering the proportion of Sc that is accompanied with leaching a major part of Fe is most likely concentrated in the mineral lattice of hematite. The remaining part of Sc (~20 %) that is resistant to leaching is presumably associated with the chemically durable zircon mineral.

On the other hand, over 50 % of zirconium (Zr) recovery has been reported during 0.6 M H_2SO_4 leaching of AoG's bauxite residue. It was accompanied by 55 % of Sc and only 3 % of Fe recovery (Lymperopoulou et al., 2017). Another study suggests that zircon, when it is present in partly amorphous fine-grained form in bauxite deposit, decomposes during sodium bicarbonate digestion of bauxite residue and therefore Sc is released from its structure (Suss et al., 2017). Therefore, it is possible that some leaching conditions also liberate Sc from zircon. The limiting factor for drawing any further conclusions is that Zr recovery has been reported only a very few times in the literature. It is suggested that future studies should take into consideration to also analyse this parameter in the leachates to confirm the fate of zircon during the recovery of Sc from bauxite residue.

Indications to the correlating leaching behaviour of Sc and Ti with regards to AoG's bauxite residue (Bonomi et al., 2017b; Ochsenkühn-Petropulu et al., 1994; Rivera et al., 2017) did not acquire any mineralogical support in the context of present work. Only about 1 % of total Sc could be found in titanium dioxides contained in bauxite residue.

Hereby further evidences are provided to explain Sc leaching behaviour during an imidazolium ionic liquid [Emim][HSO_4] leaching of bauxite residue (prepared in cooperation with C. Bonomi; Bonomi et al., 2017a, 2017b). After 3 hours of leaching at 150 °C, about 31 % of Sc and 7 % of Fe were recovered. It can be observed from the diffractogram of leaching residues, that the first Sc-bearing phase to be almost dissolved is goethite, when compared to raw bauxite residue (**Figure 64**). At the same time, practically all the hematite has remained in the residues. This supports the hypothesis that the easily extractable proportion of Sc in bauxite residue is associated with goethite phase. As already explained before, Sc concentration associated with goethite is substantially higher than the hematite-bound Sc (section 7.1, **Table 19**, **Table 20**). Other phases leached during the early stages of the experiment are gibbsite, calcite and hydrogarnet, but Sc is not found in these phases. The newly formed phase is anhydrite ($CaSO_4$). Maximum recovery of Sc, 78 %, is achieved at 200 °C together with the complete dissolution of Fe, indicating to the major part of Fe occurring in hematite. Once again, the remaining unrecovered Sc is possibly fixed in zircon.

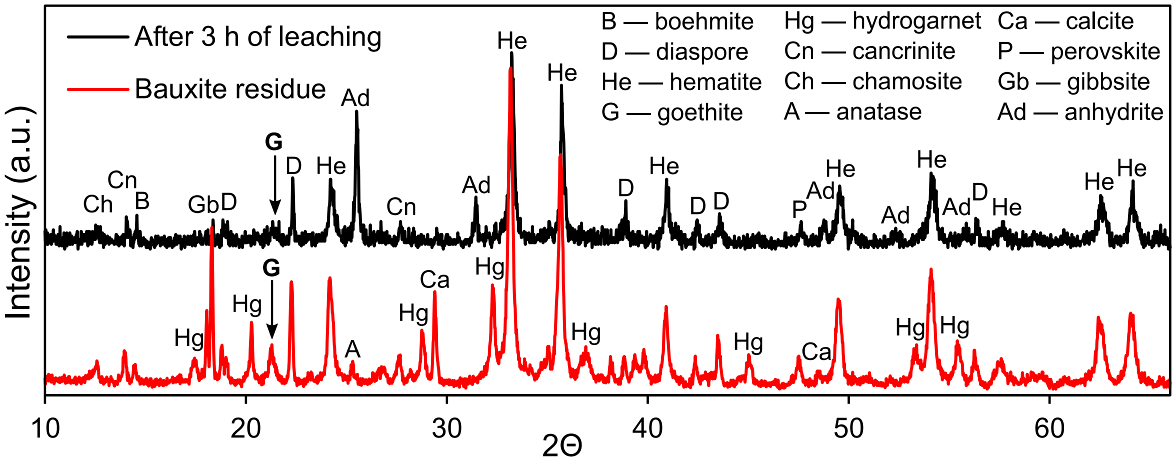

Figure 64. Diffractogram of raw bauxite residue compared to diffractogram of residue after 3 h of leaching.

8. Conclusions

The fate of selected trace elements in terms of their mineralogy and distribution in the Bayer process was investigated, based on the case study in Aluminium of Greece refinery. It is evident that Bayer process materials, whether they are bauxite residue or process liquors, are enriched in certain trace elements (Ga, V, As in liquors; REEs, Sc, Cr, Th, etc. in residue). Together with the continuous development and improvement of extraction technologies, the trace elements could be recovered as valuable by-products of the Bayer process. Specific conclusions are summarised in the following three sections.

8.1 Distribution of Trace Elements

Bauxite trace elements introduced to the Bayer process studied in this work are roughly divided in two categories: (1) those that are at least partly soluble in the caustic leaching and accumulate to an extent into processing liquor, namely Ga, V, As, U as well as Cr, and (2) those that are not soluble in the caustic leaching, namely Sc, Th and the REEs. The trace elements in the first category accumulate to process liquor until the specific saturation level of each metal, and then the input and output flows equilibrate. In the Bayer process output flows, only Ga and U possess the property of entering to the composition of aluminium hydroxide product. In the case of Ga, 70% of the initial quantity of the metals ends up in aluminium hydroxide and in the case of U it is 10%. The rest of Ga and U are separated from the process with bauxite residue. With respect to the second category, those metals (Sc, Th, REEs) are transferred through the process mostly only in the composition of solid material flows. Sc, Th and REEs are not found in aluminium hydroxide product and their mass transfer to bauxite residue is typically at least 98%.

The investigation of Bayer process scales and other minor products led to a conclusion that the affinity of Al-containing Bayer process secondary phases to incorporate Ga into their composition follows the relative intensity of hydrogarnet > gibbsite > cancrinite. It was also revealed from the analyses of minor Bayer process materials, that perovskite can capture significant amounts of trace elements such as Mg (2 wt%), Cr (0.2 wt%), V (0.1–0.2 wt%) and Ni (0.6 wt%) into its lattice. The highest concentrations of V per mineral phase are associated with hydrogarnets, where V level can reach up to 2.5 wt% V_2O_5.

8.2 REE Phases

A careful and dedicated investigation of bauxite residue by EPMA and HRTEM revealed that there are several types of discrete REE phases contained in bauxite residue. The relatively most abundant of them is a LREE ferrotitanate ($(REE,Ca,Na)(Ti,Fe)O_3$) phase, that chemically resembles the naturally occurring loparite except for the absence of niobium. However, plenty of synthetic REE perovskite compounds exist that are like the LREE ferrotitanates observed in the present study. LREE ferrotitanates form a solid solution between the ideal end-members $(Ca,Na)(Ti,Fe)O_3$ and $(REE,Ca,Na)(Ti,Fe)O_3$. These occurrences further sub-divide into Ce predominant and Nd-La predominant types. The Ce predominant form also contains up to 2.7 wt % Th. Calcium ferrotitanate particles with low LREE concentration (<5 wt %) seem to be rather concentrated into the very fine (<1 µm) particulates of bauxite residue. LREE ferrotitanates are formed during the Bayer process digestion by an in-situ transformation of the precursor bauxite LREE minerals contained in the bauxite feed. Thus, the composition of the newly formed phases depends on (1) the chemical composition of the precursor REE phases and (2) the extent of incorporation of Na as well as dissolved Fe and Ti ions into their composition. The latest reaction products are those with the prevailing concentration of Ca and with a low (<5 wt%) LREE concentration and they are mostly found among the nano-scaled bauxite residue particles.

Minor amounts of LREEs are found as carbonates and phosphates, referring to the partial resistance of these phases to Bayer process digestion conditions. A part of Ce and minor presence of other lanthanides were found to be associated with manganese phases in the form of adsorption on their surface or in manganese particle cavities. These occurrence forms are thought to be secondary, created from the fast precipitation of a small proportion of dissolved lanthanides.

Heavy REEs are found in bauxite residue in the same form as in bauxite, namely as Y phosphate phases (xenotime/churchite). Their major constituent, Y, is seconded by other HREEs like Gd, Dy and Er. Some Y is incorporated into mixed REE phases.

The presence of Bayer process derived calcium ferrotitanate shells around LREE particles probably hinders the immediate solubility of LREE grains during REEs leaching from bauxite residue. It can be assumed that the complex LREE ferrotitanates dissolve less readily than LREE fluorocarbonate minerals found in bauxites.

Present work concludes that REEs are found among bauxite residue's microscale particulate as discrete phases with a high REE concentration and among nano-scaled particulate in the composition of calcium ferrotitanate phases. It is anticipated that bauxite residue or bauxite ore could become a sustainable and responsible source of REEs.

The findings presented here are currently the only explanation of REE, except for cerium, occurrences in bauxite residue. However, further work is necessary to enhance the understanding of how REEs occur in bauxite residue.

8.3 Sc Occurrences

The present work sets a first benchmark in characterizing the modes of Sc occurrences in European bauxite residue. The close association of Fe phases and Sc in bauxite and its residue, as indicated by previous authors, has been clearly confirmed. The claim was complemented with the quantification of Sc in its host minerals. Confirmed distinction of goethite hosting appreciable amount of Sc in addition to hematite was made. The average Sc concentration in the hematite matrix of the analysed Greek Parnassos-Ghiona bauxite samples is 200 mg/kg and in the hematite matrix of AoG's bauxite residue it is 170 mg/kg. The latter is due to the dilution effect of Sc-depleted lateritic bauxite feed in the production flowsheet of AoG. In bauxite residue, hematite hosts 55 ± 20 % of total Sc while goethite accounts for about 25 ± 20% of total Sc. Zircon hosts about 10 ± 5 % of the total Sc budget in bauxite residue.

The probable Sc occurrence mode in hematite is the isomorphous substitution of Sc^{3+} and Fe^{3+}. Minor hosts of Sc are titanium dioxides and aluminium oxyhydroxides, the latter represented by diaspore and boehmite. Since diaspore and boehmite are digested in the Bayer process, about 10% of Sc contained in them could be released from their lattice and transferred through surface adsorption to goethite or other particles of bauxite residue. The rest of the mineral phases in bauxite and bauxite residue system are not associated with Sc, concluding from the present evidences.

Sc concentrations in the main mineral matrices were cross-checked using two methods, EPMA-WDS and LA-ICP-MS and the quantification results of the two methods were in excellent agreement. It is evident that Sc occurs in different forms in different bauxites and their residues. It is necessary to investigate the nature of Sc occurrence in various materials case-by-case.

New evidence of Sc leaching behaviour from bauxite residue shows that Sc is first released from goethite, then from hematite and the unrecovered proportion of Sc is likely associated with zircon.

The characterization of Sc in the worldwide bauxite inventory deserves thorough geochemical surveying, because the literature review revealed the relative scarcity of information. The thorough understanding of the characteristics of Sc in bauxite deposits is crucial, because a large proportion of this valuable metal with an increasing demand on the market is thought to be associated with bauxites. Further work is encouraged to characterize Sc in the <1 µm fraction of bauxite residue. Also, it could be of high interest to speciate further the properties of Sc in bauxite residue by performing advanced analyses such as the X-ray absorption near-edge structure (XANES) spectroscopy, µXRF and µXRD methods.

Appendix A

Table A 1. Trace element composition of the bauxites in the feed of AoG (mg/kg). If multiple options are available, then the measurements indicated with bold are used for mass balance calculations. Asterix (*) marks a measurement in an alternative sub-sample.

Ana-lyte	**Method**	**Karst**				**Mixed karst**	**Lateritic**	
		DD-BX	ST-BX	HS-BX	TU-BX	DC-BX	TR-BX	GH-BX
As	INAA	74.7±5.5	160.0±13.0	218±17.0	64.0±3.9	109.0±8.0	11.5±0.3	26.6±1.5
As	ICP-MS	**128±5**	**122±6**	**99±2**	**70±14**	**111±9***	na	57±3
Ce	ICP-MS	208±0	177±2	177±3	265±4	195±0	<10	29±0
Ce	INAA	217±8	177±5	180±4	267±3	200±5	9±0	34±1
Cr	ICP-MS	693±64	588±50	590±51	442±35	768±10*	138	521±5*
Cr	INAA	1170±50	920±51	942±38	670±46	1145±55	109±7	264±12
Dy	ICP-MS	10.2±0.1	10.9±0.9	<10	22.2±0.5	8.6±0.0*	<10	5.6±0.4*
Er	ICP-MS	5.9±0.4*	7.2±0.8*	<10	10.6±0.2*	5.6±0.0*	<10	3.8±0.5*
Eu	ICP-MS	<2*	2.4±0.9*	<10	4.2±0.5*	<2*	<10	<2*
Eu	INAA	2.7±0.3	2.4±0.4	1.4±0.1	3.4±0.3	2.0±0.1	0.5±0.2	0.8±0.2
Ga	ICP-MS	58±0	60±1	66±1	69±4	60±0	60±1	57±1
Gd	ICP-MS	11.4±0.1	10.8±0.8	<10	25.2±1.2	8.5±0.0*	<10	<10
Ho	ICP-MS	<2*	2.2±0.1*	<10	3.2±0.0*	<2*	<10	<2*
La	ICP-MS	58±1	63±3	<50	145±15	67±2	<50	<50
La	INAA	51.3±1.6	60.3±2.4	46.7±1.7	129.0±1.0	46.6±1.3	5.0±0.4	19.1±1.3
Lu	ICP-MS	<2*	<2*	<2*	<2*	<2*	<10	<2*
Lu	INAA	1.26±0.19	0.98±0.01	0.92±0.02	1.61±0.01	0.95±0.07	0.37±0.04	0.39±0.00
Nd	ICP-MS	53.5±3.8	53.8±4.1	31.9±0.4	92.3±3.4	42.5±0.9	<10	12.0±0.1
Nd	INAA	42±2	38±5	23±3	70±0	32±0	<5	13±1
Pr	ICP-MS	13.2±0.1	12.7±0.5	<10	23.1±1.1	10.3±0.1	<10	<10
Sc	INAA	53.7±0.9	43.1±0.7	43.1±0.6	56.0±0.8	50.0±0.8	7.1±0.0	8.4±0.2
Sm	ICP-MS	11.1±0.1	10.9±0.9	<10	20.1±4.0	10.2	<10	5.9±0.0*
Sm	INAA	10.4±0.9	8.7±0.4	5.7±0.6	17.2±0.5	9.2±0.0	0.6±0.1	2.0±0.2
Tb	ICP-MS	<2*	2.3±0.5*	<10	2.8±0.0*	<2*	<10	<2*
Tb	INAA	<0.5	<0.5	<0.5	<0.5	<0.5	<0.5	<0.5
Tm	ICP-MS	<2*	<2*	<2*	<2*	<2*	<10	<2*
Y	ICP-MS	47.5±0.4	46.7±0.8	46.1±0.6	92.7±2.7	44.8±0.3	11.4±1.3	17.2±0.3
Yb	ICP-MS	6.2±0.4*	7.0±0.4*	<10	11.4±0.2*	6.0±0.0*	<10	3.6±0.3*
Yb	INAA	7.2±0.7	6.1±0.4	5.9±0.4	11.5±0.2	6.9±0.6	2.1±0.3	2.5±0.3

Table A 2. Trace element composition of Bayer process intermediate solids and by-products (mg/kg). If multiple options are available, then the measurements indicated with bold are used for mass balance calculations. Asterix (*) marks an alternative sub-sample.

Analyte	**Method**	**Intermediate**		**By-product**		
		BF-DG	SW-DS	RM-FP	RM-2010	DC-RE
As	INAA	**769.0**	60.2±4.1	238.0±34	-	**98.9±6.1**
As	ICP-MS	1007±2	**99±23**	**214±34**	228±23	77±4
Ce	ICP-MS	155±0	47±1	363±6	382±17	137±4
Ce	INAA	177	47±3	377±2	-	118±1
Cr	ICP-MS	658±1	335±11	1429±97	1931±19	450±50
Cr	INAA	765±345	304±5	1570±120	-	483±34
Dy	ICP-MS	<10	<10	16.9±0.0*	18.3±0.6	8.2±0.1
Er	ICP-MS	<10	<10	12.4±1.3	12.2±0.2	5.5±0.1
Eu	ICP-MS	<10	<10	4.6±1.1*	4.1±0.9	<2
Eu	INAA	1.3±0.2	0.8±0.3	4.0±0.4	-	1.8±0.2
Ga	ICP-MS	113±7	93±2	41±0*	38±1	55±5
Gd	ICP-MS	<10	<10	17.5±0.0*	19.8±0.2	9.1±0.1
Ho	ICP-MS	<10	<10	4.1±0.1*	3.7±0.0	<2
La	ICP-MS	51±1	<50	135±1*	125±7	56±5
La	INAA	44.2±7.0	15.3±0.8	104.0±1	-	52.0±0.2
Lu	ICP-MS	<10	<10	2.2±0.0*	2.0±0.0	<2
Lu	INAA	0.78±0.12	0.45±0.01	1.90±0.05	-	0.70±0.07
Nd	ICP-MS	38.9±0.2	12.0±0.0	86.5±0.9	97.4±9.5	45.3±0.3
Nd	INAA	26.0	<5	65±2	-	55±17
Pr	ICP-MS	<10	<10	21.7±0.1	26.3±0.6	12.1±0.5
Sc	INAA	41.5	14.9±0.4	97.7±0.1	-	27.3±0.3
Sm	ICP-MS	<10	<10	20.4±2.6	18.4±2.0	8.1±0.1
Sm	INAA	8.1±0.4	2.2±0.1	17.9±1.0	-	9.1±0.1
Tb	ICP-MS	<10	<10	3.3±0.0*	3.0±0.1	<2
Tb	INAA	<0.5	<0.5	<0.5	-	<0.5
Tm	ICP-MS	<10	<10	<2*	<2	<2
Y	ICP-MS	38.3±0.1	17.2±0.4	89.5±0.4*	98.8±3.5	39.9±1.7
Yb	ICP-MS	<10	<10	12.6±0.0*	12.9±0.2	5.9±0.1
Yb	INAA	6.5±0.4	2.7±0.2	13.5±0.0	-	5.4±0.1

Table A 3. Trace element composition of Bayer process products and lime (mg/kg). Asterix (*) marks an alternative sub-sample.

Analyte	Method	Products		Lime
		HY-AL	CA-AL	CA-OX
As	INAA	<0.5	<0.5	4.0
As	ICP-MS	<61	<12*	na
Ce	ICP-MS	<10	<2*	<10
Ce	INAA	<3±0	<3	<3
Cr	ICP-MS	<64	na	na
Cr	INAA	<5	<5	<5
Dy	ICP-MS	<10	<2*	<10
Er	ICP-MS	<10	<2*	<10
Eu	ICP-MS	<10	<2*	<10
Eu	INAA	<0.2	<0.2	<0.2
Ga	ICP-MS	85±1	83±0	<50
Gd	ICP-MS	<10	<2*	<10
Ho	ICP-MS	<10	<2*	<10
La	ICP-MS	<50	<50	<50
La	INAA	<0.5	<0.5	2.5
Lu	ICP-MS	<10	<2*	<10
Lu	INAA	<0.05	<0.05	<0.05
Nd	ICP-MS	<10	<10	<10
Nd	INAA	<5	<5	<5
Pr	ICP-MS	<10	<2*	<10
Sc	INAA	<0.1	<0.1	0.8
Sm	ICP-MS	<10	<2*	<10
Sm	INAA	<0.1	<0.1	0.2
Tb	ICP-MS	<10	<2*	<10
Tb	INAA	<0.5	<0.5	<0.5
Tm	ICP-MS	<10	<2*	<10
Y	ICP-MS	<10	<10	<10
Yb	ICP-MS	<10	<2*	<10
Yb	INAA	<0.2	<0.2	0.3

Table A 4. Composition of Bayer liquors.

Analyte	Unit	Method	Repetition	CL	PL	SL	BF	SW
Al_2O_3	g/l	titr.	A	143	188.3	115.3		
Al_2O_3	g/l	titr.	B	137.6	192.8	109.7		
Al_2O_3	g/l	titr.	C		192.3	105	125.4	51.3
Al_2O_3	g/l	titr.	D	136.2	195.3	104.4		
Al_2O_3	g/l	titr.	A-D average	138.9	192.2	108.6		
Na_2O	g/l	titr.	A	213.4	162.2	174.6		
Na_2O	g/l	titr.	B	215.3	158.7	171.1		
Na_2O	g/l	titr.	C		157.3	171.1	209.9	113.1
Na_2O	g/l	titr.	D	217.7	159.5	170.1		
Na_2O	g/l	titr.	A-D average	215.5	159.4	171.7		
As	mg/L	XRF	D	181	146	129		
As	mg/L	INAA	D	131.6 ± 16.2	110.8 ± 5.4	99.6 ± 5.4		
Ba	mg/L	XRF	D	<17	22	26		
Br	mg/L	XRF	D	53	43	35		
Br	mg/L	INAA	D	40.7 ± 0.0	33.6 ± 0.5	31.4 ± 0.8		
Ca	mg/L	AAS-1	A		14.9	16.5		
Ca	mg/L	AAS-1	C		0.9			
Ca	mg/L	XRF	D	32	64	49		
Ce	mg/L	ICP-MS	B	<0.04	<0.04	<0.04		
Ce	mg/L	XRF	D	<36	<35	63		
Ce	mg/L	INAA	D	<2	<2	<2		
Co	mg/L	XRF	D	<1	<1	<1		
Cr	mg/L	AAS-2	A	1.7	1.5	<0.3	<0.3	<0.3
Cr	mg/L	ICP-MS	B	1.42	1.4	1.3		
Cr	mg/L	XRF	D	28	33	16		
Cs	mg/L	XRF	D	15	12	27		
Cs	mg/L	INAA	D	<0.5	<0.5	1.4 ± 1		
Cu	mg/L	XRF	D	2.2	0.8	0.4		
Eu	mg/L	INAA	D	<0.1	<0.1	<0.1		
Fe	mg/L	UV	A		9.6	3.39		
Fe	mg/L	AAS-2	A	2.7	2.15	0.33		
Fe	mg/L	UV	C		9.2			
Fe	mg/L	XRF	D	54	70	43		

Table A 4 continued.

Analyte	Unit	Method	Repetition	CL	PL	SL	BF	SW
Ga	mg/L	ICP-OES	B	367	267.2	279.7		
Ga	mg/L	ICP-OES	C		303.2	300.4	295.3	216.1
Ga	mg/L	ICP-OES	B-C average	367	285.2	290.05		
Ga	mg/L	XRF	D	>281	>253	>208		
Gd	mg/L	ICP-MS	B	<0.04	<0.04	<0.04		
Hf	mg/L	XRF	D	4	5	3		
Hg	mg/L	XRF	D	<1	0.3	0.7		
Hg	mg/L	INAA	D	<0.5	<0.5	<0.5		
I	mg/L	XRF	D	301	212	225		
In	mg/L	XRF	D	2	1	1		
K	g/l	AAS	A	14.4	13.7	13.8		
La	mg/L	ICP-MS	B	<0.04	<0.04	<0.04		
La	mg/L	XRF	D	<26	33	19		
La	mg/L	INAA	D	<0.3	<0.3	<0.3		
Lu	mg/L	INAA	D	<0.03	<0.03	<0.03		
Mg	mg/L	AAS-2	A	<0.1	<0.1	<0.1		
Mg	mg/L	XRF	D	926	790	562		
Mn	mg/L	AAS	A	1.05	1.05	0.15		
Mo	mg/L	XRF	D	622	471	438		
Mo	mg/L	INAA	D	394 ± 58	318 ± 26	273 ± 3.4		
Nb	mg/L	XRF	D	<2	<2	<2		
Nd	mg/L	ICP-MS	B	0.1095	0.0949	0.2173		
Nd	mg/L	INAA	D	<3	<3	<3		
Ni	mg/L	AAS-2	A	4.15	3.8	0.59		
Ni	mg/L	AAS-2	C		4.8	<4	4.4	<4
Ni	mg/L	XRF	D	2	1	1		
Rb	mg/L	XRF	D	58	43	42		
Sb	mg/L	XRF	D	5	3	7		
Sc	mg/L	ICP-MS	B	0.4261	0.2751	0.2195		
Sc	mg/L	INAA	D	<0.05	<0.05	<0.05		
Si	mg/L	AAS-1	A		544	520		
Si	mg/L	AAS-2	A	578.5	457	120.2		
Si	mg/L	XRF	D	448	1154	446		
Sm	mg/L	INAA	D	<0.05	<0.05	<0.05		
Sm	mg/L	INAA	D	<0.05	<0.05	<0.05		
Sn	mg/L	XRF	D	<3	<3	<2		
Zn	mg/L	AAS	A	1	0.35	<0.04		
Zn	mg/L	AAS	C		<0.8	<0.8	0.8	1.4
Zn	mg/L	XRF	D	4	8	2		
Zr	mg/L	XRF	D	1996	1957	1455		
Ta	mg/L	XRF	D	5	<2	<1		
Tb	mg/L	INAA	D	<0.3	<0.3	<0.3		

Table A 4 continued.

Analyte	Unit	Method	Repetition	CL	PL	SL	BF	SW
Th	mg/L	XRF	D	2	2	1		
Th	mg/L	ICP-MS	B	<0.2	<0.2	<0.2		
Th	mg/L	INAA	D	<0.1	<0.1	<0.1		
Ti	mg/L	AAS	B	~1	~1	~1		
Ti	mg/L	XRF	D	<3	<3	<3		
U	mg/L	ICP-MS	B	0.2254	1.28	1.27		
U	mg/L	XRF	D	<1	<1	<1		
U	mg/L	INAA	D	0.4	0.3	0.4 ± 0.1		
V	mg/L	XRF-st	A		263	292		
V	mg/L	AAS-2	A	251.5	524.75	62.6		
V	mg/L	ICP-OES	B	426.1	304.4	329.1		
V	mg/L	ICP-OES	C		285.9	300.3	127.3	314.3
V	mg/L	ICP-OES	B-C average	426.1	295.15	314.7		
V	mg/L	XRF	D	494	377	383		
W	mg/L	XRF	D	65	51	45		
W	mg/L	INAA	D	34 ± 1	27 ± 5	21 ± 1		
Y	mg/L	ICP-MS	B	<0.04	<0.04	<0.04		
Y	mg/L	XRF	D	<5	<5	<5		
Yb	mg/L	INAA	D	<0.1	<0.1	<0.1		
Yb	mg/L	XRF	D	18.2	14.2	11		

Table A 5. Distribution of trace elements that accumulate to process liquors. In mg/kg, normalised to the mass of aluminium hydroxide produced.

		Cr	As	V	Ga	U
	I HMS					
In:	B3 Standard (ST-BX)	155±14	34±2	164	17±0	2.1±0.2
	B3 Delphi-Distomo (DD-BX)	578±53	107±4	332	48±0	5.8±0.4
	sum	**733**	**141**	**496**	**65**	**7.9**
Out:	B3 Mixed bauxite (DC-BX)	734±10	106±9	450	57±0	7.6±0
	Decalc. Residue (DC-RE)	37±4	20±1	36	11±0	0.6±0
	sum	**771**	**126**	**486**	**68**	**8.2**
	difference	5%	-11%	-2%	5%	4%
	II Grinding, preheating of karst bauxite					
In:	B3 Mixed bauxite	734±10	106±9	450	57±0	7.6±0
	B3 Mixed from stock	429±6	62±5	263	33±0	4.5±0
	Turkish bauxite	45±4	7±1	49	7±0	0.8±0.1
	B2 bauxite	10±1	2±0	11	1±0	0.1±0
	Concentrated liquor	11	978±120	3168	2729	12.9
	sum	**1229**	**1155**	**3941**	**2827**	**25.9**
Out:	Karst solid fraction	1234±2	1443	3366	212±13	19.3±4.3
	Karst liquid fraction	<2.5	n/a	1052	2441	n/a
	sum	**1234**	**1443**	**4418**	**2653**	**19.3**
	difference	104%	-24%	12%	11%	-6%
	III Grinding, desilication of lateritic bauxite					
In:	Lateritic bauxite	60±1	5±0	112	26±1	1.4±0.1
	Spent liquor	0.3	24±1	75	67	0.3
	sum	**60.3**	**29**	187	**93**	**1.7**
Out:	Later. solid fraction	123±4	22±2	109	34±1	1.6±0.1
	Later liquid fraction	<0.1	n/a	101	69	n/a
	sum	**123**	**22**	**210**	**103**	**1.6**
	difference	104%	-24%	12%	11%	-6%
	IV Digestion, settling, washing					
In:	Karst solid fraction	1234±2	1443	3366	212±13	19.3±4.3
	Karst liquid fraction	<2.5	n/a	1052	2441	n/a
	Later. solid fraction	123±4	22±2	109	34±1	1.6±0.1
	Later liquid fraction	<0.1	n/a	101	69	n/a
	Lime	<0.3	0.3	4	<3	<0.03
	sum	**1357**	**1465.3**	**4632**	**2756**	**20.9**
Out:	Bauxite residue	1265±86	189±30	903	36±5	12.7±0.7
	Pregnant liquor	15.6	1236±60	3292	2981	14.3
	sum	**1280.6**	**1425**	**4195**	**3017**	**27**
	difference	-6%	-3%	-9%	9%	29%

Table A 5 continued.

			Cr	As	V	Ga	U
	V Precipitation						
In:	Pregnant liquor		15.6	1236±60	3292	2981	14.3
Out:	Aluminium hydroxide		<5	<0.5	<10	85±1	1.2
	Spent liquor to evap.		13.2	1012±51	3199	2843	12
	Spent liquor to later.		0.3	24±1	75	67	0.3
		sum	**13.5**	**1036**	**3274**	**2995**	**13.5**
		difference	-13%	-16%	-1%	0%	-6%
	VI Evaporation				0		
In:	Spent liquor		13.2	1012±51	3199	2843	12
					0		
Out:	Concentrated liquor		10.6	978±50	3168	2729	12
		difference	-20%	-3%	-1%	-4%	0%
	VII Calcination						
In:	Aluminium hydroxide		<5	<0.5	<10	85±1	1.2
					0		
Out:	Calcined alumina		<4	<0.4	<8	67±0	0.7
	Aluminium hydroxide to stock		<1	<0.1	<2	16±0	0.3
		sum				83	1
		difference				-2%	-17%
	Internal balance						
In:	Karst bauxite		1218±16	177±14	773	99±0	13.1±0.1
	Lateritic bauxite		60±1	5±0	112	26±1	1.4±0.1
	Digestion liquors		10.9	1002±122	3243	2796±	13.2
	Lime		<0.3	0.3	4	<3	<0.003
		sum	**1288.9**	**1184.3**	**4132**	**2921**	**27.7**
Out:	Aluminium hydroxide		<5	<0.5	<10	88±2	1.2
	Spent liquor		13.5	1036±51	3274	2910	13.2
	Bauxite residue		1265±86	18930	903	36±5	12.7±0.7
		sum	**1278.5**	**1225**	**4177**	**3034**	**27.1**
		difference	-1%	3%	1%	4%	-2%
In:	**External balance**						
	Karst bauxite		1218±16	177±14	774	99±0	13.1±0.1
	Lateritic bauxite		60±1	5±0	112	26±1	1.4±0.1
	Lime		<0.3	0.3	4	<3	<0.003
		sum	**1278**	**182.3**	**890**	**125**	**14.5**
Out:	Aluminium hydroxide		<5	<0.5	<10	88±2	1.2
	Bauxite residue		1265±86	189±30	903	36±5	12.7±0.7
		sum	**1265**	**189**	**903**	**124**	**13.9**
		difference	-1%	4%	1%	-1%	-4%

Table A 6. Distribution of trace elements that do not accumulate to process liquors based on ICP-MS data. In mg/kg, normalised to the mass of aluminium hydroxide produced.

		La	Ce	Pr	Nd	Sm
	I HMS					
In:	B3 Standard (ST-BX)	18±1	49±1	3.5±0.1	15±1.1	3±0.3
	B3 Delphi-Distomo (DD-BX)	48±1	174±0	11±0.1	44.7±3.2	9.3±0.1
	sum	**66**	**223**	**14.5**	**59.7**	**12.3**
Out:	B3 Mixed bauxite (DC-BX)	64±2	186±0	9.8±0.2	40.6±0.9	9.8±0
	Decalc. Residue (DC-RE)	11±1	27±1	2.4±0.1	9.1±0.1	1.6±0
	sum	**75**	**213**	**12.2**	**49.7**	**11.4**
	difference	14%	-4%	-16%	-17%	-7%
	II Grinding, preheating of karst bauxite					
In:	B3 Mixed bauxite	64±2	186±0	9.8±0.2	40.6±0.9	9.8±0
	B3 Mixed from stock	37±0	109±0	5.7±0	23.7±0.5	5.7±0
	Turkish bauxite	15±2	27±0	2.3±0.1	9.3±0.3	2±0.4
	B2 bauxite	1±0	3±0	<0.2	0.6±0	0.1±0
	Concentrated liquor	<0.3	<0.3	n/a	<22	<0.4
	sum	**117**	**325**	**17.8**	**74.2**	**17.6**
Out:	Karst solid fraction	97±2	291±2	<18.8	73.2±0.4	15.2
	Karst liquid fraction	n/a	n/a	n/a	n/a	n/a
	sum	**97**	**291**		**73.2**	**15.2**
	difference	-17%	-10%		-1%	-14%
	III Grinding, desilication of lateritic bauxite					
In:	Lateritic bauxite	2±0	4±1	<4.3	<4.3	0.3±0
	Spent liquor	<0.01	<0.01	n/a	<0.01	<0.01
	sum	**2**	**4**			**0.3**
Out:	Later. solid fraction	6±0	17±0	<3.7	4.4±0	0.8±0
	Later liquid fraction	n/a	n/a	n/a	n/a	n/a
	sum	**6**	**17**		**4.4**	**0.8**
	difference	200%	325%			167%
	IV Digestion, settling, washing					
In:	Karst solid fraction	96±2	291±0	<18.8±0	73.2±0.4	15.2±0.8
	Karst liquid fraction	n/a	n/a	n/a	n/a	n/a
	Later. solid fraction	6±0	17±0	<3.7	4.4±	0.8±0
	Later. liquid fraction	n/a	n/a	n/a	n/a	n/a
	Lime	0.2	<0.2	<0.7	<0.3	0.01
	sum	**102.2**	**308**		**77.6**	**16.0**
Out:	Bauxite residue	120±1	321±5	19.2±0.1	76.6±0.8	18.1±2.3
	Pregnant liquor	<0.4	<0.4	n/a	<33	<0.6
	sum	**120**	**321**		**76.6**	**18.1**
	difference	17%	4%		-1%	13%

Table A 6 continued.

			La	Ce	Pr	Nd	Sm
In:	**External balance**						
	Karst bauxite		117±3	325±1	17.8±0.2	74.2±1.4	17.6±0.4
	Lateritic bauxite		2±0	4±0	<4.3	<4.3	0.3±0
	Lime		0.2	<0.2	<0.7	<0.3	0.01
		sum	**119.2**	**329**	**17.8**	**74.2**	**17.9**
Out:	Aluminium hydroxide		<0.5	<3	<10	<5	<0.1
	Bauxite residue		120±1	321±5	19.2±0.1	76.6±0.8	18.1±2.3
		sum	**120**	**321**	**19.2**	**76.6**	**18.1**
		difference	1%	-2%	8%	3%	1%

Table A 6 continued.

			Gd	Dy	Er	Yb	Y	Th
	I HMS							
In:	B3 Standard		3±0.2	3±0.3	2±0.2	1.9±0.1	13±0.2	14.7±1.1
	B3 Delphi-Distomo		9.5±0.1	8.5±0.1	4.9±0.3	5.2±0.3	39.6±0.3	42.7±1.4
		sum	**12.5**	**11.5**	**6.9**	**7.1**	**52.6**	**57.4**
Out:	B3 Mixed bauxite		8.1±0	8.2±0	5.4±0	5.7±0	42.8±0.3	48.9±1
	Decalc. residue		1.8±0	1.6±0	1.1±0	1.2±0	8±0.3	3.1±0.1
		sum	**9.9**	**9.8**	**6.5**	**6.9**	**50.8**	**52**
		difference	-21%	-15%	-6%	-3%	-3%	-9%
	II Grinding, preheating of karst bauxite							
In:	B3 Mixed bauxite		8.1±0	8.2±0	5.4±0	5.7±0	42.8±0.3	48.9±1
	B3 Mixed from stock		4.7±0	4.8±0	3.1±0	3.3±0	25±0.2	28.6±0.6
	Turkish bauxite		2.5±0.1	2.2±0.1	1.1±0	1.1±0	9.3±0.3	4.5±0.1
	B2 bauxite		<0.2	<0.2	<0.2	0.1±0	0.8±0	1±0
	Concentrated liquor		<0.3	n/a	n/a	<1.5	<0.3	<2
		sum	**15.3**	**15.2**	**9.6**	**10.2**	**77.9**	**83**
Out:	Karst solid fraction		<18.8	<18.8	<18.8	12.2±1.1	71.9	71
	Karst liquid fraction		n/a	n/a	n/a	n/a	n/a	n/a
		sum				**12.2**	**71.9**	**71**
		difference				20%	-8%	-14%
	III Grinding, desilication of lateritic bauxite							
In:	Lateritic bauxite		<4.3	<4.3	<4.3	0.9±0.1	4.9±0.6	10.7±0.6
	Spent liquor		<0.01	n/a	n/a	<0.04	<0.01	<0.05
		sum				**0.9**	**4.9**	**10.7**
Out:	Later. solid fraction		<3.7	<3.7	<3.7	1±0.1	6.3±0.1	10.6±1.3
	Later liquid fraction		n/a	n/a	n/a	n/a	n/a	n/a
		sum				**1**	**6.3**	**10.6**
		difference				11%	29%	-1%

Table A 6 continued.

		Gd	Dy	Er	Yb	Y	Th
	IV Digestion, settling, washing						
In:	Karst solid fraction	<18.8	<18.8	<18.8	12.2±1.1	71.9±0.2	70.9±8.4
	Karst liquid fraction	n/a	n/a	n/a	n/a	n/a	n/a
	Later. solid fraction	<3.7	<3.7	<3.7	1±0.1	6.3±0.1	10.6±1.3
	Later. liquid fraction	n/a	n/a	n/a	n/a	n/a	n/a
	Lime	<0.7	<0.7	<0.7	0.02	<0.7	<0.01
	sum				**13.22**	**78.2**	**81.5**
Out:	Bauxite residue	15.5±0	15±0	9.9±0.1	11.2±0.3	79.2±1.3	93
	Pregnant liquor	<0.4	n/a	n/a	<2.2	<0.4	<2
	sum	**15.5**	**15**	**9.9**	**11.2**	**79.2**	**93**
	difference				-15%	1%	14%
In:	**External balance**						
	Karst bauxite	15.3±0.1	15.2±0.1	9.7±0	10.2±0	77.9±0.5	83±1.5
	Lateritic bauxite	<4.3	<4.3	<4.3	0.9±0.1	4.9±0.6	10.7±0.6
	Lime	<0.7	<0.7	<0.7	0.02	<0.7	<0.01
	sum	**15.3**	**15.2**	**9.7**	**11.12**	**82.8**	**93.7**
Out:	Aluminium hydroxide	<10	<10	<10	<0.3	<10	<0.2
	Bauxite residue	15.5	15±0	9.9±0.1	11.2±0.3	79.2	93±2.1
	sum	**15.5**	**15**	**9.9**	**11.2**	**79.2**	**93**
	difference	1%	-1%	2%	1%	-4%	-1%

Table A 7. Distribution of trace elements that do not accumulate to process liquors based on INAA data. In mg/kg, normalised to the mass of aluminium hydroxide produced.

		La	Ce	Nd	Sm
	I HMS				
In:	B3 Standard	16.8±0.7	49±1	11±1	2.4±0.1
	B3 Delphi-Distomo	42.8±1.3	181±7	35±2	8.7±0.8
	sum	**59.6**	**230**	**46**	**11.1**
Out:	B3 Mixed bauxite	43±2.7	191±5	31±0	8.8±0
	Decalc. residue	10.4±0	24±0	11±3	1.8±0
	sum	**53.4**	**215**	**42**	**10.6**
	difference	-10%	-7%	-9%	-5%
	II Grinding, preheating of karst bauxite				
In:	B3 Mixed bauxite	43±2.7	191±5	31±0	8.8±0
	B3 Mixed from stock	27.5±1.7	112±3	18±0	5.1±0
	Turkish bauxite	13±0.1	27±0	7±0	1.7±0.1
	B2 bauxite	0.8±0	3±0	0±0	0.1±0
	Concentrated liquor	<0.3	<0.2	<22	<0.4
	sum	**84.3**	**333**	**56**	**15.7**
Out:	Karst solid fraction	82.9±13.1	332±0	49	15.2±0.8
	Karst liquid fraction	n/a	n/a		n/a
	sum	**82.9**	**332**	**49**	**15.2**
	difference	-2%	0%	-13%	-3%
	III Grinding, desilication of lateritic bauxite				
In:	Lateritic bauxite	2.2±0.2	4±0	<2	0.3±0
	Spent liquor	<0.01	<0.01	<0.01	<0.01
	sum	**2.2**	**4**		**0.3**
Out:	Later. solid fraction	5.6±0.3	17±1	<2	0.8±0
	Later liquid fraction	n/a	n/a	n/a	n/a
	sum	**5.6**	**17**		**0.8**
	difference	155%	325%		167%
	IV Digestion, settling, washing				
In:	Karst solid fraction	82.9±13.1	332±0	49	15.2±0.8
	Karst liquid fraction	n/a	n/a	n/a	n/a
	Later. solid fraction	5.6±0.3	17±1	<2	0.8±0
	Later liquid fraction	n/a	n/a	n/a	n/a
	Lime	0.2	<0.2	<0.3	0.01
	sum	**88.7**	**349**	**49**	**16.01**
Out:	Bauxite residue	92.1±0.9	334±2	58±2	15.8±0.9
	Pregnant liquor	<0.4	<0.4		<0.6
	sum	**92.1**	**334**	**58**	**15.8**
	difference	4%	-4%	18%	-1%

Table A 7 continued.

		La	Ce	Nd	Sm
In:	**External balance**				
	Karst bauxite	84.3±2	333±8	56±0	15.7±0.1
	Lateritic bauxite	2.2±0.2	4±0	<2	0.3±0
	Lime	0.2	<0.2	<0.3	0.01
	sum	**86.7**	**337**	**56**	**16.01**
Out:	Aluminium hydroxide	<0.5	<3	<5	<0.1
	Bauxite residue	92.1±0.9	334±2	58±2	15.8±0.9
	sum	**92.1**	**334**	**58**	**15.8**
	difference	6%	-1%	4%	-1%

Table A 7 continued.

		Eu	Yb	Lu	Sc
	I HMS				
In:	B3 Standard	0.7±0.1	1.7±0.1	0.27±0.00	12.0±0.2
	B3 Delphi-Distomo	2.3±0.3	6±0.6	1.05±0.16	44.8±0.8
	sum	**3**	**7.7**	**1.32**	**56.8**
Out:	B3 Mixed bauxite	1.9±0.1	6.6±0.6	0.91±0.07	47.8±0.8
	Decalc. residue	0.4±0	1.1±0	0.14±0.01	5.5±0.1
	sum	**2.3**	**7.7**	**1.05**	**53.3**
	difference	-23%	0%	-20%	-6%
	II Grinding, preheating of karst bauxite				
In:	B3 Mixed bauxite	1.9±0.1	6.6±0.6	0.91±0.07	47.8±0.8
	B3 Mixed from stock	1.1±0.1	3.9±0.4	0.53±0.04	27.9±0.4
	Turkish bauxite	0.3±0	1.2±0	0.16±0	5.6±0.1
	B2 bauxite	0.02±0	0.1±0	0.02±0	0.8±0
	Concentrated liquor	<0.7	<0.7	<0.22	<0.4
	sum	**3.32**	**11.8**	**1.62**	**82.1**
Out:	Karst solid fraction	2.4±0.4	12.2±0.8	1.46±0.23	77.9±0
	Karst liquid fraction	n/a	n/a	n/a	n/a
	sum	**2.4**	**12.2**	**1.46**	**77.9**
	difference	-28%	3%	-10%	-5%
	III Grinding, desilication of lateritic bauxite				
In:	Lateritic bauxite	0.2±0.1	0.9±0.1	0.16±0.02	3.1±0
	Spent liquor	<0.02	<0.02	<0.01	<0.01
	sum	**0.2**	**0.9**	**0.16**	**3.1**
Out:	Later. solid fraction	0.3±0.1	1±0.1	0.16±0	5.5±0.1
	Later liquid fraction	n/a	n/a	n/a	n/a
	sum	**0.3**	**1**	**0.16**	**5.5**
	difference	50%	11%	0%	77%

Table A 7 continued.

		Eu	Yb	Lu	Sc
	IV Digestion, settling, washing				
In:	Karst solid fraction	2.4±0.4	12.2±0.8	1.46±0.23	77.9±0
	Karst liquid fraction	n/a	n/a	n/a	n/a
	Later. solid fraction	0.3±0.1	1±0.1	0.16±0	5.5±0.1
	Later liquid fraction	n/a	n/a	n/a	n/a
	Lime	<0.01	0.02	<0.003	0.1
	sum	**2.7**	**13.22**	**1.62**	**83.5**
Out:	Bauxite residue	3.5±0.4	12±0	1.68±0.04	86.5±0.1
	Pregnant liquor	<1.1	<1.1	<0.33	<0.6
	sum	**3.5**	**12**	**1.68**	**86.5**
	difference	30%	-9%	4%	4%
In:	**External balance**				
	Karst bauxite	3.32±0.2	11.8±0.9	1.62±0.1	82.1±1.2
	Lateritic bauxite	0.2±0.1	0.9±0.1	0.16±0	3.1±0
	Lime	<0.01	0.02	<0.003	0.1
	sum	**3.52**	**12.72**	**1.78**	**85.3**
Out:	Aluminium hydroxide	<0.2	<0.2	<0.05	<0.1
	Bauxite residue	3.5±0.4	12±0	1.68±0	86.5±0.5
	sum	**3.5**	**12**	**1.68**	**86.5**
	difference	-1%	-6%	-6%	1%

Appendix B

Table B 1. Normalised HRTEM-EDS semi-quantitative analysis of the nano-scaled calcium ferrotitanate particles.

Measurement no.	O	Na	Mg	Al	Si	S	Ca	Ti	V	Cr	Fe	Co	Zr	La	Ce	Nd	Th	Sum
2-22	9.6	2.4	n/a	0.9	1.6	n/a	28.3	39.2	n/a	0.6	11.0	1.1	n/a	1.8	3.3	0.2	n/a	100.0
4-23	24.6	2.9	n/a	0.6	1.5	n/a	26.8	36.3	0.5	n/a	5.2	n/a	n/a	0.1	1.4	0.0	n/a	100.0
2-24	25.8	1.7	n/a	4.4	5.4	0.4	15.9	21.2	n/a	0.8	23.1	n/a	n/a	0.0	0.8	0.5	n/a	100.0
3-24	21.6	3.2	n/a	0.6	1.7	n/a	29.5	38.6	n/a	n/a	2.1	0.2	n/a	0.0	2.1	0.3	n/a	100.0
2-58	19.5	2.4	n/a	0.9	1.4	n/a	25.2	32.0	n/a	0.6	14.0	n/a	n/a	2.8	0.9	0.2	n/a	100.0
4-25	17.9	2.0	n/a	1.1	1.6	n/a	31.8	40.3	0.7	n/a	3.4	n/a	n/a	0.0	1.1	0.0	n/a	100.0
2-57	10.5	2.9	n/a	0.9	2.1	n/a	33.1	41.7	n/a	0.6	2.9	1.1	n/a	0.9	2.8	0.1	0.4	100.0
3-7	21.1	1.7	n/a	0.6	1.6	n/a	28.6	35.6	n/a	n/a	10.1	n/a	n/a	0.0	0.6	0.0	n/a	100.0
2-41	17.7	2.4	n/a	1.0	1.7	n/a	25.1	31.0	n/a	0.7	18.0	1.0	n/a	0.0	0.9	0.2	0.4	100.0
3-63	3.9	1.4	n/a	1.0	2.0	n/a	39.6	47.7	n/a	0.4	3.4	n/a	n/a	0.0	0.5	0.2	n/a	100.0
2-42	11.5	1.2	n/a	0.8	1.6	n/a	26.9	32.2	n/a	0.8	23.9	n/a	n/a	0.0	0.4	0.3	0.4	100.0
2-14	23.1	2.6	n/a	n/a	2.1	n/a	31.1	36.9	n/a	0.5	2.7	n/a	n/a	0.5	0.3	0.2	n/a	100.0
2-21	19.8	2.7	n/a	0.9	1.6	n/a	29.5	34.9	n/a	0.7	8.1	0.9	n/a	0.4	0.6	0.1	n/a	100.0
2-15	14.8	1.4	n/a	1.6	1.5	n/a	26.8	31.4	n/a	0.6	21.6	n/a	n/a	0.0	0.2	0.1	n/a	100.0
3-6	12.8	0.8	n/a	0.7	1.2	n/a	27.4	32.0	n/a	0.6	24.1	n/a	n/a	0.0	0.4	0.1	n/a	100.0
3-69	16.9	2.4	1.0	1.9	n/a	n/a	32.7	38.0	n/a	n/a	3.1	n/a	0.6	2.6	0.8	0.0	n/a	100.0
2-71	27.2	2.9	n/a	1.5	1.7	n/a	27.9	32.1	n/a	0.6	2.8	0.9	n/a	1.5	0.8	0.0	n/a	100.0
1-17	33.9	1.6	n/a	3.9	2.9	n/a	20.6	18.5	n/a	0.4	17.7	n/a	n/a	n/a	0.5	n/a	n/a	100.0
4-9	24.2	n/a	n/a	n/a	1.9	n/a	32.8	37.1	0.5	n/a	2.5	n/a	0.5	n/a	0.5	0.0	n/a	100.0

Appendix C

Table C 1. EPMA-WDS quantification of Parnassos-Ghiona horizon B3 bauxite (DD-BX) hematite matrix.

Analyte	1	2	3	4	5	6	7	8	9	10	11	12	Average	S.D.
Fe_2O_3 (wt %)	84.91	83.50	83.02	88.94	88.95	87.31	86.12	63.53	88.96	92.07	90.49	92.27	85.84	7.66
TiO_2 (wt %)	3.52	3.09	2.68	2.96	3.43	3.40	2.31	1.84	2.48	3.08	2.47	2.61	2.82	0.51
Al_2O_3 (wt %)	9.65	13.62	15.64	8.53	8.13	9.72	11.97	36.59	9.51	5.71	7.56	5.32	11.83	8.36
SiO_2 (wt %)	1.10	1.08	1.37	1.22	1.08	1.03	1.19	1.26	1.16	0.99	1.06	1.14	1.14	0.11
Na_2O (wt %)	0.02	0.00	0.01	0.00	0.02	0.01	0.00	0.00	0.00	0.00	0.00	0.00	0.01	0.01
CaO (wt %)	0.13	0.16	0.15	0.21	0.12	0.14	0.14	0.09	0.16	0.15	0.16	0.16	0.15	0.03
MgO (wt %)	0.02	0.03	0.05	0.04	0.04	0.03	0.03	0.04	0.04	0.03	0.02	0.03	0.03	0.01
Cr_2O_3 (wt %)	0.30	0.25	0.23	0.27	0.21	0.21	0.21	0.13	0.21	0.20	0.22	0.24	0.22	0.04
V_2O_3 (wt %)	0.10	0.09	0.09	0.09	0.09	0.08	0.10	0.06	0.08	0.10	0.10	0.10	0.09	0.01
Sc (mg/kg)	240	280	230	260	270	250	250	200	250	270	270	290	260	20
Total (wt %)	99.78	101.86	103.26	102.29	102.10	101.95	102.10	103.59	102.64	102.37	102.13	101.90	102.16	0.92

Table C 2. EPMA-WDS quantification of Parnassos-Ghiona horizon B3 bauxite ST-BX hematite matrix.

Analyte	1	2	3	4	5	6	7	8	9	10	11	12	13	14	15	16	Average	S.D.
Fe_2O_3 (wt %)	93.37	93.79	96.22	97.16	95.21	96.31	97.47	95.99	96.66	96.05	94.48	97.86	95.08	97.06	97.30	95.48	95.97	1.32
TiO_2 (wt %)	2.31	2.67	1.76	2.45	2.72	2.42	2.09	2.32	2.85	2.51	2.81	3.53	2.53	2.69	2.31	2.54	2.53	0.38
Al_2O_3 (wt %)	8.99	2.90	1.87	1.42	1.94	2.07	2.02	2.68	1.72	1.95	1.73	1.47	2.25	1.03	3.10	2.37	2.47	1.82
SiO_2 (wt %)	0.56	0.56	0.46	0.67	0.73	0.81	0.43	0.58	0.45	0.73	0.79	0.33	0.64	1.72	0.30	0.49	0.64	0.33
Na_2O (wt %)	0.02	0.02	0.01	0.02	0.02	0.03	0.01	0.03	0.01	0.02	0.03	0.00	0.06	0.02	0.00	0.02	0.02	0.01
CaO (wt %)	0.11	0.11	0.07	0.08	0.16	0.14	0.10	0.12	0.07	0.12	0.14	0.05	0.18	0.12	0.07	0.15	0.11	0.04
MgO (wt %)	0.00	0.01	0.00	0.00	0.01	0.01	0.00	0.00	0.00	0.01	0.01	0.00	0.02	0.02	0.00	0.02	0.01	0.01
Cr_2O_3 (wt %)	0.15	0.19	0.34	0.16	0.18	0.15	0.18	0.17	0.31	0.18	0.18	0.21	0.17	0.17	0.30	0.18	0.20	0.06
V_2O_3 (wt %)	0.23	0.23	0.31	0.32	0.20	0.25	0.20	0.24	0.21	0.24	0.23	0.16	0.23	0.31	0.29	0.22	0.24	0.04
Sc (mg/kg)	120	120	130	200	200	200	230	180	100	190	200	80	180	180	180	150	170	40
Total (wt %)	105.75	100.51	101.06	102.31	101.19	102.20	102.53	102.16	102.28	101.84	100.43	103.63	101.18	103.17	103.71	101.49	102.21	1.37

Table C 3. EPMA-WDS quantification of bauxite residue hematite-dominant particles, Sc-depleted population.

	1	**2**	**3**	**4**	**5**	**6**	**7**	**8**	**9**	**10**	**11**	**12**	**13**	**14**	**15**	**16**	**17**
Fe_2O_3 (wt %)	101.11	100.80	100.84	92.34	88.48	88.49	86.91	94.56	95.79	94.43	94.13	91.54	93.72	95.29	95.17	88.93	96.68
TiO_2 (wt %)	1.56	1.52	1.54	1.72	0.87	0.77	1.61	1.26	0.73	0.96	0.99	1.19	0.96	0.93	0.84	1.53	0.49
Al_2O_3 (wt %)	0.11	0.15	0.16	2.03	6.23	6.27	5.56	1.20	1.62	1.32	0.96	0.93	1.98	1.90	2.01	2.10	1.86
SiO_2 (wt %)	0.07	0.10	0.12	1.30	1.55	1.49	1.68	1.30	0.93	1.42	1.57	2.26	0.54	0.68	0.56	0.58	0.81
Na_2O (wt %)	0.03	0.01	0.01	0.98	0.20	0.11	0.39	1.13	0.50	0.67	0.61	0.55	0.28	0.36	0.26	0.35	0.41
CaO (wt %)	0.10	0.13	0.13	0.82	0.52	0.52	0.55	0.48	0.37	0.37	0.60	0.51	0.36	0.35	0.37	0.41	0.40
MgO (wt %)	0.00	0.00	0.00	0.04	0.00	0.02	0.00	0.04	0.20	0.14	0.27	0.28	0.15	0.13	0.19	0.20	0.18
Cr_2O_3 (wt %)	0.08	0.09	0.09	0.08	0.04	0.06	0.04	0.15	0.01	0.03	0.03	0.15	0.02	0.05	0.03	0.04	0.03
V_2O_3 (wt %)	0.28	0.28	0.29	0.03	0.14	0.13	0.11	0.08	0.03	0.01	0.03	0.03	0.02	0.03	0.02	0.02	0.02
Sc (mg/kg)	0	10	30	40	30	30	0	50	10	10	20	50	20	30	50	30	80
Total (wt %)	103.34	103.08	103.18	99.34	98.04	97.85	96.83	100.19	100.18	99.35	99.18	97.45	98.04	99.73	99.45	94.16	100.88

Table C 3 continued.

	18	**19**	**20**	**21**	**22**	**23**	**24**	**25**	**26**	**27**	**28**	**29**	**30**	**31**	**32**	**Average**	**S.D.**
Fe_2O_3 (wt %)	96.48	92.52	91.99	93.09	91.22	94.75	92.53	97.13	95.76	95.84	92.72	89.60	91.01	92.32	95.65	93.81	3.49
TiO_2 (wt %)	0.60	1.78	1.03	1.05	1.19	0.34	0.58	0.21	0.16	0.17	0.31	0.34	0.19	0.56	4.61	1.02	0.82
Al_2O_3 (wt %)	1.95	2.24	1.34	1.34	1.30	1.69	1.71	2.42	2.30	1.83	1.17	1.10	1.44	1.61	1.29	1.91	1.47
SiO_2 (wt %)	0.75	0.30	1.43	1.49	1.49	1.38	0.86	0.63	0.66	0.98	1.82	2.69	2.48	1.39	0.19	1.11	0.68
Na_2O (wt %)	0.36	0.14	0.62	0.61	0.63	0.67	0.45	0.30	0.30	0.57	0.27	0.64	0.69	0.52	0.09	0.43	0.27
CaO (wt %)	0.35	0.28	0.71	0.68	0.71	0.61	0.45	0.30	0.27	0.34	0.50	0.50	0.52	0.44	0.39	0.44	0.17
MgO (wt %)	0.19	0.30	0.27	0.24	0.34	0.16	0.15	0.21	0.19	0.15	0.38	0.25	0.28	0.11	0.00	0.16	0.11
Cr_2O_3 (wt %)	0.02	0.03	0.04	0.03	0.04	0.02	0.02	0.01	0.02	0.01	0.01	0.02	0.01	0.02	0.27	0.05	0.05
V_2O_3 (wt %)	0.02	0.02	0.04	0.03	0.03	0.02	0.03	0.02	0.01	0.02	0.02	0.02	0.03	0.03	0.53	0.07	0.12
Sc (mg/kg)	50	60	0	10	20	50	40	40	30	20	0	10	20	80	80	30	20
Total (wt %)	100.72	97.62	97.45	98.56	96.95	99.66	96.76	101.24	99.66	99.90	97.20	95.15	96.64	97.01	103.04	98.99	2.28

Table C 4. EPMA-WDS quantification of bauxite residue hematite-dominant particles, Sc-hosting population.

	1	2	3	4	5	6	7	8	9	10	11	12	13
Fe_2O_3 (wt %)	85.62	96.26	98.22	93.47	93.02	95.90	92.74	87.46	89.47	95.13	95.09	94.95	93.64
TiO_2 (wt %)	5.25	2.41	2.61	5.22	3.73	2.28	2.20	3.52	3.53	1.45	1.57	7.42	8.69
Al_2O_3 (wt %)	1.83	2.37	1.03	0.96	2.06	2.48	2.46	1.92	2.05	1.42	1.41	0.73	0.70
SiO_2 (wt %)	0.45	0.69	0.40	0.16	0.41	0.46	0.31	2.00	0.45	2.11	2.00	0.31	0.35
Na_2O (wt %)	0.31	0.14	0.13	0.10	0.20	0.10	0.09	1.04	0.24	0.56	0.52	0.09	0.10
CaO (wt %)	1.50	0.45	0.21	0.28	0.34	0.18	0.16	1.00	0.54	0.38	0.57	0.16	0.18
MgO (wt %)	0.02	0.01	0.00	0.01	0.01	0.01	0.00	0.05	0.02	0.03	0.03	0.00	0.00
Cr_2O_3 (wt %)	0.45	0.11	0.03	0.16	0.30	0.33	0.27	0.18	0.26	0.18	0.16	0.08	0.08
V_2O_3 (wt %)	0.59	0.28	0.29	0.14	0.13	0.19	0.22	0.12	0.12	0.05	0.05	0.13	0.14
Sc (mg/kg)	120	160	210	120	190	160	120	290	220	260	230	160	180
Total (wt %)	96.03	102.74	102.95	100.52	100.24	101.95	98.47	97.32	96.72	101.33	101.43	103.90	103.91

Table A 4 continued.

	14	15	16	17	18	19	20	21	22	23	24	Average	S.D.
Fe_2O_3 (wt %)	85.79	86.07	90.84	94.35	88.17	85.55	94.68	94.75	95.99	94.84	86.61	92.02	4.06
TiO_2 (wt %)	4.04	4.06	2.94	2.69	4.91	3.71	3.17	3.59	2.78	3.39	10.45	3.98	2.17
Al_2O_3 (wt %)	1.77	1.87	1.93	3.36	1.60	1.81	1.63	1.52	2.42	1.90	1.65	1.79	0.60
SiO_2 (wt %)	0.42	0.46	1.79	0.98	0.53	0.34	0.44	0.59	0.15	0.54	0.66	0.71	0.60
Na_2O (wt %)	0.18	0.21	1.02	0.42	0.28	0.09	0.22	0.20	0.08	0.26	0.27	0.29	0.26
CaO (wt %)	0.39	0.45	1.05	0.27	0.70	0.36	0.57	0.50	0.31	0.50	0.69	0.49	0.32
MgO (wt %)	0.03	0.02	0.09	0.02	0.17	0.04	0.02	0.08	0.03	0.03	0.03	0.03	0.04
Cr_2O_3 (wt %)	0.39	0.38	0.14	0.30	0.37	0.18	0.19	0.14	0.31	0.17	0.48	0.24	0.12
V_2O_3 (wt %)	0.21	0.22	0.06	0.19	0.10	0.12	0.15	0.21	0.10	0.16	0.14	0.17	0.11
Sc (mg/kg)	120	100	380	180	160	290	170	130	200	160	240	190	70
Total (wt %)	93.24	93.76	99.91	102.61	96.86	92.24	101.08	101.60	102.21	101.80	101.03	99.74	3.39

Table C 5. EPMA-WDS quantification of bauxite residue's goethite particles.

	1	2	3	4	5	6	7	8	9	10	11	12	Average	S.D.
Fe_2O_3 (wt %)	94.91	94.58	80.13	88.91	83.07	80.62	84.88	81.58	84.83	85.62	84.72	86.87	85.89	4.84
TiO_2 (wt %)	0.23	0.20	7.81	0.33	9.33	6.08	0.42	1.11	1.02	1.25	0.21	0.28	2.36	3.34
Al_2O_3 (wt %)	0.17	0.08	0.51	0.15	0.69	1.14	1.64	2.45	0.84	0.81	0.03	0.52	0.75	0.72
SiO_2 (wt %)	1.32	1.53	1.39	1.70	1.59	2.41	2.35	2.51	2.09	2.04	1.36	1.82	1.84	0.43
Na_2O (wt %)	0.16	0.12	0.15	0.20	0.46	0.56	0.48	0.77	0.45	0.60	0.05	0.29	0.36	0.23
CaO (wt %)	0.17	0.13	0.10	0.14	0.17	0.40	0.29	0.78	0.44	0.48	0.20	0.21	0.29	0.20
MgO (wt %)	0.01	0.00	0.01	0.00	0.00	0.12	0.14	0.20	0.30	0.31	0.00	0.00	0.09	0.12
Cr_2O_3 (wt %)	0.01	0.01	0.02	0.00	0.07	0.11	0.03	0.04	0.10	0.13	0.02	0.03	0.05	0.04
V_2O_3 (wt %)	0.03	0.02	0.08	0.01	0.11	0.09	0.04	0.05	0.04	0.04	0.01	0.04	0.05	0.03
Sc (mg/kg)	830	420	400	300	290	60	80	130	30	260	470	650	330	240
Total (wt %)	97.13	96.75	90.26	91.47	95.53	91.55	90.27	89.53	90.12	91.32	86.67	90.15	91.73	3.15

Table C 6. EPMA-WDS quantification of diaspore/boehmite matrices of bauxite samples.

	1	2	3	4	5	6	7	8	9	10	Average	S.D.
Fe_2O_3(wt %)	7.27	4.42	3.88	3.26	3.11	2.80	3.81	2.90	7.39	6.81	4.56	1.86
TiO_2 (wt %)	0.30	0.18	0.16	0.15	0.11	0.10	0.18	0.14	0.82	0.30	0.24	0.21
Al_2O_3(wt %)	87.46	91.22	88.24	91.11	91.57	90.98	92.68	85.71	87.82	89.62	89.64	2.23
SiO_2 (wt %)	0.30	0.64	0.45	0.92	0.40	0.61	0.65	0.52	0.33	0.44	0.53	0.18
Na_2O (wt %)	0.01	0.00	0.00	0.00	0.01	0.01	0.01	0.04	0.01	0.03	0.01	0.01
CaO (wt %)	0.03	0.01	0.02	0.04	0.02	0.03	0.05	0.04	0.05	0.03	0.03	0.01
Sc (mg/kg)	20	10	0	0	10	0	0	0	20	10	10	10
Total (wt %)	95.38	96.48	92.76	95.48	95.21	94.53	97.38	89.35	96.42	97.23	95.02	2.41

Table C 7. EPMA-WDS quantification of diaspore/boehmite dominant particles of bauxite residue.

	1	**2**	**3**	**4**	**Average**	**S.D.**
Fe_2O_3 (wt %)	2.95	2.52	4.14	1.14	2.69	1.24
TiO_2 (wt %)	1.70	0.97	0.59	0.17	0.86	0.65
Al_2O_3 (wt %)	88.56	88.14	86.90	86.23	87.46	1.08
SiO_2 (wt %)	0.14	0.11	0.67	0.00	0.23	0.30
Na_2O (wt %)	0.00	0.00	0.01	0.01	0.00	0.00
CaO (wt %)	0.07	0.02	0.35	0.14	0.15	0.15
Sc (mg/kg)	20	10	30	0	15	15
Total (wt %)	93.42	91.76	92.67	87.68	91.38	2.56

References

Abhilash, Sinha, S., Sinha, M.K., Pandey, B.D., 2014. Extraction of lanthanum and cerium from Indian red mud. Int. J. Miner. Process. 127, 70–73. https://doi.org/10.1016/j.minpro.2013.12.009

Adam, C., Krüger, O., 2017. Challenges in analysing rare earth elements in different waste matrices to determine recovery potentials, in: Book of Abstracts, 2nd Conference on European Rare Earth Resources. Presented at the 2nd Conference on European Rare Earth Resources, Heliotopos Conferences Ltd., Santorini, Greece, 28-31 May 2017, pp. 237–239.

Adams, J.A.S., Richardson, K.A., 1960a. Radioactivity of aluminum metal. Econ. Geol. 55, 1060–1063. https://doi.org/10.2113/gsecongeo.55.5.1060

Adams, J.A.S., Richardson, K.A., 1960b. Thorium, uranium and zirconium concentrations in bauxite. Econ. Geol. 55, 1653–1675. https://doi.org/10.2113/gsecongeo.55.8.1653

Adamson, A.N., Bloore, E.J., Carr, A.R., 2013. Basic Principles of Bayer Process Design, in: Donaldson, D., Raahauge, B.E. (Eds.), Essential Readings in Light Metals. John Wiley & Sons, Inc., pp. 100–117.

Aiglsperger, T., Proenza, J.A., Lewis, J.F., Labrador, M., Svojtka, M., Rojas-Puron, A., Longo, F., Ďurišová, J., 2016. Critical metals (REE, Sc, PGE) in Ni laterites from Cuba and the Dominican Republic. Ore Geol. Rev. 73, 127–147.

Akcil, A., Akhmadiyeva, N., Abdulvaliyev, R., Abhilash, Meshram, P., 2017. Overview on Extraction and Separation of Rare Earth Elements from Red Mud: Focus on Scandium. Miner. Process. Extr. Metall. Rev. 0, 1–7. https://doi.org/10.1080/08827508.2017.1288116

Ali, S.H., 2014. Social and Environmental Impact of the Rare Earth Industries. Resources 3, 123–134. https://doi.org/10.3390/resources3010123

Alkan, G., Xakalashe, B., Yagmurlu, B., Kaussen, F., Friedrich, B., 2017. Conditioning of Red Mud for Subsequent Titanium and Scandium Recovery–A Conceptual Design Study. World Metall. – Erzmetall 70, 5–12.

Anders, E., Grevesse, N., 1989. Abundances of the elements: Meteoritic and solar. Geochim. Cosmochim. Acta 53, 197–214.

Astakhova, N.V., Sattarova, V.V., 2012. The REE species and their distribution in ferromanganese crusts in the Sea of Japan. Russ. Geol. Geophys. 53, 649–656. https://doi.org/10.1016/j.rgg.2012.05.003

Atta, N.F., Galal, A., El-Ads, E.H., 2016. Perovskite Nanomaterials – Synthesis, Characterization, and Applications, in: Pan, L., Zhu, G. (Eds.), Perovskite Materials – Synthesis, Characterisation, Properties, and Applications. InTech, London, UK, pp. 107–151.

Atwood, D.A., 2012. The rare earth elements: fundamentals and applications. John Wiley & Sons, University of Kentucky, Lexington, KY, USA.

Authier-Martin, M., Forte, G., Ostap, S., See, J., 2001. The mineralogy of bauxite for producing smelter-grade alumina. JOM 53, 36–40. https://doi.org/10.1007/s11837-001-0011-1

Bánvölgyi, G., 2016. Scale formation in alumina refineries, in: Proceedings of the 34th International Conference and Exhibition ICSOBA, Travaux 45. Quebec, Canada, 3-6 October, pp. 1–14.

Bánvölgyi, G., Toth, A.C., Tassy, I., 1991. In situ formation of sodium aluminum hydrosilicate from kaolinite. Light Met. 5–15.

Bárdossy, G., 1982. Karst bauxites: bauxite deposits on carbonate rocks, Developments in Economic Geology 14. Elsevier Scientific Pub. Co., Amsterdam, Netherlands.

Bárdossy, G., Pantó, G., 1973. Trace mineral and element investigation in bauxites by electron-probe, in: Proceedings. Presented at the 3rd International Congress of ICSOBA, Nice, pp. 47–53.

Bárdossy, G., Pantó, G., 1971. Investigation of bauxites with the help of electron-probe. TMPM Tschermaks Min Petr Mitt 15, 165–184.

Bayer, K.J., 1892. A Process for the Production of Aluminum Hydroxide, patent no 65604, Germany,. 65604.

Bayer, K.J., 1888. A Process for the Production of Aluminum Hydroxide, patent no 43977, Germany,. 43977.

Binnemans, K., Jones, P.T., Blanpain, B., Van Gerven, T., Pontikes, Y., 2015. Towards zero-waste valorisation of rare-earth-containing industrial process residues: a critical review. J. Clean. Prod. 99, 17–38. https://doi.org/10.1016/j.jclepro.2015.02.089

Binnemans, K., Jones, P.T., Müller, T., Yurramendi, L., 2018. Rare Earths and the Balance Problem: How to Deal with Changing Markets? J. Sustain. Metall. 4, 126–146. https://doi.org/10.1007/s40831-018-0162-8

Blankova, T.N., Kalinin, A.I., Kalinina, N.E., Khamatdinova, G.S., 1977. Neutron-activation analysis of bauxites and products of their processing. J. Radioanal. Chem. 38, 341–349. https://doi.org/10.1007/BF02520211

Bolanz, R.M., Kiefer, S., Göttlicher, J., Steininger, R., 2018. Hematite (α-Fe2O3) – A potential Ce4 + carrier in red mud. Sci. Total Environ. 622–623, 849–860. https://doi.org/10.1016/j.scitotenv.2017.12.043

Boni, M., Rollinson, G., Mondillo, N., Balassone, G., Santoro, L., 2013. Quantitative mineralogical characterization of karst bauxite deposits in the southern Apennines, Italy. Econ. Geol. 108, 813–833. https://doi.org/10.2113/econgeo.108.4.813

Bonomi, C., Davris, P., Balomenos, E., Giannopoulou, I., Panias, D., 2017a. Ionometallurgical leaching process of bauxite residue: a comparison between hydrophilic and hydrophobic ionic liquids, in: Proceedings, Travaux 46. Presented at the 35th International ICSOBA Conference, ICSOBA, Hamburg, Germany, 2-5 October 2017, pp. 557–564.

Bonomi, C., Giannopoulou, I., Panias, D., 2017b. Correlation of scandium and titanium during leaching of bauxite residue (red mud) by an imidazolium ionic liquid, in: Balomenos, E., Marinos, D. (Eds.), Book of Abstracts. Presented at the 2nd Conference on European Rare Earth Resources, Heliotopos Conferences Ltd., Santorini, Greece, pp. 182–184.

Borra, C.R., Blanpain, B., Pontikes, Y., Binnemans, K., Van Gerven, T., 2016. Recovery of rare earths and other valuable metals from bauxite residue (red mud): a review. J. Sustain. Metall. 2, 365–386. https://doi.org/10.1007/s40831-016-0068-2

Borra, C.R., Pontikes, Y., Binnemans, K., Van Gerven, T., 2015. Leaching of rare earths from bauxite residue (red mud). Miner. Eng. 76, 20–27. https://doi.org/10.1016/j.mineng.2015.01.005

Boulangé, B., Carvalho, A., 1997. The bauxite of Porto Trombetas, in: Carvalho, A., Boulangé, B., Melfi, A.J., Lucas, Y. (Eds.), Brazilian Bauxites. NUPEGEL, Departamento de Geologia Geral Universidade de Sao Paulo, Brasil, São Paulo - Paris.

Breiter, K., Förster, H.-J., Škoda, R., 2006. Extreme P-, Bi-, Nb-, Sc-, U- and F-rich zircon from fractionated perphosphorous granites: The peraluminous Podlesí granite system, Czech Republic. Lithos, Compositional Variation in Metamorphic Accessory Phases 88, 15–34. https://doi.org/10.1016/j.lithos.2005.08.011

Brookins, D.G., 1988. Eh-pH Diagrams for Geochemistry. Springer Science & Business Media, ISBN 978-3-642-73093-1, Berlin, Germany.

Brookins, D.G., 1983. Eh-pH diagrams for the rare earth elements at 25 C and one bar pressure. Geochem. J. 17, 223–229.

Burke, I.T., Mayes, W.M., Peacock, C.L., Brown, A.P., Jarvis, A.P., Gruiz, K., 2012. Speciation of Arsenic, Chromium, and Vanadium in Red Mud Samples from the Ajka Spill Site, Hungary. Environ. Sci. Technol. 46, 3085–3092. https://doi.org/10.1021/es3003475

Buzgar, N., Apopei, A.I., 2009. The Raman study of certain carbonates. Analele Stiintifice Univ. Al Cuza Din Iasi Sect 2 Geol. 55, 97–112.

Campbell, L.S., Henderson, P., Wall, F., Nielsen, T.F., 1997. Rare earth chemistry of perovskite group minerals from the Gardiner Complex, East Greenland. Mineral. Mag. 61, 197–212.

Castor, S.B., Hedrick, J.B., 2006. Rare earth elements, in: Kogel, J.E., Trivedi, N.C., Barker, J.M., Krukowski, S.T. (Eds.), Industrial Minerals & Rocks: Commodities, Markets, and Uses. Society for Mining, Metallurgy, and Exploration, Littleton, Colorado, United States of America, pp. 769–779.

Chassé, M., Griffin, W.L., O'Reilly, S.Y., Calas, G., 2017. Scandium speciation in a world-class lateritic deposit. Geochem. Perspect. Lett. 105–114. https://doi.org/10.7185/geochemlet.1711

Chester, R., Jones, F., Loan, M., Oliveira, A., Richmond, W.R., 2009. The dissolution behaviour of titanium oxide phases in synthetic Bayer liquors at 90 °C. Hydrometallurgy 96, 215–222. https://doi.org/10.1016/j.hydromet.2008.10.009

Chin, L.A.D., 1988. The state-of-the-art in Bayer process technology, in: Proceedings. Presented at the TMS Annual Meeting, TMS, Phoenix, USA, 25–28 January 1988, pp. 49–53.

Christmann, P., 2018. Towards a More Equitable Use of Mineral Resources. Nat. Resour. Res. 27, 159–177. https://doi.org/10.1007/s11053-017-9343-6

Christmann, P., Arvanitidis, N., Martins, L., Recoché, G., Solar, S., 2007. Towards the Sustainable Use of Mineral Resources: A European Geological Surveys Perspective. Miner. Energy - Raw Mater. Rep. 22, 88–104. https://doi.org/10.1080/14041040701405662

Cook, J., Nuccitelli, D., Green, S.A., Richardson, M., Winkler, B., Painting, R., Way, R., Peter Jacobs, Skuce, A., 2013. Quantifying the consensus on anthropogenic global warming in the scientific literature. Environ. Res. Lett. 8, 024024. https://doi.org/10.1088/1748-9326/8/2/024024

Cui, J., Hope, G.A., 2015. Raman and Fluorescence Spectroscopy of CeO2, Er2O3, Nd2O3, Tm2O3, Yb2O3, La2O3, and Tb4O7. J. Spectrosc. 2015, 1–8. http://dx.doi.org/10.1155/2015/940172

Davris, P., Balomenos, E., Panias, D., Paspaliaris, I., 2016. Selective leaching of rare earth elements from bauxite residue (red mud), using a functionalized hydrophobic ionic liquid. Hydrometallurgy 164, 125–135. https://doi.org/10.1016/j.hydromet.2016.06.012

Davris, P., Balomenos, E., Panias, D., Paspaliaris, I., 2014. Leaching of rare earths from bauxite residues using imidazolium based ionic liquids, in: Book of Proceedings. Presented at the ERES2014: 1st European Rare Earth Resources Conference, Heliotopos Conferences Ltd., Milos, pp. 241–251.

Davris, P., Balomenos, E., Taxiarchou, M., Panias, D., Paspaliaris, I., 2017. Current and Alternative Routes in the Production of Rare Earth Elements. BHM Berg- Hüttenmänn. Monatshefte 162, 245–251. https://doi.org/10.1007/s00501-017-0610-y

De Faria, D.L.A., Venâncio Silva, S., Oliveira, M.T., 1997. Raman microspectroscopy of some iron oxides and oxyhydroxides. J. Raman Spectrosc. 28, 873–878. https://doi.org/10.1002/(SICI)1097-4555(199711)28:11<873::AID-JRS177>3.0.CO;2-B

Deady, É.A., Mouchos, E., Goodenough, K., Williamson, B.J., Wall, F., 2016. A review of the potential for rare-earth element resources from European red muds: examples from Seydişehir, Turkey and Parnassus-Giona, Greece. Mineral. Mag. 80, 43–61. https://doi.org/10.1180/minmag.2016.080.052

Derevyankin, V.A., Porotnikova, T.P., Kocherova, E.K., Yumasheva, I.V., Moiseev, V.E., 1981. Behaviour of scandium and lanthanum in the production of alumina from bauxite. Izv. Vysshikh Uchebnykh Zaved. Tsvetnaya Metall. 86–89.

Downs, A.J., 1993. Chemistry of Aluminium, Gallium, Indium, and Thallium. Springer Science & Business Media.

Dubinin, A.V., 2004. Geochemistry of Rare Earth Elements in the Ocean. Lithol. Miner. Resour. 39, 289–307. https://doi.org/10.1023/B:LIMI.0000033816.14825.a2

Eliopoulos, D., Economou, G., Tzifas, I., Papatrechas, C., 2014. The potential of rare earth elements in Greece, in: Book of Proceedings. Presented at the ERES2014: 1st European Rare Earth Resources Conference, Heliotopos Conferences Ltd., Milos, Greece, pp. 308–316.

European Commission, Deloitte Sustainability, TNO, British Geological Survey, Bureau de Recherches Géologiques et Minières, 2017. Study on the review of the list of critical raw materials 1–93. https://doi.org/10.2873/876644

Evans, K., 2016. The history, challenges, and new developments in the management and use of bauxite residue. J. Sustain. Metall. 2, 316–331. https://doi.org/10.1007/s40831-016-0060-x

Eyer, S., Nunes, M., Dobbs, C., Russo, A., Burke, K., 2005. The analysis of beryllium in Bayer solids and liquids, in: Proceedings of the 7th International Alumina Quality Workshop. Presented at the Seventh International Alumina Quality Workshop, Perth, Australia, 16–21 October, Perth, Australia, 16–21 October, pp. 254–257.

Fenerty, M.J., 1960. Production of fused alumina, patent no. US2961296 A. US2961296 A.

Feng, D., Maram, P.S., Mielewczyk-Gryń, A., Navrotsky, A., 2016. Thermochemistry of rare earth perovskites Na3xRE0.67−xTiO3 (RE = La, Ce). Am. Mineral. 101, 1125–1128. https://doi.org/10.2138/am-2016-5529

Feret, F.R., See, J., 2010. A comparative study of analytical methods of trace elements in bauxite and red mud, in: Proceedings of the 18th International Symposium ICSOBA Travaux, No. 35,. Presented at the 18th International Symposium ICSOBA, Zhengzhou, China, 25-28 November, pp. 68–83.

Figueiredo, A.M.G., Avristcher, W., Masini, E.A., Diniz, S.C., Abrão, A., 2002. Determination of lanthanides (La, Ce, Nd, Sm) and other elements in metallic gallium by instrumental neutron activation analysis. J. Alloys Compd., Proceedings of the Rare Earths` 2001 Conference 344, 36–39. https://doi.org/10.1016/S0925-8388(02)00301-8

Frenzel, M., Ketris, M.P., Seifert, T., Gutzmer, J., 2016. On the current and future availability of gallium. Resour. Policy 47, 38–50. https://doi.org/10.1016/j.resourpol.2015.11.005

Gamaletsos, P., Godelitsas, A., Chatzitheodoridis, E., Kostopoulos, D., 2007. Laser μ-Raman investigation of Greek bauxites from the Parnassos-Ghiona active mining area, in: Bulletin of the Geological Society of Greece. Presented at the 11th International Conference of the Geological Society of Greece: “Geoenvironment – Past – Present – Future,” Athens, Greece, pp. 736–746.

Gamaletsos, P., Godelitsas, A., Kasama, T., Goettlicher, J., Steininger, R., 2016. Nano-mineralogy & -geochemistry of karst bauxites (Greece): Implications of the origin of the deposits, in: Goldschmidt Conference Abstracts. Presented at the V.M. Goldschmidt Conference, Yokohama, Japan.

Gamaletsos, P.N., 2014. Mineralogy and geochemistry of bauxites from Parnassos-Ghiona mines and the impact on the origin of the deposits (PhD). National and Kapodistrian University of Athens, Athens.

Gamaletsos, P.N., Godelitsas, A., Kasama, T., Church, N.S., Douvalis, A.P., Göttlicher, J., Steininger, R., Boubnov, A., Pontikes, Y., Tzamos, E., Bakas, T., Filippidis, A., 2017. Nano-mineralogy and -geochemistry of high-grade diasporic karst-type bauxite from Parnassos-Ghiona mines, Greece. Ore Geol. Rev. 84, 228–244. https://doi.org/10.1016/j.oregeorev.2016.11.009

Gamaletsos, P.N., Godelitsas, A., Kasama, T., Kuzmin, A., Lagos, M., Mertzimekis, T.J., Göttlicher, J., Steininger, R., Xanthos, S., Pontikes, Y., Angelopoulos, G.N., Zarkadas, C., Komelkov, A., Tzamos, E., Filippidis, A., 2016. The role of nano-perovskite in the negligible thorium release in seawater from Greek bauxite residue (red mud). Sci. Rep. 6, 1–13. https://doi.org/10.1038/srep21737

Garau, G., Castaldi, P., Santona, L., Deiana, P., Melis, P., 2007. Influence of red mud, zeolite and lime on heavy metal immobilization, culturable heterotrophic microbial populations and enzyme activities in a contaminated soil. Geoderma 142, 47–57. https://doi.org/10.1016/j.geoderma.2007.07.011

Gawu, S.K.Y., Amissah, E.E., Kuma, J.S., 2012. The proposed alumina industry and how to mitigate against the red mud footprint in Ghana. J. Urban Environ. Eng. 6, 48–56. https://doi.org/10.4090/juee.2012.v6n2.048056

Gelencsér, A., Kováts, N., Turóczi, B., Rostási, Á., Hoffer, A., Imre, K., Nyirő-Kósa, I., Csákberényi-Malasics, D., Tóth, Á., Czitrovszky, A., Nagy, A., Nagy, S., Ács, A., Kovács, A., Ferincz, Á., Hartyáni, Z., Pósfai, M., 2011. The Red Mud Accident in Ajka (Hungary): Characterization and Potential Health Effects of Fugitive Dust. Environ. Sci. Technol. 45, 1608–1615. https://doi.org/10.1021/es104005r

Gladyshev, S.V., Akcil, A., Abdulvaliyev, R.A., Tastanov, E.A., Beisembekova, K.O., Temirova, S.S., Deveci, H., 2015. Recovery of vanadium and gallium from solid waste by-products of Bayer process. Miner. Eng. 74, 91–98. https://doi.org/10.1016/j.mineng.2015.01.011

Goodenough, K.M., Wall, F., Merriman, D., 2017. The Rare Earth Elements: Demand, Global Resources, and Challenges for Resourcing Future Generations. Nat. Resour. Res. 1–16. https://doi.org/10.1007/s11053-017-9336-5

Goronovski, A., Joyce, P.J., Björklund, A., Finnveden, G., Tkaczyk, A.H., 2018. Impact assessment of enhanced exposure from Naturally Occurring Radioactive Materials (NORM) within LCA. J. Clean. Prod. 172, 2824–2839. https://doi.org/10.1016/j.jclepro.2017.11.131

Govindaraju, K., 1982. Report (1967–1981) on four ANRT rock reference samples: diorite DR-N, serpentine UB-N, bauxite BX-N and disthene DT-N. Geostand. Newsl. 6, 91–159. https://doi.org/10.1111/j.1751-908X.1982.tb00347.x

Govindaraju, K., Roelandts, I., 1989. 1988 compilation report on trace elements in six ANRT rock reference samples: diorite DR-N, serpentine UB-N, bauxite BX-N, disthene DT-N, granite GS-N and potash feldspar FK-N. Geostand. Geoanalytical Res. 13, 5–67. https://doi.org/10.1111/j.1751-908X.1989.tb00465.x

Gräfe, Markus, Landers, M., Tappero, R., Austin, P., Gan, B., Grabsch, A., Klauber, C., 2011a. Combined application of QEM-SEM and hard X-ray microscopy to determine mineralogical associations and chemical speciation of trace metals. J. Environ. Qual. 40, 767–783. https://doi.org/10.2134/jeq2010.0214

Gräfe, M., Power, G., Klauber, C., 2011. Bauxite residue issues: III. Alkalinity and associated chemistry. Hydrometallurgy 108, 60–79. https://doi.org/10.1016/j.hydromet.2011.02.004

Gräfe, Markus, Tappero, R., Landers, M., Gan, B., Austin, P., Taylor, Z., Klauber, C., 2011b. Micron-scale characterization of minerals, metals and processes in bauxite residue, in: Travaux. Presented at the ICSOBA 2011 - International Seminar on Bauxite Residue (Red Mud), International Committee for the Study of Bauxite, Alumina & Aluminium (ICSOBA), Goa, India, pp. 15–27.

Gray, F., Kramer, D.A., Bliss, J.D., 2013. Gallium and gallium compounds, in: Kirk-Othmer Encyclopedia of Chemical Technology. John Wiley & Sons, Inc. https://doi.org/10.1002/0471238961.0701121219010215.a01.pub3

Gregg, J.M., Bish, D.L., Kaczmarek, S.E., Machel, H.G., 2015. Mineralogy, nucleation and growth of dolomite in the laboratory and sedimentary environment: A review. Sedimentology 62, 1749–1769. https://doi.org/10.1111/sed.12202

Grice, J.D., Maisonneuve, V., Leblanc, M., 2007. Natural and Synthetic Fluoride Carbonates. Chem. Rev. 107, 114–132. https://doi.org/10.1021/cr050062d

Gu, H., Wang, N., 2013. Leaching of uranium and thorium from red mud using sequential extraction methods. Fresenius Environ. Bull.

Gu, H., Wang, N., Yang, Y., Zhao, C., Cui, S., 2016. Features of distribution of uranium and thorium in red mud. Physicochem. Probl. Miner. Process. 53, 110–121. https://doi.org/10.5277/ppmp170109

Habashi, F., 2013. Extractive metallurgy of rare earths. Can. Metall. Q. 52, 224–233. https://doi.org/10.1179/1879139513Y.0000000081

Habashi, F., 2006. Gallium update, in: Proceedings of the 17th International Symposium ICSOBA, Travaux Vol. 33 No. 37. Presented at the 17th International Symposium ICSOBA, Montréal, Canada, 1-4 October 2006, pp. 141–153.

Hanchar, J.M., 2015. Zircon, in: Rink, W.J., Thompson, J.W. (Eds.), Encyclopedia of Scientific Dating Methods, Encyclopedia of Earth Sciences Series. Springer Netherlands, pp. 959–962. https://doi.org/10.1007/978-94-007-6304-3_58

Hatipoğlu, M., Türk, N., Chamberlain, S.C., Murat Akgün, A., 2010. Metabauxite horizons containing remobilized-origin gem diaspore and related mineralization, Milas-Muğla province, SW Turkey. J. Asian Earth Sci. 39, 359–370. https://doi.org/10.1016/j.jseaes.2010.04.016

Hertel, T., Blanpain, B., Pontikes, Y., 2016. A Proposal for a 100 % Use of Bauxite Residue Towards Inorganic Polymer Mortar. J. Sustain. Metall. 2, 394–404. https://doi.org/10.1007/s40831-016-0080-6

Hieronymus, B., Kotschoubey, B., Boulègue, J., 2001. Gallium behaviour in some contrasting lateritic profiles from Cameroon and Brazil. J. Geochem. Explor. 72, 147–163. https://doi.org/10.1016/S0375-6742(01)00160-1

Hoatson, D.M., Jaireth, S., Miezitis, Y., 2011. The major rare-earth-element deposits of Australia: Geological setting, exploration and resources. Technical report, Australian Government, Geoscience Australia, ISBN 978–1–921954–02–3 http://www.ga.gov.au/corporate_data/71820/Complete_Report.pdf.

Horovitz, C.T., 1975. Scandium — its occurrence, chemistry, physics, metallurgy, biology and technology. Academic Press.

Hudson, L.K., 1965. Gallium as a by-product of alumina manufacture. J. Met. 17, 948–951. https://doi.org/10.1007/BF03397179

Hudson, L.K., Misra, C., Perrotta, A.J., Wefers, K., Williams, F.S., 2000. Aluminum Oxide, in: Ullmann's Encyclopedia of Industrial Chemistry. Wiley-VCH Verlag GmbH & Co. KGaA.

Ilić, Z., Mitrović, A., 1989. Determination of gallium in Bayer process sodium aluminate solution by inductively coupled plasma atomic emission spectrometry. Anal. Chim. Acta 221, 91–97. https://doi.org/10.1016/S0003-2670(00)81942-X

Jaireth, S., Hoatson, D.M., Miezitis, Y., 2014. Geological setting and resources of the major rare-earth-element deposits in Australia. Ore Geol. Rev. 62, 72–128. https://doi.org/10.1016/j.oregeorev.2014.02.008

Jordens, A., Cheng, Y.P., Waters, K.E., 2013. A review of the beneficiation of rare earth element bearing minerals. Miner. Eng. 41, 97–114. https://doi.org/10.1016/j.mineng.2012.10.017

Kanehira, S., Kanamori, S., Nagashima, K., Saeki, T., Visbal, H., Fukui, T., Hirao, K., 2013. Controllable hydrogen release via aluminum powder corrosion in calcium hydroxide solutions. J. Asian Ceram. Soc. 1, 296–303. https://doi.org/10.1016/j.jascer.2013.08.001

Kawashima, N., Shi, L., Xu, N., Li, J., Gerson, A.R., 2016. Characterisation of single-stream Bayer plant heat exchanger scale. Hydrometallurgy 159, 75–86. https://doi.org/10.1016/j.hydromet.2015.10.025

Kossoff, D., Dubbin, W.E., Alfredsson, M., Edwards, S.J., Macklin, M.G., Hudson-Edwards, K.A., 2014. Mine tailings dams: Characteristics, failure, environmental impacts, and remediation. Appl. Geochem. 51, 229–245. https://doi.org/10.1016/j.apgeochem.2014.09.010

Krook, J., Svensson, N., Eklund, M., 2012. Landfill mining: A critical review of two decades of research. Waste Manag. 32, 513–520. https://doi.org/10.1016/j.wasman.2011.10.015

Lafuente, B., Downs, R.T., Yang, H., Stone, N., 2015. The power of databases: The RRUFF project, in: Armbruster, T., Danisi, R.M. (Eds.), Highlights in Mineralogical Crystallography. DE GRUYTER, Berlin, München, Boston, pp. 1–30. https://doi.org/10.1515/9783110417104-003

Lamerant, J.-M., 1995. Process for extracting gallium from Bayer liquors using an impregnated absorbent resin, patent no. US5424050 A. US5424050 A.

Lamerant, J.-M., 1992. Process for extracting and purifying gallium from Bayer liquors, patent no US5102512 A. US5102512 A.

Laskou, M., 2001. Chromite in karst bauxites, bauxitic laterites and bauxitic clays of Greece, in: Piestrzynski et al (Ed.), Mineral Deposits at the Beginning of the 21st Century. Presented at the 6th Biennial SGS Meeting, Swets & Zeitlinger Publishers Lisse, Krakow, Poland, pp. 1091–1094.

Laskou, M., Andreou, G., 2003. Rare earth elements distribution and REE-minerals from the Parnassos–Ghiona bauxite deposits, Greece, in: Mineral Exploration and Sustainable Development, 7th Biennial SGA Meeting, Athens. Millpress, Rotterdam. pp. 89–92.

Laskou, M., Economou-Eliopoulos, M., 2013. Bio-mineralization and potential biogeochemical processes in bauxite deposits: genetic and ore quality significance. Mineral. Petrol. 107, 471–486. https://doi.org/10.1007/s00710-012-0257-z

Laskou, M., Economou-Eliopoulos, M., 2007. The role of microorganisms on the mineralogical and geochemical characteristics of the Parnassos-Ghiona bauxite deposits, Greece. J. Geochem. Explor. 93, 67–77. https://doi.org/10.1016/j.gexplo.2006.08.014

Laskou, M., Economou-Eliopoulos, M., Mitsis, I., 2010. Bauxite ore as an energy source for bacteria driving iron-leaching and bio- mineralization. Hell. J. Geosci. 45, 163–174.

Lavalou, E., Bosca, B., Keramidas, O., 1999. Alumina production from diasporic bauxites. Light Met. 55–62.

Lavrenchuk, V.N., Stryapkov, A.V., Kokovin, E.N., 2004. Scandium in bauxite and clay. GUP SO Kamensk-Uralsk Printshop.

Li, Z., Din, J., Xu, J., Liao, C., Yin, F., Lǚ, T., Cheng, L., Li, J., 2013. Discovery of the REE minerals in the Wulong–Nanchuan bauxite deposits, Chongqing, China: Insights on conditions of formation and processes. J. Geochem. Explor., Rare earth elements: The role of geology, exploration, and analytical geochemistry in ensuring diverse sources of supply and a globally sustainable resource 133, 88–102. https://doi.org/10.1016/j.gexplo.2013.06.016

Liu, Z., Zong, Y., Li, H., Zhao, Z., 2018. Characterization of scandium and gallium in red mud with Time of Flight-Secondary Ion Mass Spectrometry (ToF-SIMS) and Electron Probe Micro-Analysis (EPMA). Miner. Eng. 119, 263–273. https://doi.org/10.1016/j.mineng.2018.01.038

Logomerac, V.G., 1971. Distribution of rare-earth and minor elements in some bauxite and red mud produced., in: Proceedings of the Second International Symposium of ICSOBA. Presented at the 2nd International Symposium of ICSOBA, Res. Inst. Non-Ferrous Metals, Budapest, Hungary, 6-10 October 1969, pp. 383–393.

Løvik, A.N., Restrepo, E., Müller, D.B., 2015. The global anthropogenic gallium system: determinants of demand, supply and efficiency improvements. Environ. Sci. Technol. 49, 5704–5712. https://doi.org/10.1021/acs.est.5b00320

Lymperopoulou, T., Tsakanika, L.-A., Ochsenkühn, K.-M., Ochsenkühn-Petropoulou, M., 2017. Optimization of mineral acids leaching process for the recovery of rare earth elements from

Greek red mud, in: Book of Abstracts. Presented at the 2nd Conference on European Rare Earth Resources, Heliotopos Conferences Ltd., Santorini, Greece, pp. 182–184.

Maksimovic, Z., Pantó, G., 1996. Authigenic rare earth minerals in karst-bauxites and karstic nickel deposits, in: Jones, A.P., Wall, F., Williams, C.T. (Eds.), Rare Earth Minerals: Chemistry, Origin and Ore Deposits, Mineralogical Society Series. Chapman & Hall, pp. 257–280.

Maksimović, Z., Panto, G., 1991. Contribution to the geochemistry of the rare earth elements in the karst-bauxite deposits of Yugoslavia and Greece. Geoderma 51, 93–109.

Maksimović, Z., Panto, G., 1980. Bastnäsite-(La) and monazite-(Nd): A new variety of monazite from the Marmara bauxite deposit (Greece). Bull Acad Serbe Sci Arts 20, 35–42.

Manceau, A., Gorshkov, A.I., Drits, V.A., 1992. Structural chemistry of Mn, Fe, Co, and Ni in manganese hydrous oxides: Part II. Information from EXAFS spectroscopy and electron and X-ray diffraction. Am. Mineral. 77, 1144–1144.

Mayes, W.M., Burke, I.T., Gomes, H.I., Anton, Á.D., Molnár, M., Feigl, V., Ujaczki, É., 2016. Advances in Understanding Environmental Risks of Red Mud After the Ajka Spill, Hungary. J. Sustain. Metall. 2, 332–343. https://doi.org/10.1007/s40831-016-0050-z

Menges, F., 2017. Spectragryph - optical spectroscopy software version 1.0.7. Universität Konstanz, Obersdorf, Germany.

Metrohm, 2018. Determination of total caustic, total soda and alumina in Bayer process liquors with 859 Titrotherm [WWW Document]. Appl. Bull. 313 E. URL http://partners.metrohm.com/GetDocument?action=get_dms_document&docid=693348 (accessed 3.23.18).

Meyer, F.M., 2004. Availability of Bauxite Reserves. Nat. Resour. Res. 13, 161–172. https://doi.org/10.1023/B:NARR.0000046918.50121.2e

Mitchell, R., 1996. Perovskites: a revised classification scheme for an important rare earth element host in alkaline rocks, in: Jones, A.P., Wall, F., Williams, C.T.W. (Eds.), Rare Earth Minerals. Chemistry, Origin and Ore Deposits, Mineralogical Society Series. Chapman and Hall, pp. 41–76.

Mitchell, R.H., Welch, M.D., Chakhmouradian, A.R., 2017. Nomenclature of the perovskite supergroup: A hierarchical system of classification based on crystal structure and composition. Mineral. Mag. 81, 411–461. https://doi.org/10.1180/minmag.2016.080.156

Miyawaki, R., Matsubara, S., Yokoyama, K., Takeuchi, K., Terada, Y., Nakai, I., 2000. Kozoite-(Nd), Nd(CO3)(OH), a new mineral in an alkali olivine basalt from Hizen-cho, Saga Prefecture, Japan. Am. Mineral. 85, 1076–1081. https://doi.org/10.2138/am-2000-0724

Moëlo, Y., Lulzac, Y., Rouer, O., Palvadeau, P., Gloaguen, É., Léone, P., 2002. Scandium Mineralogy: Pretulite with Scandian Zircon and Xenotime-(y) Within an Apatite-Rich Oolitic Ironstone from Saint-Aubin-Des-Châteaux, Armorican Massif, France. Can. Mineral. 40, 1657–1673. https://doi.org/10.2113/gscanmin.40.6.1657

Mohapatra, B.K., Mishra, B.K., Mishra, C.R., 2012. Studies on metal flow from khondalite to bauxite to alumina and rejects from an alumina refinery, India, in: Suarez, C.E. (Ed.), Light Metals. John Wiley & Sons, Inc., pp. 87–91.

Momade, F.W.Y., Gawu, S.K.Y., 2009. Geochemical and mineralogical characteristics of Lithomargic clay types from Awaso Bauxite Deposit, Ghana: implications for possible industrial utilization. J. Sci. Technol. 29, 96–106.

Mongelli, G., 1997. Ce-anomalies in the textural components of Upper Cretaceous karst bauxites from the Apulian carbonate platform (southern Italy). Chem. Geol. 140, 69–79. https://doi.org/10.1016/S0009-2541(97)00042-9

Mongelli, G., Boni, M., Oggiano, G., Mameli, P., Sinisi, R., Buccione, R., Mondillo, N., 2017. Critical metals distribution in Tethyan karst bauxite: The cretaceous Italian ores. Ore Geol. Rev. 86, 526–536. https://doi.org/10.1016/j.oregeorev.2017.03.017

Mordberg, L.E., 1993. Patterns of distribution and behaviour of trace elements in bauxites. Third Int. Symp. Geochem. Earth Surf. 107, 241–244. https://doi.org/10.1016/0009-2541(93)90183-J

Mordberg, L.E., Stanley, C.J., Germann, K., 2001. Mineralogy and geochemistry of trace elements in bauxites: the Devonian Schugorsk deposit, Russia. Mineral. Mag. 65, 81–101.

Mouchos, Evangelos, Wall, F., Williamson, B., 2017. High-Ce REE minerals in the Parnassus-Giona bauxite deposits, Greece. Appl. Earth Sci. 126, 82–83. https://doi.org/10.1080/03717453.2017.1306281

Mouchos, E., Wall, F., Williamson, B.J., Palumbo-Roe, B., 2017. Easily leachable rare earth element phases in the Parnassus-Giona bauxite deposits, Greece. Bull. Geol. Soc. Greece 50, 1952–1958. https://doi.org/10.12681/bgsg.14245

Newson, T., Dyer, T., Adam, C., Sharp, S., 2006. Effect of structure on the geotechnical properties of bauxite residue. J. Geotech. Geoenvironmental Eng. 132, 143–151.

Nickel, E.H., McAdam, R.C., 1963. Niobian perovskite from Oka, Quebec; a new classification for minerals of the perovskite group. Can. Mineral. 7, 683–697.

Nuccetelli, C., Pontikes, Y., Leonardi, F., Trevisi, R., 2015. New perspectives and issues arising from the introduction of (NORM) residues in building materials: A critical assessment on the radiological behaviour. Constr. Build. Mater. 82, 323–331. https://doi.org/10.1016/j.conbuildmat.2015.01.069

Ochsenkühn-Petropoulou, M., Ochsenkühn, K., Luck, J., 1991. Comparison of inductively coupled plasma mass spectrometry with inductively coupled plasma atomic emission spectrometry and instrumental neutron activation analysis for the determination of rare earth elements in Greek bauxites. Spectrochim. Acta Part B At. Spectrosc. 46, 51–65.

Ochsenkühn-Petropulu, M., Lyberopulu, T., Ochsenkühn, K.M., Parissakis, G., 1996. Recovery of lanthanides and yttrium from red mud by selective leaching. Anal. Chim. Acta 319, 249–254. https://doi.org/10.1016/0003-2670(95)00486-6

Ochsenkühn-Petropulu, M., Lyberopulu, T., Parissakis, G., 1994. Direct determination of lanthanides, yttrium and scandium in bauxites and red mud from alumina production. Anal. Chim. Acta 296, 305–313. https://doi.org/10.1016/0003-2670(94)80250-5

Ochsenkühn-Petropulu, M., Ochsenkühn, K.M., 1995. Rare earth minerals found in Greek bauxites by scanning electron microscopy and electron probe micro-analysis. Microsc. Anal. 33–34.

Okudan, M.D., Akcil, A., Tuncuk, A., Deveci, H., 2015. Effect of parameters on vanadium recovery from by-products of the Bayer process. Hydrometallurgy 152, 76–83. https://doi.org/10.1016/j.hydromet.2014.12.003

Papanastassiou, D., Contaroudas, D., Solymár, K., 2006. Processing and marketing of Greek diasporic bauxite for metallurgical and non-metallurgical applications, in: Proceedings of the 17th International Symposium of ICSOBA, “Aluminium: From Raw Materials to Applications”, Travaux Vol. 33, No. 37. Presented at the 17th International Symposium of ICSOBA, ICSOBA, Montréal, Canada 1-4 October.

Papp, E., Zsindely, S., Tomcsanyi, L., 1971. Molybdenum and zinc traces in the Bayer process., in: Proceedings of the 2nd International Symposium ICSOBA. Presented at the 2nd International Symposium ICSOBA, Res. Inst. Non-Ferrous Metals, Budapest, Hungary, 6-10 October 1969, pp. 395–402.

Patterson, S., H., 1967. Bauxite Reserves and Potential Aluminum Resources of the World, Geological Survey Bulletin. United States Government Printing Office, Washington, USA.

Patterson, S., H., Kurtz, H., F., Olson, J., C., Neeley, C., L., 1986. World bauxite resources, Geological Survey Professional Paper. United States Government Printing Office, Washington, USA.

Petrakova, O., Klimentenok, G., Panov, A., Gorbachev, S., 2014. Application of modern methods for red mud processing to produce rare earth elements., in: Book of Proceedings. Presented at the ERES2014: 1st European Rare Earth Resources Conference, Heliotopos Conferences Ltd., Milos, pp. 241–251.

Petrascheck, W.E., 1989. The genesis of allochthonous karst-type bauxite deposits of Southern Europe. Miner. Deposita 24, 77–81. https://doi.org/10.1007/BF00206306

Pontikes, Y., 2007. Utilisation of red mud in the heavy clay industry (Αξιοποίηση της ερυθράς ιλύος στη βιομηχανία παραδοσιακών κεραμικών) (PhD thesis). University of Patras, Department of Chemical Engineering, Patras, Greece. http://dx.doi.org/10.12681/eadd/18054.

Popova E. A., Yakovenchuk V. N., Lushnikov S. G., Krivovichev S. V., 2015. Structural phase transitions in loparite-(Ce): evidences from Raman light scattering. J. Raman Spectrosc. 46, 161–166. https://doi.org/10.1002/jrs.4587

Pourret, O., Davranche, M., 2013. Rare earth element sorption onto hydrous manganese oxide: A modeling study. J. Colloid Interface Sci. 395, 18–23. https://doi.org/10.1016/j.jcis.2012.11.054

Power, G., Gräfe, M., Klauber, C., 2011. Bauxite residue issues: I. Current management, disposal and storage practices. Hydrometallurgy 108, 33–45. https://doi.org/10.1016/j.hydromet.2011.02.006

Proenza, J., Aiglsperger, T., Villanova-de-Benavent, C., Torró i Abat, L., Rodríguez-García, D., Ramírez, A., Rodríguez Servicio, J., Nacional, G., Republic, D., 2017. Discovery of REE minerals hosted in karst bauxite ores from the Sierra de Bahoruco, Pedernales, Dominican Republic, in: Mineral Resources to Discover. Presented at the 14th SGA Biennial Meeting, Québec, pp. 1321–1324.

Radusinović, S., Jelenković, R., Pačevski, A., Simić, V., Božović, D., Holclajtner-Antunović, I., Životić, D., 2017. Content and mode of occurrences of rare earth elements in the Zagrad karstic bauxite deposit (Nikšić area, Montenegro). Ore Geol. Rev. 80, 406–428. https://doi.org/10.1016/j.oregeorev.2016.05.026

Reid, S., Tam, J., Yang, M., Azimi, G., 2017. Technospheric Mining of Rare Earth Elements from Bauxite Residue (Red Mud): Process Optimization, Kinetic Investigation, and Microwave Pretreatment. Sci. Rep. 7, 1–9. https://doi.org/10.1038/s41598-017-15457-8

Riley, G., Cornell, R.M., Clarke, P., Fletcher, S., Cornell, J.B., n.d. Effect of titanium species on the precipitation of boehmite under digestion conditions. Hydrometallurgy. https://doi.org/10.1016/j.hydromet.2016.03.015

Ripple, W.J., Wolf, C., Newsome, T.M., Galetti, M., Alamgir, M., Crist, E., Mahmoud, M.I., Laurance, W.F., 2017. World Scientists' Warning to Humanity: A Second Notice. BioScience 67, 1026–1028. https://doi.org/10.1093/biosci/bix125

Rivera, R.M., Ounoughene, G., Borra, C.R., Binnemans, K., Van Gerven, T., 2017. Neutralisation of bauxite residue by carbon dioxide prior to acidic leaching for metal recovery. Miner. Eng. 112, 92–102. https://doi.org/10.1016/j.mineng.2017.07.011

Riveros, P.A., 1990. Recovery of gallium from Bayer liquors with an amidoxime resin. Hydrometallurgy 25, 1–18. https://doi.org/10.1016/0304-386X(90)90060-F

Rollinson, H.R., 1993. Using geochemical data: evaluation, presentation, interpretation. Pearson Education Limited, Harlow, UK.

Ruan, H.D., Frost, R.L., Kloprogge, J.T., 2001. Comparison of Raman spectra in characterizing gibbsite, bayerite, diaspore and boehmite. J. Raman Spectrosc. 32, 745–750. https://doi.org/10.1002/jrs.736

Sajó, I.E., 2008. X-Ray diffraction quantitative phase analysis of Bayer process solids, in: Proceedings. Presented at the 10th International Congress of ICSOBA, Bhubaneshwar, India.

Sajó, I.E., 2005. XDB Powder Diffraction Phase Analytical System version 3.107. Budapest.

Samson, I.M., Chassé, M., 2016. Scandium, in: White, W.M. (Ed.), Encyclopedia of Geochemistry, Encyclopedia of Earth Sciences Series. Springer International Publishing, Cham, Switzerland, pp. 1–5. https://doi.org/10.1007/978-3-319-39193-9_281-1

Santana, F., Tartarotti, F., 2012. Alumina recovery estimation through material balance in Alumar refinery, in: Proceedings of the 19th International Symposium ICSOBA,Travaux, No. 42. Presented at the 19th International Symposium ICSOBA, Belém, Brazil, October 29 - November 2, pp. 1–6.

Santini, T.C., 2015. Application of the Rietveld refinement method for quantification of mineral concentrations in bauxite residues (alumina refining tailings). Int. J. Miner. Process. 139, 1–10. https://doi.org/10.1016/j.minpro.2015.04.004

Sato, C., Kazama, S., Sakamoto, A., Hirayanagi, K., 2013. Behavior of radioactive elements (uranium and thorium) in Bayer process, in: Donaldson, D., Raahauge, B.E. (Eds.), Reprinted in Essential Readings in Light Metals. John Wiley & Sons, Inc., pp. 191–197.

Schlegl, R., Weber, M., Wruss, J., Low, D., Queen, K., Stilwell, S., Lindblad, E.B., Möhlen, M., 2015. Influence of elemental impurities in aluminum hydroxide adjuvant on the stability of inactivated Japanese Encephalitis vaccine, IXIARO®. Vaccine, Vaccine Engineering 33, 5989–5996. https://doi.org/10.1016/j.vaccine.2015.05.103

Schulte, R.F., Foley, N.K., 2014. Compilation of gallium resource data for bauxite deposits (No. 2331–1258). US Geological Survey.

Selvi, P., Ramasami, M., Samuel, M.H.P., Sripriya, R., Senthilkumar, K., Adaikkalam, P., Srinivasan, G.N., 2004. Gallium recovery from Bayer's liquor using hydroxamic acid resin. J. Appl. Polym. Sci. 92, 847–855. https://doi.org/10.1002/app.20047

Shaw, D.M., 1957. The geochemistry of gallium, indium, thallium—a review. Phys. Chem. Earth 2, 164–211. https://doi.org/10.1016/0079-1946(57)90009-5

Singh, U., Mishra, R.S., 2012. Simultaneous multielemental analysis of alumina process samples using inductively coupled plasma spectrometry (ICP-AES). Anal. Chem. Indian J. 11, 1–5.

Smith, P., 2017. Reactions of lime under high temperature Bayer digestion conditions. Hydrometallurgy, Hydrometallurgy Special Issue: AQW Conference 2015 170, 16–23. https://doi.org/10.1016/j.hydromet.2016.02.011

Songqing, G., 2017. The Evolution of Alumina Production Technology in China, New Challenges and Trends, in: Proceedings, Travaux 46. Presented at the 35th International ICSOBA Conference, ICSOBA, Hamburg, Germany, pp. 135–144.

Songqing, G., Zhonglin, Y., 2016. Preheaters and digesters in the Bayer digestion process, in: Essential Readings in Light Metals. Springer, Cham, pp. 356–361. https://doi.org/10.1007/978-3-319-48176-0_47

S&P Global Platts, a division of S&P Global Inc., 2018. Methodology and Specifications Guide, Nonferrous [WWW Document]. URL https://www.platts.com/methodology-specifications/metals (accessed 3.3.18).

Sugita, K., Kobayashi, Y., Taguchi, Y., Takeda, S., Ota, Y., Ojiri, M., Oda, K., Sano, H., 2012. Method of recovering rare-earth elements, patent no US20150086449 A1, United States of America. US20150086449 A1.

Suss, A., Kuznetsova, N.V., Kozyrev, A., Panov, A., Gorbachev, S., 2017. Specific features of scandium behavior during sodium bicarbonate digestion of red mud, in: Travaux 46. Presented at the 35th International ICSOBA Conference, ICSOBA, Hamburg, Germany, pp. 491–504.

Suss, A., Panov, A. v, Pajwani, R., Shah, H., Sinyavsky, V., Stolyar, M., 2002. High titanium bauxites: Specific feature of mineral composition and behaviour in Bayer process, in: Proceedings of the 6th International Alumina Quality Workshop. pp. 180–184.

Suss, A., Paromova, I., Panov, A., Shipova, O.V., Kutkova, N.N., 2008. Behaviour of Berylium in Alumina Production from Bauxites by Bayer Process and Development of Reliable Method of Its Determination, in: De Young, D.H. (Ed.), Proceedings of the Light Metals Conference, Volume 1, Aluminum and Bauxite. TMS (The Minerals, Metals and Materials Society), New Orleans, LA, USA, 9-12 March, pp. 107–112.

Suss, A.G., Rydashevsky, L.S., 1996. Behaviour of bauxite titanium minerals in Bayer process and their influence on the incrustation of heating surfaces. Methods of deposits prevention, in: Travaux No. 27. Presented at the 11th International Symposium of ICSOBA, Balatonfüred, Hungary.

Sweegers, C., de Coninck, H.C., Meekes, H., van Enckevort, W.J.P., Hiralal, I.D.K., Rijkeboer, A., 2001. Morphology, evolution and other characteristics of gibbsite crystals grown from pure and impure aqueous sodium aluminate solutions. J. Cryst. Growth 233, 567–582. https://doi.org/10.1016/S0022-0248(01)01615-3

Teas, E.B., Kotte, J.J., 1980. The effect of impurities on process efficiency and methods for impurity control and removal, in: Proceedings of JBI-JGS Symposium Titled “Bauxite / Alumina Industry in the Americas.” Presented at the JBI-JGS Symposium, Kingston, Jamaica, pp. 100–129.

Thirumalairajan, S., Girija, K., Hebalkar, N.Y., Mangalaraj, D., Viswanathan, C., Ponpandian, N., 2013. Shape evolution of perovskite LaFeO3 nanostructures: a systematic investigation of growth mechanism, properties and morphology dependent photocatalytic activities. RSC Adv. 3, 7549–7561. https://doi.org/10.1039/C3RA00006K

Valeš, V., Matějová, L., Matěj, Z., Brunátová, T., Holý, V., 2014. Crystallization kinetics study of cerium titanate CeTi2O6. J. Phys. Chem. Solids 75, 265–270. https://doi.org/10.1016/j.jpcs.2013.10.001

Valeton, I., 1972. Bauxites, Developments in Soil Science 1. Elsevier Publishing Company, Amsterdam, Netherlands.

Valeton, I., Biermann, M., Reche, R., Rosenberg, F., 1987. Genesis of nickel laterites and bauxites in Greece during the Jurassic and Cretaceous, and their relation to ultrabasic parent rocks. Ore Geol. Rev. 2, 359–404. https://doi.org/10.1016/0169-1368(87)90011-4

Vidal, O., Rostom, F., François, C., Giraud, G., 2017. Global Trends in Metal Consumption and Supply: The Raw Material–Energy Nexus. Elements 13, 319–324. https://doi.org/10.2138/gselements.13.5.319

Vind, J., Malfliet, A., Bonomi, C., Paiste, P., Sajó, I.E., Blanpain, B., Tkaczyk, A.H., Vassiliadou, V., Panias, D., 2017a. Modes of occurrences of scandium in Greek bauxite and bauxite residue. Submitt. Miner. Eng. 15122017.

Vind, J., Paiste, P., Tkaczyk, A.H., Vassiliadou, V., Panias, D., 2017b. The behaviour of scandium in the Bayer process, in: Book of Abstracts. Presented at the 2nd Conference on European Rare Earth Resources, Heliotopos Conferences Ltd., Santorini, Greece, pp. 190–191.

Wagh, A.S., Pinnock, W.R., 1987. Occurrence of scandium and rare earth elements in Jamaican bauxite waste. Econ. Geol. 82, 757–761. https://doi.org/10.2113/gsecongeo.82.3.757

Wall, F., Rollat, A., Pell, R.S., 2017. Responsible Sourcing of Critical Metals. Elements 13, 313–318. https://doi.org/10.2138/gselements.13.5.313

Wang, Q., Deng, J., Liu, X., Zhang, Q., Sun, S., Jiang, C., Zhou, F., 2010. Discovery of the REE minerals and its geological significance in the Quyang bauxite deposit, West Guangxi, China. J. Asian Earth Sci., Tectonics of the Indian Subcontinent 39, 701–712. https://doi.org/10.1016/j.jseaes.2010.05.005

Weber, W.H., Hass, K.C., McBride, J.R., 1993. Raman study of CeO2: Second-order scattering, lattice dynamics, and particle-size effects. Phys. Rev. B Condens. Matter 48, 178–185.

Wellington, M., Valcin, F., 2007. Impact of Bayer Process Liquor Impurities on Causticization. Ind. Eng. Chem. Res. 46, 5094–5099. https://doi.org/10.1021/ie070012u

Whittington, B.I., 1996. The chemistry of CaO and Ca(OH)2 relating to the Bayer process. Hydrometallurgy 43, 13–35. https://doi.org/10.1016/0304-386X(96)00009-6

Xiao, J., 1996. Distribution characteristics of scandium in the red mud of industrial wastes. Geol Geochem 82–86.

Yagmurlu, B., Dittrich, C., Friedrich, B., 2017. Precipitation Trends of Scandium in Synthetic Red Mud Solutions with Different Precipitation Agents. J. Sustain. Metall. 3, 90–98. https://doi.org/10.1007/s40831-016-0098-9

Yamada, Y., 2010. X-ray fluorescence analysis by fusion bead method for ores and rocks. Rigaku J 26, 15–23.

Yang, H., Dembowski, R.F., Conrad, P.G., Downs, R.T., 2008. Crystal structure and Raman spectrum of hydroxyl-bästnasite-(Ce), CeCO3(OH). Am. Mineral. 93, 698–701. https://doi.org/10.2138/am.2008.2827

Zaitsev, A.N., Chakhmouradian, A.R., Siidra, O.I., Spratt, J., Williams, C.T., Stanley, C.J., Petrov, S.V., Britvin, S.N., Polyakova, E.A., 2011. Fluorine-, yttrium- and lanthanide-rich cerianite-(Ce) from carbonatitic rocks of the Kerimasi volcano and surrounding explosion craters, Gregory Rift, northern Tanzania. Mineral. Mag. 75, 2813–2822. https://doi.org/10.1180/minmag.2011.075.6.2813

Zhang, N., Li, H.-X., Cheng, H.-J., Liu, X.-M., 2017. Electron probe microanalysis for revealing occurrence mode of scandium in Bayer red mud. Rare Met. 36, 295–303. https://doi.org/10.1007/s12598-017-0893-x

Zhang, N., Li, H.-X., Liu, X.-M., 2016. Recovery of scandium from bauxite residue—red mud: a review. Rare Met. 35, 887–900. https://doi.org/10.1007/s12598-016-0805-5

Zhao, Z., Long, H., Li, X., Fan, Y., Han, Z., 2012a. Precipitation of vanadium from Bayer liquor with lime. Hydrometallurgy 115–116, 52–56. https://doi.org/10.1016/j.hydromet.2011.12.001

Zhao, Z., Yang, Y., Xiao, Y., Fan, Y., 2012b. Recovery of gallium from Bayer liquor: A review. Hydrometallurgy 125–126, 115–124. https://doi.org/10.1016/j.hydromet.2012.06.002

Zhong-Lin, Y., Song-Qing, G., 1995. Development of research on the scaling problem in Bayer process. Light Met. 155–159.

Zhuk, Y., 2017. Critical Assessment of the Mineralogical Collections at Uppsala University using Raman Spectroscopy (MSc). Uppsala University, Uppsala, Sweden.

Zoldi, J., Solymar, K., Zambo, J., Jonas, K., 1987. Iron hydrogarnets in the Bayer process. Light Met. 105–111.